Int J CARS (2013) 8 (Suppl 1):S263–S336
DOI 10.1007/s11548-013-0880-0

Construction of local probabilistic atlas based on relationship between organ location and its application to pancreas segmentation

C. Chu[1], Y. Hayashi[2], Y. Nimura[2], M. Oda[2], K. Misawa[3], T. Kitasaka[4], D. Rueckert[5], K. Mori[1,2]
[1]Nagoya University, Graduate School of Information Science, Nagoya, Japan
[2]Nagoya University, Strategy Office, Information and Communications Headquarters, Nagoya, Japan
[3]Aichi Cancer Center, Nagoya, Japan
[4]Aichi Institute of Technology, School of Information Science, Nagagute, Japan
[5]Imperial College London, Department of Computing, London, United Kingdom

Keywords Pancreas · Segmentation · Probabilistic Atlas · Organ Relationship

Purpose

The development of a CAD system for pancreatic cancer diagnosis is desired by radiologists. The accurate segmentation of the pancreas from CT image is a crucial first step in such a CAD system.

Pancreas segmentation of CT images is a challenging task. Most of the previous organ segmentation methods based on global probabilistic atlases (PAs) are robust in segmentation of the liver, the spleen, the kidneys, and other organ regions. However, only few of them perform well in segmenting the pancreas. The best performance among them is only 58 % of Jaccard index. However, this is still low compared to the segmentation performance for other organs.

Pancreas segmentation of abdominal CT images is difficult due to the large difference between patients in regards to pancreatic shape and position. Global PAs of pancreas often have diffuse probability maps that are not informative for pancreas segmentation. However, the pancreas has specific positional relationships with the surrounding organs including the liver. Based on the information from these surrounding organs, we identified a local region containing the pancreas. We then constructed PAs in this local region to reduce the large difference in the pancreatic shape and position between patients.

This paper proposes a method for the construction of local PAs and its application to pancreas segmentation. We summarize our method in the following two steps. In the first step, we use the location of liver to estimate the center of gravity of the pancreas to identify the existence region of pancreas. In the second step, PAs are constructed in each existence region of pancreas for each target image dynamically. In this context, the target image refers a new image in which segmentation is performed. We apply the constructed PAs to a MAP estimation and graph cuts method to obtain the final segmentation results.

Methods

VOI identification of the pancreas

The pancreas has specific positional relationships with the surrounding organs, especially with the liver. It is elongated between the liver and the spleen. Since many segmentation methods can generate very robust and accurate results for liver segmentation, we use the center of gravity of the entire liver area and an average distance between the liver and the pancreas to estimate the center of gravity of the pancreas. Then we extract a cubic region which is centered at the pancreas' center of gravity with sides of lengthr [voxels] in the axial, coronal, and sagittal directions. This region is referred to as VOI of the pancreas in our paper. We apply this process to all of the atlas images and the target image. Here, the atlas image is a CT image with a manual segmentation result of organs.

Construction of PAs

After we extract the VOI for all of the atlas images and target images, we construct PAs for each target image in the VOI region dynamically.

In the VOI region, we firstly register all of the atlas images to the target image using an MRF-based non-rigid registration method. We then calculate the similarities between the target image and all of the atlas images. We select theNtop ranked similar atlas images that have higher similarities. By fusing the selectedNatlas images, we generate a PA for target image.

We then apply the PA to the MAP estimation to obtain a rough segmentation result. The rough segmentation result is then refined by a graph cuts method. Figure 1 shows the flowchart of the proposed method.

Results

We evaluated the proposed method on a dataset of 100 cases of 3D portal-phased abdominal CT images. For all of the 100 images, we computed a segmentation result of pancreas with a leave-one-out strategy. The parameterris set as 150 [voxels] for the VOI identification process. For the construction of PAs, we chose top rankedNsimilar atlas CT images for the target image. The Jaccard index is used as evaluation criteria. An average Jaccard index of segmentation results of 60.0 ($\pm$18.2) % was obtained for case of $N = 15$ in our experiment. The segmentation performance is better

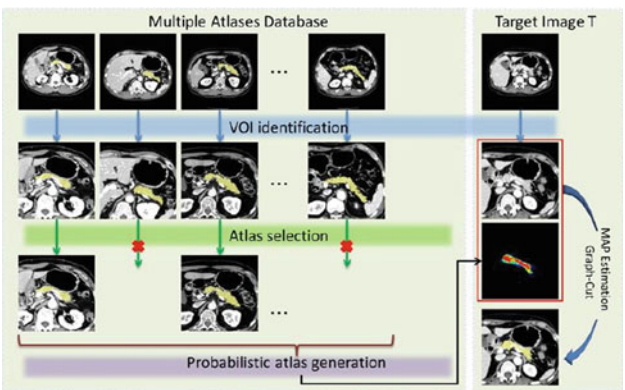

Fig. 1 Flowchart of the proposed method

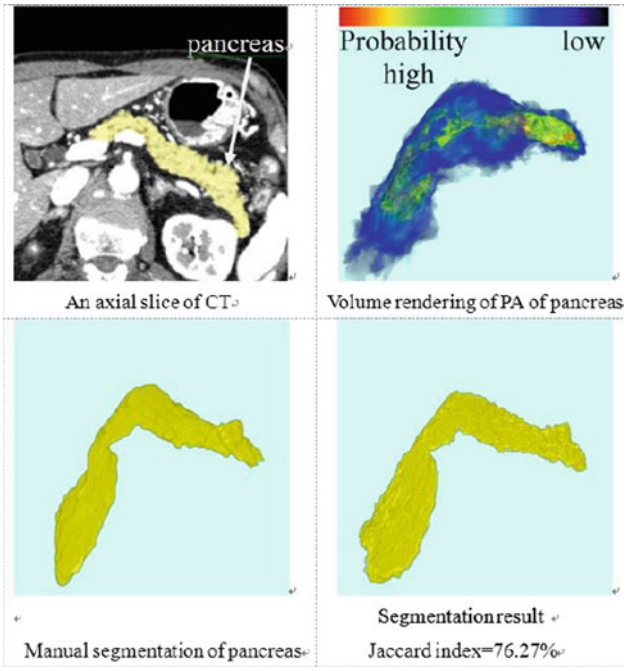

Fig. 2 Example of segmentation result of pancreas

than the best reported performance of the previous methods. Figure 2 shows an example of segmentation result.

In our research, the best performance was obtained when N = 15. This number would changes if the number of the atlas image was changed. More experiments are need to find the most appropriate value of the parameterN.

We used the value of 150 [voxels] as the radiusrof the VOI. From our observation, some parts of the stomach, liver, spleen, and other organs are still included in the VOI of the pancreas by using this value. To construct PAs which represents the pancreas area much better, the size of the VOI should be reduced to remove outside areas of the pancreas from the VOI.

Conclusion

This paper presented a construction method of local PAs for the pancreas. We applied it to pancreas segmentation from 3D abdominal CT images. We extract VOI of the pancreas and construct PAs dynamically for segmentation of each target image. We evaluated the segmentation performance of the proposed method in 100 CT images. The segmentation result showed 60.0 % in terms of Jaccard index, which is higher than all of the other previous works. Future work includes improvement of the VOI extraction, improvement of similar atlas image selection method, and increasing of the number of the atlas images.

The liver imaging atlas: an interactive E-learning tool for liver imaging

O. Kolokythas[1], S. Osman[1], S. Zaidi[1], L. Peguero Alemany[1], S. Bastawrous[1,2], A. Tornow[3], L. Mitsumori[1], C. Cuevas[1], P. Bhargava[1,2], G. Phillips[1,4], M. Dighe[1], C. Sadro[1], N. Lalwani[1], D. Coy[1]

[1]University of Washington, Radiology, Seattle, WA, United States
[2]VA Puget Sound Health Care System Home, Seattle, WA, United States
[3]Columbus Radiology Corporation, Columbus, OH, United States.
[4]Seattle Children's Hospital, Seattle, WA, United States

Keywords Liver · Imaging · Internet · E-Learning

Purpose

The objective is to introduce the Liver Imaging Atlas—a freely available, comprehensive, and interactive web-based atlas of liver imaging designed for use by diagnostic radiologists as a imaging reference and as an educational aid for radiologists-in-training.

Methods

We have designed and developed an interactive open source platform to which computed tomography (CT), magnetic resonance (MR), and ultrasound images of liver disease have been uploaded to create a comprehensive atlas of liver imaging. Each case is categorized by its modality-specific imaging features such as contrast enhancement characteristics, disease category, and final diagnosis.

A user-friendly interface was designed to allow radiologists to review the cases in different ways, based on their needs. For instance, the cases in the atlas can be searched and retrieved based on the presence or absence of one or more imaging features, which allows the user to construct image-based differential diagnoses. Users can view cases based on diagnostic categories (e.g., infection, primary neoplasm, etc.) and switch between the CT, MR and ultrasound modalities.

To facilitate use of the Liver Imaging Atlas for radiology educators and trainees, a training mode was designed, which allows users to view the cases as unknowns. The bookmark feature was designed to facilitate collection of cases by users and educators, and the email feature to aid communication of interesting cases between users.

Results

The interactive website www.liveratlas.org is powered solely by open source systems. It allows the authors to upload and categorize multimodality cases with liver pathology using a dedicated tagging system that form a relational database. For each search the user must select an imaging modality—CT, MR or ultrasound. Searches can be saved and run in each modality.

Users can search the atlas and retrieve cases by one or more imaging features, diagnoses, disease categories, or by free text search.

Features are divided into structural and imaging features. Imaging features are those that are specific to each modality such as dynamic contrast enhancement pattern. Structure features are those characteristics that are usually shared between imaging modalities.

Searching and retrieving cases using disease categories is performed by a Boolean search function—i.e., logic of "or" or "and" operations—which allows users to perform broad or narrow searches, respectively.

The relational database allows seamless switching between search modes. For example, if a search performed using features or free text retrieves cases with different diagnoses, the user can then select any of the diagnoses or disease category to view all cases with the chosen diagnosis or disease category. Quiz mode can be used by educators to show cases to trainees as unknowns, or by the trainees themselves as a self-assessment tool. Each case has been categorized by its level of difficulty (1 = easy, 2 = moderate, 3 = difficult). This allows trainees and educators to customize their assessments to an appropriate level. All searches and operations can be performed to include all or a single specified level of difficulty.

Cases can be shared via emailed link or bookmarked to a user account. The bookmark feature allows educators to prepare presentations or training sessions. Search operations can be performed with the entire atlas, bookmarked cases, or a subset of bookmarked cases.

More cases will be entered into the system in the future to allow for more disease entities not currently available and in order to keep the atlas updated with the newest techniques within the three imaging modalities.

Conclusion

The website www.liveratlas.org is a free, interactive, and comprehensive atlas of liver imaging designed for radiologists as a reference

and learning tool of liver pathology on CT, MR and ultrasound. It allows radiologists in practice and in training to view examples of common and rare liver pathologies, explore and sharpen their differential diagnoses in specific clinical scenarios, assess their knowledge of liver imaging, and select cases to save and share. The atlas database is constantly updated and expanded to broaden its scope and depth.

Comparison of overall accuracy in Linac- and cyberknife-radiosurgery

M. Hoevels[1], H. Treuer[1], S. Hunsche[1], K. Luyken[1], M. Ruge[1], F. El Majdoub[1], M. Maarouf[1]
[1]University Hospital of Cologne, Stereotaxy, Cologne, Germany

Keywords Radiosurgery · CyberKnife · Linac · Accuracy · E2E-test

Purpose

The cyberknife (Accuray, Sunnyvale, USA)was in the first hand designed for the treatment of intracranial lesions. Therefore the demand for the system-wide overall accuracy is very pronounced and is specified to 0.95 mm by the manufacturer.

This level of accuracy is regarded as an essential precondition for a safe application of radiosurgery, in particular for intracranial or spinal lesions.

Methods

In order to establish and maintain this level of accuracy, a specialized variant of the system test, the so called End-to-End(E2E)-test, is provided by the cyberknife system. An essential part of this E2E-test is the head-neck-phantom as shown below, which includes the ball-cube. This structure consist of two materials with different Hounsfield values and therefore the ball can be easily identified as target volume, while containing two gafchromic films in order to measure the dose distribution in two orthogonal planes at the same time. This phantom undergoes the same procedure as performed in patient treatment, including CT imaging, treatment planning and dose delivery. The operator of the E2E-test is widely assisted by the MULTIPLAN planning system in several concerns:

1. The definition und alignment of the target volume onto the image of the ball
2. The alignment of the dose distribution onto this target volume
3. The standardized evaluation of the exposed films by an external program.

In this study the design of the E2E-test is ported to Linac radiosurgery, with the head-neck-phantom being fixed to the stereotactic frame. The definition of the target volume and the dose alignment is driven by a specialised home grown software, while the dose calculation for the micro-MLC is done by the VIRTUOS program (Fig. 1).

The refinement of the dose placement is done in several iterations: the initial target point is placed in the center of gravity of the target volume. The resulting dose cube is reimported and the field displacement with respect to the contour is calculated. Delta values for the X-, Y- and Z-axis are determined and applied for the next iteration (Fig. 2).

The standardized evaluation of the exposed films utilizes the same software from Accuray.

Results

By porting this method from the cyberknife to the Linac, the overall accuray in Linac radiosurgery as described by the E2E-test can be determined in an almost equivalent manner to the cyberknife system. With this approach, quantitative results of achievable overall accuracy under realistic and standardized conditions for both treatment modalities can be evaluated. Preliminary results show almost comparable results in both modalities in our institution.

Fig. 1 Phantom planning in Multiplan

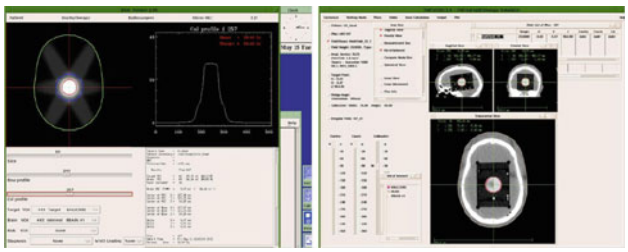

Fig. 2 Alignment and calculation of the dose distribution

Conclusion

Our results suggest, that the targeting and dose delivery of the cyberknife is not superior to a treatment performed by a well-adjusted Linac, with respect to physical dose distribution. Other advantages, such as the lack of invasive fixation and the more comfortable course of the treatment procedure for the patient still persist.

Development of non-invasive CT scan based monitoring in studying pulmonary toxicity induced by whole thoracic irradiation

C. Zhou[1,2,3], J. Bauer[2], S. Brons [2], M. Moustafa[1,2,3], Y. Dai[1,2,3], J. Debus [1,2,3], A. Abdollahi[1,2,3], L. Cao[3,4]
[1]Translational Radiation Oncology, National Center for Tumor Diseases (NCT), German Cancer Research Center (DKFZ), Heidelberg, Germany
[2]Heidelberg Ion Therapy Center (HIT), Department of Radiation Oncology, University Heidelberg Medical School, Heidelberg, Germany
[3]German Consortium for Translational Cancer Research (DKTK), German Cancer Research Center (DKFZ), Heidelberg, Germany
[4]Division of Medical Physics in Radiology, German Cancer Research Center (DKFZ), Heidelberg, Germany

Keywords Quantitative CT monitoring · 3-Dimentional segmentation · Micro-CT · Pulmonary toxicity · Whole thoracic irradiation

Purpose

Quantitative assessment of lung toxicity in mouse models based on CT investigation has been intensively studied. The currently available methods, however, are biased by subjective selection of region of interests (ROIs) [1, 2] and/or the limited animal throughput when

using respiratory-gated small animal scanners [3]. The purpose of this study is to establish a method to quantify the lung parenchyma density and volume based on an objective 3D segmentation algorithm, and to correlate these data with high resolution animal micro-CT device.

Methods

Whole thoracic proton and photon irradiation was administrated to 6–8 weeks C57BL/6 mice (Taconis, Bomholtvej, Denmark), with a single fraction dose of 20 Gy. Prior to thoracic irradiation, mice were anesthetized by an intraperitoneal application of 0.36 ml/kg Rompun 2 % (Bayer HealthCare) and 0.54 ml/kg Ketamin 10 % (Pfizer). CT imaging was performed under isoflurance anesthesia (2 % isoflurane, 2 l/min oxygen).

Proton irradiation was administrated at the Heidelberg Ion Therapy Center (HIT). The mice were treated with specially designed devices in which multiple animals were simultaneously immobilized. Photon irradiation was delivered by X-RAD 320 X-ray Biological Irradiator (Precision X-ray, Inc., 320.0 kV/12.5 mA) with a gantry position in horizontal direction and the mice in supine position.

A clinical PET/CT scanner (Biograph mCT, Siemens) was applied for quantitative CT imaging pre- and post-irradiation. The standard protocol employed for the CT portion of PET/CT was as follows: 80 kV with 80 mAs, a pitch of 0.6 mm, slice thickness of 0.6 mm and acquisition time of 32 s. X-ray exposure is approximately 4.14 mGy per scan. Images were reconstructed using the filter kernel H50 s (Siemens) into a transaxial FOV of 138 × 138 mm^2 as a 512 × 512 matrix, where three animals were included in one scan.

Images acquired from the clinical CT scanner were viewed and analyzed in OsiriX Imaging Software (OsiriX v.3.9.4 64bit version, Pixmeo SARL, Switzerland). Because of the relatively low-resolution feature of the images, the HU intensities of micro-vasculature were averaged with the surrounding air-contained tissues. The lung, together with all the micro-structures, was thereby segmented using a 3D regional growing algorithm with a lower threshold of −900 HU and an upper threshold of −100 HU. Trachea and primary bronchi were manually resected upon segmentation. Volume sizes and mean HU values within the segmented area were calculated for quantitative assessment of pulmonary toxicity.

Micro-CT imaging with a specific small animal CT system was also performed at the corresponding time points for further validation of clinical CT results. CT acquisitions were performed at 40 kV tube voltage, 0.4 mA anode current, 1 s acquisition time per projection, 240 projections per 360° rotation. Images were reconstructed into a matrix of 256 × 256 × 512 with a voxel size of 0.13 mm.

Results

The three-dimensional segmentation using regional growing algorithm represented a good isolation of lung from surrounding tissues, attributing to its full air-containing property. From the 16 weeks post irradiation images, lungs irradiated with photon beams exhibit an apparently alternated morphology in comparison to the age-matched control. More prominent modifications are observed in proton treated mice with a sharply contracted volume.

We next sought to determine the lung density and volume changes, the two key quantitation readouts for longitudinal monitoring. Lung density, represented as the mean HU value of the entire lung area in CT, was calculated from segmented lungs. Significant statistical differences between the proton/photon irradiated mice was observed after 16 weeks post-irradiation ($p = 0.05$ and $p = 0.004$, respectively). This is also in alignment with reduced overall lung volume in irradiated mice. These findings were confirmed by high resolution micro-CT monitoring.

Conclusion

Small animal pulmonary toxicity has been previously studied with different strategies, e.g., respiratory-gated micro-CT [3] and inflated lung ex vivo imaging [4]. To our knowledge, in vivo CT lung parenchyma density quantification is hitherto based on ROIs selection, acquired from a micro-CT [1] or high resolution CT scanner [2]. This is rather subjective as which may not completely represent the lung as a full organ and inter-individual variations are also inevitable. The 3D segmentation we report in this study offers a novel approach for an objective assessment. It is incorporating the bronchioles, alveoli and capillaries as an entire functioning part of a lung, provides a more comprehensive assessment of lung parenchyma.

In contrast to current CT and micro-CT methods, in which animal is exposed to 120–150 mGy X-ray during imaging [5], the dose in the present imaging protocol is as low as 4.14 mGy. Moreover, three mice were included per scan but in a relatively short acquisition time of 32 s, indicating a good feasibility for large scale animal trials.

In conclusion, quantitative 3D lung segmentation based CT assessment is reliable, objective and sensitive in studying murine radiation pulmonary toxicity. In addition, in comparison to conventional CT investigations, it provides superior reproducibility and cost-effectiveness.

References

[1] Jackson IL, Vujaskovic Z, Down JD (2010). Revisiting strain-related differences in radiation sensitivity of the mouse lung: recognizing and avoiding the confounding effects of pleural effusions. Radiat Res 173:10–20.

[2] Abdollahi A, Li M, Ping G, Plathow C, Domhan S, Kiessling F, Lee LB, McMahon G, Gröne HJ, Huber PE (2005). Inhibition of platelet-derived growth factor signaling attenuates pulmonary fibrosis. J Exp Med. 201:925–935.

[3] Badea C, Hedlund LW, Johnson GA (2004) Micro-CT with respiratory and cardiac gating. Med. Phys. 31:3324–3329

[4] Chaturvedi A, Lee Z (2005) Three-dimensional segmentation and skeletonization to build an airway tree data structure for small animals. Physics in Medicine and Biology. 50(7):1405–1419

[5] Cavanaugh D, Johnson E, Price RE, Kurie J, Travis EL, Cody DD (2004) In vivo respiratory-gated micro-CT imaging in small-animal oncology models. Molecular Imaging 3(1): 55–62.

The usage of deformable phantoms for personalized dosimetry in radionuclide therapy

S. Wiessalla[1], H.R. Kulkarni[1], C. Schuchardt[1], R.P. Baum[1], M. Blaickner[2]

[1]Zentralklinik Bad Berka, Theranostics Centre for Molecular Radiotherapy and Molecular Imaging, Bad Berka, Austria

[2]AIT Austrian Institute of Technology, Health & Environment Department, Vienna, Austria

Keywords Deformable phantom · Peptide receptor radionuclide · Personalized dosimetry · Subdivision surface

Purpose

State of the art, three dimensional (3D) and voxel-based dosimetry approaches in radionuclide therapy are capable to calculate the absorbed dose to each voxel. However, without any form of segmentation of the underlying PET/CT or SPECT/CT data the affiliation of a voxel, i.e., the organ or tissue, is not known a priori. Manual segmentation is an option but very time consuming and prone to intra-observer variations. Therefore the aim of this work is to lay the foundation for a radionuclide therapy treatment planning system that is able to perform dose calculations on a fully segmented as well as deformable phantom which matches the individual patient anatomy and thus enables personalized dosimetry.

Methods

The computational approach consists of two basic steps: (i) semiautomatic segmentation of a few organs of interest on the CT, producing a subdivision surface (SubD) that describes the organ boundaries and serves as blueprint for the (II) non-uniform deformation of a

predefined, deformable SubD phantom. For this a Python code was implemented which superimposes an initial, quadrangular surface mesh on a tomographic image and then uses a 3D gradient vector flow (GVF) algorithm to make the initial surface converge at the organs' surface. In the second step predefined SubD phantoms produced in previous works were used. The deformation of the respective SubD organ is realized by means of a signed distance field that morphs the surface to match the topology of the segmentation result and thus takes the shape of the individual organ.

Results

The 3D-GVF proves to be stable as well as convergent for binary test data and requires very little computation time (<1 s). The morphing algorithm for the SubD surface is also stable and works independently of its initial positioning, i.e., at the morphing's outset the surface can be partially inside and outside the segmented binary matrix. Surface coordinates of the transformed SubD organs are retained and can be used as reference points for atlas mapping. All SubD structures can be discretized into any voxel size and thus incorporate every given PET or SPECT data, thus enabling personalized, voxel based dosimetry in a fully segmented spatial domain.

Conclusion

The use of deformable SubD phantoms combines voxel based, personalized dosimetry with the advantage of a fully segmented phantom that matches the individual patient's anatomy. In future works the computer models will be applied to clinical ^{68}Ga-DOTA PET/CT and ^{177}Lu-DOTA SPECT/CT scans of peptide receptor radionuclide therapy (PRRNT) patients from the Zentralklinik in Bad Berka in order to retrospectively perform personalized dosimetry and to subsequently investigate the dose–response relationship and organ toxicities of gastroenteropancreatic neuroendocrine tumours (GEP-NET) treated with PRRNT.

Optimized order estimation for autoregressive models to predict respiratory motion

R. Dürichen [1], T. Wissel[1], A. Schweikard[1]
[1]Institute for Robotics and Cognitive Systems, University of Luebeck, Luebeck, Germany

Keywords Computer assisted radiation therapy · Respiratory motion compensation · Autoregressive models · Information criteria

Purpose

The compensation of tumor movements is a challenging problem in stereo-tactic body radiotherapy (SBRT). In recent years, precise irradiation of moving tumors while sparing surrounding critical structures has become more and more feasible due to new technical developments such as dynamically adjusting multileaf collimators, robotic patient couches, Vero or the CyberKnife Synchrony system [1]. All techniques mentioned have to compensate for various sources of latencies. In the case of the CyberKnife Synchrony system, the latency is 115 ms and mainly caused by mechanical limitations, image acquisition and processing time. For other systems, e.g., robotic couches, the time delays can be up to 300–400 ms. This systematic error can be reduced by time series prediction of external surrogates.

In recent years, several approaches have been investigated. As many prediction algorithms are based on the autoregressive (AR) properties of the signal, one important parameter is the model order p. It defines the number of previous observations needed to perform an accurate prediction.

Here, we investigate different approaches for estimating the model order p for respiratory motion data. We exemplarily chose a classical least mean square (LMS) and the wavelet based LMS (wLMS) algorithm—one of the currently most promising prediction. We aim to increase the practicability of these algorithms by evaluating the Akaike information criterion (AIC), the corrected Akaike information criterion (AICc) and the Bayesian information criterion (BIC) on the first minute of the signal.

Methods

For our experiments, we use a data set, which consists of 304 motion traces and is available online (http://signals.rob.uni-luebeck.de). The signal amplitude y_t of the motion traces was equidistantly sampled ($f_s = 26$ Hz) and has a length of N samples. Let δ be the prediction latency, which is $\delta = 3$ samples in case of the CyberKnife, corresponding to 115 ms. The output of the prediction algorithm is denoted by $\hat{y}_{t+\delta}$. To compare the prediction results, irrespective of the patient specific respiration amplitude, all experiments were evaluated with respect to the relative root mean square (RMS) error. It is defined as squared prediction error relative to the squared prediction error in case of no prediction [2].

Ernst et al. [2] showed that respiratory motion signals can be predicted with high accuracy by combining an à trous wavelet decomposition with least mean square (LMS) methods. The signal is described as superposition of $J + 1$ scales, containing of the detail coefficients W_j and the approximation coefficients c_J. Assuming AR properties for W_j and c_J, an LMS prediction algorithm can be applied to each scale. Thus, for each LMS predictor, a model order p_j, valid for a certain frequency range, can be selected. The predicted point $\hat{y}_{t+\delta}$ is the sum of the predictions of each scale.

To calculate the optimal order p, we estimate the autoregression coefficients a_p and the residual root mean square (RMS_p) error using Burg's method. Generally, as the order increases, the model is capable of explaining more complex characteristics and the error decreases. Unfortunately, it is not straightforward to determine the optimal model order without cross validation, which requires further data. Several information criteria have been developed to overcome this problem. Here, we evaluate AIC, AICc and BIC, which are defined as [3]:

$$AIC = N * \log(RMS_p) + 2p, \quad AIC_c = AIC + \frac{2p(p+1)}{N-p}, \quad BIC = n * \log(RMS_p) + p * \log(N) \tag{1}$$

The optimal orders p_{AIC}, p_{AICc} and p_{BIC} are the orders which minimize the corresponding information criteria.

Results

In a first experiment, we compare the order estimations of the information criteria using 12 randomly chosen traces for the LMS and wLMS predictor. We compute the optimal order on a training set ($t_{train} = 1$ min) and use these orders to predict on a test set (the following $t_{test} = 5$ min). As a ground truth, the RMS_{rel} of the LMS and wLMS algorithm was computed on the test set by grid search for orders p grid $= \{1, \ldots, 100\}$. The estimated order for BIC was lower than for AIC and AICc, which led to a worse prediction accuracy. AIC and AICc always estimated the same model order, indicating that no further correction term is needed. Based on these results AIC was evaluated on all 304 motion traces. Beside computing the AIC order for LMS and wLMS on the original signals (LMS_{AIC} and $wLMS_{AIC}$), the AIC order $p_{AIC,j}$ was computed for each wavelet scale. We refer to the prediction results of this method as $wLMS_{AIC,scale}$. All AIC based algorithms have been compared to the results of the original wLMS implementation $wLMS_{org}$ [2]. The cumulative rel. RMS error difference is shown in Fig. 1, defined as the rel. RMS difference between one the one hand LMS_{AIC}, $wLMS_{AIC}$, $wLMS_{AIC,scale}$ and on the other hand $wLMS_{org}$. The auxiliary line at 0 % separates the percentage of data for which AIC based algorithms are better or equally good as $wLMS_{org}$. This is the case for 66.5 % of the data for LMS_{AIC}, for 83.7 % for $wLMS_{AIC}$ and for 92.7 % for $wLMS_{AIC,scale}$.

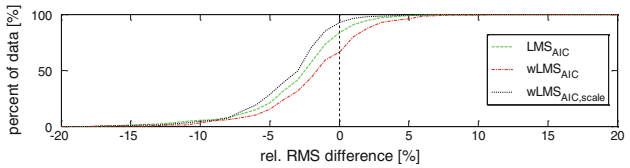

Fig. 1 Cumulative histogram for the rel. RMS error difference between $wLMS_{org}$ and LMS_{AIC}, $wLMS_{AIC}$ and $wLMS_{AIC,scale}$ for 304 motion traces

Conclusion

We conclude that among the investigated information criteria, the highest prediction accuracy can be achieved by using the Akaike information criterion. In case of wLMS, the original implementation was improved for 85.1 % of the cases using AIC. Finally, we want to highlight that due to its general characteristics, this order estimation is not limited to wLMS and can be used for other respiratory motion algorithms.

References

[1] Schweikard A, Glosser G, Bodduluri M, Murphy MJ, Adler JR (2000) Robotic Motion Compensation for Respiratory Movement during Radiosurgery, Computer Aided Surgery, no. 5, pp. 263–277.

[2] Ernst F, Schlaefer A, Schweikard A (2007) Prediction of Respiratory Motion with Wavelet-Based Multiscale Autoregression, Medical Image Computing and Computer-Assisted Intervention—MICCAI 2007, vol. 4792, pp. 668–675, Brisbane.

[3] Hastie T, Tibshirani R, Frieman J (2011) The Elements of Statistical Learning: Data Mining, Inference, and Prediction. Springer Berlin.

Comparative evaluation study for centerline and straight-line length of the external carotid artery based on 3D-CT angiography

T. Ohya[1], T. Iwai[1], K. Mitsudo[1], T. Kato[2], N. Kanazawa[2], J. Wang[2], H. Liao[2], E. Kobayashi[2], I. Sakuma[2], I. Tohnai[1]

[1]Yokohama City University Graduate School of Medicine, Dept. of Oral and Maxillofacial Surgery, Yokohama, Japan

[2]The University of Tokyo Graduate School of Engineering, Dept. of Precision Engineering, Tokyo, Japan

Keywords Centerline · Length · External carotid artery · Intra-arterial infusion · CT angiography

Purpose

Superselective intra-arterial chemo radiotherapy via the superficial temporal and/or occipital artery is effective treatment for oral cancer clinically. This catheterization can provide high concentration anticancer drugs into the tumor feeding arteries (the maxillary, facial and lingual artery). However, this method requires surgeon's experiences and skills for catheter placement into the target artery because they can't see the tip of catheter directly. Surgeons rely on the two-dimentional C-arm image intraopelatively. There are main problems associated with this technique such as the prolonged operation time, increased radiation exposure and increased dose of contrast medium, especially in difficult cases. To overcome these problems, we have developed a prototype of electromagnetic maxillofacial catheter navigation system [1]. This system provides the operator the three-dimensional external carotid artery (ECA) image intraoperatively. But the difference between three-dimentional ECA measurement (e.g., surface rendering models created using CTA image) and two-dimentional ECA measurement (e.g., two-dimentional C-arm image) is not clear. If the straight-line length from frankhorizontal plane (F–H plane) to each bifurcation points have a strong correlation to the curve (ECA centerline length), surgeons does not need to create the centerline in each patient because we can estimate the centerline length by the straight-line length. Actually,Yonenaga et al.[2] reported that each straight-line length between F–H plane and bifurcation was measured by carotid artery (CA) of cadavers. We need to verify whether the simple straight-line lengh becomes to be great helpful for knowing the centerline length which was close to actual catheter path. Thus, the aim of this study was to clarify the difference between ECA centerline length and straight-line (perpendicular to F–H plane) length, and to clarify the correlation between straight-line and centerline.

Methods

A multislice CT scanner (Aquilion 64; Toshiba Medical Systems, Tokyo, Japan) with 0.5-mm × 64-slice collimation was used for scanning CTA image. The scanning conditions were 120 kV, 250 mA, slice interval: 0.5 mm, slice thickness: 1.0 mm,512 × 512pixel,pixel size: 0.43 × 0.43 mm^2. Fifteen patients who were scanned by CTA (pre-treatment for oral cancer) were selected at random and thirty arteries were analyzed. The segmentation procedure (binary image processing of CTA images) was carried out using Mimics ver. 14.01 (Materialize, Leuven, Belgium). CA and maxillofacial surface rendering bone models were reconstructed by the proposed method [3]. The CA centerlines were extracted automatically by Mimics. The fiducial bifurcation points were as follows:

vA: superior thyroid artery via common carotid artery (CCA), vB: internal carotid artery and ECA via CCA, vC: lingual artery via ECA, vD: facial artery via ECA, vE: occipital artery via ECA, vF: maxillary artery via ECA.

In addition, F–H plane model (box-shaped surface rendering model) was created. The model size was 250 × 250 × 1 mm. F–H plane model was set up manually under the conditions that the lower surface come in contact with the both sides of infraorbital margin and the superior border of left external acoustic pore with one another. Straight-line between F and H plane and CA bifurcation point was measured as follows:

First, position coordinates of three points on underside of F–H plane were measured at random. The coefficients a, b, c, d of F–H plane Eq. (1) were calculated by these position coordinates.

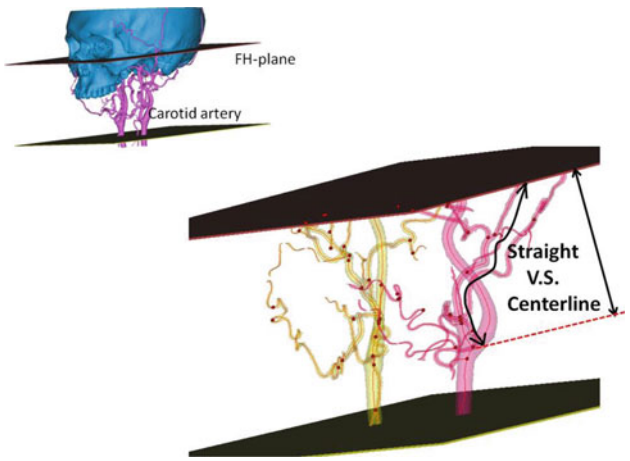

Fig. 1 Two lengths were compared

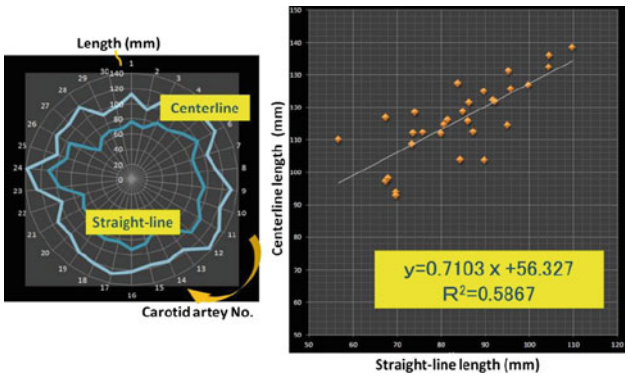

Fig. 2 Analysis of length between F–H plane and bifurcation point vB (Moderate correlation)

$$ax + by + cz + d = 0 \quad (1)$$

Next, position coordinates A (x_1, y_1, z_1) of bifurcation point were measured using the extracted centerline. Finally, straight-line lengths h (perpendicular to F–H plane) were calculated by Eq. (2).

$$h = (ax_1 + by_1 + cz_1 + d)\,(a^2 + b^2 + c^2)^{-1/2} \quad (2)$$

This method could prevent from human error because three points used for deciding F–H plane did not matter at any position.

Finally, centerlines (ECA length) between F–H plane and bifurcation point were compared to straight-lines between F–H plane and bifurcation point (Fig. 1).

Results

The straight-line (a) and centreline (b) lengths from F–H plane to each bifurcation points (vA-vF) were indicated as follows [mean ± std. (mm)].

vA; (a)80.27 ± 10.04, (b)111.08 ± 9.31, vB; (a)83.98 ± 12.77, (b)115.98 ± 11.84, vC; (a)67.41 ± 7.91, (b)97.00 ± 8.39, vD; (a)59.51 ± 8.70, (b)88.26 ± 11.63, vE; (a)61.13 ± 8.69, (b)90.19 ± 11.97, vF; (a)27.07 ± 2.50, (b)39.91 ± 6.75.

In addition, *p* value (p, student's *t* test) and coefficient of determination R^2 (R^2) of (a) and (b) were indicated as follows; vA; (p) p2) 0.3382, vB; (p) p2) 0.5867, vC; (p) p2) 0.1621, vD; (p) p2) 0.4056, vE; (p) p2) 0.413, vF; (p) p2) 0.2006.

Conclusion

We proved that the centerlines of ECA were about 27 mm longer than the straight-lines (perpendicular to F–H plane). The length was too long, considering catheter path. Additionally, the present study did not show a strong correlation between centerline and straight-lines length (Fig. 2). Therefore, it is considered that surgeons had better to obtain the three-dimensional ECA length (centerline) when they want to know the distance to insert a catheter or guide wire.

Segmentation of aortic valve from ultrasound image based on probability estimation

Y. Nie[1], Z. Luo[1], J. Cai[2], L. Gu[1]
[1]Shanghai Jiao Tong University, School of Biomedical Engineering, Shanghai, China
[2]Ruijin Hospital, Department of Cardiac Surgery, Shanghai, China

Keywords Aortic valve · Probability estimation · Ultrasound image segmentation · Continuous max-flow approach

Purpose

The geometric features of the aortic valve have been proven very valuable in Transcatheter Aortic Valve Implantation (TAVI) [1]. In order to provide accurate image-guidance for TAVI, several works have been done on the registration between intra-operative ultrasound (US) image and a model derived from pre-operative computed tomography (CT) [2], in which the segmentation of aortic valve from US image is one of the paramount and challenging steps. A large amount of approaches have been proposed for US image segmentation, where edge-oriented algorithm and region growing method are traditional, and active shape model (ASM), dynamic programming (DP), active contour model (snakes), level set and other improved algorithms are popular in recent years. However, due to the low quality of US image and the motion of the three leaflets of aortic valve, the segmentation accuracy could be compromised using above methods.

To obtain accurate segmentation of aortic valve in real time and further provide reliable support for registration in TAVI, we propose a novel segmentation method for short-axis view US image using probability estimation.

Methods

Probability Estimation

The position and geometric features of aortic valve change a lot during a cardiac cycle as it opens and closes regularly. In order to get appropriate prior information for all images in different cardiac phases, five prior images evenly spanning a cardiac circle are first selected with aortic valve manually segmented by an expert. Following, a composite centroid for above five segmentation results and five independent centroids for each segmentation result are respectively calculated, then composite probability estimation (CPE) is constructed based on both intensity and distance between each pixel and the composite centroid, and five single probability estimations (SPE) are respectively constructed based on both intensity and distance between each pixel and the corresponding centroid of each segmentation result. In addition, for each prior image, the typical foreground and background intensity, which can represent its corresponding foreground and background, are calculated respectively.

Energy Function Construction

In energy function construction, the current probability estimation is first acquired by using CPE on the current input image, followed by Otsu algorithm. Then a similarity metric (SM) is calculated to find out the prior image best matching the current input US image. The prior image with the maximal SM value is regarded as the prior information for the aortic valve, the corresponding typical foreground and background intensity of which are used to construct the energy function for the current input image. Afterwards, a graphic processing unit (GPU) accelerated continuous max-flow (CMF) approach [3] is employed to get an initial segmentation result, which is then multiplied by the SPE of the best matching prior image. Finally, the accurate segmentation of aortic valve is obtained.

Results

The evaluation was carried out over 90 short-axis cardiac US sequences acquired from 2 subjects, and a total of 180 images were automatically segmented. The image data were acquired from Ruijin Hospital using a GE Vivid 7 US machine, and we performed our experiments under Windows XP on an Intel Core i7 computer with NVIDIA GeForce GTX 560 graphics card with 1 GB display memory and 256 bit data width. For evaluation purpose, contrast experiments between the automatic segmentation and the corresponding manual segmentation which is regarded as the ground truth were performed, and Average Symmetric Contour Distance (ASCD), Dice Metric

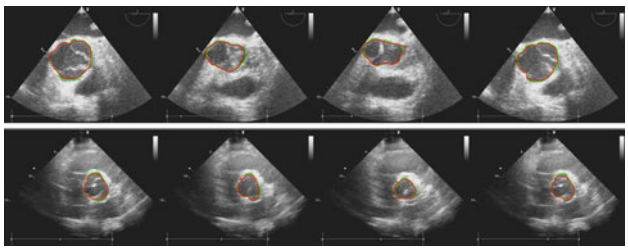

Fig. 1 Segmentation results showing four points in the cardiac cycle for one human and one swine. *Green line* represents the ground truth. *Red line* depicts the contour extracted by the proposed method. *First row* from frames 1, 12, 26 and 35; *Second row* from frames 44, 49, 53 and 63

Table 1 ASCD, DM, reliability of the algorithm (in pixels), and average time load to process a frame over 2 subjects (180 images) for the proposed method; statistics of the ASCD and DM expressed as mean ± standard deviation

Items	Average symmetric contour distance	Dice metric	Reliability (d = 0.95)	Time per frame (ms)
Our method	1.81 ± 0.34	0.96 ± 0.01	0.83	39.28 ± 5.23

(DM) and Reliability of the algorithm were employed as scoring system [4].

The segmentation results for both the proposed automatic method and the independent manual method are shown in Fig. 1, which demonstrates that the contours correlate well with each other. Details of ASCD, DM and Reliability of the algorithm are summarized in Table 1, where the real-time computational time for per frame is 39.28 ± 5.23 ms.

Conclusion

A novel method making full use of probability estimation of prior images is proposed for the segmentation of the aortic valve in US image. Experiment results show that the probability estimation and GPU based CMF can achieve accurate and real-time segmentation of aortic valve in short-axis view, which can provide reliable support for registration in TAVI. In the future, more clinical work will be done to perform the proposed method in the segmentation of intra-operative US image and test its practical applicability in TAVI.

Acknowledgments

This research work is partially supported by the Chinese NSFC research fund (61190120, 61190124, 61271318), the Shanghai municipal health bureau research fund (2011216) and Biomedical engineering fund of Shanghai Jiao Tong University (YG2012MS21).

References

[1] Moss RR, et al (2008) Role of echocardiography in percutaneous valve implantation. JACC: Cardiovascular Imaging, vol. 1, 15–24

[2] Lang P, et al (2012) Feature identification for image-guided transcatheter aortic valve implantation. SPIE Medical Imaging, 83162X-83162X-14

[3] Yuan J, et al (2010) A study on continuous max-flow and min-cut approaches. Computer Vision and Pattern Recognition. IEEE Conference on, 2217–2224

[4] Heimann T, et al (2009) Comparison and evaluation of methods forliver segmentation from CT datasets. Medical Imaging, IEEE Transactions on, vol. 28, 1251–1265

Rapid prototyping of cerebral arteries: a perfect scenario to develop innovative endovascular devices

G. Lupi[1], F. Chiellini[2], D. Puppi[2], G. Lo Presti[3], V. Ferrari[3], M. Ferrari[3], D. Caramella[4], R. Vannozzi[1]

[1]University and Hospital of Pisa, Neuroscience—Division of Neurosurgery, Pisa, Italy

[2]Biolab, Pisa, Italy

[3]University of Pisa, Endocas, Pisa, Italy

[4]University of Pisa, Diagnostic and Interventional Radiology, Pisa, Italy

Keywords Wet-spinning · Microbial polyesters · Silicon replica · Cerebro vascular by pass · Micro vascular anastomosis

Purpose

Complex vascular aneurysms, skull base tumors and some neoplasms that enwrap cerebral arteries sometimes require an intra-cranial or extra-intracranial by-pass to preserve and/or increase cerebral blood flow. Recent advances in technology have made possible to handle even more complex pathologies. Nonetheless the surgical procedure could be relatively too long and subsequent neurological deficits could occur. Since vascular reconstruction is often performed in narrow and deep gaps, the time spent in suturing the donor to the recipient vessel is one of the main factors affecting results. A new vessel-connection device could produce a faster and safer surgery. Our aim was to develop a physical scenario that helps our team to set up and test a new endovascular scaffold. The scaffold is intended to shorten and simplify the cerebral small diameter vascular anastomosis with limited or none circulatory arrest.

Methods

We selected the optimal CT-angiography (CTA) data set among those in our database, in terms of contrast and spatial resolution. The selected CTA was acquired with a post-contrastographic acquisition to extract arteries from its most contrasted phase. The slice thickness was 0.5 mm to obtain optimal resolution of the selected structures. Starting from this dataset we obtained the quantitative geometrical and topological data of the standard Willis' arteries. The chosen data set was segmented so that we obtained a perfect virtual replica of the inner diameters of the cerebral arteries. For this purpose, a semi-automatic tool, the EndoCAS Segmentation Pipeline integrated in the open source software ITK-SNAP 1.5 (www.itksnap.org) was used as previously described [1]. The mould of the arterial tree was then fabricated using the 3D printer (Dimension Elite 3D printer), starting from the previous segmentation. The mould correspond to the arterial lumen with the same shape and size of the original. We used the 3D arterial lumen as a base to smear pourable silicon (Dragon Skin® series by Smooth on) (DSFxPro). After complete silicone curing, the solid replica of the arteries was removed so that the arterial lumen was preserved (Fig. 1). The silicon replica represented a realistic physical scenario that helps our multi-disciplinary team to engineer the endovascular scaffold. Starting from the replica, we prepared bioactive micro-structured polymeric scaffolds employing a fabrication method based on rapid prototyping (RP). According to the mechanical features of the arterial replica we decided to build different endovascular scaffolds. All the scaffolds were made of poly(3-hydroxybutyrate-co-3-hydroxyhexanoate) (PHBHHx) and developed by a computer-assisted wet spinning technique. Poly(3-hydroxybutyrate-co-3-hydroxyhexanoate) (PHBHHx, 12 mol % HHx, Mw = 300,000 g/mol) was purified according to the procedure reported by Motaet al [3]. A 25 % w/v PHBHHx solution was prepared by dissolving 1.00 g of PHBHHx in 4 ml of chloroform under vigorous stirring at 30 °C for 3 h. The resultant solution was gently stirred for 1 h at room temperature in order to remove the remaining bubbles. PHBHHx scaffolds were fabricated with a 0–90° lay-down pattern by computer-aided wet-spinning technique as previously described [2]. Different processing parameters for the fabrication of PHBHHx scaffolds with different external sizes and different between fibres axes (dF = 0.2

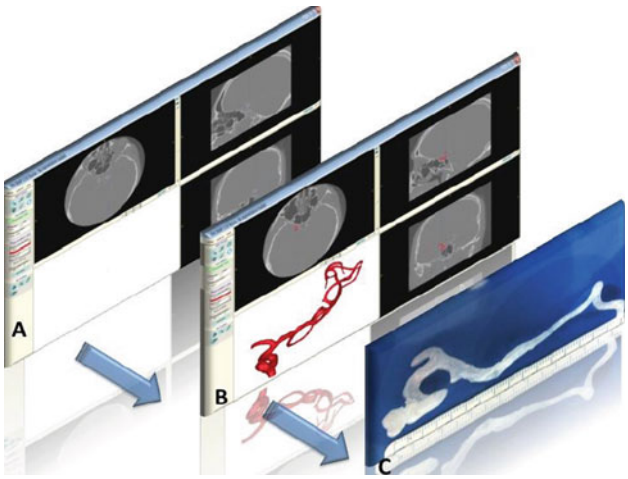

Fig. 1 Step wise creation of the 3D silicon replica. From the *left* to the *right*: **a** the chosen CTA dataset, **b** the 3D virtual model obtained by the segmentation procedure, **c** A silicon replica of the internal carotid artery and its main branches achieved from virtual model

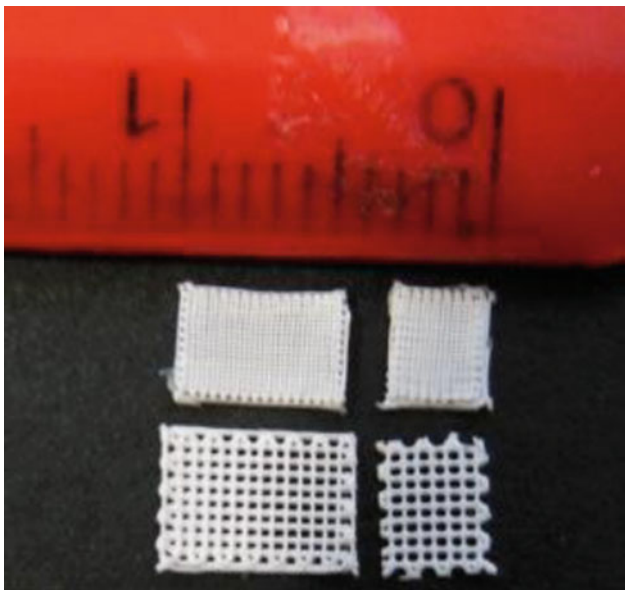

Fig. 2 Endovascular PHBHHx meshes tailored to the silicon replica, different shapes and sizes are presented

and 0.5 mm), such as needle inner diameter (din), flow rate (F), the needle translation velocity (Vtr), inter-fiber needle stop time (tstop) and initial distance between the needle tip and the bottom of the beaker (Z0), were investigated. The scaffolds were designed with sizes suitable for covering either half or the whole inter-luminal circumference in a 5 mm segment of a small calibre blood vessel with an inner diameter of roughly 2 mm. At least we designed PHBHHx planar meshes with different sizes and internal microstructure. Size and shape were designed to allow the endothelium to fill the pores and the inner surface of the implanted meshes (Fig. 2).

Results

According to the geometrical features of the arterial replica we built different endovascular meshes made of PHBHHx. The replica

Table 1 Optimized processing parameters for PHBHHx scaffolds fabrication

Scaffolds properties		Processing parameters					
dF (mm)	Size (mm^2)	d_{in} (mm)	F (ml/h)	V_{tr} (mm/min)	t_{stop} (ms)	d_Z (mm)	Z_o (mm)
0.5	4 × 5	0.2	0.2	120	100 + 25	0.1	1
0.5	4 × 5	0.2	0.2	150	100 + 25	0.1	1
0.5	7 × 5	0.2	0.2	120	100 + 25	0.1	1
0.2	4 × 5	0.2	0.1	100	100 + 25	0.08	1
0.2	7 × 5	0.2	0.1	100	100 + 25	0.08	1

Note: *dF* distance between axes of parallel fibers within the same layer, d_{in} the inner diameter of dispensing needle, *F* solution flow rate, V_{tr} X–Y translation velocity of the needle, t_{stop} inter-fiber needle stop time, d_Z inter-layers needle translation, Z_0 the initial distance between the needle tip and the bottom of the beaker

allowed us to engineer the PHBHHx meshes with different sizes. We selected sizes suitable for covering either half or the whole inter-luminal circumference (4 × 5 or 7 × 5 mm) in a 5 mm segment of a vessel with an inner diameter of roughly 2 mm. The inter-fibers distance was varied (0.5–0.2 mm) in order to allow the endothelium to colonize the pores and the inner surface of the implanted mesh. The optimized processing parameters for manufacturing PHBHHx scaffolds with different external sizes and inter-fibers distance are reported in Table 1.

Conclusion

In our opinion the angio-architecture silicon replica can be of paramount importance for improving the scaffold's design process. Since our team consisted of clinicians, physicists, chemists, biologists and engineers we decided to build a physical replica of the Willis' arteries prior to choosing the most appropriate biomaterial, shape and size of the endovascular device. The investigated computer-aided wet-spinning technique is well suited for the fabrication of PHBHHx scaffolds with external sizes and internal architecture tailored to the arterial replica. We consider this approach of paramount importance for improving any scaffold's design process. Moreover this procedure represents both a link between the laboratory and the "in vivo" testing and a reduction of the costs-related tests.

References

[1] Ferrari V, Cappelli C, Megali G, Pietrabissa A (2008) An anatomy driven approach for generation of 3D models from multi-phase CT images. IJCARSVolume 3 (Supplement 1)

[2] Mota C, Puppi D, Dinucci D, Gazzarri M, Chiellini F (In Press, Issue July 2013) Additive Manufacturing of Star Poly(ε-caprolactone) Wet-spun Scaffolds for Bone Tissue Engineering Applications. Journal of Bioactive End Compatible Polymers..

[3] Mota C (2012) a novel approach to the fabrication of scaffolds for tissue engineering. vol.PhD. Pisa, Italy: Pisa University, p.163

Indicators for lumens distinction on 3D CT aortic dissection images

N. Fetnaci[1], P. Łubniewski[1], B. Miguel[2], C. Lohou[1]
[1]Clermont Université, Université d'Auvergne, UMR 6284 CNRS ISIT. Clermont-Ferrand, France
[2]CHU Gabriel Montpied, Service de Chirurgie Cardio-Vasculaire, Pôle Cardiologie Clermont-Ferrand, France

Keywords Aortic dissection · Lumens distinction · Segmentation · CT aortic images

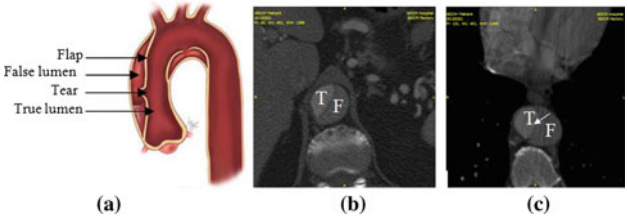

Fig. 1 **a** Schematic representation of an aortic dissection [5], **b** 2D grayscale slice without tear, **c** 2D grayscale slice with one tear (*white arrow*); T means true lumen, F means false lumen

Purpose

Our works are related to the planning and assistance to manage aortic dissections during interventions. Aortic dissection is a life-threatening medical emergency associated with high rates of morbidity and mortality. It consists in one or several tears which begin in the intima allowing blood to travel through a diseased media layer. This process cleaves the normal bed of blood into two lumens (true lumen and false lumen) separated by an intimal membrane also called flap (Fig. 1a). See Fig. 1b, c for a 2D slice retrieved from one of our CT images.

Recently, we have proposed a segmentation of the true and false lumens separately on 3D CT aortic dissection images [1] (see Table 1b). Our aim was to provide a 3D view of the lumens that we can difficultly obtain either by volume rendering or by another visualization tool which only directly gives the outer contour of the aorta; or by other segmentation methods because they mainly directly segment either only the outer contour of the aorta or other connected arteries and organs both. This segmentation was realized by modifying the speed term of the classical fast marching method. More particularly, the front propagation stops around intimal tears by dealing with intensity values (gradient).

Our works consist in registering the segmented results from a CT aortic dissection image onto an angiographic sequence in order to assist clinicians during their interventions. An automatic lumen distinction allows us to propose a better control for endoprosthesis landing: the stent-graft trajectory must remain only inside the true lumen and not to pass through the false lumen.

In this paper, we present two indicators to easily distinguish true and false lumens in our segmented results. More precisely, these indicators are also based on intensity.

Methods

Mainly, there exist two types of aortic dissections: Type B when the ascending aorta is not dissected, Type A when the ascending aorta is dissected [2].

In case of a Type B dissection, the true lumen can be determined in the following way: we first consider an image cross-section immediately above the heart showing the two lumens; the lumen with smaller cross-sectional area is necessarily the false one, as it ends close to this cross-section. However, for patients with Type A dissection, this rule cannot be used. In the following, we only consider Type A case.

Usually, the image intensity is higher in the true lumen. Therefore, we define our first indicator (ind1) as the mean intensity of a given segmented lumen. Sometimes, there is no significant intensity difference between the two lumens: thus we propose a second indicator (ind2) to take into account both the mean intensity and the voxels distribution. This indicator is based on Bayesian probability [3]:

$$\text{ind2} = (P * P_1)/P_2$$

where, P denotes the mean intensity of the current lumen, P_1 denotes voxels distribution in the current lumen, P_2 denotes voxels distribution in the other lumen. All these values belong to.

As far as we know, there is only a single work about lumens distinction: this is Kovács work [4] based on cross-sectional area.

Table 1 Segmentation results and indicator values for our CT aortic dissection images

Aorta volume rendering	Lumens volume rendering	Ind1	Ind2	Decision	3D reconstruction with the marching cubes algorithm
Patient 1		236	0.643	True	
		138	0.778	False	
Patient 2		220	0.599	True	
		142	0.801	False	
Patient 3		200	0.632	True	
		154	0.681	False	
(a)	(b)	(c)	(d)	(e)	(f)

This method requires the flap segmentation. Flap retrieval is difficult due to the small thickness of such membrane and sometimes to the low resolution of images. Our indicators computing does not require flap segmentation.

Note that although calcifications only appear in true lumens; we do not take into account such a case because they are not systematic in each dissection.

Results

Our processing method is constituted of the two following steps: the first one is the classical fast marching method to delineate the volume of interest around the aorta (Table 1a); the second one is our adapted fast marching method which allows us to obtain the two separated lumens (Table 1b). In Table 1c, d are given indicators values.

In these three images, we have the highest intensities values ofind1for the true lumens, with a mean intensity of 219 for a true lumen, 145 for the false one and 74 for the deviation. We have the lowest values ofind2for the true lumen with a mean value of 0.627 for a true lumen, 0.753 for the false one and 0.126 for the mean deviation. In Table 1f are given the 3D reconstruction of the final results, in blue is rendered the true lumen and in red is rendered the false lumen.

Conclusion

Due to our segmentation of the two lumens separately, it was relatively easy to propose two indicators to distinguish lumens. Our future works consists in testing our indicators in a larger dataset and also taking into account specific collateral arteries birth. This study will also assist clinicians during endoprosthesis landing by a registration of this distinction onto angiographic sequences.

References

[1] Fetnaci N, Łubniewski P, Miguel B, Lohou C (2013) 3D segmentation of the true and false lumens on CT aortic dissection images. SPIE Electronic Imaging.

[2] Erbel R, Alfonso F, Boileau C, Dirsch O, Eber B, Haverich A, Rakowski H, Struyven J, Radegran K, Sechtem U, Taylor J, Zollikofer, C (2001) Diagnosis and management of aortic dissection. European Heart Journal 22, 1642–1681.

[3] Jaynes, E.T (1986) Bayesian Methods: General Background. An introductory tutorial. In Proceedings of Maximum entropy and Bayesian Methods in Applied Statistics, 1–25.

[4] Kovács T, Cattin P, Alkhadi H, Wildermuth S, Székely G (2006) Automatic segmentation of the Vessel Lumen from 3D CTA

Images of Aortic Dissection. In Proceedings of Bildverarbeitung für die Medizin, 161–165.
[5] Center for Aortic Diseases (2012), "Aortic dissection", The University of Chicago Medicine. http://www.ucaorta.org/aortic-dissection.html.

Multiple parameter optimization of coronary artery ostia finder in cardiac MRI

M. Pietsch[1], S. Mollus[1], A. Saalbach[2], I. Wächter[2], Y.-C. Böring[3], S. Grünig[3], M. Neizel[3], B. Sievers[3], J. Balzer[3], M. Kelm[3], J. Weese[2]
[1]Philips Research Europe, Aachen, Molecular Imaging Systems, Aachen, Germany
[2]Philips Research Europe, Hamburg, Digital Imaging, Hamburg, Germany
[3]Universitätsklinikum Düsseldorf, Klinik für Kardiologie, Pneumologie und Angiologie, Düsseldorf, Germany

Keywords TAVI · Coronary artey ostia · Cardiac magnetic resonance · Parameter optimization · Pattern recognition

Purpose

The therapy of choice to treat severe symptomatic aortic stenosis is the replacement of the aortic valve. Transcatheter aortic valve implantation (TAVI) has proven to be a suitable minimally invasive therapeutic alternative for high-risk patients whose physical frailty or coexisting conditions do not allow surgical intervention [1].

The analysis of the aortic root is crucial to decide whether to implant and to choose suitable prostheses size and type. To prevent coronary ostia stenosis, the position of the coronary artery ostia and their distances to the native aortic valve leaflets have to be known. To assess these parameters beforehand multi-modal imaging in computed tomography (CT), transesophageal and transthoracic echocardiography as well as magnetic resonance imaging (MRI) in combination with manual measurements are key. However, manual length measurements in three-dimensional images are fault-prone. Therefore we strive for an automated approach of geometrical aortic root assessment and coronary ostia detection. Recently, different methods for automatic cardiac segmentation dedicated to CT have been proposed [2, 3]. However, CT has many drawbacks for the multi-morbid TAVI patient in terms of radiation and burden due to nephrotoxic iodine-based contrast agent. Thus (sensitivity encoded) cardiac 3D MRI is growing in relevance and dedicated automated analysis methods are required.

We propose and evaluate a method for model-based coronary ostia detection in MRI which builds upon a recently introduced approach for the detection of coronary artery ostia in CT. [4] As pre-requisite a model-based segmentation of the heart is performed with established segmentation methods. Then a multi-parametric search algorithm analyzes image contrast and geometric parameters on the surface of the patient-specific mesh. Since MRI lacks well defined gray-levels, high resolved features and is likely to be affected by MR-specific imaging artifacts, careful parameterization to generalize the proposed algorithm for a large range of image characteristics is required. Thus, we not only extended the available technique for MRI data: we also applied extensive brute-force multi-parameter optimization to circumvent intuition-driven and subjective parameter sets. With this unique approach we improved the algorithm's performance and stability to make it suitable for cardiac MRI.

Method

The dataset for parameter optimization consists of 22 MR and 21 corresponding CT images originating from 22 different TAVI patients. Three experts used dedicated workstation software to retrospectively annotate ground truth (GT) landmarks of the left and right coronary artery ostia (LCAO, RCAO) as well as four points marking the annulus plane for each image. The ostia search was performed on automatically generated meshes using a recently introduced segmentation model specifically trained on TAVI MRI data.

The ostia finder searches on the mesh surface for bright half spheres each surrounded by a dark ring. The image contrast and the weight of these two features, as well as their physical dimensions and relative alignment remain free parameters. These mostly floating point variables are possibly image specific (image contrast, quality, cardiac phase, anatomy) and partially dependent upon another (e.g., geometrical parameters), see Fig. 1.

Therefore a huge ten-dimensional search space was generated, and for each of its almost 600,000 tuples, the ostia positions of all patients were evaluated. The Euclidean distance between candidate and GT LCAO and RCAO positions as well as the clinically more relevant distances between ostia and valve plane were used as objective functions. The validation was performed using five-fold cross-validation by dividing the mesh surface area to search for ostia candidates into subsets defined by the GT ostia positions of the training data.

Results

GT ostia positions and especially aortic valve plane definitions showed distinct inter-observer variability. The Pearson correlation coefficient between the 21 matching CT and MRI GT LCAO to valve plane displacements could be improved from $r = 0.68$ to $r = 0.93$ utilizing valve planes derived from hard-coded landmarks on the mesh surface instead of expert valve plane annotations.

The correlation of LCAO to valve plane distances generated with ostia positions found using the best parameter set to GT reference annotations was $r = 0.91$. Due to the extensive parameter optimization, the ostia finder's accuracy for the left coronary artery could be improved by 10 % compared to the CT parameter set applied to MRI data.

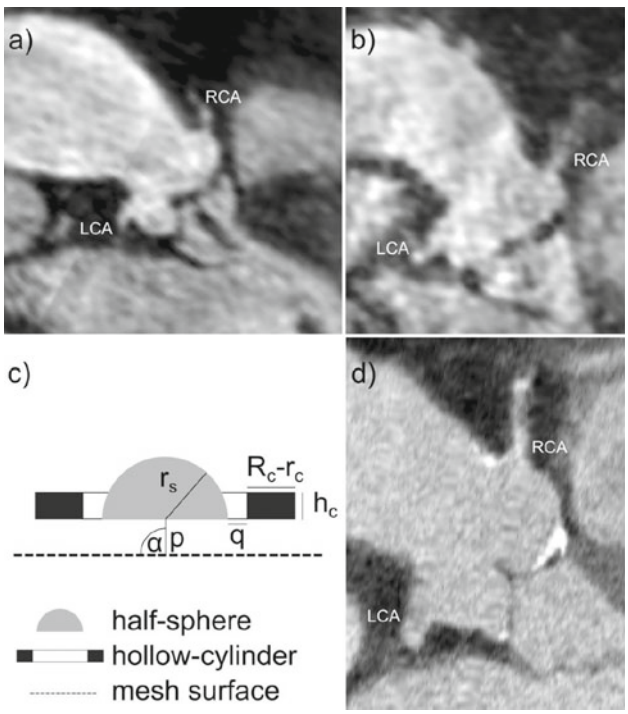

Fig. 1 MR images with good (**a**) and challenging (**b**) image quality for detection of left (LCA) and right coronary artery (RCA) ostia positions. For comparison of image quality a CT image corresponding to figure **b** is displayed in **d**. The drawing in **c** shows some of the ostia finder parameters: *p* the distance between mesh surface and ostia analysis which can be angled by α, the inner and outer radius of the hollow-cylinder (r_c and R_c respectively), its height h_c, the half-sphere's radius r_s and the spacing between the two features q

An approach to consecutively optimize single ostia finder parameters did not lead to any improvement in RCAO detection using MRI data. Although our multiple parameter optimization facilitated RCAO detection (RCAO to valve plane correlation r = 0.57), it still remains challenging. The detection of RCAO positions was presumably hindered by a generally higher tortuosity and spatial variability as well as worse motion artifacts compared to the left coronary artery.

Conclusion

Automatic ostia detection performs as good as manual ostia detection if the image quality is sufficient. In the application of TAVI screening it was shown that clinically relevant measures could be automatically derived using segmentation and ostia finder results.

Brute-force multi-parameter optimization is a powerful technique to reduce the dimensionality and complexity of a multi-parametric image processing algorithm and is very helpful to increase the robustness and quality of a segmentation algorithm. Furthermore this technique can be used to tailor a given algorithm to other imaging modalities such as CT, echocardiograms or rotational angiography.

References

[1] Cribier A, et al (2002), Percutaneous transcatheter implantation of an aortic valve prosthesis for calcific aortic stenosis: first human case description. Circulation 106(24), p. 3006–3008.
[2] Ecabert O, et al (2008), Automatic Model-Based Segmentation of the Heart in CT Images, IEEE Trans Med Imaging. 27(9): 1189–201.
[3] Ecabert O, et al (2011), Segmentation of the heart and great vessels in CT images using a model-based adaptation framework., Med Image Anal. 15(6):863–76.
[4] Waechter I, et al (2010), Patient specific models for planning and guidance of minimally invasive aortic valve implantation. Med Image Comput Comput Assist Interv. 13(Pt 1):526–33.

Reconstruction of vessels physiological shape for quantification of stenosis in peripheral vascular diseases

A. Chiarini[1], G. Crimi[1], L. Ribatto[1], G. Di Cosmo[1], D. Testi[1]
[1]SCS srl, B3C, Bologna, Italy

Keywords Vessel model · Lesion recognition · Peripheral vasculopaty · Computer aided planning

Purpose

Cardiovascular diseases (CVD), particularly coronary heart disease, stroke transient attacks, peripheral arterial disease and the vascular complications of diabetes are major causes of disability and death in developed countries. Among CVD, disease of peripheral arteries gives rise to major morbidity and mortality: around 20 % of the population over 60 years old has peripheral arterial disease and symptoms can become severe and progressive in about 20 % causing major limitation through pain on walking; progressive disease can result in critical limb ischemia, which is the major cause of amputation. Endovascular treatments such as stenting and angioplasty are becoming the preferred approach for the treatment of many vascular occlusive diseases: a vascular surgeon or an interventional radiologist will percutaneously insert wires and catheters to cross a stenosed artery, the balloon-tipped catheter is used to open the artery (angioplasty) followed in many cases by the use of a vascular stent.

Quantification of vascular disease is a crucial step in computer aided planning (CAP) applications that address this pathology: the classification of the lesion gives the clinician an indication according the TASC guidelines. A method to face this problem is to measure the pathological vessel diameter along the stenosed tract to plan the stent model and size. However, this process might result interactive and time-consuming to be followed in the clinical practice.

A few methods for automatically quantifying vascular morbidity by means of vessel measures exist and they approach the problem by reconstructing the physiological stenotic morphology by geometrical interpolation.

We propose a novel method which is sufficiently generic to take in input a centerline and a set of associated sectional diameters and it creates a geometrical model of the patient vessel: this geometry features all the parameters necessary for lesion classification and treatment planning. Furthermore, an improved version addresses both occlusive lesions and aneurysms showing better results in computational times and memory requirement, a key feature for an effective clinical planning tool.

Methods

In order to implement our method, we designed a deformable vessel model that approximates the patient vessel. It is a semi-parametric object which determines a tubular surface defined by connected circular sections. Each section is univocally defined by a central point, a radius and a normal.

A vessel model can be created starting from both 2D images (2D angiography) or a 3D volume (e.g., CTA, MRA, …) by interactive user input in the former case and in the latter case an algorithm based on complementary geodesic field for the centerline and radius extraction.

The proposed algorithm is divided into two phases: (a) lesions tracts classification and (b) centerline deformation.

a. Lesions recognition algorithm is based on a iterative linear regression algorithm which estimates the healed radius at each point of the centerline. At first, a regression line is computed and all the points out of tolerance thresholds are classified as lesions. Then, a new regression line is computed ignoring previously classified zones, so that a better estimation is made by considering the normal tracts of the vessel. By means of process, we obtain at the same time a classification of lesion zones and the estimation of the reconstructed vessel diameter profile. The algorithm sensitivity has been empirically defined for lower leg vessels but it can be adjusted case by case according to anatomic zone and disease type. We had demonstrated algorithm convergence and stability (Fig. 1).
b. Centerline deformation is usually needed since asymmetric vessel lesions alter quantitative measurement. The problem of a correct reconstruction is the reduction of lesion effect without losing vessel curvature and torsion. We implemented a self-organized system where global behavior emerges from local interaction: local forces are applied to centerline points in lesions areas in order to correct centerline position step by step. We apply four force types: elastic, bending, constriction and friction.

Elastic and bending forces depend on the model structure: elastic force is a point attraction force between neighbor points which moves all the points set to a common line and it is proportion to points

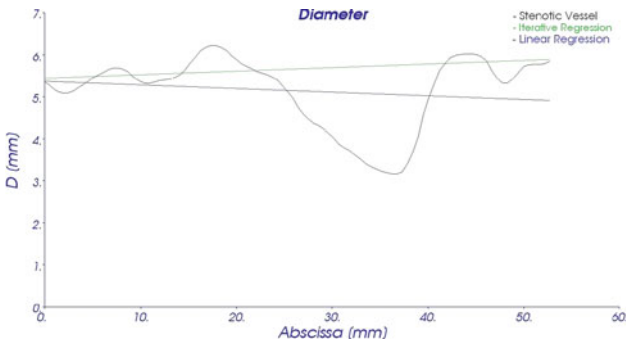

Fig. 1 Comparison between linear regression and interactive regression

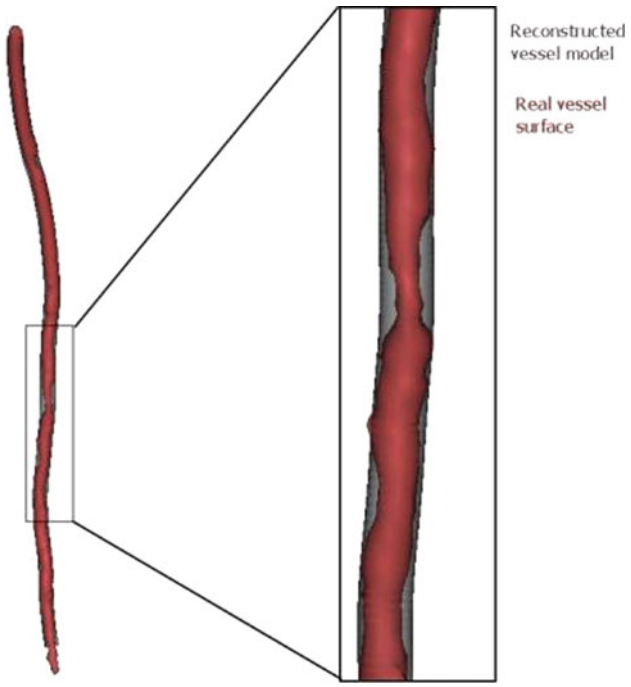

Fig. 2 Vessel model overlapping real vessel surface

distance; bending force represents vessel resistance to be bent and it is correlated with the angle between consecutives points.

Constriction force guarantees to keep a physiological shape of the reconstructed sections. This force is applied only when the reconstructed section goes out of the estimated maximum/minimum vessel circumference.

Friction force avoids the accumulated forces to create unpredictable effects and deformed vessel shape.

All these forces act simultaneously in all the lesions tracts at time steps for an empirically predetermined duration. Forces system solution is provided by Runge–Kutta 4 solver, a method that involves evaluating derivatives at multiple points for each time step. At the end of the deformation, centerline position represents the estimation of the physiologic vessel centerline points.

Results

Validation of the algorithm is still work in progress but first results seem encouraging. The algorithm was tested with two types of experiments: on phantom data to have a known ground truth and on clinical data for investigate the generalization capacity.In the first experiment, we create a set of healthy phantom vessels and we added stenoses of different shape factors. Then we compared the reconstructed physiological centerline with the ideal one. We found that the reconstructed centerlines with a good approximation overlap the ideal ones. Then, we used the algorithm on clinical images and we found that reconstructed vessels surfaces qualitatively approximate the vessel surface obtained with segmentation (Fig. 2).

We monitored execution times in all the experiments: they ran in a range of 0.5–3 s on a standard PC (intel i5 with 4 GB of RAM). The memory footprint remained constant during execution and negligible if compared to the clinical data loaded.

Conclusions

Our work focuses on the implementation of a fast algorithm for automatic vessel reconstruction and lesion recognition. The major strengths of this algorithm are quasi-real time model deformation, intuitive parameters adjusting and minimal user interaction to be seamlessly integrated in a CAP application. A future work might focus on an extension of the algorithm to total occlusions.

Innovative 3D model for early diagnostics of cerebrovascular disorders

G. Machtoub[1]
[1]Universitätsklinikum, Leipzig, Germany

Keywords Finite difference time domain · 3-D simulation · Brain imaging · Cerebrovascular disorders

Purpose

Significant technological advancements in brain imaging and clinical testing have demonstrated the feasibility of transcranial acoustic therapy in the brain using noninvasive adaptive transskull focusing techniques. The acoustic waves can be used to stimulate small brain regions with size of about 1 mm. Such non-invasive examination can also be used to detect hardening of the arteries in early stages, and bust blood clots in the brain without causing collateral damage [1–2].

In this work, a 3-D dynamic model has been developed for simulation of a nonlinear acoustic wave propagation through a human head phantom. The model is based on the Finite Difference Time Domain method for modeling the acoustic pressures and thermal fields [3–4]. The numerical simulation is intended for investigating the paramerters that affect the characteristics of propagation in early stages of cerebrovascular disorders associated with brain injuries.

Methods

The model uses the Finite Difference Time Domain (FDTD) method to solve the acoustic equations which are valid for a nonlinear wave propagation in a complex heterogeneous structure of biological tissues. The approach is based on resonance and anti-resonance of waves taking into account propagation delays for reflections through intervening tissue boundaries of different acoustical impedances. The waves propagate in multi-layered medium consists of bones, skin, fat, and brain layers. Properties of the various tissues found within the human head such as density, sound speed, and frequency dependent attenuation due to back scattering loss, were employed in the simulations. The acoustic parameters of brain tissues are close to that of water and considered for temperatures in the range between 20 and 37 °C.

Results

The 3D dynamic simulation presents the transmission, reflection and scattering characteristics in the multi-layered biological structure. Taking into account the medium heterogeneities, the simulation approach is able to estimate the thermal absorption induced by bones. The wave dispersion has been monitored with density fluctuations using different frequencies. The model predicts the phase and amplitude aberrations on wavefronts, and the acoustic pressure that makes it possible to study the mechanisms associated with cerebrovascular disorders.

Conclusion

A new dynamic model using the FDTD method has been developed for simulation of the nonlinear acoustic fields and thermal absorption patterns in the human head. The model employs a pressure-density relation that incorporates the effects of medium heterogeneities and nonlinearity. The findings offer a way to improve the diagnostics of cerebrovascular disorders as it gives insights on distribution of pressure levels and distorted waveforms associated with some anomaly in brain physiology.

References

[1] Tufail Y, Matyushov A, Baldwin N, et al. (2010) Transcranial Pulsed Ultrasound Stimulates Intact Brain Circuits. Neuron, 66 (5): 681–694.
[2] Maxwell AD, Cain CA, Duryea AP, et al. (2009) Noninvasive thrombolysis using pulsed ultrasound cavitation therapy histotripsy. Ultrasound Med Biol. 35(12):1982–94.
[3] Nagra, Amit S (1998) FDTD analysis of wave propagation in nonlinear absorbing and gain media BIEEE Trans Antennas Propag 46: 334–340.
[4] Hallaj I, Cleveland R (1999) FDTD simulation of finite-amplitude pressure and temperature fields for biomedical ultrasound. J Acoust Soc Am.105:L8–12.

Comprehensive evaluation of latest HD 2D/3D laparoscopic monitors and comparison to a custom built 3D mirror based display and a prototype autosteoreoscopic 3D monitor

D. Wilhelm[1,2], S. Reiser[2], N. Kohn[1,2], M. Witte[3], U. Leiner[3], L. Mühlbach[3], D. Ruschin[3], W. Reiner[3], H. Feussner[1,2]
[1]Klinikum rechts der Isar, München, Germany
[2]Technical University of Munich, MITI working group for minimally invasive therapy and intervention, München, Germany
[3]Fraunhofer, Heinrich Hertz Institute, Berlin, Germany

Keywords Laparoscopy · Visualization · Autostereoscopic · 3D · Monitor technology

Purpose
Theoretically superior to standard 2D monitors 3D video systems did not achieve a breakthrough in laparoscopy up to now because of lower resolution, uncomfortable use and higher work-load. Furthermore visual alterations, such as eye strains, diplopia and blur have been associated with the use of stereoscopic displays. Latest 3D monitors including autostereoscopic displays and high resolution are constructed to overcome these restrictions.
Methods
Prospective randomized study on 48 individuals with different experience levels in laparoscopic surgery. Comprehensive and highly standardized evaluation of three different 3D displays (a glasses based 3D HD monitor, a autosteroscopic display and, a mirror based and theoretically ideal 3D display) and comparison to a commercially available 2D HD display (Fig. 1) by assessing multiple performance and mental workload parameters, as well as test subjects' ratings during a laparoscopic suturing task (Fig. 2). As performance parameters we evaluated the time to complete the task and measured the precision of stitching, as well as electromagnetic tracking of instruments provided information on the instruments path length and movement velocity. The NASA TLx questionnaire was used to assess the mental work load of test persons. Subjective rating focused on the usability of each monitor, the perception of visual discomfort and on the quality of image transmission of each system.
Results
All performance parameters were superior with the conventional 3D HD glasses-based display as compared to the 2D and the autostereoscopic display, but were often significantly exceeded by a custom built mirror 3D display. Subjects performed the task faster and with a higher precision, when visualization was achieved with the 3D HD display and mirror display, as well as the instrument path length was shortened by means of improved depth perception. Work-load parameters as evaluated by the NASA task load index did not show significant differences. Test persons complained of impaired vision

Fig. 1 Illustration showing the different workplaces, including a conventional 2D and 3D HD monitor, a prototype autostereoscopic 3D display of Fraunhofer HHI and a custom built monitor system using an arrangement of mirrors (Fraunhofer HHI) which is supposed to provide the best possible 3D reproduction

Fig. 2 Experimental setup for evaluation of different 3D and a 2D laparoscopic monitors. Subjects had to complete a laparoscopic suturing task under standardized conditions. Procedure time, electromagentic tracking of instruments and accuracy of suturation were assessed as performance parameters, while the NASA Tlx score provided information concerning the mental work load. To prevent bias laparoscopic cameras and video devices were idententical among the different workplaces (Karl Storz® 3D TIPCAM NTSC)

while using the autostereoscopic monitor, while no visual discomfort was reported on the 3D HD display and the mirror display. Particularly the 3D HD and the 2D HD display were rated as user-friendly and applicable in daily work. Test results were not influenced remarkably by the training level of involved test persons.
Conclusion
Latest 3D HD displays will improve performance of surgical interventions resulting in a faster performance and higher precision without causing a higher mental workload to the user. Thereby they have the potential to significantly impact on the further development of minimally invasive surgery. However, as shown by the custom built 3D mirror display, this effect can even be improved thus stimulating the further research. The autostereoscopic display on the other hand offers an innovative solution for glasses-free stereoscopic visualization; however, the system could not convince completely during this study.

Automatic Abdominal Lymph Node Segmentation based on Radial Structure Tensor Analysis

Y. Nimura[1], Y. Nakamura[2], Y. Hayashi[1], T. Kitasaka[3], K. Furukawa[4], K. Misawa[5], K. Mori[1,2]
[1]Nagoya University, Information and Communications Headquarters, Nagoya, Japan
[2]Nagoya University, Graduate School of Information Science, Nagoya, Japan
[3]Aichi Institute of Technology, Faculty of Information Science, Toyota, Japan
[4]Nagoya University, Graduate School of Medicine, Nagoya, Japan
[5]Aichi Cancer Center Hospital, Department of Gastroenterological Surgery, Nagoya, Japan

Keywords Abdominal lymph node · Segmentation · Radial structure tensor analysis · Computer-aided detection

Purpose
This paper describes a method of abdominal lymph node (LN) segmentation based on radial structure tensor (RST) analysis. LN analysis is one of important parts of lymphadenectomy, which is a surgical procedure to remove one or more LNs in order to evaluate

them for the presence of cancer. Also, physicians routinely assess LNs to evaluate the effectiveness of treatment and the disease progress by using CT scans. Therefore, it is important to detect and extract LNs automatically from CT scan.

Several methods for automated LN detection and segmentation are proposed. As LNs can be characterized as blob-like structures of varying size and shape within a specific intensity interval, Feuerstein et al. and Oda et al. utilized Hessian analysis to extract mediastinal and abdominal LNs, respectively [1,2]. These methods have high sensitivity. However, there are a lot of false positives (FPs), and the shape of extracted LNs does not correct. These Hessian based methods rely on the assumption that the local shape can be estimated sufficiently by the local Hessian. Therefore, the response of Hessian analysis becomes unstable in the marginal region of a local structure. Furthermore, the assumption is not sufficed by LNs. Because the typical distance between a LN and surrounding structures is smaller than their extent, and a Gaussian filter in Hessian analysis would blend a LN and surrounding structures into each other. To solve this problem about Hessian analysis, Wiemker et al. proposed RST analysis, which is an extension of the general structure tensor analysis [3]. The RST correlates position and direction of the gradient vectors in a local neighborhood. As Hessian based analysis, also RST yields positive and negative eigenvalues which can be utilized to discriminate between difference shapes.

This paper proposes a method of automatic abdominal LN segmentation based on RST analysis. In Section 2, we describe the detailed procedures of the proposed method. Section 3 shows experimental results of abdominal LN segmentation.

Method

Overview

The proposed method consists of two steps: (a) LN segmentation based on RST analysis, (b) FP reduction based on connected component analysis. In step (a), we extract LN candidates by utilizing RST analysis in each voxel of CT scan. In step (b), we eliminate FPs by utilizing volume and shape of connected components.

LN segmentation based on RST analysis

First, we extract LN candidates by utilizing RST analysis. RST is given by

$$T(x) = \sum_i \sum_j \alpha(x_{ij}) \cdot g(x_{ij}) \cdot r_i^T,$$

where $\boldsymbol{x}$ and $\boldsymbol{x}_{ij}$ are positions. The i is index of direction, and j is index of sampling point according to direction i. The $\alpha(\boldsymbol{x}_{ij})$, $\boldsymbol{g}(\boldsymbol{x}_{ij})$, and $\boldsymbol{r}_i$ are the local opacity of $\boldsymbol{x}_{ij}$, the local gradients of $\boldsymbol{x}_{ij}$, and normalized direction vector from x to $\boldsymbol{x}_{ij}$, respectively. The $\alpha(\boldsymbol{x}_{ij})$ is given by

$$\begin{aligned}&\alpha(x_{ij}) = \{\\ &0 \text{ if } f(x_{ij}) \le f_{\min}\\ &1 \text{ if } f(x_{ij}) \ge f_{\max}\\ &(f(x_{ij}) - f_{\min})/(f_{\max} - f_{\min}) \text{ otherwise},\end{aligned}$$

where $f(\boldsymbol{x}_{ij})$ is intensity value of $\boldsymbol{x}_{ij}$ in CT scan, and $f_{\min}$ and $f_{\max}$ are parameters. And the $\boldsymbol{x}_{ij}$ is given by

$$x_{ij} = x + j \cdot \Delta r \cdot r_i,$$

where Δr is step size of RST computation. In order to avoid the extent of surrounding structures, RST analysis introduces a mechanism of ray termination based on accumulated opacity in ray casting. Wiemker et al. defined the accumulated opacity α_i of direction $\boldsymbol{r}_i$ as

$$\alpha_i = \alpha_{i-1} + (1 - \alpha_{i-1}) \cdot \alpha(x_{ij}) \cdot \Delta r,$$

Each ray is terminated if either the radius R ($R = j \cdot \Delta r$) becomes larger than a certain maximum radius $R_{\max}$ or if the accumulated opacity approaches 1. The $\boldsymbol{T}(\boldsymbol{x})$ obtained by this procedure is generally not symmetric. Therefore, we symmetrize the RST by adding the transposed matrix as $\boldsymbol{T}_s(\boldsymbol{x}) = \boldsymbol{T}(\boldsymbol{x}) + \boldsymbol{T}(\boldsymbol{x})^T$ to obtain real number solution. Then, in order to extract candidates of LNs, we utilized blobness $B(\boldsymbol{x})$ in the same way as Hessian based methods. The $B(\boldsymbol{x})$ is defined as

$$\begin{aligned}&\mathrm{B(x)} = \{\\ &|\lambda_2|^2|\lambda_0| \text{ if} \lambda_0 \le \lambda_1 \le \lambda_2\\ &0 \text{ otherwise},\end{aligned}$$

where λ_0, λ_1, and λ_2 are eigenvalues of $\boldsymbol{T}_s(\boldsymbol{x})$ ($|\lambda_0| \ge |\lambda_1| \ge |\lambda_2|$). We obtain voxels, which $B(\boldsymbol{x})$ are greater than zero, as LN candidates.

False positive reduction

The LN candidates include a lot of FPs. In this step, we eliminate FPs by utilizing volume V and spherical index S of connected components. LNs can be generally observed as spherical objects of a certain size in CT scans. Therefore, we remove the component which satisfies any of following conditions:

$$\begin{aligned}&V < V_{\min}\\ &V > V_{\max}\\ &S < S_{\min},\end{aligned}$$

where $V_{\min}$, $V_{\max}$, and $S_{\min}$ are parameters in order to remove FPs. Finally, we obtain the remained components as LNs.

Results

We have evaluated the proposed method by sensitivity and visual inspection of LNs extracted. In the experiment, we utilized 23 cases of contrast enhanced 3-D abdominal CT scans, which include 55 LNs. Acquisition parameters of the CT scans are: 512 × 512 [pixels], 238–521 [slices], 0.625–0.782 [mm/pixel], 0.5–1.0 [mm] reconstruction interval. The parameters utilized in the experiment were $\Delta r = 1.0$ [mm], $f_{\min} = 35$ [HU], $f_{\max} = 45$ [HU], $R_{\max} = 15.0$ [mm], $V_{\min} = 21\pi$ [mm^3] (volume of sphere with 5.0 [mm] diameter), $V_{\max} = 300\pi$ [mm^3] (volume of sphere with 30.0 [mm] diameter), and $S_{\min} = 0.2$.

Figure 1 shows examples of LNs extracted by the proposed method. These shapes are also correctly by visual inspection. The sensitivity of the proposed method was 81.8 % with 107 FPs per case. Figure 2 shows examples of FPs and false negatives (FNs). Some of FPs exist in the intestinal wall and blood vessel. The FP reduction process of the proposed method does not utilize surrounding regions. However, the proposed method can extract the shape of LNs correctly. Therefore, these FPs may be removed by information of surrounding regions. We consider that a machine learning approach based on these information is one of solution of improvement of the

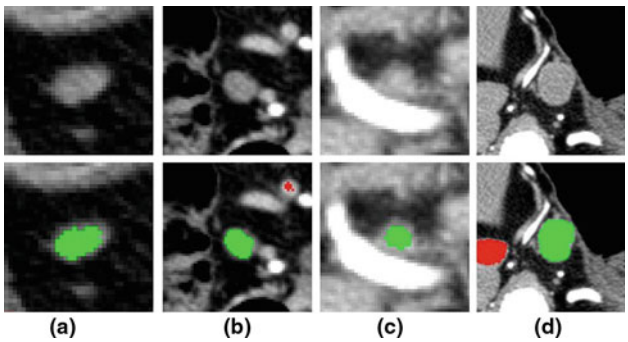

Fig. 1 Examples of LNs extracted by the proposed method. In each subfigure, the original CT scans are shown on the *upper row* (window level: 30 [HU], window width: 300 [HU]) and overlaid with extracted LNs on the *bottom row*. Extracted LNs (true positives) are colored in *green*. FPs are colored in *red*

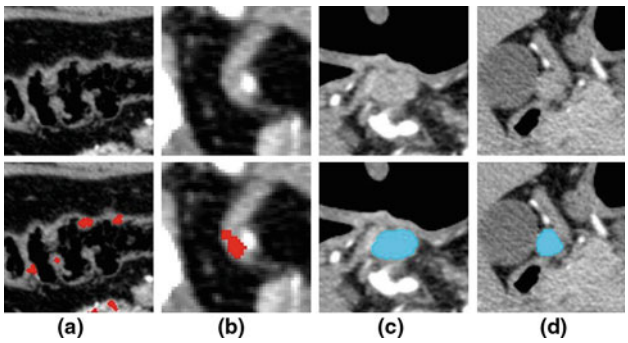

Fig. 2 Examples of FPs and FNs. In each subfigure, the original CT scans are shown on the *upper row* (window level: 30 [HU], window width: 300 [HU]) and overlaid with extracted FPs and FNs on the *bottom row*. FPs and FNs are colored in *red* and *blue*, respectively

FP reduction process. FNs are caused by LN connected to surrounding structures which have similar intensity. Such LN reduces its spherical index. Therefore, it was removed by FP reduction process. In order to resolve this problem, it is necessary to improve RST analysis that can extract local structures separately.

Conclusion

This paper proposed a method of automatic abdominal LN segmentation based on RST analysis. The experimental result reveals that the sensitivity of the proposed method was 81.8 % with 107 FPs per case. The proposed method could extract the shapes of LNs correctly. Future work includes: false positive reduction based on machine learning approach, improvement of RST analysis, and application to LN analysis and surgical planning.

References

[1] Feuerstein M, Glocker B, Kitasaka T, Nakamura Y, Iwano S, Mori K (2012) Mediastinal atlas creation from 3-D chest computed tomography images: application to automated detection and station mapping of lymph nodes. Medical Image Analysis 16(1):63–74

[2] Oda M, Kitasaka T, Fujiwara M, Misawa K, Mori K (2012) Method for detecting enlarged lymph nodes from 3D abdominal CT images with a multi-shape and multi-scale ellipsoidal structure detection filter. Abdominal Imaging 2012, LNCS 7601:238–245

[3] Wiemker R, Klinder T, Bergtholdt M, Meetz K, Carlsen IC, Bulow T (2013) A Radial Structure Tensor and Its Use for Shape-Encoding Medical Visualization of Tubular and Nodular Structures. IEEE Trans. on Visualization and Computer Graphics 19(3):353–366

Low-latency deformable registration for focused ultrasound treatment

D. Lübke[1], J. Gerhardt[1], C. Grozea[1]
[1]Fraunhofer FOKUS, Viscom, Berlin, Germany

Keywords Deformable registration · Prediction · Ground-truth · Optical tracking

Purpose

We propose here a combination of state-of-the-art optical tracking and image processing methods to perform low-latency deformable registration during MRI guided focused ultrasound surgery (FUS), a non-invasive treatment for abdominal tumors. The aim is to continuously track points in a 3-dimensional region of interest (here the liver) in order to measure respiratory motion and finally compensate

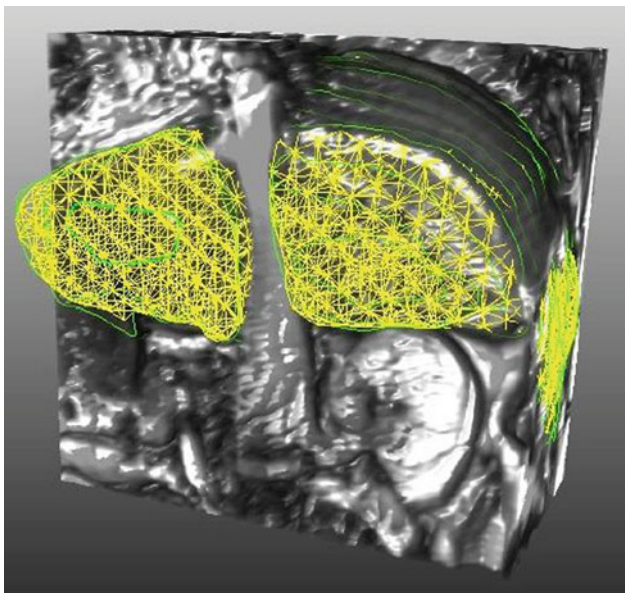

Fig. 1 Tetrahedral liver mesh segmented from MR image

for it. In a previous experiment we have successfully demonstrated motion prediction using semi-automatically marked points in MR images as ground-truth to train a predictor model that solely relies on breathing sensors and the previously marked points [1]. Additionally we have made experiments to use those marked points as movable sampling points in a 3D tetrahedral deformable mesh that has been constructed from a MR image segmentation of the liver. When applying the motion vectors to those sampling points, the simulated mesh exposes approximate behaviour of the liver under respiratory motion (see Fig. 1).

Methods

The method presented here is our approach to retrieve the ground-truth, respectively the sampling points for the simulation fully automatically and with low latency. In a more sophisticated approach, we plan to use the positions from the predictor model as sampling points for the simulation.

For evaluation we have used two MR image sequences of 12 min each recorded with two healthy volunteer test-subjects. Each 3D MRI volume consists of 28 slices with a latency of 220 ms between each slice, summing up to 6.16 s per volume. The first 3D MRI volume for each subject has been used as a reference, where each slice is used to train reference keypoints and descriptors. All subsequent slices are then matched to their reference counterpart to determine the motion for each matched keypoint.

Before performing the actual matching, each slice is being preprocessed, involving a histogram equalization to increase the overall contrast and bilateral filtering to reduce noise without blurring the edges. The processed image is then used to calculate SURF [2] keypoints and SIFT [3] descriptors which are fed to a k-Nearest Neighbors matching. Finally we employ RANSAC classification to remove possible outliers and to preserve high consistency in the actual matching.

The first few MRI volumes are used as an internal learning and evaluation phase to determine which keypoints from the reference slices can be found most reliably in the subsequent slices, as only those keypoints are suitable to serve as ground-truth to update the predictor model.

Results

Although the method is limited due to the compromise between image quality and MRI sequence recording latency, we have

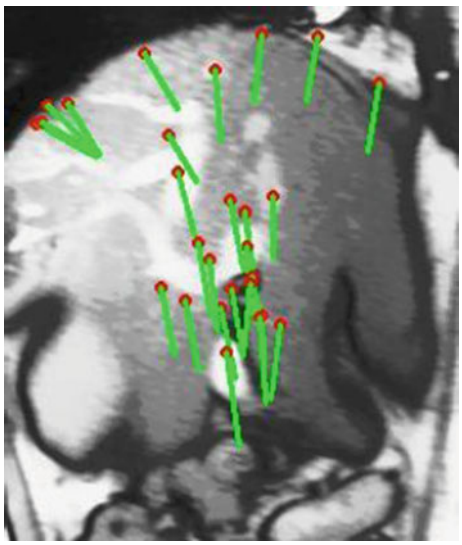

Fig. 2 Re-occurring matches with large displacement

obtained convincing results. The SURF keypoint detector could find a sufficient number of keypoints, while the number of re-occurring reference keypoints in subsequent timepoints is high enough to derive motion for those points over a full breathing cycle (Fig. 2). However, due to the generally low contrast and fairly high noise in liver MR images, those features are limited to blood-vessels or the organ's boundary. Additionally, using this method we were able to fulfill the real-time criteria, i.e., processing time_per_slice <MRI_ latency_per_slice.

Conclusion

The proposed combination of image processing methods enabled us to retrieve well distributed keypoints across the region of interest containing the liver, which previously was lacking relevant trackable information due to low contrast and high noise. The keypoints are well suitable to generate appropriate SIFT/SURF descriptors which expose high distinctiveness and allow robust tracking. The matched keypoints in subsequent timepoints showed good repeatability which make them suitable to either update the predictor model or to serve as sampling points in the deformable simulation. Finally, even a CPU SURF implementation is fast enough to fulfill our timing requirements, which even allows larger regions of interest when using GPU implementations of SURF. Adaptions of the above described method are possible, e.g., it is possible to update the reference images to cope with global motion or drifts that can occur during FUS treatment. Additionally we plan for the future to extend the matching to also consider adjacent slices as well as applying the same matching to a different perspective than only the original slices, i.e., by flipping the 3D volume by 90° and process the flipped perspective's slices to determine motion in the third dimension.

References

[1] Grozea C, Lübke D, Dingeldey F, Schiewe M, Gerhardt J, Schumann C, Hirsch J (2012) ESWT—tracking organs during focused ultrasound surgery. IEEE International Workshop on Machine Learning for Signal Processing (MLSP)

[2] Bay H, Ess A, Tuytelaars T, Van Gool L (2008) SURF: Speeded Up Robust Features. Computer Vision and Image Understanding (CVIU), Vol. 110, No. 3, pp. 346–359

[3] Lowe DG (2004) Distinctive image features from scale-invariant keypoints. International Journal of Computer Vision, 60, 2, pp. 91-110

Computer visualization of the posterior cruciate ligament

P. Zarychta[1]

[1]Silesian University of Technology, Biomedical Engineering, Gliwice, Poland

Keywords Posterior cruciate ligament · Image segmentation · Measure of fuzziness · Fuzzy connectedness · Fuzzy clustering

Purpose

The main aim of this research is extraction and three-dimensional visualization of the posterior cruciate ligament (PCL). Posterior cruciate ligaments (together with anterior cruciate ligament and collateral ligaments ensure rotational stability of the extended knee) belong to the group of anatomical structures, which are frequently susceptible to injuries. The success of ligaments reconstructive procedure depends on many factors, mainly an accurate diagnosis based on the location, segmentation and 3D visualization of these anatomical structures. Computer visualization of the posterior cruciate ligaments provides a way for better understanding the ligament function in the knee joint. Further, properly validated 3D models can be used in the design of knee implant systems.

Methods

The block diagram of the presented methodology providing the major outline of the overall algorithm is given in Fig. 1. In this research in order to lower of the computational complexity and to increase of the efficiency an automatical procedure of the extracting 2D regions of interest (ROI) that include the PCL structure has been elaborated. This procedure has been based on the analysis of the T1-weighted MR

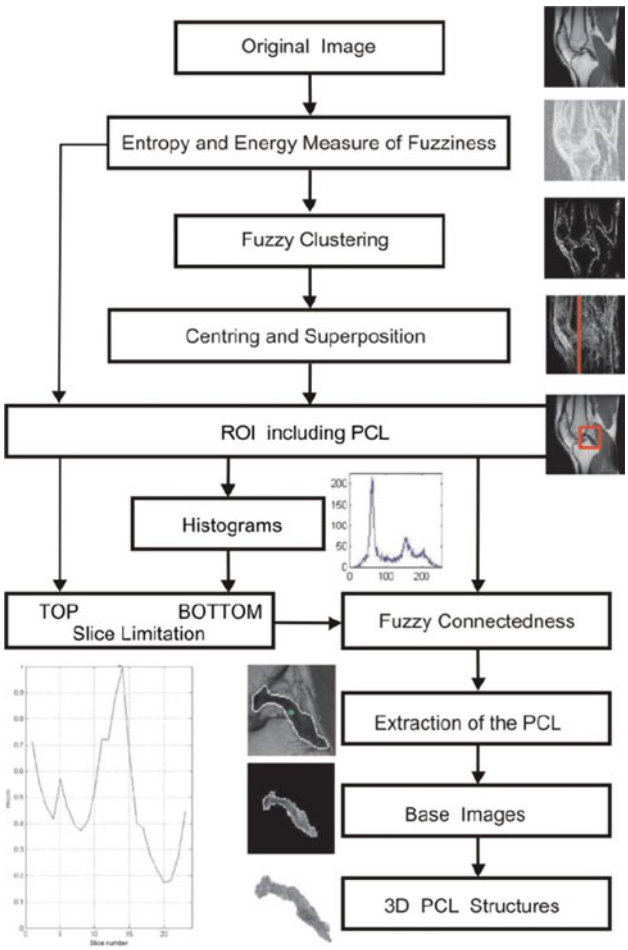

Fig. 1 The block diagram

slices in a sagittal series and the processed area has been reduced meanly three times. The location procedure of the posterior cruciate ligament on the T1-weighted MR slices of the knee joint is based on the entropy and energy measures of fuzziness and fuzzy c-means (FCM) algorithm with median modification. In the first step a main axis running along the thighbone and tibia is determined. In the next steps the main axis permits four ROI 2D edges to be found: upper and lower edge—maximum distance between the main axis and right edge of thighbone and tibia respectively, right and left edge—shift of the main axis by distance between the main axis and right and left edge of tibia respectively. The segmentation process of the PCL structures is based on a fuzzy connectedness concept. Generally this is an iterative method, that permits the fuzzy connectedness to be determined with respect to the chosen image pixel (pixel included in the extracted structure). Result a 3D visualization procedure is rotates the segmented structure of the posterior cruciate ligament. The 3D PCL structures we can observe in whichever plane in two ways: only the 3D PCL structure or the 3D PCL structure against the knee joint background. This method has been implemented in MATLAB and tested on the clinical T1- and T2-weighted MR slices of the knee joint. The 3D display is based on the Visualization Toolkit (VTK).

Results

The methodology has been tested on 68 clinical T1- and T2-weighted MR studies. This group consists of 56 healthy and 12 pathological cases of the posterior cruciate ligaments. On the basis of comparing the original T1-weighted MR slices of the knee joint with the segmented PCL structures the radiologists stated that in 62 (91 %) cases the proposed posterior cruciate ligament segmentation method yielded correct results. The evaluation has been performed by two radiologists and in 62 studies (91 %) the PCL segmentation has pasted the test. Ten ligaments are presented in Fig. 2. The breaking of thighbone structures in the vicinity of the knee joint excludes the possibility of using the proposed algorithm for finding the 2D ROI, which includes the PCL. This kind of pathology is not a common case. Its diagnosis is not a difficult problem for radiologists and does not require from them a time-consuming analysis of the T1-weighted MR slices of the knee joint. The presented methodology does not yield correct results in case of a lack of thighbone and tibia location along the same axis. This application allows for a deviation of 20° between both bones. The deviation of more than 20° was found in patients with degeneration in the knee joint and causes an incorrect location of the 2D ROI.

Conclusion

On the basis of the described methodology a software application has been built. This application is dedicated for the cruciate ligament diagnosis and makes it possible to show the PCL structures in the 3D space. The presented method of enhancing the idea of fuzzy image creating and using the entropy and energy measures of fuzziness to the posterior cruciate ligament location in the T1-weighted MR slices of the knee joint and fuzzy connectedness idea to the segmentation of that structure, seems to be very effective and promising.

Fig. 2 3D views of the PCL structures for 10 different studies

3D scanning of chronic wounds and scars for documentation and archiving of the therapy process

S. Holtzhausen[1], Ch. Schöne[1], R. Aschoff[2], M. Schild[2], H. Meissner[3], P. Sembdner[1], R. Stelzer[1]

[1]TU Dresden, Chair of Design Technology and CAD, Dresden, Germany

[2]University Clinical Center, Dermatology Polyclinic, Dresden, Germany

[3]University Clinical Center, Dental Prostheses Polyclinic, Dresden, Germany

Keywords Fringe projection · Wound documentation · Planimetry · 3D scanning

Purpose

In present medical dermatological practice, 2D information is used for documentation of wounds or skin tumours [1]. This includes digital photos as well as the application of planimetry. It is possible to efficiently document therapy states and therapies as a function of time by analysing and using digital 3D information about skin ulcersas well as keloids or hypertrophied scars that can be recorded by means of advanced 3D-scanning technology.

Methods

An objective documentation of chronic wounds is, among other things, necessary for the description of healing processes [2]. Measurement of size both initially and during the healing process is the most essential parameter. Documentation should be carried out by means of a method that is accurate, reliable and objective as possible in the development of new wound products as well. The therapeutic application of silicone-based wound dressings was checked in an open monocentric pilot study. We used a biocompatible silicon grid with no active agents by a company. Additionally, we engineered analysis methods for chronic wounds and tested them within this study.

In recent years progress in new sensor technology has made it possible to reduce scanning times to milliseconds [3]. Furthermore, hand-guided or hand-held apparatuses, and their miniaturization, have become more important in medical practice.

For the investigations, we used two different 3D scanners that are suitable for hand-guided use: zSnapper portable by VIALUX and kolibr*i CORDLESS,* engineered by the Fraunhofer IOF Jena, both based on fringe projection. Instead of this, other related works use laser-based triangulation systems [4]. These methods have disadvantages in terms of detected texture, accuracy and the sensitivity of specular light.

As a result of 3D scanning, we obtain ordered scanned point data or faceted triangular meshes. Using the scanned data, it is possible to represent the wound boundary as a 3D curve. The individual

boundary segments are described by the corresponding measuring points located on the wound boundary.

With the closed three-dimensional wound boundary curve, the curve length can be determined as a documentation parameter. At the same time, it is possible to quantify the area of the region included by the curve by summing up the faceted partial surfaces. This value can also be used for documentation purposes and represents the wound area. To determine further characteristics, the curve of the skin surface under healthy conditions must be ascertained. It is thus an asset that biological objects, and human skin in particular, are continuous in a mathematical sense in bounded regions and are relatively simply to describe.

To calculate the geometry of the healthy skin, the region bounded by the wound boundary curve, that is the region within the wound, is eliminated from the data record. Curvature at the wound boundary can be determined by means of a defined boundary region. The curvatures are used as a basis to calculate support splines. These take a tangential course to the healthy wound boundary.

These support splines make it possible to estimate surface points, from which, in turn, the surface is discretely described by triangulation. The results correspond to a skin surface free of defects [5].

The calculation of the healthy skin structure makes it possible to estimate the wound volumes in the region that is included by the wound area and the healthy area.

The areas represented in Fig. 1, either the area of the complete surface of the wound region or that of the calculated healthy skin region, can be brought together using an assigned value. This H factor (healing factor), stands for a calculated value that brings the area of the wound and the healthy area into proportion.

As a rule, the wound- or scar area is larger than the healthy area. As a result, the H factor is less than 1. If the H factor approximates 1, then both areas are roughly the same. Whereas the length of the wound boundary may vary widely in case of interactive selection, the H factor is relatively robust in terms of its value.

Results

3D scanning makes it possible to represent a chronic wound in a contactless manner. Thus, the method can be used for documentation of the healing process.

After recording with the optical scanner (Fig. 2), we obtain textured triangles that describe surfaces. The gray scale texture of the surface corresponds to the real contrast values of the wound. Based on the texture and the three-dimensional representation of the wound, the doctor can define the wound boundary. To do this, the doctor marks line segments on the data record. With the developed program KTC_WoundControl we may immediately calculate the surface curve of the skin regions in a healthy condition. The curve is approximated, taking into account the boundary regions of the wound. Other parameters determined are the boundary length and the wound area, as well as the volume between the surfaces, known as the wound volume.

The pilot study is aimed at recording and objectifying the volumetric change of chronic wounds by means of the 3D measuring technique in the therapeutic use of silicone-based wound dressings. The values were consistent with the clinical process of the wound. In other words, the volumes and areas of the ulcer determined by the 3D measuring technique also decreased during wound healing. In the case studied here, wound area decreased by 37.16 % and the wound volume by 97.98 % in 28 days (doctor's round 3). Healing was achieved after 56 days (doctor's round 4). Moreover, surface measuring by means of 3D scanning proved to be more precise than the planimetric method.

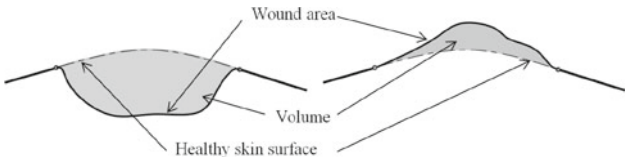

Fig. 1 Volume and surface for wounds (*left*) and scars (*right*)

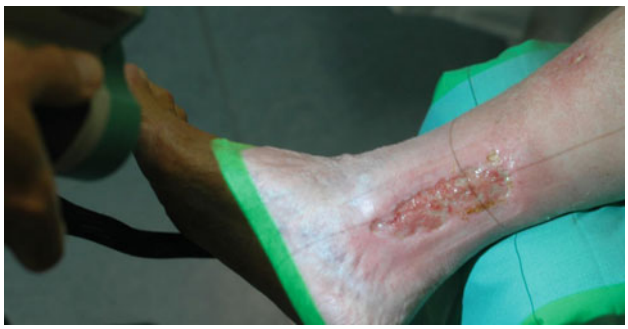

Fig. 2 Application of the 3D hand-held scanner (kolibri CORDLESS, Fraunhofer Institute for Applied Optics and Fine Mechanics IOF), example: leg wounds

Conclusion

With the software solution we have developed, the doctor can directly measure the wound area during or immediately after the consultation. This makes it possible to document the therapy process over several months and to estimate the degree of success of the treatment. Subsequent research projects will focus on computer-assisted determination of the wound boundary, which will reduce the influence of the doctor's subjective perception.

References

[1] Allen S, (1967) A simple technique for recording varicose ulcers. Practitioner 199:97–9

[2] AWMF-Leitlinien-Register Nr. 037/009, (2010) Diagnostik und Therapie des Ulcus cruris venosum, S.1–93

[3] Munkelt C, Bräuer-Burchardt C, Kühmstedt P (2007) Cordless hand-held optical 3D sensor proceedings of SPIE, Vol. 6618 66180D-1

[4] Kecelj-Leskovec N, Jezersek M, Mozina J, Pavlovic M (2007) Measurement of venous leg ulcers with laser-based three dimensional method: Comparison to computer planimetry with photography. Wound Repair and Regeneration: 767–771

[5] Ernst S. (2009) Plausible Reperatur von Löchern in Dreiecksnetzen. Dissertation Otto-von-Guericke-Universität Magdeburg

Evaluation of circulating blood volume using ultrasound imaging of the internal jugular vein

K. Qian[1], T. Ando[1], K. Nakamura[2], H. Liao[1], E. Kobayashi[1], I. Sakuma[1]

[1]The University of Tokyo, School of Engineering, Tokyo, Japan

[2]The University of Tokyo Hospital, Department of Emergency and Critical Care Medicine, Tokyo, Japan

Keywords Internal jugular vein · Ultrasound image · Snakes · Speckle tracking

Purpose

Evaluation of circulating blood volume is important in assessing the status of patients in critical and intensive care. Although the central venous pressure (CVP) and the stroke volume variation (SVV) have been used for the evaluating the circulating blood volume, these methods are invasive and difficult to perform during emergencies. Some recent studies have attempted to evaluate the circulating blood volume using the ultrasound image of internal jugular vein (IJV), located on the left and right side of the neck [1]. Although some studies have suggested that ultrasound images of the IJV can be used

for the analysis of circulating blood volume, accurate extraction of IJV is necessary to reduce errors and determine appropriate indicators to evaluate the circulating blood volume. Therefore, this study was designed to develop a new algorithm for dynamic segmentation of IJV, and evaluate the accuracy of our algorithm.

Methods

Our algorithm is based on snakes [2] and speckle tracking models. Snakes are one form of active contour models, were used for various segmentations in the ultrasound image [3]. Although the snakes algorithm can be applied to various image types, the tracking often fails because the calculation is strongly affected by local solutions that are derived from the noise of the image. While it may be possible to reduce the error by constricting the control points of the snakes inside the region of interest (ROI), but it cannot follow fast motion because the actual edge will be outside ROI. To solve these problems, a new algorithm using speckle tracking-assisted snakes were proposed. As the ROI of the control points of the snakes tracking algorithm was dynamically moved using speckle tracking, ROI size can be decreased leading to a reduction in the tracking error. Our algorithm includes the following two steps:

1. Move the control points of the snakes along the motion of the tissue using speckle tracking.
2. Perform the original snakes and converge it along the edge.

The accuracy of the extraction was evaluated to validate the developed algorithm. valuated by comparing the region extracted using our algorithm with the one extracted manually by a doctor from the emergency department. The manual extraction was performed using a pen tablet to extract the contour. The evaluation method used in this experiment was based on the method proposed by Zijdenbos et al. [4]. The extraction was evaluated by the following similarity index (S):

$$S = 2 \times \frac{A \cap M}{A + M} \quad (1)$$

Here A is the area of the automatically extracted region, and M is the area of the manually extracted region, two regions are similar when S is close to 1.The similarity index of the proposed method, the snakes, and the speckle tracking were evaluated separately. Five frames were evaluated, which were randomly chosen from 11 ultrasound videos of the IJV. All the frames of one movie were also evaluated, to observe the change in the similarity index over time. A paired t test was performed to ascertain if the differences in the results obtained with the three methods were statistically significant. The t test was used for the verification because they were results of the same movie.

Results

Our algorithm enabled more accurate tracking compared with standard methods. Figure 1 illustrates the results of the evaluation. The

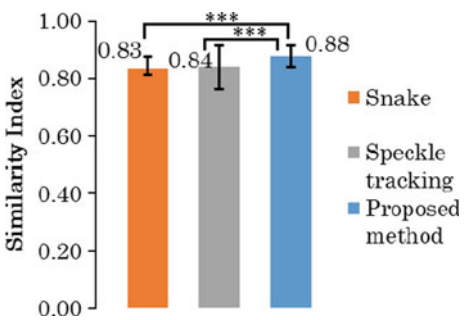

Fig. 1 Evaluation results for each method

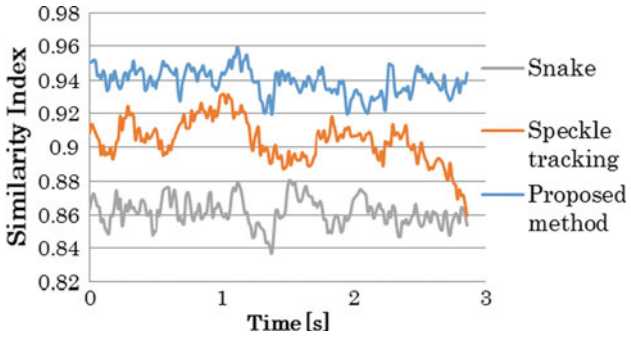

Fig. 2 Changes of similarity index in time series

similarity index of the original snakes, standard speckle tracking, and our method was 0.83 ± 0.04, 0.84 ± 0.08, and 0.88 ± 0.04, respectively. The difference between our method and the original snakes, and the difference between our method and the standard speckle tracking was statistically significant ($p < 0.001$). Figure 2 illustrates the change of similarity index over time for all methods. The similarity index of speckle tracking decreased with time. In contrast, the similarity index was almost constant for the standard snakes and the proposed method. However, the average value for our method was higher than those of the standard snakes.

Conclusion

The results of evaluation of the extraction demonstrated that our algorithm enabled more accurate extraction of IJV area compared with other standard methods. Because our algorithm moves ROI of the control points of snakes using speckle tracking, the size of ROI can be downsized that leads to a reduction in error. The validation experiment demonstrated that our algorithm gives higher performance compared with the standard snakes or speckle tracking.

References

[1] Donahue SP, Wood JP (2009) Correlation of sonographic measurements of the internal jugular vein with central venous pressure. Am J Emerg Med 27(7):851–855
[2] Kass M., Witkin A (1988) Snakes—Active Contour Models. International Journal of Computer Vision 1(4):321–331
[3] Li M, Kambhamettu C (2005) Automatic contour tracking in ultrasound images. Clinical Linguistics & Phonetics. 19(6–7):545–554
[4] Zijdenbos AP, Dawant BM (1994) Morphometric analysis of white matter lesions in MR images: method and validation. 13(4):716–24

Relief Map of the upper cortical subarachnoid space

A. Lebret[1], Y. Kenmochi[2], J. Hodel[3], A. Rahmouni[4], P. Decq[5], E. Petit[1]
[1]Université Paris-Est, LISSI, Créteil, France
[2]Université Paris-Est, LIGM, UMR 8049 CNRS, Marne-la-Vallée, France
[3]Hôpital Saint Joseph, Radiology Department, Paris, France
[4]Hôpital Henri Mondor, Radiology Department, Créteil, France
[5]Hôpital Henri Mondor, Neurosurgery Department, Créteil, France

Keywords Cerebrospinal fluid · Cortical subarachnoid space · Relief map · Computer-aided diagnosis

Purpose

Hydrocephalus is a neurological disorder that usually results from obstruction of the cerebrospinal fluid (CSF) outflow in the ventricles or in the subarachnoid space. MRI offers a great deal of information to specialists in the clinical diagnosis and treatment processes of

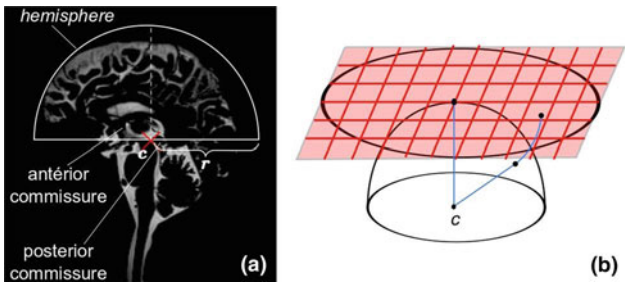

Fig. 1 Sagittal cross section of an original image (**a**) and Lambert projection on the 2D grid (**b**)

hydrocephalus. Recently we have proposed a new MRI sequence that significantly highlights the CSF and a segmentation method to assess its space volumes [1]. Those studies indicate us that the fluid distribution in the cortical subarachnoid space varies significantly, according to whether or not there is a pathology. However, visualization and analysis of the fluid distribution, particularly that of cortical sulci, remain difficult in 3D.

This paper proposes a method to retrieve a 2D relief map of the CSF in the upper cortical subarachnoid space from the 3D images. We define the upper cortical subarachnoid space as the region located above the plane that passes through the anterior and the posterior commissures. The posterior commissure is located behind the top of the cerebral aqueduct that can be readily detected in the 3D images (See Fig. 1). This new representation provides both qualitative and quantitative information on the fluid distribution that surrounds the brain.

Methods

A *relief map* is generated as a 2D digital image where each pixel corresponds to the amount of fluid between the center of the cortical subarachnoid space, i.e., the posterior commissure, and an observation point of the outside of the head. Such 3D observation points are positioned on the hemisphere that covers the upper space. We explain how to generate a relief map from a 3D image in the following.

1. Positioning the hemisphere and image pre-processing

The center c of the hemisphere is manually set by a specialist with respect to the given data from the anatomical viewpoint. After setting c, the radius r is then calculated such that it is more than the maximum distance from c to voxel points of the CSF volume (see Fig. 1). Images are cropped through the cut-off plane and the ventricular space is removed, then they are binarized to obtain a voxel set.

2. Projection of voxel centers onto the hemisphere

Once we have the hemisphere with center c and radius r, we project each voxel center point v onto the hemisphere by drawing a three-dimensional line going through c and v and obtaining its intersection with the hemisphere. This intersection is the projected point of v on the hemisphere, denoted by p.

3. Mapping from the hemisphere to the plane

All the points p on the hemisphere are now projected on a 2D plane. For this goal, we use the Lambert equal-area projection as it possesses the following interesting properties: bijection, diffeormophism, and area-preservation [2]. On the other hand, it preserves neither angle nor distance, and thus shapes are distorted in the plane. However, such distortion is less observed if the projection is restricted to the hemisphere centered at the projection point. The following formulas are applied for each point of the hemisphere $\mathbf{p} = (x,y,z)$ such that $(x - c_x)^2 + (y - c_y)^2 + (z - c_z)^2 = r^2$ and $z \geq c_z$, to obtain the 2D point $\mathbf{P} = (X,Y)$ located in the disc with center at the origin and radius $\sqrt{2r}$:

$$X = (2r/(r + z - c_z))^{1/2}(x - c_x),$$

$$Y = (2r/(r + z - c_z))^{1/2}(y - c_y).$$

4. Voting in the 2D digitized disc

For generating a relief map, we digitize the disc, obtained by the Lambert projection, with a square grid of pixel size $\sqrt{2r/N}$. The obtained 2D image containing this digitized disc thus has the support of size $(N + 1) \times (N + 1)$. Each projected point **P** then votes for the pixel that contains **P** itself. After this voting procedure for all projected points, each pixel has a vote as its altitude, so that the relief map is produced.

The relief map has the following properties: the total amount of altitudes in the map is equal to the volume of the initial 3D voxel set; each voxel is associated to only one pixel in the relief map. As we use the Lambert equal-area projection, we suppose that every pixel has a similar altitude for a digitized solid-hemispherical object at center (c_x,c_y,c_z).

Results

Experiments were performed on 38 MR images of different subjects (12 healthy volunteers and 26 hydrocephalus patients, ages: 23–91). Figure 2 shows examples of relief maps obtained with our method.

Quantitative assessments on relief maps were carried out by calculating the ratio of the fluid area to the projection disc area (96.18 % ± 0.78 for healthy adults and 88.95 % ± 5.97 for pathological cases) and the first moments [3]. The latter indicate that for pathological cases the fluid distribution is depleted in the posterior region of the brain asymmetrically towards the frontal region: the relative change of the centroid position along the horizontal axis to healthy adults is −10.55 % and that of the skewness is +337 %. This shows up the capability of this approach to quickly verify that the fluid distribution has returned to a normal state after a surgery as shown in Fig. 2.

Conclusion

This work uses a new MRI sequence that significantly highlights the CSF, and succeeds in providing a relief map of the upper cortical subarachnoid space. Our tool allows to visualize and estimate the fluid

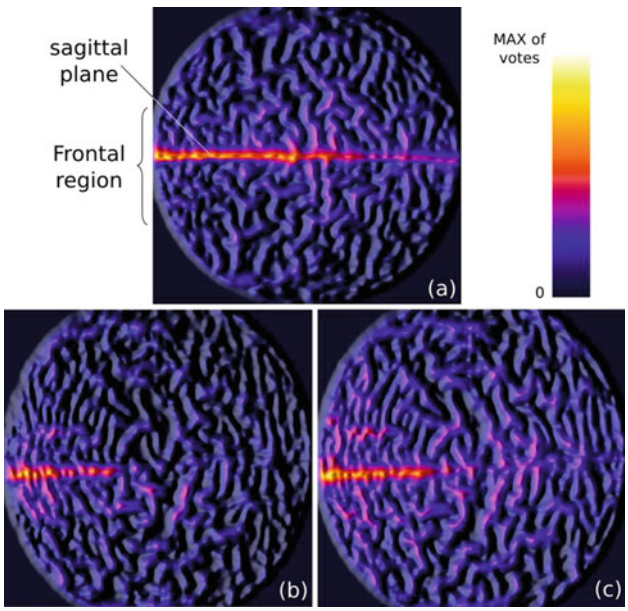

Fig. 2 Colored relief maps for an healthy adult (**a**), and an hydrocephalus patient before (**b**) and after (**c**) a surgery. The frontal region of the fluid is on the *left part* of the map. The sagittal plane separates the map horizontally and appears brighter

volume and its distribution into the upper space. This new ability may represent an important breakthrough for diagnosis and for monitoring patients, particularly those suffering from hydrocephalus, before and after surgery.

References

[1] Hodel J, Lebret A, Petit E, Leclerc X, Zins M, Vignaud A, Decq P, Rahmouni A (2012) European Radiology, doi:10.1007/s00330-012-2732-7

[2] Bugaevskij LM, Snyder J (1995) Map Projections: A Reference Manual. CRC Press

[3] Flusser J (2006) Moment invariants in image analysis. Transactions on Engineering, Computing and Technology 11(2), 196–201

Design and construction of 3D breast tumor phantoms for studying morphological effects on biomechanical properties

P.-L. Yen[1], R.-H. Fan[1], D. Chen[2], Y.-J. Chu[1], H.-C. Hsu[1]

[1]National Taiwan University, Department of Bio-Industrial Mechatronics Engineering, Taipei, Taiwan

[2]ChungHua Christian Hospital, Department of Surgery, ChungHua, Taiwan

Keywords Breast cancer diagnosis · Biomechanics · Tumor phantom · Statistical shape model · Principal component analysis

Purpose

Tumor morphology has been confirmed to be closely correlated to its benignity or malignance in breast cancer diagnosis. The correlations have been extensively investigated and applied in clinical practice. Although the tumor morphology is very useful for breast cancer diagnosis, there are also certain amounts of false cases where the morphology information along is not adequate for making accurate diagnosis. However this ambiguity of distinguishing tumor may be resolved if their biomechanical properties are taken into account. Therefore quantitative analysis of the biomechanical properties of tumors has received massive attentions and a large number of methods for measuring tumor's biomechanical properties have been proposed in recent decades. However a systematic representation of tumor phantoms which the tumor's phantom can efficiently represent the morphological and biomechanical information for experimental investigation is still lacking. In this paper we proposed a statistical shape model for describing 3D breast tumor's shape and construction of a set of tumor phantoms which represents the typical tumor shapes together with different mechanical properties.

Methods

Image acquisition, processing, segmentation and 3D reconstruction

Data base for breast tumors are from 3D ultrasound images acquired from GE Healthcare Voluson 73. Total number is 259, including 145 benign tumors and 114 malignant ones. Each 3D ultrasound image was processed as 199 slices and the resolution of each slice is 181 × 163 pixels. After manual localizing the breast tumor and defining ROI (region of interest), these images were inputted to open source software ITK for image enhancement, segmentation (based on snakes, active contour models) and 3D reconstruction (in STL format) and then inputted to open source software VTK for display.

3D Tumor model resampling

A statistic shape model is constructed to represent 3D tumor by PDM (point distribution method) and PCA (Principal Component Analysis). The aim of statistical shape model for 3D breast tumor is to build a model which is capable of representing both typical shape and variability. First step is to decide the landmarks. However unlike human anatomy there are no specific anatomical features among breast tumors. We chose an equally distributed point model for describing 3D tumor shapes. At the same time we decided to reduce the total points of the 3D tumor model down to 1,272 with taking into account of model accuracy and computation simplicity. The equal distributed points of sphere for resampling the 3D tumor model is formulated by an icosahedron with further triple sub-division. Each triangle on the sampling sphere will find the corresponding triangle on the 3D tumor model.

Alignment and PCA

In order to be able to compare equivalent points from different shape, these points are aligned with respect to a coordinate system. In this case the 3D tumor model is aligned by defining a coordinate system, in which the origin is defined as the center of mass, X-axis as the longest axis of the tumor, Y-axis the longest axis which is perpendicular to X-axis and thus Z-axis as the cross of X-axis and Y-axis. Alignment of the point set of each tumor model is achieved by scaling, rotation and translation of the coordinate systems. Each tumor is represented by a vector in a 3n space after alignment. The principle axes fitted to the data set can be calculated by PCA. Each calculated principal axis represents a variation mode. The variation mode describes the tendency of these landmark points moving among these tumors.

Design and manufacturing of 3D Tumor Phantoms

In tumor phantom determination, we design to select the first two variation modes and varying the associated weighting from $+2\sigma$ to -2σ as shown in Fig. 1. Then the tumor phantoms are scaled to the size from 6 mm to 15 mm. The shapes of tumor phantoms are in STL format and output to Solidworks software for tumor mold design (Fig. 2). The mold is then manufactured by a rapid prototyping machine and the materials for making tumor phantoms is from room temperature vulcanizing silicon material (General Silicones Co. Ltd., Taiwan). Two-package types: GS-875, RTV-664, and RTV-4020 can be adjusted their proportions for different stiffness.

Results

Total numbers of 200 tumor phantoms have been manufactured by combination of first two variation modes with 5 different weighting, 4 different sizes and 4 different types of stiffness. This tumor phantom set was further located into breast phantoms as embedded inclusions to simulate the breast with lesions in prone pose. We utilized these phantoms in tumor indentation and sliding tests for collection and analysis of the reaction forces and torques. The measured data show that the first two shape variation modes are adequate to reflect the biomechanical properties of tumor as the experiment showed that increase of more variation modes to the tumor phantom made no significant difference on the measured outputs.

Conclusion

We have successfully built a statistical shape model for breast tumor phantom construction from 3D ultrasound images. These constructed phantoms can effectively reflect the effects of tumor's morphology on the biomechanical properties. In the future we will utilize these phantoms to investigate specific mechanical properties, such as stiffness and mobility of tumors in conjunction with morphological

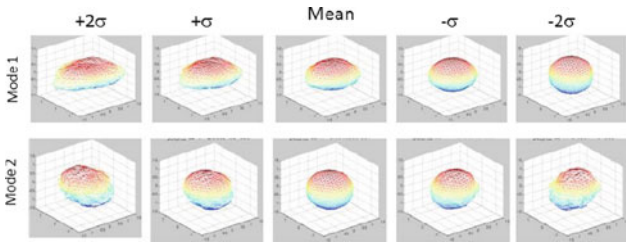

Fig. 1 First two shape variation modes of the statistics shape model of breast tumors

Fig. 2 Design and rapid prototyping the mold for 3D tumor phantom with various shapes and sizes

features of 3D ultrasound images to improve the prediction of tumor's benignity or malignance in breast cancer diagnosis.

Quantification of longitudinal tumor changes using PET imaging in 3D slicer

P. Mercea[1], A. Fedorov[2], S. Pieper[3], R. Beichel[4,5], M.-A. Park[6], J. Hainer[6], M. Foley Kijewski[6], L. Horky[6], R. Kikinis[2], H. Dickhaus[1]
[1]University of Heidelberg, Dept. of Medical Informatics, Heidelberg, Germany
[2]Brigham and Women's Hospital, Dept. of Radiology, Boston, USA
[3]Isomics Inc., Cambridge, MA, USA
[4]The University of Iowa, Dept. of Electrical and Computer Engineering, Iowa City, USA
[5]The University of Iowa, Dept. of Internal Medicine, Iowa City, USA
[6]Brigham and Women's Hospital, Dept. of Nuclear Medicine, Boston, USA

Keywords PET imaging · SUV quantification · Open-source medical imaging computing · Quantitative image analysis

Purpose

Assessment of time series of Positron Emitted Tomography (PET) can be used for monitoring tumor response in cancer treatment. In clinical practice, PET analysis is based on normalized indices such as those based on standard uptake value (SUV) [1, 2, 3]. Development and validation of such methods for the purposes of clinical research require a common open platform that can be used both for prototyping and sharing of the analysis methods, and for their evaluation by clinical users. This work was motivated by the lack of such platform for quantitative PET analysis. It was our goal to develop and evaluate an open source software tool for quantitative analysis of tumor changes from PET image data. Our second goal was to make this platform extensible. Extensibility makes the platform also suitable for prototyping PET-specific segmentation and quantification methods.

Methods

We have chosen 3D Slicer 4 (http://slicer.org), a free open source software application for medical image computing, as a platform for this work [4]. The functionality has been implemented as a 3D Slicer extension that guides the operator through a series of workflow steps. These steps include import of DICOM PET/CT studies, segmentation of findings and presentation of the analysis results. The key components of the analysis are the following.

Visualization

For the qualitative analysis as well as for registration and segmentation, the image data is visualized as PET/CT fusion images in 2D slice views. Interactive 3D volume rendering of the PET data is available for quick overview and hot spot localization. The results of the quantitative analysis are visualized as plots by using 3D Slicer charting capabilities see Fig. 1. Visualization settings are initialized automatically by the software, but can be modified by the user.

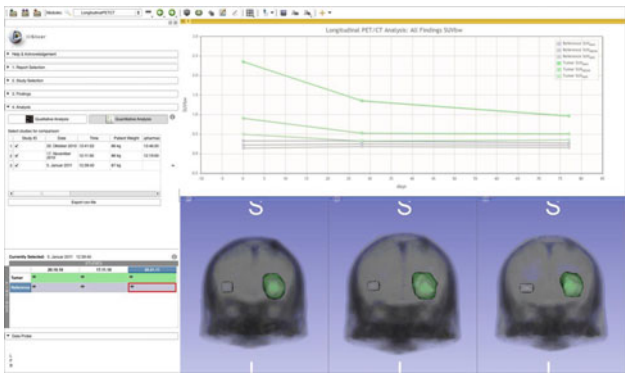

Fig. 1 Illustration of the analysis results produced by the developed software. Analysis summary includes SUV values, longitudinal analysis results chart and volume rendering of the PET data and VOI surface for brain FLT PET (scans were 4–7 weeks apart, ~5 mCi was injected, and acquired for 30 min starting 30 min after injection)

Segmentation

Segmentation of the volumes of interest (VOIs) corresponding to the lesions is a preliminary step for PET quantification. The Editor module of 3D Slicer has been integrated into the analysis workflow, providing access to a variety of segmentation tools. The plugin architecture of the Editor module simplifies integration of new segmentation algorithms implemented as ITK or VTK filters.

Quantification

SUV for the segmented VOIs were calculated for longitudinal analysis of tumor changes. The default quantification method in this work uses the body weight as normalization factor for the SUV parameter (SUV_{bw}) [3] and calculates the minimum, mean and maximum SUV_{bw} values for a given VOI. The application of this rather simple normalization factor, in contrast to the usage of body surface area or lean body mass, improves the applicability of our tools in clinical research practice. The parameters needed for the calculation of the latter indices are often missing in the DICOM headers of common PET data. Due to the architectural modularity of the software, the computation algorithms for the quantification can also be extended by other researchers in order to prototype and develop more sophisticated quantification methods.

Evaluation

Heuristic usability evaluation [5] with clinical and software development experts was conducted after the completion of a first stable release of the module. Heuristic evaluation is a usability inspection method in which three or more evaluators examine an user interface for usability issues applying a set of heuristics to the interface and assess the severity of each violation. Our setup included two different groups of evaluators composed of 3 clinical experts in the field of PET research in one group and 4 Slicer development experts in the other group. To evaluate the reproducibility of quantification, 8 evaluators who were not specialized in PET assessment applied the software to analyze the same dataset.

Results

The functionality was implemented as an extension to the 3D Slicer software platform. This extension is free open source and is interoperable with Windows, Mac and Linux operating systems. Timing needed for processing was assessed on an Apple Macbook Pro (Dual Core i7, 2.7 GHz, OSX 10.7) with DICOM image data from GE, Phillips and Siemens PET/CT scanners. Usability tests have shown

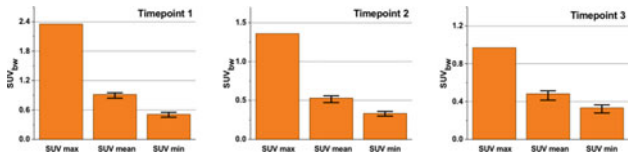

Fig. 2 Summary statistics for comparative evaluation of quantitative analysis results. Maximum SUV_{bw} values are reproducible while the mean and minimum fluctuate on average 4.53 %

that a 3 timepoint longitudinal tumor quantification, in which minimum, mean and maximum SUV_{bw} values for a segmented VOI is calculated for every timepoint, for PET/CT head data with brain tumor can be performed in less than 2:30 min by a trained user. As expected, the maximum SUV results were consistent, while mean and min SUV indices exhibited variability, see Fig. 2. Results from the heuristic usability evaluation revealed some minor usability problems associated to the graphical user interface, mostly reported by the software development experts. Whereas the evaluation results from the clinical experts group identified additional desired capabilities rather than usability details.

Conclusion

An extensible, free open source tool for longitudinal PET analysis of tumor changes using PET imaging has been developed. The current configuration covers the basic requirements for PET quantification. More sophisticated PET segmentation and quantification algorithms can be incorporated in the future, leveraging the extensible software architecture.

Acknowledgments

This work was supported in part by NIH grants CA151261 and CA140206.

References

[1] Tomasi et al. Importance of Quantification for the Analysis of PET Data in Oncology: Review of Current Methods and Trends for the Future. Mol Imag Biol. 2011.

[2] Passero et al. Response assessment by combined PET-CT scan versus CT scan alone using RECIST in patients with locally advanced head and neck cancer treated with chemoradiotherapy. Annal Oncol. 2010.

[3] Boellaard R. Standards for PET image acquisition and quantitative data analysis. J Nuc Med. 2009;50:11S–20S.

[4] Fedorov et al. 3D Slicer as an image computing platform for the Quantitative Imaging Network. Magnetic resonance imaging. 2012;30(9):1323–1341.

[5] Nielsen J, Molich R. Heuristic evaluation of user interfaces. Proceedings of ACM CHI'90; 1990.

High resolution 3D imaging of lung cancer mice in vivo and in situ using phase contrast imaging

L. Zhang[1], M. Wu[1], S. Luo[1]

[1]Capital Medical University, School of Biomedical Engineering, Beijing, China

Keywords Lung cancer · Medical image processing · Phase contrast imaging · Three-dimensional visualization

Purpose

Lung cancer is a major fatal malignancy worldwide. The survival depends on stage. Early detection of the lung cancer is known to improve the chances of successful treatment [1, 2]. In many patients, only when the cancer has already spread beyond the original site and sever symptoms appear, they realized they need medical attention [3]. Phase contrast imaging (PCI), which has high spatial resolution and superior soft tissues sensitivity, provides a new way to non-invasive lung imaging [4]. Compared with other main PCI methods, in-line X-ray phase contrast imaging (IL-XPCI) is the simplest and the most straightforward, making it more suitable for clinical applications than other methods [5].The purpose of the current study was to apply PCI into lung cancer study.

Methods

The study samples are nude mice (6 weeks, body weight 16 g ± 1 g) which were injected with 30 μL PC-9 tumor cell suspension (2.0 × 107 cells per ml) into the lung. The experiment was made 7 days after the injection. They were divided into two groups: quasi-static inflation group and live animal imaging group. Mice in the first group were humanely euthanized via anesthesia overdose. We inserted an endotracheal tube into the mid-cervical trachea via a tracheotomy to inflated air by an air filled syringe. And then the mice were mounted on the rotation stage. Mice in the second group were anaesthetized by an intraperitoneal injection of chloralic hydras. And then an endotracheal tube was inserted, via a tracheotomy, into the mid-cervical trachea and connected to a small animal ventilator. So the breath could be externally regulated. The in-line phase contrast imaging experiment was performed at X-ray imaging and biomedical application beamline (BL13W1) of Shanghai Synchrotron Radiation Facility (SSRF). After phase contrast imaging, the two groups' images were segmented and reconstructed in three dimensions (3D) to study the deformation of the lung structures during breath.

Results

We demonstrate the measurement of respiratory airway morphological deformations at functional residual capacity (FRC) and total lung capacity (TLC). It revealed a significant increase in airway diameter at TLC. The 3D visualization of the same lung at FRC and TLC are shown in Fig. 1a, b. At FRC some collapse parts of the lung can be found (pointed by the arrow). This is due to the oppression of the tumor. Meanwhile, the tumor volume decreased dramatically. It was rendered in yellow color (Fig. 1c, d). At TLC, the airspace clearly increased. The tumor volume decreased from 2.22 to 1.38 mm^3. Figure 2 is a detailed demonstration of one small section of the lung. These images provided a magnified view of the alveolar sacs and the alveoli at FRC and TLC. The model can be cut at any angle, varied in size, and rotated in real time. As shown in Fig. 2, it is easy to investigate the breathing deformation of the lung on the alveolar level. Furthermore, we showed our initial attempt of live animal three-dimensional lung imaging.

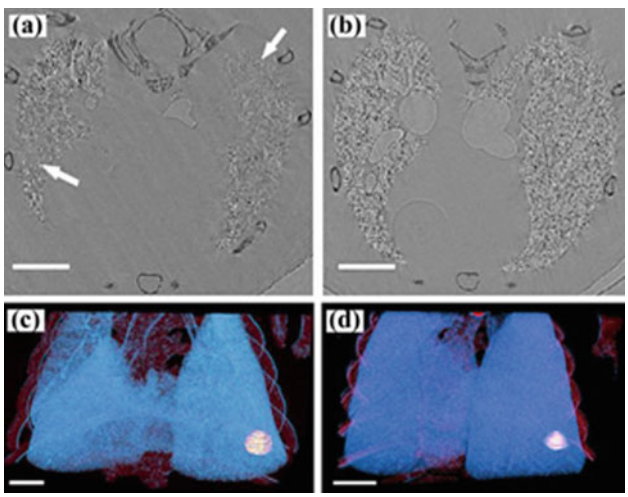

Fig. 1 Lungs with tumor at two breath state **a** A CT slice of the lung at FRC. **b** A CT slice of the same lung at TLC. **c** 3D volume rendering of the lung at FRC. **d** 3D volume rendering of the lung at TLC. The tumor was rendered in *yellow color*. Scale bar: 5 mm

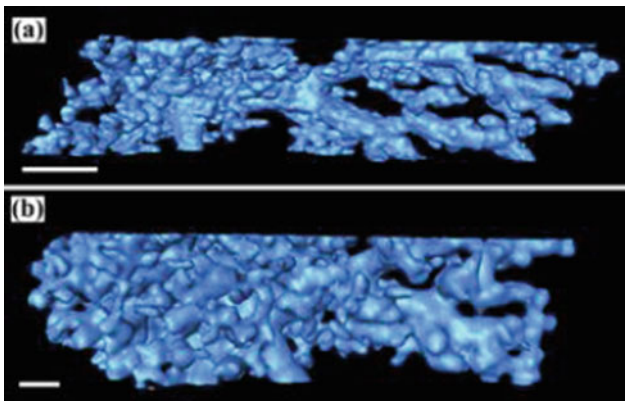

Fig. 2 Detailed demonstration of one small section of the lung **a** FRC, **b** TCL. Scale bar: 500 μm

Conclusion

Phase contrast imaging is a powerful tool for lung imaging and quantifying morphology changes in lung cancer model. It adds significant biological and clinical information on the mechanisms and structures of lung cancer.

Acknowledgments

The authors acknowledge the staff from beamline BL13W1 of Shanghai Synchrotron Radiation Facility, China, for their kindly support of the experiment. Our project number is 11sr0082. This study was supported by the National Natural Science Foundation of China, Grant No. 60532090 and 30770593, and by the 7th Framework Programme of the European Community, Grant Agreement Number PIRSES-GA-2009-269124.

References

[1] Hoffman PC, Mauer AM, Vokes EE (2000) Lung cancer. Lancet 355: 479–485

[2] Sera T, Uesugi K, Yagi N et al. (2008) High resolution visualization of tumours in rabbit lung using refraction contrast X-ray imaging. Eur J Radiol 68: S54-S57

[3] Greene FL (2002) AJCC cancer staging manual. Springer-Verlag, Berlin

[4] Wilkins SW, Gureyev TE, Gao D et al. (1996) Phase-contrast imaging using polychromatic hard X-rays. Nature 384: 335–338

[5] Lewis RA (2004) Medical phase contrast X-ray imaging: current status and future prospects. Phys Med Biol 49: 3573–3583

A hybrid flexible rendering pipeline for real-time 3D medical imaging using GPU-accelerated integral videography

J. Wang[1], I. Sakuma[1], H. Liao[1]

[1]Graduate School of Engineering, The University of Tokyo, Tokyo, Japan

Keywords 3D medical imaging · Integral videography · Graphics processing unit · Rendering pipeline

Purpose

Computer-generated integral videography (IV) is an autostereoscopic 3D imaging and display technique which can produce animated 3D images with motion parallax [1]. However, it suffers from low rendering frame rate and the difficulty of incorporating IV functionality into existing graphics pipelines. We propose a flexible rendering pipeline for computer-generated IV with GPU acceleration, which is suitable for real-time 3D imaging of both anatomical models and medical volumes. This work has two main contributions: 1. a hybrid flexible rendering pipeline which could be easily merged into existing OpenGL rendering pipelines to provide IV functionality and 2. real-time 3D imaging performance with high image resolution using a consumer-level GPU. The proposed rendering pipeline can change modes freely between normal rendering and IV rendering at run time.

Methods

Computer-generated IV is in essence, the process of sampling the virtual 4D light field produced by geometric data (medical data in our case) [2]. The light field is defined on the light slab consisting of the screen (LCD display) and its front convex lens array. The value of the light field depends on the medical data and the chosen optical model. The IV rendering process is to synthesize the color of rays passing through each screen pixel and its nearest lens center. For surface models, it is difficult to directly sample the desired light field. Assume there is a parallel grid plane in front of the screen. The number of sub-grids is the same as the number of pixels covered by lens pitches. Moving the view point to each center of the sub-grid and performing off-axis projection renderings obtain a series of viewport images. The rays passing each pixel and its nearest lens center can be re-sampled using linear interpolation on the viewport images. For volumetric data, raycasting is a direct way to sample the light field: for each pixel, a ray connecting the pixel and its nearest lens center is cast and the composite color after the ray interacts with the volume is calculated.

The IV rendering procedures for both surface models and volumetric data are time-consuming and can be intrinsically implemented in a parallel way, which is extremely suitable for GPU processing. Modern OpenGL has a programmable rendering pipeline which can be executed on GPUs. Shader programs run in parallel in the vertex and fragment processors on a GPU. Our surface model IV rendering pipeline is described as follows: Geometric data is loaded into OpenGL as a vertex buffer object (VBO) and is processed by shaders to create viewport images. A proxy geometry that covers the whole screen pixels is drawn and processed by IV shaders to generate IV elemental images. Similarly, our volume IV rendering pipeline is as follows: Volumetric data is loaded into OpenGL as a 3D texture with 4 color channels: x, y, z components represent the image gradient and the alpha component represents the intensity. The raycasting procedure is implemented in the IV shader which is performed in parallel for all pixels. Figure 1 illustrates the proposed hybrid rendering pipeline combining both surface model IV rendering and volume IV rendering. The hybrid rendering pipeline allows choosing the IV rendering pipeline most appropriate for the input data type. The client program transfers anatomical models or medical volumes to GPU memory beforehand (or in real-time when rendering a stream of 3D volumes, e.g., 4D US image). User interaction devices and/or external trackers are used to interact with the OpenGL camera for locating the IV sampler and triggering the rendering pipeline to update the 3D display. As shaders can be dynamically loaded into the GPU at run time, the rendering pipeline could be changed flexibly by loading different shaders to achieve various visual effects.

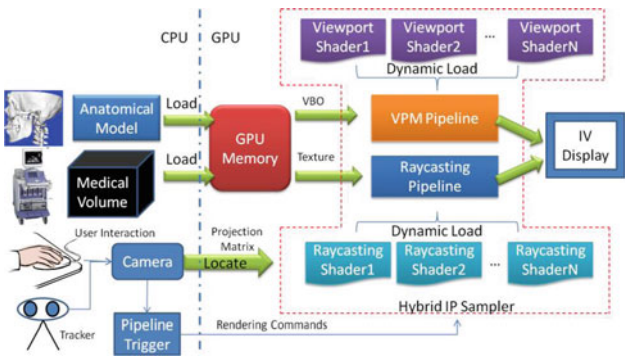

Fig. 1 Proposed IV rendering pipeline

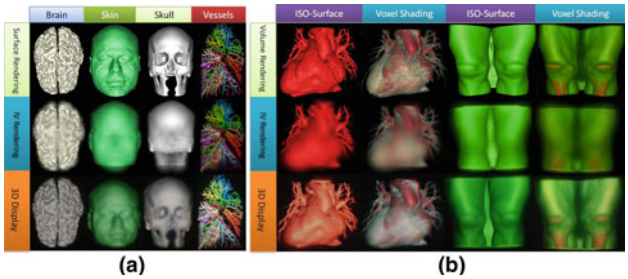

Fig. 2 **a** Anatomical model rendering results. **b** Medical volume rendering results

Results

Evaluations of the proposed rendering pipeline were performed by using several 3D imaging examples. The CPU and GPU were an Intel Core i7-3960X CPU (3.30 GHz) and a NVIDIA GeForce GTX580 GPU. The IV display screen has a resolution of 3,840 × 2,400. Brain, skin, skull and pulmonary vessel (PV) models were used for surface model IV rendering; a heart and a knee volume were used for volume IV rendering. Two optical models (iso-surface and voxel shading) were implemented in the raycasting procedures. Fig. 2 shows the rendering results. The rendering time (s) are given as follows (Name:GPU/CPU): Brain:0.026/5.978, Skin:0.025/5.968, Skull:0.029/6.025, PV:0.056/6.118, Heart-iso:0.357/61.631, Heart-shading: 0.467/94.503, Knee-iso: 0.083/28.119, Knee-shading: 0.145/56.127.

Conclusion

The results show that our GPU implementation is at least 109 times faster than a CPU implementation and at most 387 times faster. The proposed pipeline could be easily merged into our 3D image-guided surgical navigation systems to achieve real-time and flexible 3D medical imaging with rich visual effects.

Acknowledgements This work was supported in part by the Communications R&D Promotion Programme (111703020) of the Ministry of Internal Affairs and Communications in Japan, and Grant-in-Aid for Scientific Research (23680049, 24650289) of the Japan Society for the Promotion of Science.

References

[1] Liao H, et al. (2010) 3-D augmented reality for MRI-guided surgery using integral videography autostereoscopic image overlay. IEEE T Bio-Med Eng 57(6):1476–1486

[2] Levoy M, Hanrahan P (1996) Light field rendering. in: proceedings of the 23rd Annual Conference on Computer Graphics and Interactive Techniques. ACM, New York, 31–42

Sparse Gaussian graphical model estimation for spatial distribution of multiple anatomical landmarks in the human body—application to an automatic landmark detection system

S. Hanaoka[1], Y. Masutani[1], M. Nemoto[1], Y. Nomura[1], S. Miki[2], T. Yoshikawa[2], N. Hayashi[2], K. Ohtomo[1]

[1]The University of Tokyo, Dept. of Radiology, Tokyo, Japan

[2]The University of Tokyo, Dept. of Computational Diagnostic Radiology and Preventive Medicine, Tokyo, Japan

Keywords Graphical lasso · Anatomical landmark · Computed tomography · Landmark point detection · Sparse gaussian graphical mode

Purpose

A sparse Gaussian graphical model (SGGM) is a statistical modeling method in which a probability distribution of given multiple variables is approximated as a multivariate Gaussian distribution with a sparse precision (inverse covariance) matrix [1]. If a certain non-diagonal factor in the precision matrix is zero, it suggests that the corresponding two variables are conditionally independent. Thus, SGGM can be regarded as a tool to estimate a graphical model, in which only conditionally dependent variables are connected by edges. It is reported that SGGM is especially useful when the number of variablespis much larger than sample sizen.

Automatic detection of a large number of anatomical landmark positions from medical images has a wide range of application in medical image analysis. For this purpose, we have been developed an automatic detection system for multiple anatomical landmarks in CT images [2]. It is able to determine over 170 landmark positions simultaneously, taking their spatial correspondence into account, by utilizing a non-sparse Gaussian statistical model on inter-landmark distances. The aim of this study is to improve the performance of our previous method by applying SGGM on inter-landmark distances. For this purpose, the graphical lasso method [1] which was proposed by Friedrich et al. was implemented with GPGPU. The probabilistic distribution of inter-landmark distances was estimated as a multiple Gaussian distribution with a sparse precision matrix. Feasibility of improvement of the landmark detection accuracy with this novel inter-landmark distance model was evaluated with clinical CT datasets.

Methods

1. Statistical model on inter-landmark distances and anatomical landmark detection system

The outline of our landmark detection system is illustrated in Fig. 1. The system consists of two subsystems: a series of single-landmark detectors and maximuma posteriori (MAP) estimation-based combinatorial optimizer. Each single-landmark detector outputs a candidate list which indicates possible candidate positions of the target landmark and their estimated likelihoods. These lists are used as an input for the following combinatorial optimization process which searches the most probable combination of the candidates. In this optimization, a prior knowledge on statistical variation of spatial distribution of anatomical landmarks in the human body is needed. In our system, this is given as a multivariate Gaussian distribution function on inter-landmark distances between all pairs of landmarks. The detail is as follows. Let the number of landmarks be M, the normalized distance between the i-th and j-th landmark ($1 \leq i<j \leq M$) be $g_{i,j}$, and the concatenated vector of all $g_{i,j}$ be $\mathbf{g} = (g_{1,2},g_{1,3},\ldots,g_{i,j},\ldots,g_{M-1,M})$. Then, the prior probability function is defined as

$$p(\mathbf{X}) = |\Theta|^{1/2} \cdot \{(2\pi)^{-1/2}\}^{M(M-1)/2} \cdot \exp(-1/2 \cdot \mathbf{g}^t \Theta \mathbf{g})$$

where $\boldsymbol{\Theta}$ is the precision matrix of $\mathbf{g}$ estimated from the training dataset.

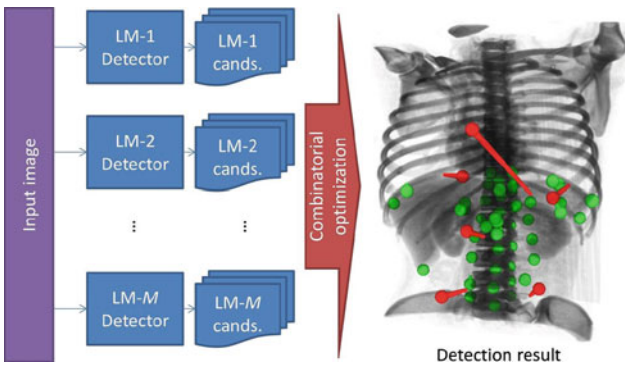

Fig. 1 Outline of landmark detection system

Note that the precision matrix needs to be estimated to determine the probability function $p(\mathbf{X})$. It is not a trivial problem because the dimension of this Gaussian distribution, $p = M(M-1)/2$, is almost always far larger than the amount of available training datasets n. When $p > n$, the sample covariance matrix S, which is simply calculated from the training dataset, will not be full rank, thus, not invertible. Therefore, an appropriate regularization is needed to estimate $\mathbf{\Theta}$ from $\mathbf{S}$.

In our previous study, this estimation was performed with Tikhonov's regularization, which leads to $\mathbf{\Theta} = (\mathbf{S} + \rho\mathbf{I})$. ($\rho$ is a parameter.) However, as Tikhonov's regularization does not provide a sparse estimation of $\mathbf{\Theta}$, this regularization method does not lead to a SGGM.

2. Graphical lasso method

To estimate a sparse precision matrix $\mathbf{\Theta}$ from the sample covariance matrix S, Yuan and Lin proposed to minimize the negative l1-penalized log-likelihood

$$-\log|\Theta| + \mathrm{trace}(\mathbf{S}\Theta) + \rho||\Theta||_1$$

Again, ρ is a parameter to control the sparsity of the resulting $\mathbf{\Theta}$. The graphical lasso method, introduced by Friedman et al., is a very efficient algorithm to solve the problem above.

The processing time of the original graphical lasso algorithm is of order $O(p^3)$, thus, of order $O(M^6)$. Thus, it can be very time consuming when the number of landmarks M is large. To overcome this problem, we implemented the graphical lasso algorithm on a GPGPU environment.

3. Evaluation

For evaluation, we compared the landmark detection performances with the sparse and non-sparse precision matrices estimated by the graphical lasso method and Tikhonov's regularization, respectively. Total 55 target landmarks are detected by corresponding single-landmark detectors as the same as the previous study. Then, these single-detector results were combinatory optimized by using the prior probability function $p(\mathbf{X})$ with the estimated $\mathbf{\Theta}$. The value of coefficient for Tikhonov's regularization and graphical lasso were 1.25 and 0.90, respectively. These values were determined empirically. The detection result of each landmark was evaluated as successful if the detected landmark point is within 2 cm distance from the manually-inputted ground truth point. Total 21 CT datasets of human abdomen with intravenous contrast agent administration were used in the evaluation. The training and evaluation of the models was performed by threefold cross validation.

Results

The entire result is shown in Fig. 2. The average successful detection ratio by the graphical lasso-based method and Tikhonov's regularization were 0.745 and 0.719, respectively. The graphical lasso-based method showed better detection ratio in 11 landmarks (20.0 %), whereas it showed worse result in 27 landmarks (49.1 %). Though the graphical lasso-based method showed slightly lesser detection accuracy, the difference was as small as 0.026 point in average. In some cases the graphical lasso-based method outputs a point very far from the true point for some landmarks (as Fig. 1 right), and it was considered as possible cause of this performance decline. Clarifying the reason of this phenomenon is desirable in future work.

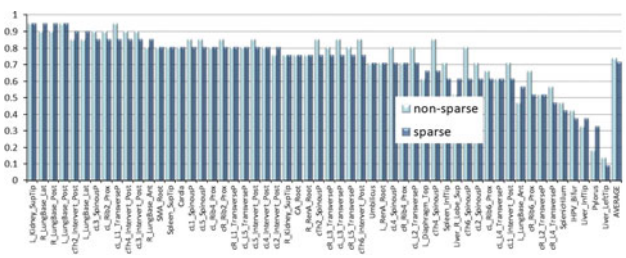

Fig. 2 Result chart

The calculation time for processing graphical lasso algorithm for one precision matrix implemented on a GPGPU (NVIDIA Tesla C2050) was approximately 12 s. On the other hand, the CPU implementation by Friedman et al. (available at http://www-stat.stanford.edu/~tibs/glasso/) took 43 s for the same problem.

Conclusion

A method to compose a sparse Gaussian graphical model of the spatial distribution of anatomical landmarks was presented. Its feasibility in automatic landmark detection task was suggested from the experimental result.

References

[1] Hanaoka S, Masutani Y, Nemoto M, Nomura Y, Yoshikawa T, Hayashi N, Yoshioka N and Ohtomo K (2012) An improved multiple anatomical landmark detection method with combinatorial optimization and Madaboost-based candidate likelihood determination. IJCARS, Volume 7 Suppl.1, pp.S330–331.

[2] Friedman J, Hastie T, Tibshirani R: Sparse inverse covariance estimation with the graphical Lasso. Biostatistics 9:432–441.

Fully automatic segmentation of white matter lesions: error analysis and validation of a new tool

H. Rusinek[1], L. Glodzik[2], A. Mikheev[1], A. Zanotti[1], Y. Li[2], M. de Leon[2]

[1]New York University, Radiology, New York, USA

[2]New York University, Psychiatry, New York, USA

Keywords Image analysis · Image segmentation · Magnetic resonance imaging · White matter lesion · Error analysis

Purpose

White matter lesions are common radiologic findings in a variety of neurological disorders. Their prevalence increases with age, as they are closely associated with vascular risk factors such as hypertension, hypercholesterolemia and diabetes. Their ubiquity in the aging brain and poorly understood etiology render their quantification essential in neurologic research and in the clinic. Accurate measurement of lesion extent and its changes over time is also important for disease monitoring and evaluation of treatments.

Brain lesions appear as signal hyper-intensities on proton-density and T2-weighted MRI sequences. Because cerebrospinal fluid (CSF) signal is also bright in these sequences, lesions are easier to discriminate on fluid-attenuated inversion-recovery (FLAIR) MRI sequence, designed to null the CSF signal.

There is an increasing need for highly automated, validated, and reproducible lesion segmentation tools. Most of the successful methods in the literature are based on supervised training or unsupervised clustering using a Gaussian model to describe normal brain tissue signal. Algorithms based on voxel clustering alone cannot differentiate between artifacts present in FLAIR images and true lesions (see Fig. 1). Moreover, many existing tools are hampered by the need to acquire complementary T1-weighted sequences or to establish an elastic transformation to morph individual subject to a brain template.

We present a new fully automatic lesion segmentation tool that is designed to efficiently and reliably segment hyperintense lesions using conventional FLAIR MRI. Our user-friendly software doesn't require complementary T1-weighted MRIs or brain templates. We analyze segmentation accuracy by using two complementary approaches. The results of automatic segmentation are compared: (a) with brain lesions segmented "manually" by two expert observers, and (b) with true lesion volumes in computer-simulated lesions.

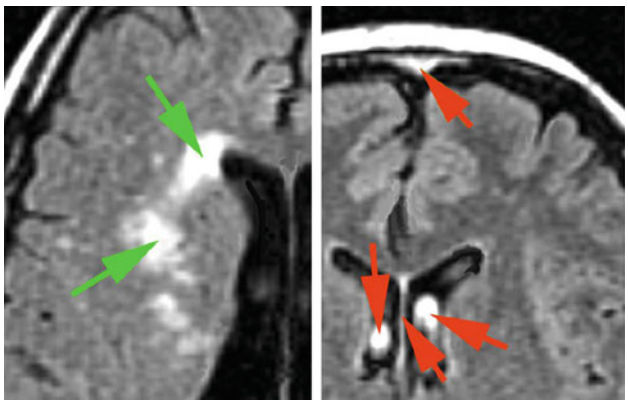

Fig. 1 *Left* axial FLAIR image of an elderly person. Lesions in periventricular and deep white matter are shown by the *green arrows*. Note poor gray/white matter differentiation. (*Right*) FLAIR image of another individual shows hyperintense signal in the fat, choroid plexus and septum pellucidum (*red arrows*), areas that must be excluded from true hyperintense lesions

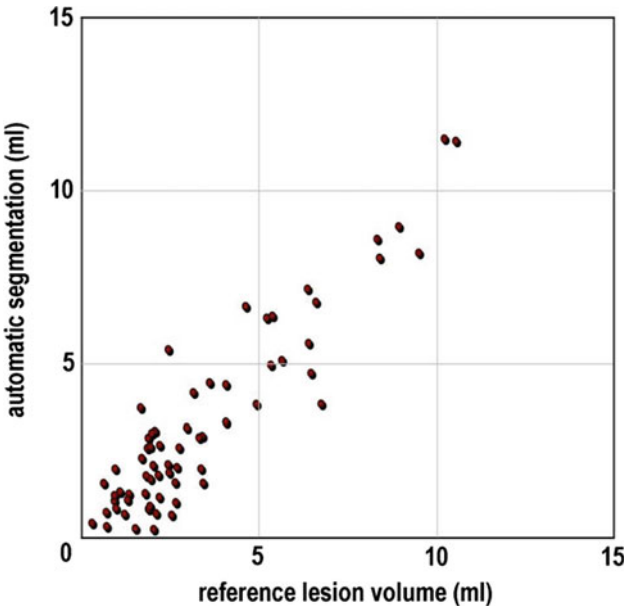

Fig. 2 Results of fully automatic lesion segmentation in 73 elderly brains are plotted against the reference volume. Automatic volumes were calibrated to remove a systematic multiplicative bias, yielding an average absolute error of 0.94 ml

Methods

The workflow starts with FLAIR image uniformity correction (N3 algorithm). The program then estimates the signal intensity of the cerebral white matter by searching the mid-coronal section of the field of view for a 1-cm cubic subregion of minimal coefficient of variability of the FLAIR signal. The resulting seed signal is used to construct the initial brain mask M_1 based on relative signal range constraints, connectivity, and surface smoothness. A new region M'_1 is constructed from M_1 by applying hole filling operator. Due to signal range constraints, ventricular CSF spaces and hyperintense lesions will be included M'_1 but not in M_1. The region M_1 is morphologically peeled (3.5 mm radius of structured element) to generate a region M_2 of presumably normal brain voxels. The goal of this step is to exclude contaminating partial volume artifacts. The lower bound for signal in lesions is computed as $s_{min} = \mu + k\sigma$, where μ is the mean value and σ the standard deviation of M_2. In the next step we compute candidate lesion by selecting from M'_1 all voxels with signal larger than s_{min}.

Several post-processing passes are then applied, aiming at noise suppression (removal of small connected components with volume <12 mm^3) and removal of connected regions with >50 % border with CSF (choroid plexus, septum) .

We quantified lesion volumes in FLAIR images of 73 cognitively healthy subjects (mean age 62.8 ± 9.8). The MRI sequence parameters were: TR 9,000 ms, TE 134 ms, TI 2500 ms, FA 140°, NEX = 1, BW = 252 Hz/pixel, FOV 220 mm, 30 × 5 mm thick slices, voxel size 0.85 mm, TA = 3 min 16 s. Cases were selected at random from participants in studies of aging and memory. Lesions were also manually segmented by two experts, a neurologist and a neuro-radiologist, both having >9 years of professional experience. For the manual segmentation, the observers had access to (1) the automated workflow, with (unlike for automatic tool) all parameters being freely adjustable and (2) an extra post-processing step, during which lesion mask could be interactively edited with a mouse-controlled paintbrush and eraser. Observers were blinded to each other results and to the fully automated lesion mask.

We have applied the algorithm to 10 computer-simulated cases with 3D lesions of variable size, ranging 52–595 mm^3, and variable lesion/brain FLAIR signal contrast. To assure realistic appearance, lesion contrast varied between 1.5 and 1.95 at the center and 1.2–1.90 at lesion borders.

Results

There was a good agreement regarding lesion volume V segmented manually by two experts, with interclass correlation coefficient (absolute agreement) of 0.923, 95 % confidence interval 0.75–0.98. The mean absolute discrepancy in expert assessment was 0.62 cm^3. Since there was no systematic reader bias between the experts (T-value = 1.24, $p = 0.24$, Pearson correlation = 0.926), measurements by the first observer were used as reference values.

The reference distribution of V was 4.6 ± 7.6 cm^3 (mean ± standard deviation). V values were distributed over a wide range 0.1–58.9 cm^3, but for only one out of 73 subjects V exceeded 25 cm^3. The distribution of V as measured by the automatic tool was 5.9 ± 7.1 cm^3. While there was a highly significant linear relationship (adjusted $R^2 = 0.972$, df = 72, $p < 0.0001$) between automatic and manual assessments, the automatic segmentation was characterized by a significant multiplicative oversegmentation bias averaging 1.36 cm^3. When automatically computed lesion volumes were calibrated to remove that bias (Fig. 2), the mean absolute error was reduced to 0.94 cm^3. The was a tight distribution of mean absolute error, with 75 percentile = 1.26 cm^3 and 90 percentile = 1.80 cm^3.

The oversegmentation bias was also observed in 10 computer simulated 3D lesions with true volume 271 ± 169 mm^3. The computed volume was 304 ± 223 mm^3. There was a highly significant linear relationship (adjusted $R^2 = 0.934$, df = 9, $p < 0.0001$) between automatic measures and true volumes.

Conclusions

We evaluated in a large cohort a new algorithm for automated segmentation of hyperintense brain lesions from FLAIR data. Unlike many existing tools, our algorithm doesn't requires high-resolution T1-weighted images. The study established a robust lesion segmentation, with mean absolute error of 0.94 cm^3 and 90 percentile about

twice as large. We had to calibrate our results to compensate for false positive misclassification of normal brain voxels as the lesions. Since there is no commonly accepted ground truth, we compared results with manual segmentation by expert observers. Future studies are needed to systematically assess our tool against other lesion measurement software. As another limitation, we restricted our evaluation to overall 3D lesion volume, but we didn't measure the spatial agreement. However, overall lesion load is the measure employed in most clinical investigations involving the significance and etiology of FLAIR lesions. In summary, we have developed a promising tool for fully automatic detection of FLAIR lesions, yielding good agreement with segmentation by experts and with simulated lesions.

A model-based approach for cervical spine mobility analysis

M.A. Larhmam[1], M. Benjelloun[1], S. Mahmoudi[1]
[1]University of Mons, Computer Science Department, Mons, Belgium

Keywords Medical imaging · Vertebra segmentation · Hough transform · K-means

Purpose

The purpose of this study is dedicated to cervical vertebra mobility analysis in conventional radiography. Indeed, vertebra detection and segmentation present an essential step toward spine motion study. However, this task becomes more challenging in conventional radiography due to low contrast and noise noticed in this medical image modality.

Based on our previous work on semi-automatic detection of vertebra [1], we propose in this paper a robust method for cervical vertebra body identification and segmentation in X-ray images. This new method enables to compute the parameters used for vertebra motion analysis.

Methods

Our contribution involves a novel combination of a modified template matching method and an unsupervised clustering algorithm. In this method, we build a geometric vertebra mean model. To achieve our vertebra detection process, manual selection of the region of interest is performed initially on the input image. After that, we first apply a preprocessing step in order to enhance image contrast and detect edges. Candidate vertebra localization is then carried out by using a modified Generalized Hough Transform (GHT) [2]. Next, an adapted cost function which computes local voted centers is used in order to filter data points. Thereafter, a K-means clustering algorithm [3] is applied to obtain the clusters distribution corresponding to the targeted vertebrae. These clusters are combined with the vote parameters to detect vertebra centers. Rigid segmentation is then carried out by using GHT parameters.

Results

Experimentations were conducted by using a set of 66 high-resolution radiographs. All these images focused on the cervical spine area. This database included 20 images inspected by a radiologist who annotated six landmarks on each cervical vertebra. This annotation generates a ground truth data for the segmentation validation step.

The detection of cervical vertebrae operated successfully on the input radiographs. The validation of the results was led by using visual examination and clinical expert landmarking.

On the other hand, to evaluate our segmentation step, we used the angle of inclination of each cervical vertebra. We compared our results with manual landmarks annotated by expert radiologist. Figure 1 shows the computing process of vertebra orientation from landmark points. The final segmentation results of the proposed method is shown in Fig. 2.

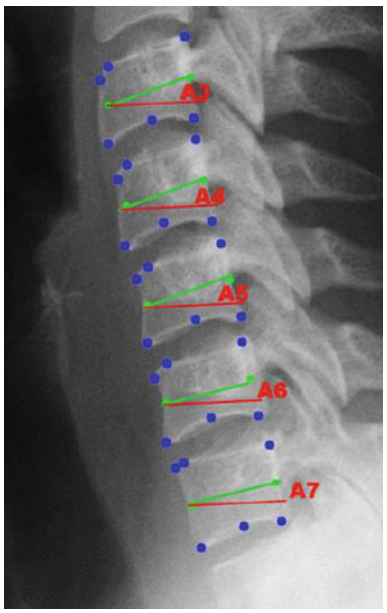

Fig. 1 Vertebra orientation computed from landmarks: the vertebra mid-plane in green and the orientation angles in *red*

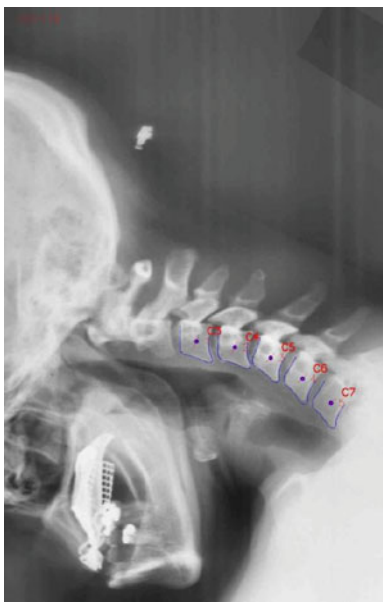

Fig. 2 Final segmentation results for C3–C7 cervical vertebrae

Conclusion

We proposed in this paper a novel method that combines a template matching model and K-means clustering to identify cervical vertebrae in X-ray images. We conducted an offline process to build the vertebra mean model and create a parametric representation of it. Thereafter, a candidate vertebra localization based on the Generalized Hough Transform was performed. Finally, we applied an adapted cost function, and K-means clustering in order to achieve vertebra identification. The proposed detection approach proved to be robust to noise and occlusion and can be applied to different image databases.

This method enables a robust identification even for missing edge detection.

As regards future work, we plan to develop a fully automatic segmentation approach based on our recent contribution, as well as improve our learning model and voting process. We also intend to study abnormal vertebra cases using MRI datasets.

References

[1] Larhmam MA, Mahmoudi S, Benjelloun M. (2012) Semi-Automatic Detection of Cervical Vertebrae in X-ray Images Using Generalized Hough Transform. Proc 3rd International Conference on Image Processing Theory, Tools and Applications. pp 396–401

[2] Ballard DH. (1981) Generalizing the Hough transform to detect arbitrary Shapes. Pattern Recogn 13(2):111–122

[3] MacQueen JB. (1967) Some Methods for classification and Analysis of Multivariate Observations. Proc 5th Berkeley Symposium on Mathematical Statistics and Probability. University of California Press. pp. 281–297.

Modification of level set hippocampus segmentation results using partial volume effects correction

M. Hajiesmaeili[1,2], J. Dehmeshki[1], T. Ellis[1,2]

[1]Quantitative Medical Imaging International Institute (QMI3), Faculty of Science, Engineering and Computing, Kingston University London, United Kingdom

[2]Digital Imaging Research Centre (DIRC), Faculty of Science, Engineering and Computing, Kingston University London, United Kingdom

Keywords Fuzzy C-mean (FCM) · Hippocampus (HC) · MRI · Partial volume effect (PVE)

Purpose

Quantitative assessment of hippocampal volume is influenced by partial volume effects (PVE) as a consequence of the occurrence of more than one tissue type in a voxel (mixed voxel) in volumetric images. In such cases, the voxel intensity depends on the imaging sequence, tissue properties and the proportion of types adjacent to the hippocampus (HC) border, such as amygdala, alveus, cerebrospinal fluid (CSF) and gray and white matter.

Methods

In this paper, we propose an algorithm to quantify partial volume effect (PVE) for HC volume correction by applying spatial fuzzy C-means (SFCM) method on level set segmentation results which used bias corrected fuzzy C-means as preprocessing.

In MR images, inhomogeneities in the magnetic fields caused by non-uniform tissue intensities [1], are typically characterized by a slowly varying gain field called a bias field [2]. Thus, proposed algorithm includes bias correction fuzzy C-means (BCFCM) as preprocessing to enhance level set segmentation results following by doing more techniques to obtain binary images. The hippocampal volumes obtained based on level set segmentation results, are not reliable because of partial volume effects. Hence, we need to take into account this factor to do volume correction. Missing mixed voxel would happen if we don't find appropriate segmentation results. Because the ground truth images were available, it was possible to compare the segmented images with images of true hippocampus using the Dice metric. Values range for Dice metric are from zero to one, where higher values indicate better agreement. In hence, for proposed method the threshold of 85 % set on segmentation results to achieve more reliable results for post-processing. For PVE estimation spatial fuzzy c-means (SFCM) presented to find membership degree for each tissue contributes to determine voxel intensity. To measure the corrected volume of HC, the non-tissue border volume respect to achieved membership degree will be deducted from the segmentation result volume.

Results

This method is applied on T1-weighted magnetic resonance (MR) images of 25 subjects with two different resolutions. Dice metric is used as validation technique of segmentation results which obtained 85 % averagely for whole datasets. The average member degrees as results of applying spatial fuzzy C-means on segmented binary images (%11 for HC and 89 % for non-HC) yields the correspondent corrected volumes for left and right HC which are respectively, 18 and 16 % for low resolution and 3 and 1 % for high resolution datasets, lower than hippocampal volume results regardless PVE based on manual segmentation.

Conclusion

This technique was tested on MRI images and evaluated by volumes of correspondent ground truth to obtain accurate measurement of hippocampal volume considering partial volume effects which is more significant for low resolution datasets.

References

[1] Sled JA (1998). A Nonparametric method for automatic correction of intensity nonuniformity in MRI data. IEEE Trans. Med. Imag, 17, 87–97

[2] Wells WM, Grimson WE, Kikinis R, Jolesz FA (1996). Adaptive segmentation of MRI data. IEEE Trans. Med. Image, 15, 429–442

Evaluation of non-contrast head CT images obtained with different reconstruction methods using texture analysis

L. He[1], M.W. Vannier[2]

[1]Beijing Tongren Hospital, Capital Medical University, Department of Radiology, Beijing, China

[2]University of Chicago, Department of Radiology, Chicago, United States

Keywords Texture Analysis · Computed Tomography · Iterative Reconstruction · iDose

Purpose

Noncontrast head CT scans are frequently obtained for routine clinical applications, and radiologists are very sensitive to subtle image characteristics. With the introduction of new dose-saving iterative reconstruction methods, comparison to standard filtered backprojection (FBP) images is required [1]. Texture is a complex set of image features which correspond to spatial patterns of local brightness variations. Texture features can be computed directly from images for use in discriminating and characterizing the visual properties of tissues and structures in CT images [2]. We developed a texture analysis based method to quantify the artifacts and noise introduced by new CT reconstruction methods and dose reduction techniques, with comparison to FBP images of the same datasets.

Methods

Synthetic images, mathematical phantoms, and routine clinical non-contrast head (NCH) CT scans were evaluated using texture analysis (ImageJ from NIH [http://rsbweb.nih.gov/ij] and Fiji software [http://fiji.se]) to obtain quantitative values for small regions including entropy, angular second moment (ASM), contrast, correlation, and inverse different moment (IDM) at 4 principal directions (0°, 90°, 180° and 270°) [3]. To quantify the image texture difference of filtered back projection (FBP) and iterative (iDose level 5, Philips Medical Systems) reconstructions of non-contrast head computed tomography (CT) images were evaluated. An expert

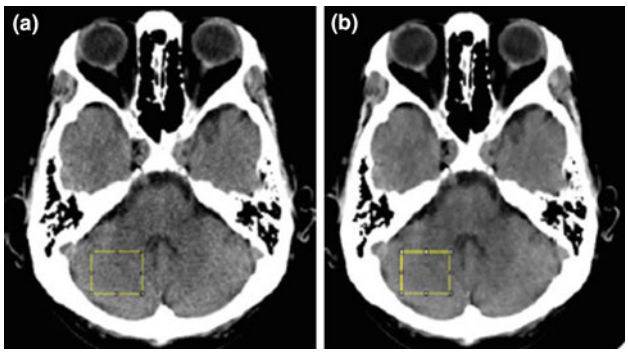

Fig. 1 Texture measurement of cerebellum reconstructed by FBP (**a**) and iDose level 5 (**b**). We captured ROIs with the same size at the same location in this pair of images to facilitate comparison of the texture parameters for these two different reconstruction techniques (Table 1)

Table 1 Texture comparison between FBP and iDose5 reconstruction of cerebellum

	Direction	ASM	Contrast	Correlation	IDM	Entropy	Mean	SD
FBP	0	0.003	465.293	0.001	0.14	7.039	44.349	20.863
	90	0.002	540.032	0.000875	0.124	7.079		
iDose5	0	0.014	37.095	0.013	0.413	4.658	12.329	5.611
	90	0.013	42.611	0.01	0.398	4.694		

neuroradiologist identified anatomic features and tissue types in NCH CT scans with small rectangular regions of interest to create a texture dictionary. Characteristic values for the texture parameters were derived for each tissue type and anatomic region using conventional FBP images [4]. An example ROI from the cerebellum (Fig. 1) was used to compute the texture parameter values shown in Table 1.

In addition, 10 head CT scans of patients (9 non-contrast CT, 1 contrast CT) were reconstructed by FBP and iDose level 5 using the same raw projection data sets and reconstruction parameters. Regions of interest (ROI) were selected at the same area with a uniform size at bone, cerebrospinal fluid (CSF), fat, muscle, gray and white matter, cerebellum, pons, mesencephalon and ocular globe. We chose multiple ROIs in some specific tissues to ensure the stability of the results: 7 in bone (maxilla, magnum foramen, occipital bone, sphenoid bone, temporal bone, frontal bone and parietal bone), 5 in CSF (prepontine cistern, lateral fissure cistern, suprasellar cistern, 4th ventricle and lateral ventricle), 2 in fat (intraorbital fat and subcutaneous fat), 2 in muscle (pterygoid muscle and occipital muscle), 3 in gray matter and 2 in white matter (level of corona radiata). A texture dictionary was developed containing the ROI samples from multiple cases and tissues to be used in comparison of the parameters computed from each NCH CT scan.

Texture parameters of each ROI were calculated for comparison between FBP and iDose level 5 iterative reconstruction images (iD5IR) using all of the available scans. Table 1 shows the results of texture parameter comparisons between FBP and iD5IR images from one patient.

Results

There were statistically significant differences between FBP and iD5IR images especially in some tissues including gray matter, white matter, cerebellum, pons, mesencephalon, fat and muscle. The iD5IR images have higher angular second moment (ASM), correlation, inverse difference moment (IDM) than FBP, which suggests iD5IR images were more homogenous and less noisy. We found that contrast, entropy and standard deviation (SD) of FBP images were higher than iD5IR since the FBP images were less homogenous and more random. Characteristic signatures for each tissue type and anatomic region were derived, based on the observed differences.

Conclusion

Texture analysis revealed significant differences in texture parameters of head CT images between FBP and iD5IR reconstruction. These quantitative differences can be a useful and quantitative tool to assess the image quality of FBP and iterative (e.g., iDose) image reconstruction.

References

[1] Singh S, Kalra MK, Gilman MD, et al. (2011) Adaptive statistical iterative reconstruction technique for radiation dose reduction in chest CT: A pilot study. Radiology, 259(2):565–573.

[2] Bharati MH, Liu JJ, MacGregor JF (2004) Image Texture Analysis: methods and comparisons. Chemometrics and Intelligent Laboratory Systems, 72:57–71.

[3] Srinivasan GN, Shobha G (2008) Statistical texture analysis. Proceeding of World Academy of Science, Engineering and Technology, 36:2070–3740.

[4] Castellano G, Bonilha L, Li LM, et al. (2004) Texture analysis of medical images. Clinical Radiology, 59:1061–1069.

Mass detection and classification algorithm on three-dimensional breast ultrasound images using the hough transform

J.-W. Jeong[1], D. Yu[2], S. Lee[1]

[1]ETRI, Bio-Medical IT Convergence Research Department, Daejeon, Korea

[2]INFINITT Healthcare Co., Image Processing Team, Seoul, Korea

Keywords Computer assisted diagnosis · Breast cancer · 3D ultrasound image · Hough transform

Purpose

Recently various researches have been reported regarding the development of the three-dimensional (3D) US scanning devices to overcome these shortcomings [1–2].

With 3D US scanners the whole breast image volumes can be acquired easily and repeatedly in a relatively short time interval practically without non-scanning breast regions. However, it should be noted that huge amount of US image volumes at each screening make radiologists to be exhausted with the diagnosis on even one case of 3D US image volume. To save the diagnostic effort using 3D US scanning devices, a computer-aided detection (CAD) system can suggest the mass candidates to enhance the radiologists' screening speed and accuracy as a preliminary diagnostic step.

In this paper we propose automatic mass detection and classification algorithm using the Hough transform and fast marching level set segmentation [3] techniques.

Methods

3D US volumetric images were acquired by Seoul National University Hospital, Seoul, Korea and diagnosed by an

experienced radiologist. Finally 68 benign and 60 malignant masses from 125 patients were confirmed with the histopathological examination.

The overall lesion detection algorithm includes masking, subsampling, contrast adjustment, median filtering, and the Hough transform. The Hough transform is usually used for the detection of curves by exploiting the duality between points on a curve and its parameters. In our study, five spheres were detected and chosen through Hough transform for each 3D US image volume.

For a detected lesion candidate, a volume of interest (VOI) in the shape of rectangular parallelepiped is manually adjusted by a radiologist and a radius-dependent contrast adjustment (RDCA) method is applied, which is a modified version of a general contrast adjustment method using a constraint Gaussian function [4] to attenuate distant pixels giving graylevel values similar to the tumor region and avoid its dependence upon the manual selection of the lesion's center.

The morphological closing operator with a cubic Structuring Element (SE) of $3 \times 3 \times 3$ pixels is applied on the resulting VOI to reduce speckle, increase contrast among distinct regions, and remove connected components of volume less than the pre-specified scale. The fast marching method [3] is used to propagate the surface locally within a rectangular-parallelepiped window with the center of the lesion.

For the segmented lesion, three morphological parameters such as depth to width ratio (DWR), modified compactness (MC) parameter, and border sharpness (BS) parameter are calculated and combined linearly with the pre-determined coefficients by the multi-linear regression analysis to improve their correlations with the clinical findings. The DWR represents the stiffness of a breast mass lesion under pressure and is widely used for the breast cancer classification for its strong dependence upon the lesion's malignancy even though its simplicity. The MC as a simple shape factor parameter is derived in order to compare how the lesion's shape is topologically circumscribed from the clinical fact that the malignant cancerous breast lesions show the speculated and irregular shape. The BS is introduced to consider the clinical findings that the margins of the benign lesions are sharply defined whereas the malignant tumors have fuzzy and blurred boundaries. For every voxel on the segmented 2-dimensional surface, its grayscale density variations in the perpendicular direction are interpolated and the partial sum of the Fourier components is obtained and analyzed.

The obtained sensitivity and specificity for discriminating malignant masses from benign masses on 3D US image volumes are compared with the previous researches. Classifier performance using the obtained parameters for the acquired data is assessed by using the area under the receiver operating characteristic (ROC) curve (Az), implying a summary measure of its ability for correct classification.

Results

Using the proposed mass detection algorithm, 62 benign and 58 malignant mass lesions were successfully detected among 68 benign and 60 malignant masses giving the detection sensitivity of 93.8 % at 0.98 false positives per volume compared to other researches [1–2]. Especially it is noted that the sensitivity of the malignant mass detection is quite enhanced to be 96.7 % at 0.60 false positives per volume. It may imply that the ultrasound volume scanner such as the automated breast ultrasound system using the proposed detection algorithm can be used for the sufficiently accurate and economically efficient annual breast cancer screening with the enhanced sensitivity for the malignant breast masses.

Using the relatively simple fast marching level set method, 60 benign and 46 malignant mass lesions among the clinically confirmed 68 benign and 60 malignant masses were successfully segmented. The segmentation failure is mainly due to the poor quality of the scanned ultrasound image volumes. Three morphological parameters were calculated and compared with the clinical decisions and the sensitivity of 91.3 % at the specificity of 73.3 % is obtained using three morphological parameters. Resulting Az values of 0.903 are found to be quite comparable to the previous researches.

It is well known that the sonographic images suffer subjective interpretation even for the experienced radiologist, the inconsistent image quality and user-dependent reproducibility. It may be noted that the influence of the resizing of the large lesion volume is trivial according to the calculational results of the accuracy parameters.

Conclusion

The proposed automatic mass detection and classification algorithm using the Hough transform and fast marching level set segmentation methods gives the mass detection sensitivity of 93.8 % at 0.98 false positives per volume quite comparable to the previous results. Automatically segmented lesion volumes were analyzed using three morphological parameters and the obtained mass classification sensitivity is 91.3 % at the specificity of 73.3 %, and the resulting Az is 0.903. Further modifications on the segmentation method are in progress.

This work was supported by the Converging Research Center Program through the Ministry of Education, Science and Technology, Republic of Korea. (2012K001520)

References

[1] Ikedo Y, Fukuoka D, Hara T, Fujita H, Takada E, Endo T, and Morita T (2007) Development of a fully automatic scheme for detection of masses in whole breast ultrasound images. Med. Phys. 34 (11):4378–4388

[2] Ikedo Y, Fukuoka D, Hara T, Fujita H, Takada E, Endo T, and Morita T (2007) Computerized mass detection in whole breast ultrasound images : Reduction of false positives using bilateral subtraction technique. Proc. Of SPIE Medical Imaging, 6514

[3] Sethian JA (1996) A fast marching level set method for monotonically advancing fronts. Proc. Natl. Acad. Sci. USA 93:1591–1595

[4] Horsch K, Giger ML, Venta LA, et al. (2001) Automatic segmentation of breast lesions on ultrasound. Med. Phys. 1652–1659

Automated aorta segmentation in low-dose CT images

Y. Xie[1], J. Padgett[1], A. M. Biancardi[1], A.P. Reeves[1]
[1]Cornell University, School of Electrical and Computer Engineering, Ithaca, New York, USA

Keywords Aorta segmentation · Computer based automated segmentation · Low-dose non-contrast CT images · Anatomy based segmentation

Purpose

To automatically accurately segment the outer surface of the aorta in low-dose chest CT images. Analysis of this segmentation may be useful in detecting aortic aneurysm and other cardiovascular abnormalities.

Methods

Vessel segmentation is particularly challenging in low-dose CT images due to the large amount of image noise. A three-stage vessel

tracking approach was developed which operates on an anatomy label map (ALM) that has been pre-computed for each image. The ALM is a pixel-based partially labelled image with the same geometry and resolution as the original CT image from which it was computed [1]. The ALM is created by a process of successive organ segmentations, commencing with the most robust CT image features. The airway lumens, lung regions, bone structures, and significant regions of fat have been identified in the ALM.

The algorithm is comprised of 3 stages: automated seed point detection inside aortic lumen, aortic centerline tracking, and aortic surface detection. Through empirical study, the axial slice at the level of carina contains a well-defined aorta that is always bounded by the left lung and vertebra. Therefore, the first stage automatically locates a seed point to initialize segmentation by searching for the largest circle that fits into the unlabeled region adjacent to left lung and vertebra in the ALM. The center of this circle is the initial seed point.

The second stage is cylinder tracking. The aorta has a cylindrical structure that can be modeled as a series of discrete cylinders. Given an initial seed point and a direction, cylindrical sections are iteratively fit to the 3D space defined by unlabeled pixels in the ALM until a specified termination condition is met. In each iteration, a series of candidate cylinders with different radii and orientations are generated and the cylinder with the largest number of unlabeled voxels is chosen as the best-fit cylinder. The outcome of the tracking algorithm is a set of center points of all the best-fit cylinders, which approximates the actual aortic centerline.

The third stage refines the aortic surface based on the centerline from the second stage. A triangular mesh model is used to sample the intensity values around the aortic region in the CT scan [2]. The model contains multiple layers that are perpendicular to the centerline. A set of rays is cast from the center of the aorta towards the surface for each layer. The intensity values of the CT image are sampled along these rays. Surface points are found by terminating rays once they reach a value below −30 HU.

This algorithm has been trained and evaluated on CT images from the I-ELCAP [3] and LIDC [4] databases. Altogether 262 non-contrast, thin slice images were used: 20 for training and 242 for testing. All images have a slice thickness of 1.25 mm or less. The testing set contains 25 low-dose images from I-ELCAP database and 89 low-dose images and 128 regular dose images from LIDC database. A set of optimal parameters was obtained from training.

Results

The outcomes were qualitatively and quantitatively evaluated for each testing case. The qualitative evaluation was conducted by superimposing the segmented aorta with other segmented organs in the ALM and observing location relative to other organs, as shown in Fig. 1. The qualitative evaluation resulted in 217 test images with accurate segmentations and 25 images with inaccurate boundaries where aorta is adjacent to other vessels. Among the 25 cases with inaccurate boundaries, 14 were low-dose and the remaining were regular dose scans. The aorta on ten randomly selected low-dose testing images was manually segmented with 10–12 slices marked per image for quantitative evaluation. The Dice Similarity Coefficient and the boundary distance between manual and automated segmentations were compared and are shown in Table 1. The average DSC was 0.940 over all slices and 0.935 and 0.944 for ascending and descending aorta slices respectively. The average boundary distance μ_D was 1.43 mm over all slices, and 1.62 and 1.30 mm for ascending and descending slices respectively. A bias term B_{pn} was also computed, and showed that the algorithm is not biased towards over segmentation or under segmentation.

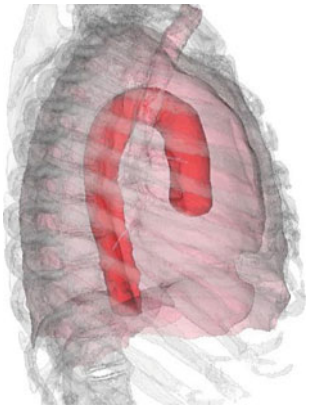

Fig. 1 3D visualization of a correctly segmented aorta

Table 1 DSC, bias B_{pn} and mean boundary distance μ_D for entire aorta, ascending and descending aorta mean boundary distance μ_D for each case

Case ID	DSC	DSC(A)	DSC (D)	B_{pn}	μ_D	μ_D(A)	μ_D(D)
1	0.935	0.929	0.941	−0.020	1.37	1.51	1.29
2	0.937	0.944	0.934	+0.066	1.23	1.26	1.21
3	0.941	0.922	0.958	−0.028	1.58	1.92	1.34
4	0.942	0.931	0.952	−0.068	1.60	1.92	1.39
5	0.941	0.944	0.939	−0.001	1.36	1.44	1.31
6	0.938	0.941	0.935	+0.013	1.39	1.56	1.26
7	0.935	0.940	0.932	−0.007	1.46	1.61	1.39
8	0.929	0.903	0.943	+0.029	1.37	1.70	1.22
9	0.952	0.950	0.954	−0.023	1.48	1.60	1.37
10	0.950	0.944	0.955	−0.033	1.43	1.71	1.25
Average	0.940	0.935	0.944	−0.007	1.43	1.62	1.30

Conclusion

A fully automated aorta segmentation algorithm has been developed for low-dose non-contrast chest CT scans and evaluated on 242 full chest scans. Visually more than 85 % of the testing cases were correctly segmented. The algorithm achieves an average DSC of 0.940 compared to manual markings and an average boundary distance of 1.43 mm. Both qualitative and quantitative evaluations show that the algorithm is able to robustly and accurately segment the aorta in low-dose non-contrast CT scans.

References

[1] A. P. Reeves, A. M. Biancardi, D. F. Yankelevitz, M. D. Cham and C. I. Henschke, "Heart Region Segmentation From Low-dose CT Scans: an Anatomy Based Approach," SPIE, 2012.

[2] J. Lee, A. P. Reeves, S. Fotin, T. Apanasovich and D. Yankelevitz, "Human Airway Measurement From CT Images," SPIE, pp. 691518, 2008.

[3] "ELCAP Public Lung Image Database", http://www.via.cornell.edu/databases/lungdb.html.

[4] S. G. Armato, III, G. McLennan, L. Bidaut, M. F. McNitt-Gray, C. R. Meyer, A. P. Reeves, B. Zhao, D. R. Aberle, C. I. Henschke, E. A. Hoffman, E. A. Kazerooni, H. MacMahon, E. J. R. van Beek, D. Yankelevitz, et al., "The Lung Image Database Consortium (LIDC) and Image Database Resource Initiative (IDRI): A Completed Reference Database of Lung Nodules on CT Scans," Medical Physics, vol. 38, pp. 915–931, 2011.

A GPU-based framework for 4D-CT lung registration

A. Santhanam[1], Y. Min, J. Neylon[1], H. Dou[1], A. Shah[2], S. Meeks[2], Patrick Kupelian[1,2]
[1]Department of Radiation Oncology, University of California, Los Angeles, USA
[2]Department of Radiation Oncology, M.D. Anderson Cancer Center Orlando, Orlando, USA

Keywords Radiotherapy · Image registration · GPU · Optical flow

Purpose

4D Computed Tomography (4D-CT) lung images enables calculating the breathing motion range for the lungs [1, 2]. A key step in enabling this calculation is the 4D-CT lung image registration process that compute the volumetric displacement of both the lung tumor as well as its surrounding tissues. Registration errors arise because of a need to account for image artifacts such as (a) Hounsfield Unit (HU) inconsistencies for an anatomic feature from lung breathing phase to another, and (b) low image contrast for anatomic structures such as parenchyma. Robust image-based registration would require investigating the registration parameters' domain and range that accounts for afore-mentioned limitations in the image data. Such a study is currently limited by the high computation time required for 4D registration.

Methods

We present a GPU based real-time 4D-CT registration framework that significantly reduces computation time and accounts for the afore-mentioned image artifacts as a step towards investigating the parameter domain and range. The registration framework uses a combination of optical flow and Thin Plate Splines (TPS) for registering 4D-CT lung datasets. The GPU based optical flow consists of three key components. First are the spatial and temporal derivatives of the image datasets. A separable 3D convolution filter is used for calculating the spatial derivatives [3]. The 3D image data, located in the GPU memory were copied into the GPU's shared memory for this purpose. For a faster computation time, the row and column 3D convolution was performed first, followed by a GPU based 3D matrix transpose that makes the data contiguous for the plane 1D convolution. It is then followed by the plane convolution and matrix transpose in order to get the data in the original arrangement. For computing the temporal derivatives, a 1D convolution among the different datasets were employed.

The second step of the GPU optical flow calculation is solving for the optical flow formulation. In our approach, we employed a Jacobi iterative solver to solve for the displacement vectors. This step is an iterative approach to solve for the displacement vectors. The final step of the GPU optical flow calculation warps the source 3D dataset using the 3D displacement vectors computed in the second step. For warping purposes, we employed a GPU based tri-linear interpolation approach.

A GPU implementation of the TPS interpolation was obtained in the following steps. As a first step, we represent the displacement in the polar coordinates. Equation (6) can be re-written as.

$$u(x(i)) = \sum_{\theta=0}^{\pi} \sum_{\theta=0}^{2\pi} \|x(i) - X(\theta, \vartheta)\| u(X(\theta, \vartheta)) \quad (1)$$

For each voxel in a given anatomy level, we compute the term $\|x(i) - X(\theta, \vartheta)\|$ by projecting a ray to compute the effective distance along every azimuthal and elevation angles. We parallelized this step using a GPU in the following steps. First, we transferred the 3D anatomy to a 3D texture memory. For every voxel in the current anatomy, we projected rays on specific directions that intersected with the previous anatomy boundary. For this purpose, we used a tri-linear texture based sampling. Using the distances, we computed the displacement of the current anatomy, which was then used as an initial displacement value for the multi-resolution 3D optical flow process.

The steps in the registration are as follows: The registration starts at the lowest resolution of a 3D volume. Within each resolution level, the volumes were registered using a multi-anatomical level GPU based 3D optical flow approach. Motion field was first computed based on the pair of surface contours in the lowest resolution. Such motion field was carried as initial motion field to motion computation of the second anatomical level volumes, which now included surface contour and large blood vessels. The motion field was then iteratively updated until the top level of anatomy volumes are registered, Then the lung volumes and anatomy maps were rescaled into a higher resolution and the multi-level optical flow registration was performed at this resolution. The process continues until the 3D volumes at the highest resolution are registered.

Results

Figure 1a, c represents as overlapping 2D slices of left lung and right lung at end-exhalation (red) and end-inhalation (green) stages. The misalignments between each of the slices are depicted in red and green colors. While the red region represents the features that are in the end-exhalation and not in end-inhalation, the green region represents the features that are in the end-inhalation and not in the end-exhalation. Overlapping the warped image with the target image where the red and green colors are not seen represents a correct image registration. Figure 1b, d represents the overlapping 2D slices of the left and right lung with the end-inhalation lung volume warped using the registration results. It can be visually seen that the registration error is minimal for each of the case. The CUDA implementation of the proposed algorithm took approximately 152 and 94 s on the Nvidia C2050 and GTX 680, respectively. Such a run-time analysis demonstrated the ability to register 4D lung data registrations in real-time.

Conclusion

In this paper, we presented a GPU based 4D-CT lung registration framework. The displacement distribution obtained using the GPU

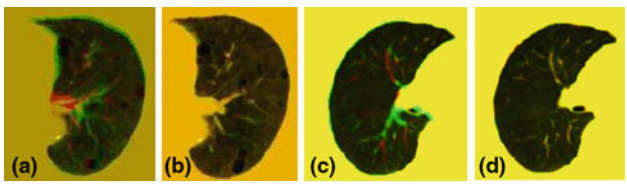

Fig. 1 The 2D lung slices of two right lung volumes at end expiration (*red*) and end inspiration (*green*) are shown **a** before and **b** after the registration. The 2D lung slices of two left lung volumes at end expiration (*red*) and end inspiration (*green*) are shown **c** before and **d** after the registration. The misalignments for each of the case are depicted in *red* and *green colors*

based registration shows the 3D heterogeneity in the lung motion during the breathing process. Future work will focus on developing a multi-local minima based approach for effectively computing the registration parameters. Such a process would precisely register 4D lung data when the image properties such as HU inconsistencies, low contrast and noise exist.

References

[1] Britton K, Dong L, Mohan R (2007) Image Guidance to Account for Interfractional and Intrafractioin Variations: From a Clinical and Physics Perspective. In J. Cox, J. Chang, and R. Komaki (ed) Image-Guided Radiotherapy of Lung Cancer. Informa Healthcare USA, Inc., New York, NY

[2] Klinder T et al. (2008) 4DCT image-based motion field extraction and analysis. SPIE Medical Imaging 2008:6914

[3] Harris M (2008) Separable convolution with CUDA. Accessed 10 January 2013

Statistical model-based femur segmentation in digital anteroposterior (AP) pelvic radiographs

W. Xie[1,2,3], J. Franke[3], C. Chen[1], P. A. Grützner[3], L.-P. Nolte[1], G. Zheng[1]

[1]University of Bern, Institute for Surgical Technology and Biomechanics, Bern, Switzerland

[2]University of Bern, Graduate School for Cellular and Biomedical Sciences, Bern, Switzerland

[3]BG Trauma Centre Ludwigshafen at Heidelberg University Hospital, Ludwigshafen, Germany

Keywords Statistical shape model · Statistical appearance model · Radiograph segmentation · Dynamic programming

Purpose

Digital plain radiography is widely used for diagnosis, medical treatment and surgical planning. Segmentation of the proximal femur in digital anteroposterior (AP) pelvic radiographs is the first step to quantitatively analyze the osteoarthritis severity of the hip, plan the joint replacement surgery, and estimate osteoporosis in bone density measurement. However, extracting the femur contour manually is a tedious job prone to subjective bias, whereas automatic segmentation needs to deal with many challenges such as poor image quality, anatomical structure overlap, femur deformity, and so on. In this paper, we present a robust, fast and accurate method to address problems of femur segmentation in AP pelvic radiographs, which is based on the combination of statistical shape model (SSM), statistical appearance model (SAM), and the dynamic programming technique.

Methods

By means of manual annotations on 67 AP-pelvic radiographs, SSM and SAM of the femur contour are firstly constructed. The generated SSM and SAM are subsequently used to segment a new AP pelvic radiograph with a three-stage approach. At the initialization stage, the mean model of SSM is coarsely registered to the femur in AP radiograph through a scaled rigid registration [1]. At the subsequent stage, Mahalanobis distance [2–3] defined on the SAM is employed as the criteria to search the suggested location for each annotated landmark. For the landmark annotated at the region of femur head, there are many candidate points with quite similar Mahalanobis distances that can be selected as its suggested location, due to the complicate anatomical structures around this region. Thus the dynamic programming technique has to be exploited to eliminate ambiguities and help make a decision. After all landmarks are assigned their suggested locations, algorithm enters the third stage. At this stage, by considering the suggested location as the proposition of next position for each annotated landmark, a regularized non-rigid registration method [4–5] deforms the current mean shape of SSMs so that the new segmentation of proximal femur is produced. The second and third stages are iteratively executed until the algorithm converges.

Results

Experiments were conducted on 100 clinical AP pelvic radiographs (note: none of them is part of the 67 training images) with a wide range of image qualities. The mean segmentation error of each tested radiograph was measured in terms of point-to-curve distances (points: deformed mean model points of SSM as the segmentation result; curve: the manually segmented contour of the femur as the ground truth). The experimental results showed an averaged mean error of 0.96 mm for all 100 tested radiographs and a running time of less than 5 *s* when our method was implemented in an un-optimized Matlab environment.

Conclusion

We proposed a fast, robust and accurate method for femur segmentation in digital AP pelvic radiographs, combining SSM and SAM with the dynamic programming. Experiments carried out have proven the efficiency, robustness and accuracy of the proposed method. This method is general enough to be extended to segmentation of other bony structures.

References

[1] Xie W, Schumann S, Franke J, Grützner PA, Nolte L-P, Zheng G (2012) Finding Deformable Shapes by Correspondence-Free Instantiation and Registration of Statistical Shape Models. In: Wang F. et al. (ed) MICCAI Workshop on MLMI 2012, LNCS 7588. Springer, Heidelberg, pp 258–265

[2] Cootes TF, Hill A, Taylor CJ, Haslam J (1994) The Use of Active Shape Models for Locating Structures in Medical Images. Image and Vision Computing 12(6):355–366

[3] Cootes TF (2000) An Introduction to Active Shape Models. In: Baldock R. and Graham J. (ed) Image Processing and Analysis. Oxford University Press, pp 223–248

[4] Zheng G, Gollmer S, Schumann S, Dong X, Feilkas T, Ballester MAG (2009) A 2D/3D Correspondence Building Method for Reconstruction of A Patient-specific 3D Bone Surface Model Using Point Distribution Models and Calibrated X-ray Images. Med Image Anal 13(6):883–899

[5] Zheng G (2010) Statistical Shape Model-based Reconstruction of a Scaled, Patient Specific Surface Model of the Pelvis from a Single Standard AP X-ray Radiograph. Med Phys 37(4): 1424–1439

Accelerating medical algorithms on heterogeneous systems

S. Melnik[1], M. Kaeseberg[1], E. Keeve[1,2]

[1]Fraunhofer Institute for Production Systems and Design Technology IPK, Systems for Medicine, Berlin, Germany, Germany

[2]Charité, Universitätsmedizin Berlin, Maxillofacial Surgery and Clinical Navigation, Berlin, Germany, Germany

Keywords Volume reconstruction · OpenCL · FDK · Heterogenous systems · GPGPU

Purpose

Algorithms for medical applications like CT reconstruction, 2D/3D matching algorithms or image processing in general suffer from long computation times. Especially for intraoperative used algorithms time is a critical factor. The steadily increasing performance of Graphics Processing Units (GPU) and the advancing development of graphics programming tools enable the transfer of computationally demanding computations from CPU to GPU.

GPGPU (General Purpose Computation on Graphics Processing Unit) programming languages enable the programmer to perform computations on GPU, which are traditionally performed by CPU, without the need of any knowledge in graphics card programming.

Generally these languages are vendor-, platform- or hardware-dependent.

With the Open Computing Language (OpenCL) the first free standard for parallel programming of heterogeneous systems emerged. OpenCL enables to perform identical code on different compute units like GPUs, CPUs or DSPs. This allows the acceleration of computationally demanding programming tasks, independent from the used hardware configuration.

In this paper we investigate the capability of OpenCL to accelerate algorithms for medical applications on various computer systems. For this purpose we exemplarily compare the execution times of a 3D reconstruction algorithm for cone-beam computed tomography (CBCT) on different computer systems.

Methods

To compare the portability between different heterogeneous systems the common FDK reconstruction algorithm by Feldkamp, Davis and Kress was implemented. The FDK algorithm is a generalization of the filtered backprojection for cone beam computed tomography with flat panel detectors.

The FDK algorithm can be decomposed into two independent steps: first the pre-weighting and filtering of projection data and second the weighted backprojection. The pre-weighting and the filtering are performed on CPU, whereas the most time consuming backprojection step is done by OpenCL, e.g., on GPU (Fig. 1).

The pre-weighting of projection data corrects the different ray integrals resulting from cone beam geometry. The subsequent row-wise ramp like filtering of the projection data enhances the reconstruction quality by suppressing blur and emphasizing details.

During the backprojection step on the GPU the information in every projection image is used to update the volume data. The implemented OpenCL code for backprojection works as follows: at first the exact position of the voxel center is computed. Afterwards a view ray from the X-ray source position through the voxel is used to calculate the intersection point of the ray with the image plane. The intersection point is then transformed into the image coordinate system to obtain the according image index. To reduce the number of operations performed per voxel, the calculation of the intersection point is done with a precalculated projection matrix. If the intersection is outside the image data the voxel value is masked out. Otherwise the four surrounding pixel values are bilinear interpolated, weighted and added to the current voxel value (Fig. 1).

The implemented OpenCL kernel features some computational problems relevant in many medical algorithms, e.g., various data reads and writes, bilinear filtering of image data, line of sight calculation and matrix/vector operations.

During the backprojection of an image for every voxel an instance of the OpenCL program (kernel) is created. That way a vast of voxels can be processed in parallel. Since the same OpenCL code can be performed by different compute units, no device specific optimization like vectorization is done.

For the backprojection the volume data and the projection images are stored in graphics memory. Since the graphics memory is limited, large volumes are reconstructed in multiple parts. Thus it is possible to reconstruct volumes that are larger than the available memory. After the reconstruction of a volume or a volume part is done, the data is copied back to CPU. The partitioning of the overall volume into multiple parts enables to use multiple OpenCL devices, where every device is responsible for the reconstruction of one or more volume parts.

To benefit from hardware accelerated interpolation on GPU the images are stored in the texture memory. For FDK reconstruction a large number of images are used, which often cannot be completely stored in graphics memory next to the volume. Therefore the needed images are copied to GPU on demand. For that purpose only a few images are stored in memory at a time. The calculations are performed without any simplified assumptions about the image acquisition trajectory (e.g., circular path).

Results

For evaluation the FDK algorithm was performed on different computer systems. For performance comparison only the runtime of the backprojection with OpenCL was measured. As test case a 1,024 × 1,024 × 1,024 voxel volume with 270 1,024 × 1,024 pixel projection images was reconstructed on each system. Since every voxel is stored as a float32 value, the overall volume needs a memory capacity of 4 gigabyte. The performance of the tested OpenCL devices, denoted as GUPS (Giga Updates per Second), is shown in Fig. 2. As it can be seen the computations on GPUs outperforms the computations on CPUs. Even the dual CPU system needs more than 5 times longer than the slowest graphics card in the test. The fastest computation times were archived with multi GPU systems. In our experiment the reconstruction time nearly scales with the number of used graphics cards.

Conclusion

In this paper we investigated the capability of OpenCL to accelerate medical algorithms. For that purpose we performed the FDK reconstruction on various computer systems. The evaluation has shown that OpenCL is well suited for the hardware acceleration of computationally demanding programming tasks on heterogeneous systems. Despite the early development state of OpenCL, for all tested

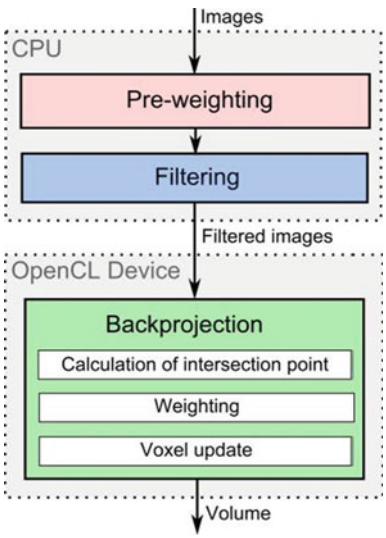

Fig. 1 Activity diagram of the implemented FDK algorithm

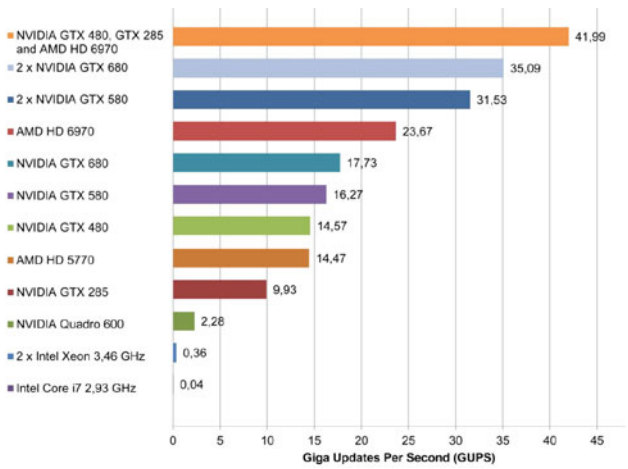

Fig. 2 Performance of the backprojection on different compute units

hardware components an OpenCL implementation was available. The same kernel could be performed on every device without any modifications. Furthermore OpenCL was able to manage different devices in parallel, e.g., for computations distributed among multiple GPUs. However, the quality and performance of implementations of the different platforms are varying. Further enhancement of OpenCL implementations probably leads to further improvements in speed.

An active shape model for porcine whole heart segmentation from multi-slice computed tomography

B. Stender[1], O. Blanck[2], B. Wang[3], A. Schlaefer[1]
[1]Medical Robotics, Institute for Robotics and Cognitive Systems, University of Luebeck, Luebeck, Germany
[2]Department of Radiotherapy, University Hospital Schleswig–Holstein, Campus Luebeck, Germany
[3]Institute of Biomedical Analytical Technology and Instrumentation, Xi'an Jiao Tong University, Xi'an, China

Keywords Anatomical modeling · Motion model · Multi-slice computed tomography · Statistical shape model · Active shape model

Purpose
Inverse Electrocardiography presents an approach to study the propagation of the cardiac depolarization front within the myocardial tissue [1]. This measuring technique could be used for non-invasive diagnosis, but further clinical research including animal models will be required. For solving the inverse problem a priori knowledge about the geometry of the whole heart is needed. Such an individualized model could automatically be extracted from computed tomography scans applying a whole heart segmentation algorithm. A set of methods which has already been successfully applied to medical image segmentation are Active Shape Models and Active Appearance Models [2]. Only a few papers have been published so far on their use for whole heart segmentation in CT imaging data [3, 4].
Methods
Due to its complex anatomy the whole heart was just once segmented manually in an end-diastolic frame of a time series. Using the Marching Cubes algorithm we generated a complex closed surface mesh, which we simplified in a second step to 10,000 faces. The final surface mesh is illustrated in Fig. 1. It was tested for successful tetrahedral volume mesh generation using Gmsh. Individualization and propagation in time was both achieved combining an affine registration (12 degrees of freedom) with a subsequent 3D non-rigid registration algorithm, as illustrated in Fig. 2. Cartesian B-Spline registration algorithms were found to be inadequate to deal with discontinuities of the deformation field as well as to recover the inherently rotational and radial motion. A modified version of Thirion's demons algorithm was used instead [5]. The algorithm uses a modified version of the optical flow equation. Regularization is achieved by Gaussian filtering.

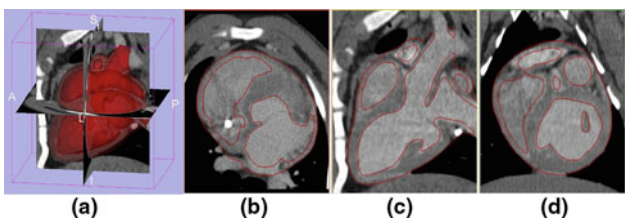

Fig. 1 **a** Simplified triangulated surface model based on manually performed segmentation. The *red* contour of the surface model is displayed along with slices of the underlying porcine contrast enhanced CT data set. **b–d** Intersection of the surface model with the axial, sagittal and coronal plane

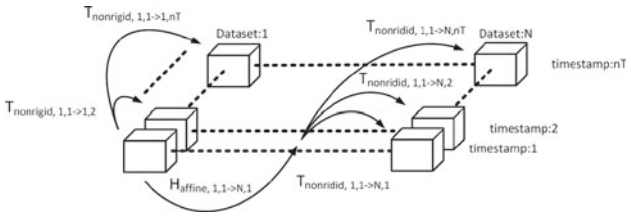

Fig. 2 Registration scheme for determination of the vertex displacement. $H_{affine,\ 1,1\ ->\ N,1}$ denotes the affine transformation from frame 1 in dataset 1 to frame 1 in dataset N. $T_{nonrigid,\ 1,1\ ->\ j,1}$ is the corresponding 3D displacement field resulting from nonrigid registration

Volumetric CT scans of 14 healthy pigs (4 domestic, 10 minipigs) formed the database including five time series (4 domestic, 1 minipig). The statistical shape model of the whole heart was built up as a point distribution model of the N vertexes included in the surface mesh. We considered changes in size between different individuals as well as shape changes due to contraction within the model. Instead of using a generalized Procrustes analysis we aligned the shapes with principal component analysis based on the end-diastolic volumes. The remaining shape variability was modeled linearly.
Results
For the five 4D datasets deformation field time-series were extracted. The patterns of the resulting mean vertex motion showed a first peak from the initial contraction and a smaller second peak presumably caused by opposing rotational motion of the ventricles during diastole. The segmentation results were evaluated by means of leave-one-out cross-validation against the results from application of the registration scheme. Despite the low number of animals included in the training data set an average vertex distance below 5 mm could be achieved on 30 volumes of domestic pigs.
Conclusion
In this paper we build a 3D statistical shape model of a closed cardiac surface consisting of the myocardial wall of all four heart chambers and the wall of the main vessels. The approach is fully-automatic, additional training data could easily be added. Future work will include an analysis on the spatial distribution of the motion amplitudes.
References
[1] Huiskamp, G.J., Greensite, F.: A new method for myocardial activation imaging IEEE Trans. Biomed. Eng., 44, 433–46 (1997)
[2] Heimann, T., Meinzer H.-P.: Statistical shape models for 3D medical image segmentation: A review. Med. Image Anal. 13(4), 543–63 (2009)
[3] Ecabert, O., Peters, J., Schramm, H., Lorenz, C., von Berg, J., Walker, M. J., Vembar, M., Olszewski, M.E., Subjamanyan, K., Lavi, G., Weese, J.: Automatic model-based segmentation of the heart in ct images. IEEE Trans. Med. Imag. 27(9), 1189–201 (2008)
[4] Zheng, Y., Barbu, A., Georgescu, B., Scheuering, M., Comaniciu, D.: Four-chamber heart modeling and automatic segmentation for 3-D cardiac CT volumes using marginal space learning and steerable features. IEEE Trans. Med. Imag. 27(11), 1668–81 (2008)
[5] Prima, S., Thirion, J.-P., Subsol, G., Roberts, N.: Automatic analysis of normal brain. Dissymmetry of males and females in MR images. MICCAI'98, 770 (1998)

Bilateral filter regularized accelerated demons for better discontinuities registration

D. Demirović[1], A. Šerifović-Trbalić[1], Ph. Cattin[2]
[1]Faculty of Electrical Engineering, University of Tuzla, Tuzla, Bosnia and Herzegovina

[2]Medical Image Analysis Center (MIAC), University of Basel, Basel, Switzerland

Keywords Medical image registration · Discontinuities · Demons method · Bilateral filter

Purpose
Non-rigid image registration methods play an important role in today's modern medical diagnostics and Image-Guided Therapy (IGT) systems and as a consequence a lot of research is devoted to it. Medical image registration seeks the geometrical transformation which maps the floating image into the spatial domain of the reference image. In the last decade techniques to measure 4D (3D + time) breathing organ motion, such as 4D-MRI [1, 2], have been introduced raising the need for techniques able to deal with the discontinuities that occur in these data set where the organs are sliding along the chest wall. Today's methods in contrast enforce a smooth deformation field in their regularization term.

Methods
In this paper we present a new approach to smooth the displacement field in the accelerated Demons registration algorithm preserving discontinuities. The accelerated Demons algorithm [3] uses Gaussian smoothing to penalize oscillatory motion in the displacement fields during registration. A Gaussian regularizer, however, can not differentiate between discontinuities and smooth part of the motion field. Our proposed algorithm uses in place of the Gaussian smoothing a bilateral smoothing technique [4] to better preserve the discontinuities.

Results
The proposed approach was tested with 2D and 3D images, and we get improvements in error metric i.e., Target Registration Error (TRE) for the well known POPI image dataset [5]. Multiple experiments were carried out in order to evaluate the proposed method, and optimal parameters taken for bilateral filter smoothing. All experiments were carried out on an Intel Core i5 2500 processor with 8 GB main memory. For the Gaussian filtered Demons method we use Insight Toolkit (ITK) implementation with unchanged internal parameters, and four resolution levels with 50 iterations for each level and $\sigma = 2.0$. For the bilateral filtered Demons we also use four resolution levels with 50 iterations each, values for $\sigma_s = 4.0$ and $\sigma_I = 50.0$. Both algorithms use a multithreaded approach with maximal four threads. The 50 iterations were enough on each level to get good convergence. The registration reduces distance to 1.13 ± 0.55 for Demons and 1.04 ± 0.54 mm for bilateral filtered Demons (Table 1).

To verify that the improvement is significant we statistically analyzed the data. All these statistical tests were performed using the software package R (release 2.14.1 for Linux, www.r-project.org). The normal distributed mean values were compared with a paired *t* test. Normality of the distributions was tested with the Kolmogorof-Smirnov test. A p value <0.05 was considered statistically significant for all tests. The statistical analysis showed that both registration approaches perform significantly better ($p < 0.05$) than not registering the images at all. Taking the accelerated Demons algorithm with Gaussian filtering as the standard, it can be shown that bilateral filtering significantly improved ($p < 0.05$) when registering with the proposed Bilateral-Demons. Running times for registering one pair of volumes were for Demons 4 min, and for Bilateral-Demons 15 min. The higher computational costs of the proposed method can be attributed to the increased complexity of the bilateral filter and the less efficient concurrent implementation of the latter.

Table 1 TRE for accelerated Demons and Bilateral-Demons for the 3D POPI data set, mean values ± standard deviation and max values are given. All measures are given in millimeters

Dataset	Before	Demons		Bilateral-Demons	
	$\mu \pm stdev$	$\mu \pm stdev$	Max	$\mu \pm stdev$	Max
00P	0.5 ± 0.5	0.79 ± 0.32	1.87	0.72 ± 0.33	1.55
20P	0.5 ± 0.6	0.76 ± 0.47	1.79	0.73 ± 0.48	1.93
30P	2.2 ± 1.8	1.41 ± 0.82	3.46	1.15 ± 0.59	2.41
40P	4.3 ± 2.5	1.23 ± 0.49	2.42	1.02 ± 0.54	3.01
50P	5.8 ± 2.6	1.19 ± 0.58	3.21	1.10 ± 0.62	2.76
60P	6.1 ± 2.9	1.07 ± 0.53	2.53	1.06 ± 0.53	2.40
70P	5.0 ± 2.3	1.89 ± 0.91	4.14	1.85 ± 0.99	3.89
80P	3.7 ± 1.6	0.90 ± 0.41	1.75	0.86 ± 0.40	1.82
90P	2.1 ± 1.1	0.90 ± 0.44	2.00	0.86 ± 0.41	2.01
Mean	3.3 ± 2.0	1.13 ± 0.55	2.58	0.96 ± 0.54	2.42

Conclusion
In this paper we propose to replace the regularization part from accelerated Demons using a bilateral filter to support anisotropic smoothness instead of isotropic as in accelerated demons algorithm [3]. Bilateral filtering has firstly been introduced to smooth gray and color images as an extension of the basic Gaussian filter it also takes into account image content namely position and intensity values, and forms a logical extension to discontinuity preserving filtering. Testing with pairs synthetic and a well known dataset of clinical images shows statistically significant improvement over the state-of-the-art Demons. This regularizer significantly improves the results in the tested cases showing discontinuities. We showed its superior performance on synthetic as well as on clinical images.

Acknowledgments
This work was supported by the Swiss National Scientific Foundation SCOPES Project IZ74Z0–137409.

References
[1] Maintz AJB,Viergever MA (2001) A Survey of Medical Image Registration in Medical Image Analysis,Vol. 2, pp. 1–36.
[2] Siebenthal Mv, Szekely G, Gamper U, Boesiger P, Lomax A, Cattin Ph (2007) 4D MR Imaging of Respiratory Organ Motion and its Variability Physics in Medicine and Biology, 52, 1547–64
[3] Wang H, Dong L, ODaniel J, Mohan R, Garden AS, Ang KK, Kuban DA, Bonnen M, Chang JY and Cheung R (2005): Validation of an accelerated demons algorithm for deformable image registration in radiation therapy, Phys Med Biol 50 2887–905
[4] Tomasi C, Manduchi R (1998) Bilateral Filtering for Gray and Color Images, in Proceedings of IEEE International Conference on Computer Vision'98, New Delhi,836–846
[5] Vandemeulebroucke J, Sarrut D, Clarysse P (2007) The POPI model, a point-validated pixel-based breathing thorax model. in XVth International Conference on the Use of Computers in Radiation Therapy (ICCR), Toronto, Canada.

Intensity-based hierarchical elastic registration using approximating splines

A. Šerifović-Trbalić[1], D. Demirović[1], P.C. Cattin[2]
[1]Faculty of Electrical Engineering, University of Tuzla, Tuzla, Bosnia and Herzegovina
[2]Medical Image Analysis Center, University of Basel, Basel, Switzerland

Keywords Gaussian elastic body splines · Image registration · Deformation field · Approximation

Purpose
We introduce a new hierarchical approach for elastic medical image registration using approximating splines. In order to obtain the dense deformation field we employ Gaussian elastic body splines (GEBS) that incorporate anisotropic landmark errors and rotational information. Since the GEBS approach is based on a physical model in form of analytical solutions of the Navier equation it can very well cope with the local as well as global deformations present in the images by varying the standard deviation of the Gaussian forces. The inclusion

of the anisotropic landmark errors and the rotation information proofs particularly interesting when registering highly non-rigidly deformed images such as breast mammogram.

Methods

The proposed GEBS approximating model is integrated into the elastic hierarchical image registration framework (HERA), which decomposes a non-rigid registration problem into numerous local rigid transformations. It follows a coarse-to-fine gradual approximation of the non-rigid deformation field to compensate spatial misalignment between two mono- or multi-modal medical images. By progressively subdividing the floating image, an image pyramid is constructed, comprising at every level of a growing number of sub-images whose centers and their related transformation parameters constitute the landmarks of the deformation field. The dense deformation field of final result is calculated using GEBS, densely interpolating the local transformations of the sub-images over whole image domain. The approximating GEBS registration scheme incorporates anisotropic landmark errors as well as rotational information. The anisotropic landmark localization uncertainties can be estimated directly from the image data and, in this case, they represent the minimal stochastic localization error, the Cramér-Rao bound. The rotational information of each landmark obtained from the hierarchical procedure is transposed in an additional angular landmark, doubling the number of landmarks in the GEBS model.

Results

The modified hierarchical registration using the approximating GEBS model is applied to register 161 image pairs from a digital mammogram database. To evaluate the performance of the proposed GEBS approximation scheme three independent experiments were conducted. The obtained results are very encouraging and the proposed approach significantly improved all registrations comparing the mean square error (MSE) in relation to approximating thin-plate splines (TPS) with the rotation information. Applicability of the approximating GEBS with the rotation information is more pronounced for the asymmetric images with the higher landmark localization uncertainties and larger elastic deformations. Although, approximating TPS can handle the anisotropic landmark errors, approximating GEBS has better control over the locality of transformation. On artificially deformed breast images the newly proposed method performed better than the state-of-the-art registration algorithm introduced by Rueckert. The average error per breast tissue pixel was less than 2.23 pixels compared to 2.46 pixels for Rueckert's method.

Conclusion

The proposed hierarchical elastic image registration approach incorporates the GEBS approximation scheme extended with anisotropic landmark localization uncertainties as well as rotational information. Our experimental results show that the proposed scheme improved the registration result significantly.

Tumor grade estimation for breast cancer in 3D ultrasound imaging

Y.-L. Huang[1], D.-R. Chen[2], P.-N. Chen[1]
[1]Tunghai University, Department of Computer Science, Taichung, Taiwan
[2]Changhua Christian Hospital, Comprehensive Breast Cancer Center, Changhua, Taiwan

Keywords Breast cancer · 3D sonography · Tumor grade · Biopsy

Purpose

Tumor grade is a system used to classify cancer cells in terms of how abnormal they look under a microscope and how quickly the tumor is likely to grow and spread. Tumor grade information of breast carcinoma is available about tumor growth and proliferation of speed, also can be used to predict whether it can make a good response to treatment. Doctors use the tumor grade and many other factors, such as cancer stage, to develop an individual treatment plan for the patient and to predict the patient's prognosis. In this study, analysis and classification is performed in the coronal pathology image (C-view imaging) [1] from three-dimensional (3D) ultrasography to capture characteristics to help physicians estimating the breast tumor grade.

Methods

Data acquisition

80 cases were obtained for this retrospective study with all patients histopathologically identified as infiltrating ductal carcinoma (IDC) case. The histologic grades were used later to match with indices extracted from image. Sonographic screenings were operated on GE Voluson 730 3D ultrasound system prior to biopsy. The 2D coronal sliced images were reconstructed from 3D volume data that have resolution varied in the range from 0.013 to 0.029 cm/pixel.

Histological grade of breast cancer

Histological grade of breast carcinoma was scored according to the Nottingham-modified Bloom-Richardson grading system [2], which is based on the microscopic evaluation of morphological and cytological features of tumor cells. Each of the three scores including tubule formation, nuclear pleomorphism, and mitotic count was given 1 to 3 points. Three scores were added together to give an overall score and a corresponding grade. Overall score 3–5, 6–7 and 8–9 were defined as grade 1, 2 and 3, respectively.

Image pre-processing and tumor contouring

The ultrasound images contain speckle noise, which has been known as an undesired effect produced by most ultrasound systems. This study utilized the bilateral filter as the pre-processing procedure to eliminate the speckle noise while also to enhance texture/boundary feature on the coronal pathology images [3]. The bilateral filter is similar to the K-means clustering and the mean shift algorithms in that it maintains a set of data points that are iteratively replaced by means. The filter's weight is based on a Gaussian distribution. Then an experienced sonography physician who was familiar with breast ultrasound interpretations manually determined contours of the tumor in the coronal pathology image. Figures 1 and 2 show the pre-processed images and determined regions for the breast tumors with grade 1 and 3,respectively.

Feature extraction

In this study, textural and intensity statistical features were utilized to estimate the tumor grade. The proposed method calculated a set of

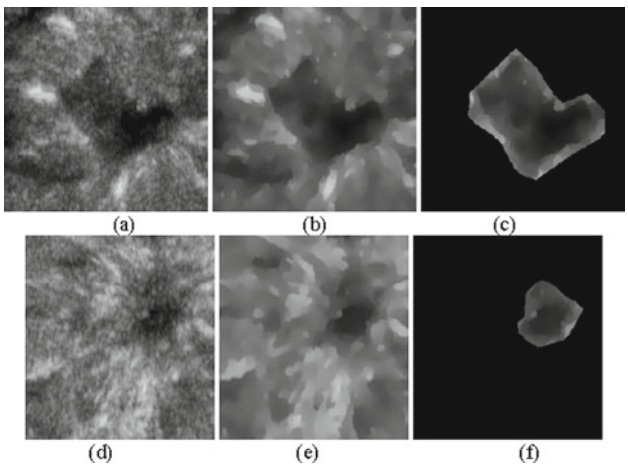

Fig. 1 Result of image pre-processing (tumor grade 1): **a**, **d** the original image; **b**, **e** the corresponding pre-processed image; **c**, **f** manually determined region of tumor

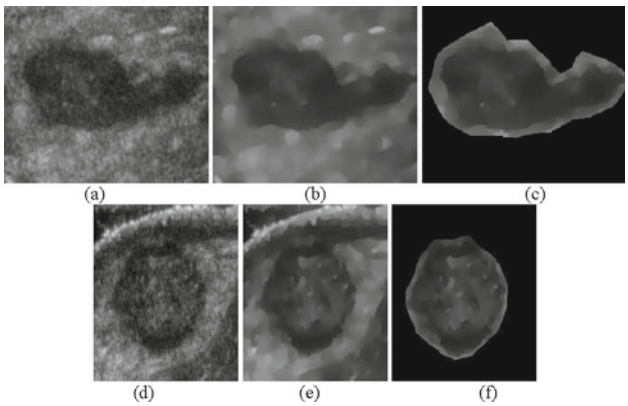

Fig. 2 Result of image pre-processing (tumor grade 3): **a**, **d** the original image; **b**, **e** the corresponding pre-processed image; **c**, **f** manually determined region of tumor

features related to the geometry of the boundary and the structure inside of the tumor. Moreover, texture is an important characteristics used to identify the objects from an image. Textural features deal with the internal structure of the tumor which can be described using this co-occurrence matrix [4]. Eight performed parameters were angular second moment (energy), inertia, correlation, the absolute value, the inverse difference, sum of entropy and the maximum probability. For quantitatively describing the intensity statistical features of the image, the useful features of the image were obtained from the intensity histogram. Statistical features used in this study included mean, sum variance, skewness, kurtosis, energy and entropy. This study found that the texture and statistical features are valuable to distinguish grade level from malignant lesions.

Grade classification

The K-means algorithm is an unsupervised classification that calculates initial class means evenly distributed in the data space and then iteratively clusters the pixels into the nearest class using a minimum distance technique. The main idea is to define k centroids (one for each cluster) which are placed in a cunning way due to different location may cause different result. The next step is to take each point belonging to a given data set and associate it to the nearest centroid. The early group is done when no point is pending. Then k new centroids are needed to re-calculate as barycenters of the clusters resulting from the previous step. After the method obtains these k new centroids, a new binding has to be done between the same data set points and the nearest new centroid. This study utilized the K-means clustering algorithm to classify and estimate breast tumor in 3D sonography to a corresponding grade.

Results

In all 80 obtained cases, there are 40 and 40 cases identified as grade 1 and 3, respectively. For the classification experiment, accuracy is 85.00 % (68/80), the sensitivity is 87.50 % (35/40), the specificity is 82.50 % (33/40), the positive predictive value is 83.30 % (35/42) and the negative predictive value is 86.80 % (33/38).

Conclusion

From the experimental results, the proposed method using the K-means algorithm with the proposed textural and statistical features is feasible for coronal pathology imaging classification. The results indicated that the proposed features can be utilized as potential predictors for tumor grades. As the proposed classification system is useful to estimate the breast tumor grade which may be the useful information for physicians to prognose the effect of treatments for malignant lesions.

Acknowledgments

This research was supported by National Science Council of the Republic of China (Taiwan) under Contract No. NSC101-2221-E-029-031.

References

[1] Rotten D, Levaillant JM, Zerat L (1999) Analysis of normal breast tissue and of solid breast masses using three-dimensional ultrasound mammography. Ultrasound in Obstetrics and Gynecology 14(2):114–124

[2] Elston CW, Ellis IO (1991) Pathological prognostic factors in breast cancer. I. The value of histological grade in breast cancer: experience from a large study with long-term follow-up. Histopathology 19:403–410

[3] Yin FF, Giger ML, Doi K, Metz CE, Vyborny CJ, Schmidt RA (1991) Computerized detection of masses in digital mammograms: analysis of bilateral subtraction images. Med Phys 18:955–963

[4] Soh LK, Tsatsoulis C (1999) Texture analysis of SAR sea ice imagery using gray level co-occurrence matrices. IEEE Trans. Geosci. Remote Sens 37(2): 780–795

Supervised learning with global features for image retrieval in atlas-based segmentation of thoracic CT

H. Ma[1,2], T. Coradi[2], G. Szekely[1], B. Haas[2], O. Goksel[1]
[1]ETH Zurich, Computer Vision Lab, Zurich, Switzerland, Switzerland
[2]Varian Medical Systems Imaging Laboratory, Baden, Switzerland, Switzerland

Keywords Machine learning · Image retrieval · Atlas-based segmentation · Thoracic CT

Purpose

Atlas-based segmentation is an essential component of computer aided planning for radiotherapy. Commercial products often have access to a large number of candidate images to be used as atlases and thus efficient mechanisms are necessitated to automatically retrieve suitable atlas images. In this study, we have first developed methods to extract global features from thoracic CT images. These include geometrical features based on both voxel intensities and the outlines of automatic approximate bone, lung, and whole-body segmentations that can be calculated in seconds. Our goal is to study image retrieval techniques using these global image features, in particular investigating the feasibility of various supervised learning algorithms. Such retrieved images are then to be used as atlasses for the atlas-based segmentation of anatomy that cannot be segmented automatically such as lymph nodes.

Methods

We use 25 global features to describe thoracic CT images. Some of these features are based entirely on a simple thresholding of voxel Hounsfield units, e.g., ratio of fat in thorax; while others are geometrical features, such as circumference, area, shape and position derived from outlines of body, lungs and bones in automatic approximate segmentations [1]; see Fig. 1a, b.

Image retrieval involves ordering a set of items according to their expected relevance for a given query. Let f_i be the row vector for these 25 features extracted for each image i. The conventional query-by-example method for retrieving images is then to use $|f_i - f_j|^2$ for each image pair as a metric to sort them. In contrast, supervised learning algorithms attempt to infer a relationship between such difference vector and the expected segmentation outcome using given supervision examples. We defined segmentation outcome as the Dice's similarity metric by comparing automatic segmentation [1] to the segmentation obtained by using deformable registration [2] of an atlas. An average Dice similarity for body, lungs and bones was used. The histogram of such Dice values for all pairs of 95 CT images in our database is seen in Fig. 1c. In order to utilize discriminative power of all features in machine learning, we used the difference vector $(f_i - f_j)$ of length 25, called *diff* in the results. To further study possibly complex

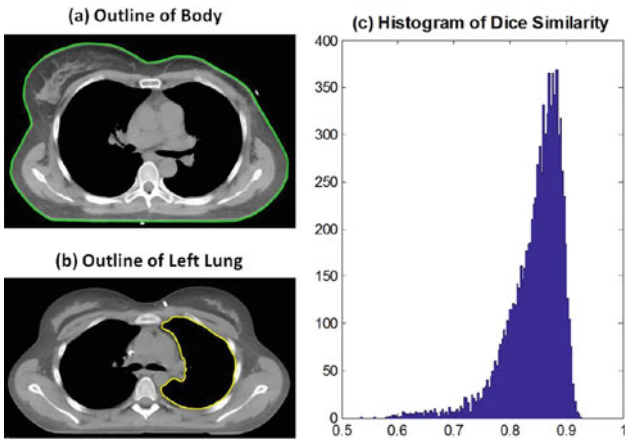

Fig. 1 Examples of global image features (**a**, **b**) and the histogram of Dice's similarity metric for all pairs of images (**c**)

nonlinear interactions between each feature component, we also used a concatenated vector $[f_i - f_j]$ of length 50, called *conc*.

Three different techniques were used to learn a regression model between image-pair vectors and outcomes. Regression trees (RT) partition the feature space into smaller cells and fit data in each cell using simple models. Ensemble methods (ENS) combine results from many weak learners into one high-quality predictor. Support vector regressor (SVR) projects data on a high dimensional space using the kernel trick to infer non-trivial input–output relations, for which we used a radial-basis kernel. We utilized the built-in Matlab functions for RT and ENS, and the LIBSVM package [3] for SVR.

Results

We employed a fivefold cross-validation scheme, i.e., the images from each fold were queried from the 76 out-of-fold images, which were also used for training the supervised techniques. This yields 95 separate queries in total. For each query, the 76 images were sorted by the L_2-norm feature difference (called NONE for no machine learning) or by regressor prediction. Figure 2a shows Pearson's correlation between such predicted Dice values and their true values for each query. Figure 2b presents the Spearman's rank correlation for images sorted using these predicted values. The relatively high correlation of NONE indicates that feature difference without learning is already a good metric for retrieval. Nonetheless, machine learning improve on this significantly, especially when concatenated features are used, with SVR *conc* performing the best. The rest of results focus on *conc* features alone.

The following ultimate clinical setting is envisioned. For a new patient image, features are extracted and a set of n most relevant (highest ranked) images are returned to the physician. The physician then picks one of these as the atlas for registration-based segmentation. Figure 2c shows the percentage of queries that return the theoretical best image.

To quantify error for returning suboptimal images, we make the assumption that a trained physician is able to pick the best possible image out of returned n images (n-hits). Accordingly, Dice Retrieval Error (DRE) is defined as the difference of the largest achievable true Dice value within n-hits and the true Dice value using the top query result. Similarly, Dice Rank Retrieval Error (DRRE) is the true rank (minus one) of the best true Dice within n-hit. These errors were then averaged over all queries and reported in Fig. 2d, e as functions of number of hits. Figure 2d shows that DRE for all methods are under 0.025 even for returning a single image. In Fig. 2e an analytical DRRE upper-bound for random queries is also shown. For retrieving a few images, DRRE of SVR and ENS is much smaller than the other techniques. However, with more images retrieved this difference becomes less significant. Although the best possible atlas may not necessarily be retrieved as seen in Fig. 2c, it is encouraging to see in Fig. 2d that such suboptimal retrievals indeed do not incur significant Dice errors.

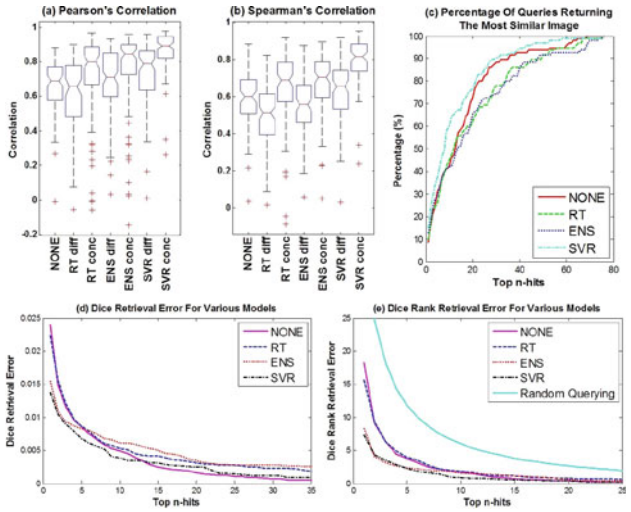

Fig. 2 Evaluation metrics: **a** Pearson's and **b** Spearman's correlation of true and estimated Dice metrics, **c** probability of returning the actual best image in the first n-hits, **d** Dice retrieval error and **e** Dice rank retrieval error for n-hits

Conclusions

We have presented a comparison of image retrieval methods for atlas-based segmentation. This study shows that geometric feature based image retrieval is a promising tool, while machine learning algorithms improve such retrieval performance. Using concatenated feature vectors has been identified as the superior approach and SVR has worked best for our particular problem. In the future, we will study the generalizability of the methods and investigate other image features to improve retrieval accuracy.

Acknowledgments

This work is partially supported by the NCCR Co-Me of the Swiss National Science Foundation.

References

[1] Haas B, et al (2008) Automatic segmentation of thoracic and pelvic CT images for radiotherapy planning using implicit anatomic knowledge and organ-specific segmentation strategies. Physics in Medicine and Biology, 53:1751–1771

[2] Wang H, et al (2005) Validation of an accelerated 'demons' algorithm for deformable image registration in radiation therapy. Physics in Medicine and Biology, 50:2887–2905

[3] Chang C-C, Lin C-J (2011) LIBSVM: a library for support vector machines. ACM Transactions on Intelligent Systems and Technology, 2(3):27

Automatic generation of initial points for CT abdominal organ segmentation

J. Juszczyk[1], E. Piętka[1]

[1]Silesian University of Technology, Faculty of Biomedical Engineering, Gliwice, Poland

Keywords Automatic segmentation · CT segmentation · Semi-automatic segmentation · Abdominal

Purpose

Fully automatic segmentation methods still fail more often than a semi-automatic process. However, automatic segmentation features important advantages. The reduction of time, a radiologist is to spend while reading and reporting a study is very important in hospitals with increasing data to be analysed. The location of segmented organs becomes an additional and very crucial step that makes the automatic segmentation more difficult than the semi-automatic approach. The location of organs, their size and shape, dependent on the image projection, are very difficult to assess.

Many robust semiautomatic segmentation methods (active contours, live-wire, region growing, fuzzy connectedness, etc.) have been developed [1–3]. However, a very important step, often performed interactively—the seed points selection to initialise the segmentation procedure is required.

In this study, a probability map has been built. After an alignment procedure the seed points are indicated. They serve as seed points or initial regions for further analysis that employs already known segmentation methods.

Methods

The probability map is derived by subjecting to the analysis clinical CT studies. The method contains three phases. First, the CT volumes are subjected to a segmentation process that extracts the anatomical structures. Then, the size normalization and adjustment are performed. Finally, the reference points that allow the studies to be aligned are located.

At the first level of building the probability map, the segmentation requires interactive indication of extracted organs. Once the starting points have been marked, a region growing algorithm has appeared to be sufficiently robust to label consecutive anatomical structures.

In order to superimpose a set of CT studies, a size normalization of the CT volume is required. Within the abdomen, the bony structures allow for the most accurate location and identification of markers. Thus, after thresholding the CT volumes at 350 HU, the further bone structures analysis has been based on modified maximum intensity projection (MIP), resulting in locating the ultimate and penultimate thoracic vertebrae. At the adjustment process, the ultimate thoracic vertebra is referred to as central point (Fig. 1). Then, employing the profile analysis, the longitude and transverse size of thorax are found. They serve as the size normalization factors.

After the segmentation and normalization process the clinical CT studies have been superimposed. The comparison of labelled structures has indicated regions of the highest probability of location of a certain anatomical structure yielding a map which indicates the probability of location of a certain anatomical structure. The highest probability indicates initial (seed) points for fully automatic segmentation. In order to implement the map, the input CT volume has to be aligned and its size is normalised. In Fig. 2 the probability map indicating the area of 95 and 50 % of voxels assigned to the liver (Fig. 2a, b) and spleen (Fig. 2c, d), respectively, is shown.

Results

The system performance has been evaluated on 30 CT abdominal studies with different numbers of slices and different range of imaged area. A total of 3,300 slices have been analysed. The location of the thoracic vertebrae, thorax size and initial point location have been evaluated. Correct location of the thoracic vertebrae has been obtained in all cases (100 %). The width of thorax assessment failed in one case reaching the rate of 97 %.

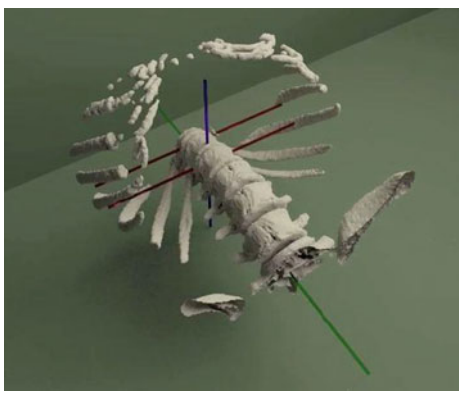

Fig. 1 The adjustment process, location of the ultimate and penultimate thoracic vertebrae are marked by red beam, central point is marked by red and blue beam cross

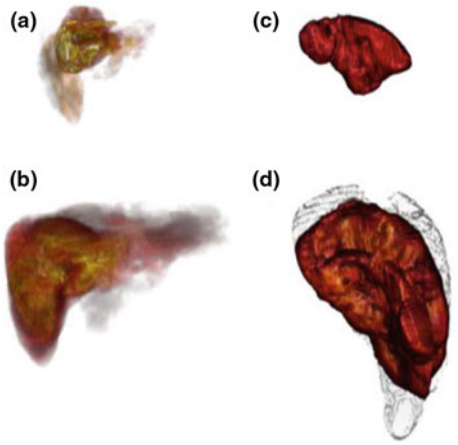

Fig. 2 The probability map indicating the area of 95 and 50 % of voxels assigned to the liver (**a**, **b**) and spleen (**c**, **d**)

The initial points have been subjected to a region growing segmentation procedure. Two testing data sets were employed. The first one contained CT volumes included in the data which served for building the probability map and segmented after a manual selection of seed points. The segmentation was evaluated for liver, spleen and kidneys. The difference between the segmentation results ranged between 2 and 5 %. Then, an independent data set was subjected to the alignment, normalization and segmentation procedures. The discrepancy between the fully automated segmentation versus a semi-automatic one ranged between 3 and 7 %. In 4 cases the seed point missed the kidney.

Conclusion

Automated segmentation of abdominal structures is a challenging task. Selection of initial points requires a knowledge of the structure location. The developed method, which generates the probability map, yields good results. Implementation of the map in the segmentation process makes the procedure fully automatic and no interaction is required from the user.

References

[1] Badura P, Pietka E (2007) Semi-Automatic Seed Points Selection in Fuzzy Connectedness Approach to Image Segmentation. Computer Recognition Systems 2, Advances in Soft Computing 45: 679–686

[2] Więcławek W, Pietka E (2012) Fuzzy Clustering in Intelligent Scissors Computerized Medical Imaging and Graphics, 36(5):396–409

[3] Czajkowska J, Badura P, Pietka E (2010) 4D Segmentation of Ewing's Sarcoma in MR Images. Information Technologies in Biomedicine, Advances in Intelligent and Soft Computing 69(2):91–101

Detection and quantification of intracerebral hemorrhage from computed tomography images with adaptive thresholding and case-based reasoning

Y. Zhang[1], M. Chen[1], W. Huang[2], Q. Hu[1]
[1]Shenzhen Institutes of Advanced Technology, Shenzhen, China
[2]Nanfang Medical University, Guangzhou, China

Keywords Intracerebral hemorrhage · Computed tomography · Adaptive thresholding · Case-based reasoning

Purpose

Intracerebral hemorrhage (ICH) can have high mortality and high risk of disability. Computed tomography (CT) head scans are the recommended modality for diagnosing and therapy of ICH. Diagnosing of ICH may be difficult when the hemorrhage is inconspicuous, while quantification is difficult as hemorrhage can have overlapping and very variable intensity. An algorithm is proposed to detect and quantify ICH.

Methods

Adaptive thresholding and case-based reasoning (CBR) are explored in four steps: preprocessing to derive the brain, adaptive thresholding based on local contrast with varied window sizes to derive candidate ICH regions, case representation to represent each candidate ICH region by parameters on context as well as intensity and geometrical characteristics, and classification of ICH by taking each candidate ICH region as a case and exploring CBR. Additionally, case base indexing and weights optimization are explored to increase the retrieval speed and improve performances. Refinement of recognized ICH is explored for quantifying ICH.

The following local thresholding with varied window size is proposed: for each voxel (x, y, z) within the brain, the corresponding local window is the window centered at (x, y, z) with a window width W(x, y, z) and height H(x, y, z); for each axial slice (z being a constant), find the maximum intensity standard deviation for all possible window widths and heights of all the brain voxels and denote it as $sd_{max}(z)$; for each voxel (x, y, z), find the minimum W(x, y, z) = H(x, y, z) such that the intensity standard deviation within the local window sd(x, y, z) is not smaller than 0.6 * $sd_{max}(z)$. With the availability of adaptive window size containing balanced background and foreground, we propose to determine local threshold T(x, y, z) based on the enhancement of Sauvola and Pietikainen's [1] formula,

$$T(x,y,z) = m(x,y,z) * (1-k) + k * m(x,y,z) * \frac{sd(x,y,z)}{1.2 * sd_{\max}(z)}$$

where m(x, y, z) is the local intensity mean, k is a constant to be determined. To speed up the adaptive local thresholding, the local intensity mean and standard deviation are calculated using integral images [2].

CBR solves a new case by retrieving similar past cases and adapting their solutions. The first step of CBR is case representation. In this paper, each ICH candidate region from adaptive thresholding on an axial slice is considered as a case, detecting ICH is converted to "whether a case is an ICH". Case representation can do reasoning on object (case) level instead of on voxel level. According to experience and experiments, 16 parameters are explored for case representation. These parameters could be classified to two groups. The first group contains five parameters to represent the context of a case within the same axial slice. The second group includes 11 parameters to describe the intensity and shape properties of a case.

Results

Validation on 426 clinical CT data indicates that the proposed algorithm has a precision of 94.4 % and recall of 79.2 % for detecting ICH regions. Visually the ICH regions calculated from adaptive thresholding plus refinement agree well with expert delineation and could quantitatively yield a segmentation accuracy of 0.950 ± 0.015 for 10 representative data with small to large ICH. Case base indexing increases the retrieval speed by 41.1 times at the expense of decreasing precision of 0.5 % and recall of 2.6 %. Genetic algorithm optimization can enhance the precision and recall to respectively 94.9 and 83.5 %.

The characteristics of those misclassified cases are: small area with medium intensity, likely to be misclassified as high signal around longitudinal fissure or sagittal sinus (Fig. 1, misclassified cases within yellow rectangles).

The error of segmentation is mainly due to decreased hemorrhage intensity (Fig. 2). It reflects the complexity of the problem itself: ICH may have very variable intensity due to factors such as variation in hemoglobin concentration. Delineating ICH with intensity similar to normal brain tissue is difficult for both the expert and any automatic algorithm. The proposed method could yield an accuracy of κ index 0.950 ± 0.016 for the 10 representative data, which is close to radiology experts.

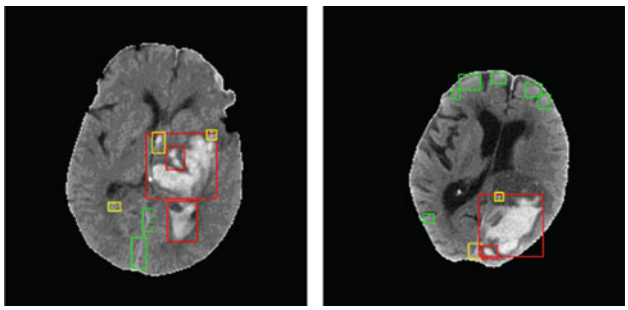

Fig. 1 Typical images of classification of the proposed CBR

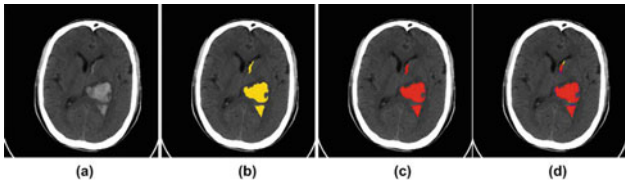

Fig. 2 An axial slice with ICH with substantial intensity change (**a**), manually delineated ICH by an expert in *yellow* (**b**), segmented ICH with the proposed method in *red* (**c**), and the difference between **b** and **c** (*red* for intersection, *yellow* for false negative and blue for false positive)

Conclusion

We have proposed an algorithm that combines adaptive thresholding and CBR for detecting and quantifying ICH. Experiments showed that adaptive thresholding could provide good candidates, while CBR could pick up the right ICH regions based on reasoning similar to human beings. The proposed method could be a potential tool for accurately detecting and quantifying ICH.

Acknowledgments

This work has been supported by: Key Joint Program of National Natural Science Foundation and Guangdong Province U1201257, and Shenzhen Key Basic Research Project JC201005270370A. Authors would like to thank collaborating hospitals (Linyi People's Hospital, Nanfang Hospital, Tiantan Hospital, and Shekou People's Hospital) for providing the real clinical data.

References

[1] Sauvola J, Pietikainen M. (2000) Adaptive document image binarization. Pattern Recognition 33: 225–236.

[2] Viola P, Jones MJ (2004) Robust real-time face detection. International Journal of Computer Vision 57(2): 137–154.

Statistical shape analysis of retroperitoneal tumors in childhood

J.-P. Schenk[1], S.M. Giebel[2]

[1]University Clinic of Heidelberg, Diagnostic and Interv. Radiol., Division of Pediatric Radiology, Heidelberg, Germany

[2]Johannes Kepler University Linz, Institut für Angewandte Statistik, Linz, Austria

Keywords Shape · Retroperitoneal tumors · Oncology · Neural networks · Classification

Purpose
The image recognition and the classification of objects according to the images are more in focus of interests, especially in medicine. A mathematical procedure allows us, not only to evaluate the amount of data per se, but also ensures that each image is processed similarly and furthermore to find a representative object for every diagnosis or class of objects. Here in this study, we propose the power of statistical shape analysis, in conjunction with neural networks for reducing white noise instead of searching an optimal metric, to support the user in his evaluation of MRI of renal tumors. Therapy of renal tumors in childhood bases on therapy optimizing SIOP (Society of Pediatric Oncology and Hematology)-study protocols in Europe.
Methods
Our research is the first mathematical approach on MRI of retroperitoneal tumors in childhood (n = 108). We use MRI in 3 planes and evaluate their potential to differentiate other types of tumour by Statistical Shape Analysis. Statistical Shape Analysis is a methodology for analyzing shapes in the presence of randomness. It allows to study two- or more dimensional objects, summarized according to key points called landmarks, with a possible correction of size and position of the object. To get the shape of an object without information about position and size, centralisation and standardisation procedures are used in some metric space. This approach provides an objective methodology for classification whereas even today in many applications the decision for classifying according to the appearance seems at most intuitive.We determine the key points or three dimensional landmarks of retroperitoneal tumors in childhood by using the edges of the platonic body (C60) and test the difference between the groups (nephroblastoma versus non-nephroblastoma).
Results
Statistical Shape Analysis is an useful tool to differentiate retroperotoneal tumors and to support diagnosis. Using Logistic Regression or Discriminant Analysis more than three quarter of all tumours can be classified correctly by the distance of each tumour to the mean shape, the position and the age of the patient. Neural Networks can be used as an alternative for Procrustean analysis or Ziezold's algorithm to calculate the mean shape or to reduce the white noise in the data. In comparison to our first study on renal tumours in 2D the power of differentiation between different kind of renal tumours has increased.
Conclusion
Statistical Shape Analysis in 2D/3D-dimensions can help to differentiate tumors before therapy, next developments should demonstrate the power in 4D, as an example heart dynamic or geometric changes of tumors after chemotherapy. By increasing the dimension step by step we have to develop and to improve the mathematical procedures according to the reality. Furthermore our procedures have to be proved on real unknown data. Only real unknown data gives us an idea of the power of prognosis. In order to ensure the high power of differentiation in the long term, we have also to consider a suitable learning procedure to sort out unknown kind of tumours.

Segmentation and visualization of pulmonary nodules in CT images based on 3D fast marching and template matching

B. Wang[1], Q. Wang[2], X. Fan[2], B. Dong[3,4], Y. Yang[4], M. Wang[1], J. Ming[1], L. Gu[3,2]
[1]Hebei University, College of Mathematics and Computer Science, Baoding, China
[2]Hebei University, Biomedical Multidisciplinary Research Center, Baoding, China
[3]Shanghai Jiao Tong University, School of Biomedical Engineering, Shanghai, China
[4]Hebei University, Affiliated Hospital, Baoding, China

Keywords Pulmonary nodules · 3D fast marching · Template matching · 3D visualization

Purpose
According to WHO reports, lung is a most frequent site of metastasis from other cancers that manifest as pulmonary nodules. Computed Tomography (CT) is shown to be the most sensitive imaging modality for the detection of pulmonary nodules [1]. Meanwhile, 3D nodule representation can help radiologists further accurately observe and diagnose its structure and characteristics. We present an effective algorithm for the 3D segmentation of lung nodules from CT images, where a 3D fast marching method is employed to segment nodules. Especially for dealing the juxta-vascular nodules [2], we develop a novel method that removes the blood vessels connected with nodules by analyzing the spatial connection characteristic between them. Finally we use marching cubes to construct segmentations for further analysis.
Methods
The first step is to segment the pulmonary nodules by using improved 3D fast marching method, which is not only able to carry out the segmentation of smooth isolated nodules such as in Fig. 1b, but also the nodules with complex structures and boundaries as shown in Fig. 2b.

The second step is to remove blood vessels connected to juxta-vascular nodules. By tracking area boundary segmented, two convex points in the joint can be detected, and the vessels could be removed by connecting the two points. We adopt the template to describe this spatial characteristic of convex points and a template matching method to find convex points. If the two detected neighboring convex points A and B satisfy that the arc length of AB and the chord length of AB are equal to or less than a certain threshold value which represents the spatial narrow feature of vessels, the cardinal splines are employed to connect A and B, and get smoother boundary curve. The attached regions, such as blood vessels, are removed.

The third step is to reconstruct 3D surface model by using marching cubes after a 3D Gaussian smoothing was applied to the segmented nodules. In order to provide radiologists better location of the nodule in chest cavity, the bone and nodules are hybrid rendered.
Results
Two sets of chest CT images are employed in the experiment with 1.25 mm slice thickness, downloaded from NCI-NBIA (https://imaging.nci.nih.gov/ncia/login.jsf/). Both of the two sets of CT images are with the resolution of 512 × 512, and cover the nodules

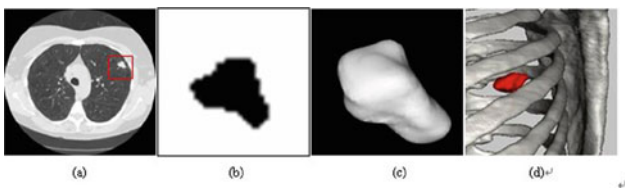

Fig. 1 Solitary pulmonary nodule segmentation. **a** The original CT with the nodule circled in the *red box*. **b** The segmented result. **c** The 3D model. **d** 3D representation with relative bones

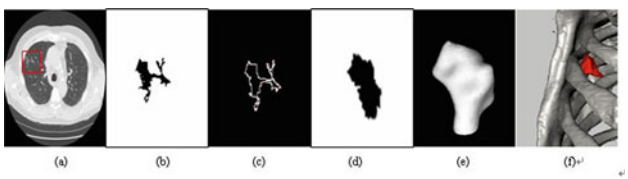

Fig. 2 The juxta-vascular nodule segmentation. **a** The original CT image. **b** The segmented nodule with blood vessels. **c** Detected convex points. **d** Final segmentation result. **e** The 3D model. **f** 3D representation with relative bones

completely. The experiment was performed on a PC Windows environment with 3.2 GHz CPU, 2.0 G memory and NVIDIA GeForce GT 430 GPU.

One dataset with 22 CT slices contains solitary pulmonary nodules, and the second dataset with the juxta-vascular nodule contains 26 CT slices. To visually demonstrate the performance of the nodule segmentation schemes, two typical examples are represented in Figs. 1 and 2. Our preliminary study shows that the distance discrepancies between the segmentation results by the computerized scheme and the radiologists are in the error range that the average maximum and mean discrepancies were 2.67 ± 1.25 and 1.07 ± 0.46 mm, respectively.

Conclusion

In this paper, we present a novel 3D lung nodule segmentation approach. The experimental results reveal that the proposed method can successfully segment nodules from CT image and can be presented in 3D. Our future work is to further combine template matching into fast marching method to obtain better segmentation and effective results.

Acknowledgments

This research work is partially supported by the Chinese NSFC research fund (61190120, 61190124 and 61271318), the Hebei University Biomedical Multidisciplinary Research center research fund (BM201110) and Technological Innovation of Undergraduate research fund (201210075008).

References

[1] Camarlinghi N, Gori I (2012) Combination of computer-aided detection algorithms for automatic lung nodule identification. Int J CARS 7:455–464

[2] Ge Z, Sahiner B (2005) Computer-aided detection of lung nodules: False positive reduction using a 3D gradient field method and 3D ellipsoid fitting. Med Phys 32(8):2443–2454

CT Image reconstruction with the Co-occurrence matrix similarity as regularization term

V. Liauchuk[1], V. Kovalev[1], I. Safonau[1], D. Stsepankou[2], J. Hesser[2]
[1]United Institute of Informatics Problems, Biomedical image analysis, Minsk, Belarus
[2]Heidelberg University Faculty of Medicine in Mannheim, Experimental Radiooncology, Mannheim, Germany

Keywords Reconstruction · Radiation therapy · Co-occurrence matrices · Anatomical prior

Purpose

The problem of Cone-Beam CT (CBCT) image reconstruction has been considered here in a context of the image-guided radiation therapy. Such an environment is typically associated with the following two major points: (a) reduction of the number of projections is desired for reducing the radiation dose substantially, and (b) availability of previous planning CT scan of the same patient taken before the treatment procedure which can potentially be utilized for constructing suitable anatomical prior.

When reducing the number of projections the problem can be considered as an ill-posed. Iterative methods, such as ART [1], are typically used to solve this class of the problems. When a priori knowledge is available it can be incorporated in the form of regularization functional. Nowadays many researchers are investigating a TV function [2], which can be represented as L1 norm minimization. Depending on the specific conditions, incorporation of a priori anatomical knowledge can be done in different ways. One of the ideas of using anatomical a priori is based on incorporating features that characterize the main elements in the image. An interesting approach in this direction is the usage of histograms [3].

The basic idea of the CBCT image reconstruction method introduced with this study is to use the prior anatomical knowledge represented by the co-occurrence matrix of a similar image. Such matrices are known as being capable of describing local image structure statistically by way of counting the frequency of spatial occurrence of certain image intensities, gradients, or local orientations, i.e., capturing their anisotropic properties [4, 5].

Methods

In contrast to the real data, where we have to deal with many inconsistencies [2], in this work we used a simulated projection data just to demonstrate how the method works. In order to introduce the method and to perform comparison with some other commonly-used methods we have used CT image slices of two different patients. In the first case (male, 45 years old with no obvious abnormalities) this was axial chest slice (see Fig. 1a) while for the second test we employed head CT slice of a patient (male, 46 years old) with malignant tumor of the head (see Fig. 2a).

The problem of image reconstruction with regularization constrain is typically formulated as finding image f that minimizes $\|M \cdot f - g\|_2^2 + \alpha \cdot R(f)$, where M denotes a system matrix, g—projection data, $\|\cdot\|_2$ denotes L2-norm, α—regularization parameter and $R(f)$ is regularization term. Total Variation (TV) minimization method is often used for regularized reconstruction, and its efficiency has been shown in a number of studies [2]. This method incorporates gradient-based Total Variation as the regularization term: $\|f\|_{TV} = \sum |\nabla f|$. The implementation of TV method is often based on

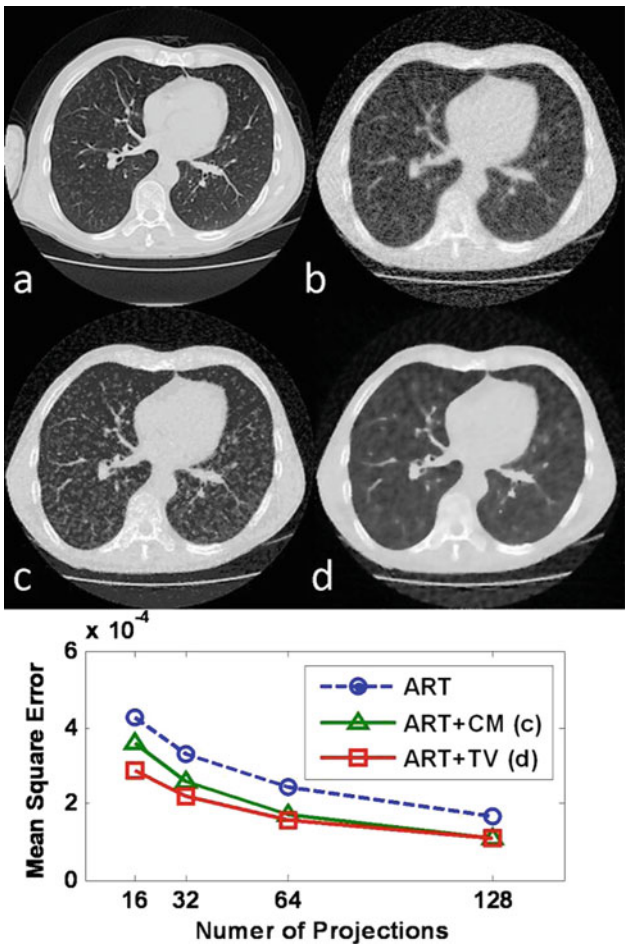

Fig. 1 Reconstruction of CT scan slice of abdomen with use of previous scan as a priori: **a** image under reconstruction; **b** previous scan, source of CM_0; **c** ART + CM reconstructed; **d** ART + TV reconstructed

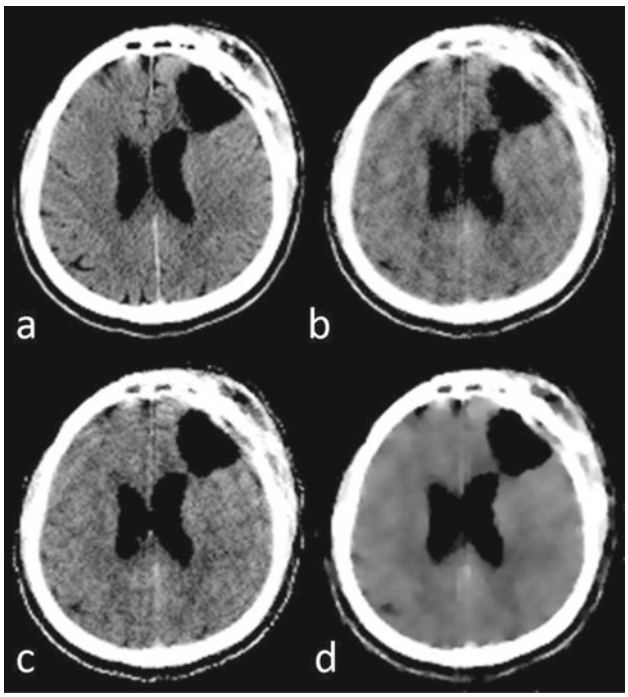

Fig. 2 Reconstruction of CT scan slice of abdomen with use of previous scan as a priori: **a** image under reconstruction; **b** previous scan, source of CM_0; **c** ART + CM reconstructed; **d** ART + TV reconstructed

traditional iterative Algebraic Reconstruction Technique (ART) [1]. Then ART provides iterative image reconstruction with TV-based filtration after each iterative step.

In this work we propose a method which incorporates co-occurrence matrices as the regularization term. In this case the a priori information on local image structure is derived directly from image data. In our method the regularization term $R(f)$ is set to $\|f\|_{CM} = \|CM(f) - CM_0\|_2$, where $CM(f)$ is co-occurrence matrix of the image under reconstruction and CM_0 represents expected local image structure. There could be different sources for calculating the co-occurrence matrix. For instance, CM_0 can be obtained (a) from image of an object, which is similar to the reconstructed one (e.g., the previous scan of the same patient); (b) by averaging co-occurrence matrices of a set of objects of the same class (e.g., average CM of abdomen CT scans if we reconstruct abdominal region) and so on.

The proposed method is also ART-based iterative algorithm. Each iteration of the algorithm includes ART iteration step followed by CM-based filtration. By CM filtration we mean here alternating previous iteration result f^k to f^{k+1} so that $\|f^{k+1}\|_{CM} < \|f^k\|_{CM}$. In this work it is done by estimating $\partial\|f\|_{CM}/\partial f_{x,y}$ and using the gradient descent method.

Results

Figures 1 and 2 represent results of reconstruction of CT scans from under-sampled projection data (64 projections out of 256 needed for accurate reconstruction). Here we perform the comparison of three methods: Algebraic Reconstruction Technique (ART) as a basic method, ART-based Total Variation minimization (ART + TV) and the proposed method with co-occurrence matrix prior (ART + CM). Previous scans data were used to derive the expected co-occurrence matrices CM_0, representing a priori knowledge in the suggested method (Fig. 1b). If compared to ART + TV technique, the suggested method produces sharper edges, doesn't over smooth the image, and small details can be distinguished more easily. However, current implementation of our method does not suppress all the noise on the image. The abilities of noise reduction with respect to the number of projections measured by Mean Square Error (MSE) are represented by the plot given at the bottom of Fig. 1. Note that the use of Total Variation term (Fig. 1d) eliminates the high frequency noise even better than the proposed method. This is because it always smoothes the reconstructed image.

Conclusion

The results reported with this study show that the suggested image reconstruction method is capable of incorporating a priori anatomical knowledge in context of image guided radiation therapy. Future work should include extensive testing on real CT projection data.

Acknowledgments

This work was supported by the grant HE 3011/32-1 from Deutsche Forschungsgemeinschaft.

References

[1] Gordon R, Bender R, Herman G (1970) Algebraic reconstruction techniques for three-dimensional electron microscopy and X-ray photography. Journal of Theoretical Biology 29(3):471–476

[2] Stsepankou D, Arns A, Ng SK, Zygmanski P, Hesser J (2012) Evaluation of robustness of maximum likelihood cone-beam CT reconstruction with total variation regularization. Physics in medicine and biology 57(19):5955–5970

[3] Thurman S, Fienup J (2007) Noise histogram regularization for iterative image reconstruction algorithms. J Opt Soc Am A Opt Image Sci Vis 24(3):608–17

[4] Kovalev VA, Kruggel F, Gertz H-J, von Cramon DY (2001) Three-dimensional Texture Analysis of MRI Brain Datasets. IEEE Transactions on Medical Imaging 20(5):424–433

[5] Kovalev VA, Petrou M, Bondar YS (1999) Texture Anisotropy in 3D Images. IEEE Transactions on Image Processing 8(3):346–360

Automated scheme for the analysis of invasive regions of breast tumour using breast MR images

R. Yoshikawa[1], S. Miyajyo[2], A. Teramoto[2], H. Fujita[3], K. Ozaki[4], O. Yamamuro[4], K. Ohmi[4], M. Nishio[5]

[1]Graduate school of Fujita Health University, Department of Medical Radiation, Toyoake, Japan

[2]Fujita Health University, Department of Radiological Technology, Toyoake, Japan

[3]Gifu University, Graduate School of Medicine, Gifu, Japan

[4]East Nagoya Imaging Diagnosis Center, Radiology, Nagoya, Japan

[5]Nagoya Radiological Diagnosis Center, Nagoya, Japan

Keywords Breast tumour · MRI · CAD · Segmentation

Purpose

In recent years, breast-conserving surgery has been used as the surgical treatment of breast cancer to improve the quality of life of women. In order to select the appropriate form of surgery, exact analysis of the invasive region of the tumour using breast MR images has become an important role in the image diagnosis. However, the many images that are obtained by multi-temporal imaging, and a variety of sequences are used for the identification of the tumour. Consequently, the diagnostic ability of the physician is decreased. Furthermore, a decrease in the diagnostic accuracy is a concern because identification of the region of the tumour is still subjective. In this study, we propose a novel method for automated analysis of the region of the tumour using dynamic contrast-enhanced breast MR images. The usefulness of this method is evaluated using a digital breast phantom and actual breast MRI images.

Methods

For this method, T1-weighted MR images of pre-, early-, and post-contrast- enhanced breast MR images are provided. First, three-

dimensional position among three phase images is adjusted on the basis of the tumour position. Thereafter, early- and late-subtraction images are obtained by subtracting early- and late-contrast- enhanced images, respectively, from the pre-contrast ones. In addition, regions in late-subtraction images with a pixel value below a predetermined threshold are excluded in order to eliminate the influence of normal mammary glands. Higher pixel values are then output by comparing the pixel values of the early- and late-subtraction images. In this way, the exact region of tumour invasion is obtained. Subsequently, using the level-set method, which is a type of dynamic contour extraction, the outline of the tumour in the tumour- extracted images is obtained. Finally, the bounding box of the tumour is calculated using the contour-extracted images; this is considered to be the result of the automated analysis of tumour invasion.

Results

In order to evaluate the usefulness of the analysis method, we evaluated the accuracy of the automated analysis of the invasive region by means of a digital phantom that mimics the mammary gland. Thus, we confirmed that the range of the invasive region has been analysed correctly. Twelve cases of breast MR images were then introduced (seven cases: breast-conserving surgery, five cases: mastectomy. All cases were diagnosed as scirrhous). These images were acquired using a 3- T unit (Signa HDXT 3.0T; GE Healthcare) at the East Nagoya Imaging Diagnosis Center (Nagoya, Japan). We compared the tumour size listed in the interpretation report by a physician and analysed the results obtained from the proposed method. The automated results of tumour invasion were accurate in nine cases of the twelve cases. The mean absolute error of the size of tumours in all cases was less than 5.0 mm.

Conclusion

In this study, we proposed a novel method of automated analysis to quantify the tumour region using dynamic contrast- enhanced breast MR images. High accuracy was obtained in the evaluation using a digital phantom. For the evaluation using actual breast MR images, the mean absolute error between the physician's interpretation and the automated result was less than 5.0 mm. These results suggest that the proposed method may be useful for the automated analysis of invasive breast tumour using breast MR images.

Accurate 3D measurement of normal knee kinematics using dynamic flat-panel detector images

T. Yamazaki[1], T. Tomita[2], Y. Sato[3], H. Yoshikawa[4], K. Sugamoto[2]
[1]Osaka University, The Center for Advanced Medical Engineering and Informatics, Osaka, Japan
[2]Osaka University Graduate School of Medicine, Orthopaedic Biomaterial Science, Osaka, Japan
[3]Osaka University Graduate School of Medicine, Radiology, Osaka, Japan
[4]Osaka University Graduate School of Medicine, Orthopaedics, Osaka, Japan

Keywords 3D normal knee kinematics · Dynamic FPD image · 2D/3D registration · Clinical application

Purpose

Quantitative assessment of dynamic knee kinematics under in vivo conditions is very important for understanding the effects of joint diseases, dysfunction and for evaluating the outcome of surgical procedures. For artificial joint implants, to achieve 3D measurement of the dynamic kinematics, 2D/3D registration techniques which use X-ray fluoroscopic images and computer-aided design model of the implants have attracted attention. These fluoroscopic techniques have also been applied for motion measurement in joints without implants in recent years, where 3D bone models created from CT or MRI images are utilized.

In previous studies, however, normal bone edges extracted from the fluoroscopic image are less well defined than metallic implant edges due to the low contrast of the material, and therefore some registration techniques have a problem of severe local minima. To eliminate this problem, it is important to perform pre-processing to accurately segment the only bone edges. However, it may be difficult to know in advance which edge points belong to the bone edges, and also the pre-processing of removing spurious edges and noises to obtain the only bone edges requires very time-consuming and labor-intensive manual operations.

The purpose of this study is to accurately determine the 3D normal knee kinematics, under the surveillance of dynamic flat-panel detector (FPD) images which can overcome the problem of detection of normal bone edges, using a robust 2D/3D registration technique even if spurious edges and noises exist in the knee images.

Methods

First, the 3D bone models of femur and tibia/fibula were created from CT scans of the subject's knee. CT scans used a 512 × 512 image matrix, 0.63 mm slices spanning approximately 100 mm above and below the joint line of the knee, and 2 mm slices through the centers of the hip and ankle to define the anatomic coordinate systems. Segmentation of the bone was performed by applying a thresholding filter, and finally the point clouds resulting from the segmentation process were converted into polygonal 3D surface models using marching cube algorithm.

Next, dynamic FPD images during the subject's knee motion were acquired as serial digital images (750 × 750x12 bits/pixels, 5.0 Hz serial spot images). To extract the knee contours from the acquired image, a Canny's edge detector was applied. The edges of a fluoroscopic bone image are not sharp like with a metallic implant because of the low contrast of the material. However, use of dynamic FPD images enabled us to easily detect bone edges.

Finally, in order to determine 3D pose of the subject's knee model from a FPD image, a robust feature-based 2D/3D registration method which use 2D knee contours images and 3D bone models was developed. The basic principle of a feature-based 2D/3D registration algorithm is that the 3D pose of a model can be determined by projecting rays from contour points in an image back to the X-ray focus and noting that all of these rays are tangential to the model surface. Therefore, 3D poses are estimated by minimizing the sum of Euclidean distances between all projected rays and the model surface. In addition, for robust registration, we introduced robust statistics into this 3D pose estimation method in order to perform accurate 2D/3D registration even if spurious edges and noises exist in the knee images. This robust estimation method employs a weight function to reduce the influence of spurious edges and noises. The weight function is defined for each contour point, and optimization is performed after the weight function is multiplied to a cost function.

In order to validate the accuracy of pose estimation for the knee bone using present 2D/3D registration method, phantom experiments were performed. Since the knee phantom used was rigidly fixed between femur and tibia/fibula, each relative pose vale can be used as gold standard value. Therefore, relative values between femur and tibia/fibula model created from CT images were used to determine poses for comparison with the estimations. X-ray images of the knee phantom were then taken in 10 different poses under the clinical condition. Experimental accuracy was assessed by comparing the estimated relative pose with the relative pose as determined by 3D model created from CT images.

We finally applied present method to 3D measurement of normal knee kinematics under clinical conditions. Six healthy male subjects, averaging 31 years (24–36), 170 cm (165–174), and 65 kg (57–80) were analyzed using the method. All subjects gave informed consent to participate in this study, and the study has been approved by an institutional research review board. Each subject subsequently performed weight-bearing squatting motion from full extension to full flexion in front of the FPD. For in vivo

kinematic analysis, the relative pose of the femur with respect to tibia/fibura was determined by employing a three-axis Euler-angle system. In addition, the medial and lateral condylar contact positions of the femur on the tibia were computed as the minimum point between femur and tibia surface of both condyles for each flexion angle.

Results

The results of phantom experiments showed the relative poses errors (RMS errors) of femur with respect to tibia/fibura were average 0.57 mm and 0.94 deg except for medial–lateral translation error.

In the results of normal knee squatting motion for clinical applications, Fig. 1 visualizes the sequential movement of femur and tibia/fibura models at arbitrary frames. The femur exhibited average 21.0° of external rotation relative to tibia during knee flexion (average from −2.8° of full extension to 146.6° of full flexion). Then, the contact position of both condyles sifted posteriorly average 13.4 mm medially and 24.6 mm laterally, respectively. As shown in Fig. 2, from full extension to about 120° of flexion, the contact positions showed a medial pivot pattern.

Conclusion

This study presented a procedure and the accuracy for accurate 3D measurement of normal knee kinematics using dynamic FPD images, and finally performed clinical applications. Utilizing the dynamic FPD images and preset robust 2D/3D registration, 3D determination of normal knee kinematics was successfully performed, and the pose estimation accuracy was found to be sufficient for analyzing normal knee kinematics of femur and tibia/fibula.

In the result of clinical applications, normal knee in squatting motion experienced femoral external rotations and a medial pivot pattern during flexion, and these measurement values were clinically similar to the previous reports.

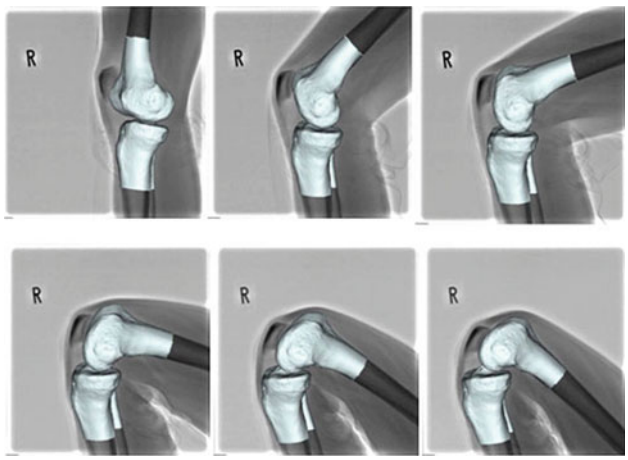

Fig. 1 Visualization of the sequential movement of femur and tibia/fibura models at arbitrary frames

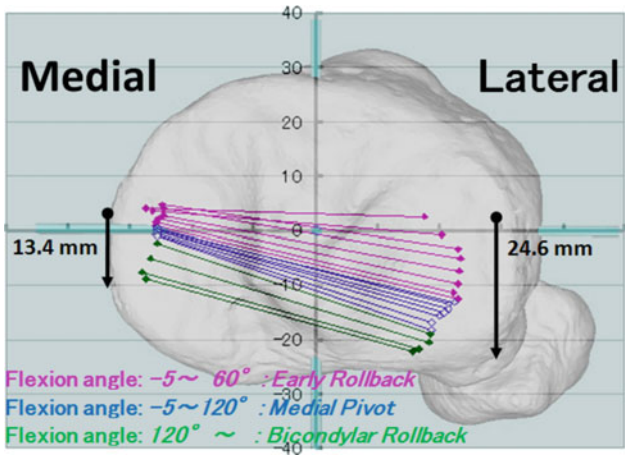

Fig. 2 Medial and lateral condylar contact positions of the femur on the tibia

Navigated needle insertion using a robotic aiming device: preliminary phantom evaluation

T. Shinaji[1], G. Toporek[2], D. Wallach[2], J. Kettenbach[3], S. Weber[2], H. Haneishi[4]

[1]Chiba University, Graduate School of Engineering, Chiba, Japan
[2]University of Bern, ARTORG Center for Biomedical Engineering Research, Bern, Switzerland
[3]University Hospital Inselspital Bern, Department of Diagnostic, Interventional and Pediatric Radiology, Bern, Switzerland
[4]Chiba University, Research Center for Frontier Medical Engineering, Chiba, Japan

Keywords Navigation system · Interventional radiology · Robotic arm · Automatic alignment

Purpose

Interventional radiology provides image-guided, minimally invasive solutions to diagnose and treat various diseases. Such procedures are typically performed percutaneously based on structural volumetric datasets such as computed tomography (CT) data, and require the interventional radiologist to accurately place a needle (biopsy needle, ablation applicator, …) into the patient's body while avoiding organs at risk and important vessels.

To provide accurate needle placement, a navigation system for interventional radiology procedures (CAS-One IR, CAScination, Bern, Switzerland) has been developed and integrated with a robotic aiming device (iSYS Medizintechnik GmbH, Kitzbühel, Austria) [1].

To achieve integration, the robotic aiming device had to be calibrated in the coordinate system of navigation system. We built a formula expressing the position of the robot's center of rotation and the orientation of its displacement axes in the coordinate system of the navigation system. Finally, automatic alignment errors achieved on a static phantom were measured.

Methods

1. Navigation system

The navigation system consists of an optical position measurement system (NDI Vicra, Northern Digital, Canada) and a set of custom-made marker shields with retro-reflective passive markers attached to the needle shaft. Automatic patient-to-image registration and patient tracking is achieved using a set of retro-reflective single marker (SM) spheres glued on the patient's skin prior to the CT acquisition and automatically detected in the CT image.

A planning module enables the physician to plan one or several needle trajectories on the CT image. A marker shield is then screwed onto the needle shaft, and the needle is placed into a needle guide attached to the robotic arm.

2. Robotic aiming device

The robotic aiming device (Fig. 1a) is composed of an upper module and a lower module, each moving laterally and longitudinally. It is attached to a carbon plate through an articulated arm with 6° of freedom. Large-scale motions are achieved by manually moving the articulated arm. Small-scale translations are achieved by moving the upper module together with the lower module, while small-scale rotations are achieved by moving only the upper module.

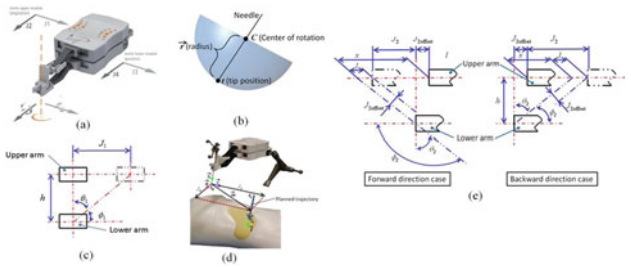

Fig. 1 Schematic diagrams used for calibration. **a** Joint coordinates of the robotic aiming device. **b** Schematic diagram of the center of rotation calibration. **c** Schematic diagram of J_1 alignment. **d** Schematic diagram of J_3 and J_4 alignment. **e** Schematic diagram of J_2 alignment

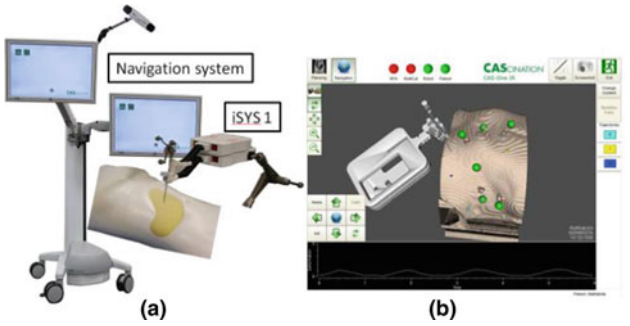

Fig. 2 Results of the integration. **a** Overview of the integration. **b** Graphical user interface for operating the robotic aiming device within the navigation system

At the beginning of the insertion, the physician manually sets the position of the articulated arm so that the planned trajectory is within the working space of the robotic aiming device. This is done with the help of a visual feedback displayed by the navigation system. The robot then automatically refines the orientation and position of the needle. The physician performs the final insertion manually by pushing the needle along the needle guide of the robot, until the navigation system informs him that the desired depth has been reached.

3. Calibration of the robotic aiming device

The robotic aiming device has 4 joint coordinates (Fig. 1a): J_1 and J_2 denote the lateral and longitudinal displacement of the upper module relative to the lower module, while J_3 and J_4 denote the lateral and longitudinal displacement of the two modules together.

Instructions to the robotic aiming device need to be given in terms of J_1, J_2, J_3 and J_4 values, while the navigation system provides information about the position of the needle tip position and needle shaft orientation only. In order to achieve automatic needle positioning, it is thus necessary to perform a calibration step relating the two coordinate systems.

Center of rotation

The position of the center of rotation of the aiming device is calculated by performing several small-scale rotations: several positions of the needle tip are thus detected by the navigation system, all satisfying the equation

$$(t_i - c) \cdot (t_i - c)^T - r^2 = 0, \tag{1}$$

where $\boldsymbol{t_i}$ is the needle tip position $\boldsymbol{i}$, and $\boldsymbol{c}$ and r are the center and radius of rotation, respectively Fig. 1b. The optimal values of $\boldsymbol{c}$ and r are obtained using Nelder-Mead method [2, 3].

Displacement axes

According to Fig. 1c:

$$J_1 = \begin{cases} -h \cdot \tan\theta_1 v, (\phi_1 \leq \pi/2) \\ h \cdot \tan\theta_1 v, (\phi_1 > \pi/2) \end{cases} \tag{2}$$

where h is the known distance between the upper and lower modules, and the angles
θ_1 and ϕ_1 are given by the navigation system. The unit vector v is as shown in Fig. 1d.
According to Fig. 1e:

$$J_2 = \begin{cases} -x - \frac{J_{2offet}}{\cos\theta_2} + J_{2offet}, (\phi_2 \leq \pi/2) \\ x - \frac{J_{2offet}}{\cos\theta_2} + J_{2offet}, (\phi_2 > \pi/2) \end{cases} \tag{3}$$

where x and $J_{2\text{offset}}$ are known from the robotic aiming device geometry, and the angles θ_2 and ϕ_2 are given by the navigation system. The unit vector u is as shown in Fig. 1d.

Finally, according to Fig. 1d:

$$\begin{cases} J_3 = m \cdot v \\ J_4 = m \cdot u \end{cases} \tag{4}$$

where $\boldsymbol{m}$, the vector from the tip of the needle to the planned entry point, is given by the navigation system.

4. Evaluation

20 Navigated punctures were performed on a non-rigid, anthropomorphic phantom. For each puncture, the Euclidean error between the planned and the achieved needle tip position was calculated by the system in the patient coordinate system. The fiducial registration error (FRE) of the automatic patient-to-image registration was also measured.

Results

It was possible to integrate robotic aiming device with an optical navigation system (Fig. 2).

The phantom was registered automatically with its CT dataset with an FRE of 0.6 mm ± 0.1 mm. Then, after roughly positioning the robot by manually moving the articulated arm, it was possible to automatically adjust the needle orientation along the planned trajectories. The resulting alignment error was 1.2 mm ± 0.2 mm.

Conclusion

Preliminary results indicate the feasibility of robotic, navigated needle orientation adjustment.

The average accuracy of the alignment was 1.2 ± 0.2 mm. However, since the robotic aiming device only positions the needle along the correct trajectory and does not insert it, the physician can manually correct this error using the graphical user interface of the navigation system,

On-going work aims at improving the automatic alignment accuracy using visual servoing.

References

[1] Wallach D, Toporek G, Weber S, Bale R and Widmann G. Comparison of free-hand navigated and aiming device navigated targeting of liver lesions. The International Journal of Medical Robotics and Computer Assisted Surgery. 2012 (major review);
[2] B. J. A. Nelder and R. Meadf, "A simplex method for function minimization," The Computer Journal, vol. 7, no. 4, pp. 308–313, 1965.
[3] R. S. Society and A. Statistics, "Algorithm AS 47 Function Minimization using a Simplex Procedure," Journal of the Royal Statistical Society. Series C (Applied Statistics), vol. 20, no. 3, pp. 338–345, 1971.

Percutaneous lung biopsy: comparison between an augmented reality CT navigation system and standard CT-guided technique

R.L. Cazzato[1], R.F. Grasso[1], E. Faiella[1], G. Luppi[1], E. Schena[1], F. Giurazza[1], R. Del Vescovo[1], F. D'Agostino[1], B. Beomonte Zobel[1]
[1]University Campus Bio-Medico of Rome, Diagnostic Imaging and Interventional Radiology, Rome, Italy

Keywords Lung biopsy · CT scan · Virtual navigation guidance · Optical tracking

Purpose

In the present paper, we evaluate a new optical-based navigation system (SIRIO, MASMEC S.p.A., Modugno, BA, Italy. http://www.masmec.org/) while performing percutaneous lung biopsies (PLBs).

The system allows optical tracking of devices used during the procedure and their real-time visualization in a model obtained from a data set of previously acquired CT images.

Methods

Patients with the following clinical features were included in the present study: pulmonary solid lesions or ground-glass opacities suspected to be malignant; no evidence of endo-bronchial disease; non-diagnosing bronchoscopy; unsuitability for ultra-sonographic guidance; good patient compliance (e.g., ability to lie in a given position or to hold the breath for a few seconds). There were no lesion size limits. Exclusion criteria were: contraindications for percutaneous interventions (e.g., abnormal coagulation) or a refusal to provide written informed consent.

SIRIO-guided PLBs were performed in 197 patients (121 male, 76 female, mean age 66.8 ± 12 years). Standard CT-guided PLBs were performed in 72 patients (48 males, 24 females, 69.1 ± 10 years). Mean lesions size in patients undergoing SIRIO-guided PLBs was 32.1 mm (±18 mm); mean size of pulmonary lesions in patients undergoing standard CT-guided PLBs was 29.2 mm (± 18 mm). Lesions distribution among different pulmonary lobes was evaluated in both groups.

Local Institutional Review Board approved this nonrandomized retrospective study; all the enrolled patients gave their written informed consent.

Procedure

All procedures were performed with a 64-MDCT (Somaton Sensation 64, Siemens, Forchheim, Germany) with the following exposure parameters: 140 kV, 110 mAs, 1 mm slice thickness. Preliminary imaging limited to the target region was obtained.

All patients underwent cytological (20GChibaneedle) and histological (18G, semi-automatic tru-cut biopsy needle) sampling with a coaxial technique. Procedures were performed under local anaesthesia and mild sedation.

SIRIO-guided PLBs

SIRIO is an intra-operative guiding system that reconstructs a 3D model from a data set of previously acquired CT images (DICOM) by means of a semiautomatic algorithm. The 3D model of the patient's chest is obtained by means of a proprietary reconstruction algorithm. The 3D model is spatially bounded to the real patient's chest through an automatic calibration procedure that uses as reference a tool previously placed on patient's chest. During the procedure, two planar projections (axial and sagittal) are shown; they are dynamically calculated from the 3D model and updated on the screen available in the operating room (Fig. 1), in accordance with the current needle position and orientation.

Following the pathway showed by SIRIO, the operator can insert the needle into the chest and advance it to the target lesion with a 2 % estimated accuracy. Once the lesion is reached, the bioptical process continues in the same way for both types of procedures. SIRIO can cope with patients' breathing and patients changing their posture.

Standard CT-guided procedures

Spatial orientation was obtained by the CT gantry laser line for the axial plane and by a row of needles positioned on the patient's chest to mark the sagittal plane. Once the best pathway was chosen, the physician advanced the needle in small steps. For each advancement re-imaging was performed to assess the new needle position.

Data collection

Lesions size and distribution among pulmonary lobes were evaluated in both groups by means of Student'sttest.

Both groups were also tested (Student'sttest) in terms of: number of CT scans, patient radiation exposure (Effective Radiation Dose = TDLP × conversion factor k; 0.017 mSv × mGy − 1 × cm − 1)[Office for Official Publications of the European Communities (1999) European guidelines on quality criteria for computed tomography, Luxembourg] and total procedure time. Complications (pneumothorax and haemorrhage) rates were also tested in both groups.

Results

There were no significant difference between lesions distribution in pulmonary lobes among the two groups (p NS). CT scans were 5.9 ± 2.4 for SIRIO-guided PLBs versus 10.3 ± 4.1 for standard CT-guided PLBs.

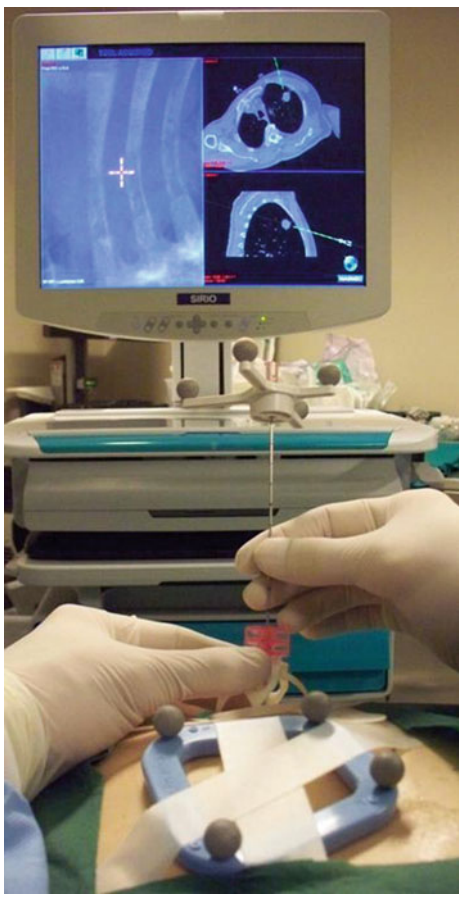

Fig. 1 Operator performing PLB and monitoring the needle advancement inside the patient's chest through SIRIO real-time tracking system

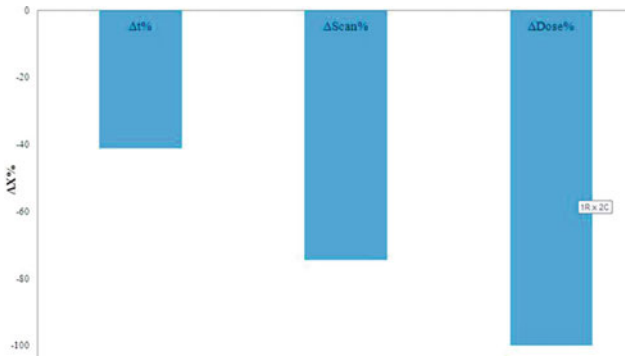

Fig. 2 Percentage differences (ΔX %) for each variable (time, number of CT scans and radiation dose to patients, left, middle and right column, respectively)

Procedural time with SIRIO decreased about 41 %, the number of CT scans about 74 % and radiation dose administered to patients was halved (Fig. 2).

The overall PNX rate was significantly lower with SIRIO than in the group undergoing standard CT-guided PLBs (9.1 vs 16.7 %,p).

Discussion

PLB is a well-established technique to diagnose pulmonary lesions of unknown origin. Performing such procedure needs imaging guidance with CT, CT-fluoroscopy and C-arm cone beam CT (CBCT) being the most popular. CT lacks a real-time control of the needle path and administers a high radiation burden to patients. On the contrary, CT-fluoroscopy and CBCT provide high spatial resolution and real-time control of the needle path even thought they raise concerns due to high radiation burden both to patients and operators [Jin KN, Park CM, Goo JM, Lee HJ, Lee Y, Kim JI, Choi SY, Kim HC (2010) Initial experience of percutaneous trans-thoracic needle biopsy of lung nodules using C-arm cone-beam CT systems. Eur Radiol 20(9):2108–2115].

Promising results may come from new guidance systems aiming at augmenting reality in a virtual environment. These tools have been recently introduced in different surgical settings. However, no complete results are available regarding the specific setting of our study (PLBs under an optical-based navigation system combined with CT-guidance) since, most studies were carried out on small and heterogeneous cohorts of patients [Wallace MJ, Gupta S, Hicks ME (2009) Out-of-plane computed tomography-guided biopsy using a magnetic-field-based navigation system. Cardiovasc Intervent Radiol 29(1):108–113].

In the present study, we presented our experience with an optically-based navigation system while performing PLBs. The system proved to be reliable and effective in reducing number of CT scan, radiation dose to patient and procedu1ral time.

Theoretical and experimental assessment of temperature distribution on pancreas during Laser Interstitial Thermotherapy (LITT)

F. Giurazza[1], E. Schena[2], P. Saccomandi[2], R. Del Vescovo[3], R.L. Cazzato[3], F. Panzera[1], M. Martino[1], F.M. Di Matteo[1], F.R. Grasso[3], B.B. Zobel[3]
[1]Università Campus Bio-Medico di Roma, Endoscopy, Rome, Italy
[2]Università Campus Bio-Medico di Roma, Engineering, Rome, Italy
[3]Università Campus Bio-Medico di Roma, Radiology, Rome, Italy

Keywords Litt · Pancreas · Cancer · Tumor ablation

Purpose

During LITT, hyperthermia due to laser-tissue interaction allows to remove neoplasias. The outcome is strongly influenced by tissue temperature (T).High mortality of pancreatic cancer encouraged us to study the chance to introduce LITT in this field. Correlation between laser settings (LS) and ablation volume was investigated in a previous study onex-vivoporcine pancreas. The aim of this study is the development of a theoretical model to predict T map in pancreas undergone LITT to choose the optimal LS. Simulations were experimentally validated by measuring T.

Methods

T was theoretically predicted and measured during both heating and cooling phases (when laser emission was stopped) at laser energy of 1500 J, two powers ($p = 3$ W and 5 W) and two treatment times (500 s and 300 s). Laser-tissue interaction was modeled by bioheat equation and simulated in Comsol Multiphysics environment [1]:

$$\rho * c\Delta T\ (x, y, z, t)/\Delta t = (kT(x, y, z, t)) + Q_l - Q_{el}$$

where ρ, c, and k are tissue density, specific heat and conductivity; Q_l and Q_e are density powers due to photon absorption in tissue and water evaporation.

Ex-vivopancreas T undergone LITT (Nd:YAG laser, $\lambda = 1064$ nm) was measured in 4 points around the applicator by fiber Bragg grating sensors (FBG) placed 1 mm upward and 1 mm downward the applicator, at distances (d) of 2 mm and 5 mm. FBG output was monitored by an optical spectrum analyzer. A thermistor was used to measure T before treatment (Fig. 1).

Results

Simulations agree with experiments (Fig. 2): (1) the highest temperature rise (ΔT_{max}) decreases with d (e.g., 67 °C at 2 mm vs 40 °C at 5 mm at 5 W); (2) ΔT_{max} increases with P (e.g., 67 °C at 5 W vs 27 °C at 3 W); 3) the highest ΔT_{max} happens downward the applicator.

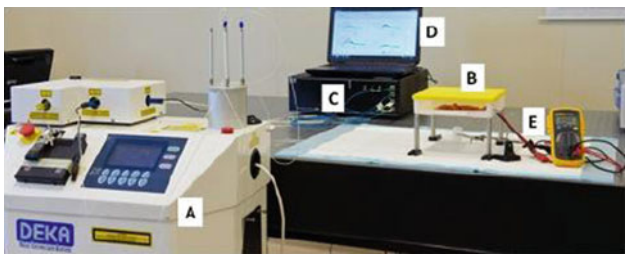

Fig. 1 Experimental set up to monitor T during LITT: **a** Nd: YAG laser, **b** mask containing pancreas, **c** optical spectrum analyzer, **d** pc for data collection, **e** NTC thermistor and multimeter

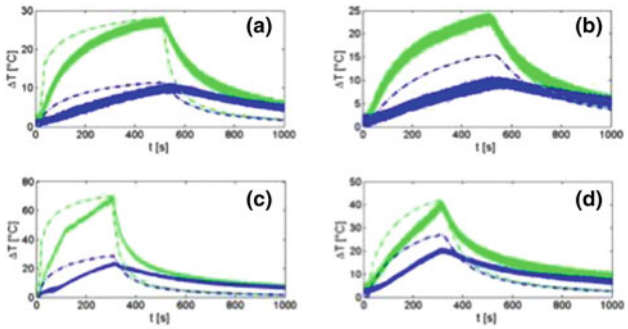

Fig. 2 Theoretical (*dashed*) and experimental (*continuous*) T upward (*blue*) and downward (*green*) the applicator at $p = 3$ W: **a** d = 2 mm; **b** d = 5 mm and at 5 W: **c** d = 2 mm; **d** d = 5 mm

Percentage variation of ΔT_{max} with d was calculated:

$$\Delta T_{max}\%(5mm - 2mm) = 100 * T_{max}(2mm) - T_{max}(5mm)/T_{max}(2mm)\,2$$

$\Delta T_{max}\%$ is -22% at 3W and -40% at 5W

Conclusion

1. ΔT_{max} increases with P and decreases with d;
2. The good agreement between theoretical data and experimental one indicates that the model should be useful to estimate T and could be a suitable tool to choose the optimal LS to produce a controlled ablated volume [2].

References

[1] Pennes HH (1948) Analysis of tissue and arterial blood temperature in the resting human forearm. Journal of Applied Physiology 1, 93–122

[2] Saccomandi P, Schena E, Caponero MA, Di Matteo FM, Martino M, Pandolfi M and Silvestri S (2012) Theoretical Analysis and Experimental Evaluation of Laser-Induced Interstitial Thermotherapy in Ex Vivo Porcine Pancreas IEEE Trans. Biomed. Eng. 59 2958–64

Assessment of laser power influence on ablation volume during laser-induced thermotherapy in ex vivo swine livers: a preliminary study

F. Giurazza[1], R. Del Vescovo[1], E. Schena[2], P. Saccomandi[2], L. Mortato[1], R.L. Cazzato[1], F.M. Di Matteo[3], F.R. Grasso[1], B.B. Zobel[1]

[1]Università Campus Bio-Medico di Roma, Dept. of Radiology, Rome, Italy

[2]Università Campus Bio-Medico di Roma, Dept. of Engineering, Rome, Italy

[3]Università Campus Bio-Medico di Roma, Dept. of Endoscopy, Rome, Italy

Keywords LITT · CT scan · Liver · Post-processing imaging

Purpose

Laser induced thermotherapy (LITT) is a minimally invasive technique used to destroy neoplastic masses in organs [1]. Laser settings play a crucial role in the outcome of LITT, since laser power (P), laser energy (E) and treatment time (t) influence the amount of the ablated volume [2]. The aim of this work is twofold: the estimation of ablated volumes (V) in ex vivo swine livers by Computed Tomography (CT) scan and the assessment of laser settings influence on V.

Methods

Nine ex vivo healthy swine livers have undergone LITT at three different lasers settings:

- $P = 1.5\,W,\ t = 210\,s,\ E = 315\,J$
- $P = 3\,W,\ t = 210\,s,\ E = 630\,J$
- $P = 5\,W,\ t = 210\,s,\ E = 1,050\,J$

We used an Nd: YAG laser in continuous mode with a wavelength of 1,064 nm. Its radiation was conveyed in a bare-fiber applicator with 300 μm core diameter.

We treated three livers for each setting, in order to assess the influence of P and E on V with a constant t.

The V estimation has been performed by CT scan imaging acquisition (Siemens® Somatom 64-slices) at 150 mAs, 120 kVp and 0.6 mm slices in spiral mode (Fig. 1).

The post-processing images software used to measure V was Osirix (Apple Inc.®, Cupertino California USA); three-dimensional representation of the induced lesions have been obtained and volumes have been semi-automatically computed (Fig. 2).

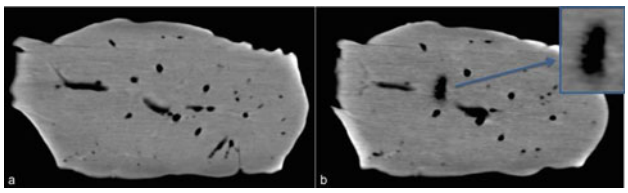

Fig. 1 CT scans of swine liver before (**a**) and after (**b**) LITT at 3 W; in **b** is shown also the detail of the ablated volume (*arrow*)

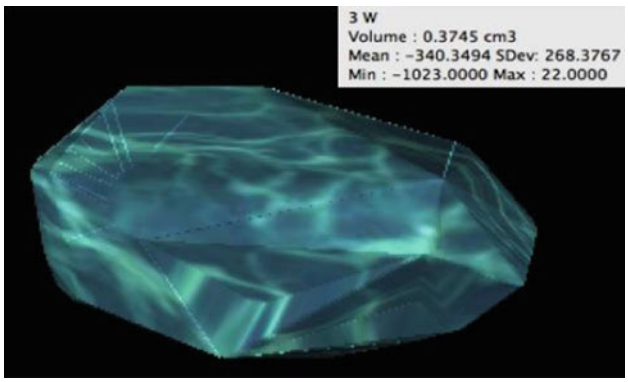

Fig. 2 Three dimensional post-processing image reconstruction of the ablated volume shown in Fig. 1; in the box are reported the volume dimension and the HU units values in terms of mean, standard deviation, minimum and maximum measurements

Results

In all the three livers treated at 1.5 W, no visible ablated V were detectable on CT images. On the other hand, ablated V were appreciated in all the six livers treated at 3 W and 5 W. The mean values of V calculated by images post-processing were 0.36 and 0.47 cm^3 at 3 and 5 W respectively. As expected, an increase of laser power causes an increase of ablated volume: the percentage increase changing P from 3 to 5 W is about 30 %. On CT scans the liver parenchima around the ablated tissue within 20 mm of distance from the core of the volume appeared hypodense suggesting a damage induced by the hyperthermia reached during the treatment; instead, at more than 20 mm, no significant morphological changes were appreciable. The volumes ablated assumed always an ellipsoidal shape.

Conclusion

Results, in terms of ablated volume in ex vivo swine livers undergoing LITT, were assessed at different lasers settings. They show absence of ablated volume at low power (1.5 W); a consistent and non linear increase of ablated volume is related to an increase of laser power as demonstrated during treatment at 3 and 5 W [3]. CT scan seems to be a valuable option to analyze the damages induced by hyperthermia during LITT in terms of shape and size of the ablated volume and of density modification of the circumstant tissues. These preliminary results could be useful to choose the optimal laser settings in order to obtain a complete and controlled removal of tumor volume and reduce the thermal damage of healthy surrounding tissues.

References

[1] Müller G, Roggan A ed. (1995) Laser-Induced Interstitial Thermotherapy, 1st edn (Washington USA: SPIE Optical Engineering Press)

[2] Saccomandi P, Schena E, Caponero M A, Di Matteo F M, Martino M, Pandolfi M and Silvestri S (2012) Theoretical Analysis and Experimental Evaluation of Laser-Induced

Interstitial Thermotherapy in Ex Vivo Porcine Pancreas IEEE Trans. Biomed. Eng. 59 2958–64
[3] Saccomandi P, Schena E, Di Matteo F M, Pandolfi M, Martino M, Rea R and Silvestri S (2011) Laser interstitial thermotherapy for pancreatic tumor ablation: Theoretical model and experimental validation Proc. 33rd Annu. Int. Conf. IEEE Eng. Med. Biol. Soc. (Boston, MA) 5585–8

Steerable needle with an actuated tip

K. Henken[1], J. Dankelman[1], J.J. van den Dobbelsteen[1]
[1]Delft University of Technology, Biomechanical Engineering, Delft, Netherlands

Keywords Steerable · Needle · Tissue model · Validation

Purpose

In many needle interventions, target accuracy is essential for the success of the treatment. However, positioning of the needle is complicated by uncontrolled deflection of the needle caused by asymmetries of the needle and inhomogeneities of the tissue. An actively steerable needle enables the clinician to control the direction of the needle during insertion, which may allow for higher target accuracy. Such a needle can also reach areas that cannot be reached with a straight needle, because other structures are blocking the way. We developed a needle that can actively be steered by means of an actuated tip. The tip is bendable and is actuated with cables, but it is stiff in axial direction. The path of such a needle can be adjusted at any time during insertion and does not require rotation of the needle. This research aims to evaluate the feasibility of needle steering by means of such an actuated tip.

Methods

Design of the steerable needle

The prototype consists of an actively steerable tip and a compliant shaft that passively follows the tip (Fig. 1). The steerable tip consists of stainless steel hinges produced by laser cutting and a conical stainless steel tip. The hinges together have a total length of 8.0 mm and the maximal steering angle is approximately 7°, in which the steering angle is defined as the orientation of the tip with respect to the direction of insertion. The shaft is a flexible PEEK tube with an inner and outer diameter of 1.5 and 2.0 mm, respectively. A ring of steering cables is positioned in the shaft and connected at the very end of the tip. The tip is actuated by pulling the cables to one side which forces the tip to bend in that direction. A core cable is added in the middle to fill up the tube and keep the steering cables in place.

Experimental set-up

The prototype is tested by applying a fixed steering angle to the needle tip and inserting it in an ex vivo model that consists of a porcine liver lobe embedded in gel. During insertion, the needle tip is tracked with ultrasound. First the needle is inserted approximately 2 cm into the model. Then a fixed steering angle of 0°, 1°, 2° or 3° to the right is applied to the tip of the needle and the needle is further inserted into the model.

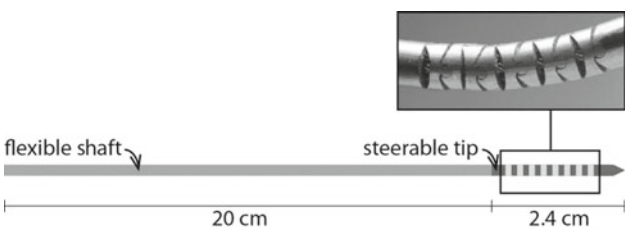

Fig. 1 Schematic view of the needle. The needle consists of a passively compliant shaft and an actively steerable tip. Actuation of the steerable tip is provided by a ring of steering cables that run through the shaft and are attached to the tip

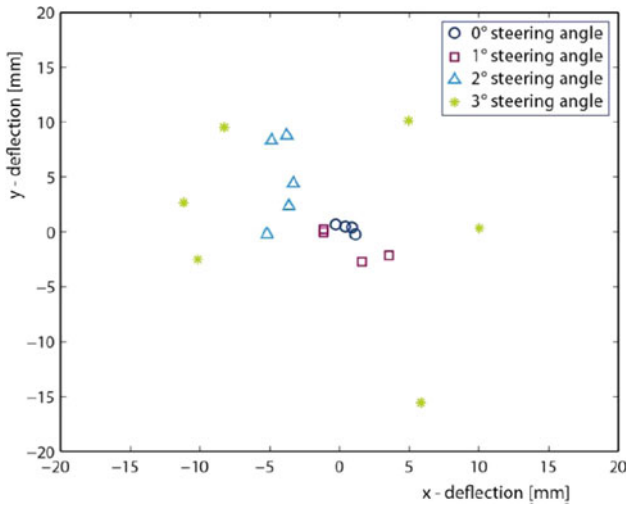

Fig. 2 Deflection of the needle in x-direction and y-direction at an insertion depth of 40 mm. Although the degree of deflection is related to the steering angle, the direction of bending was not controllable in this needle

Results

Figure 2 shows the positions in x- and y-direction of the needle tip at an insertion depth of 40 mm for each experiment (the needle is inserted in the z-direction through the origin). When the needle tip was straight, the path of the needle during insertion was almost straight as well. Actuating the needle tip in the x-direction results in sideway deflections in x- and y-direction of the needle during insertion. When a steering angle of 0°, 1°, 2°, and 3° is applied to the tip, the ranges of needle deflection were 0.58–1.2 mm, 1.1–4.1 mm, 4.3–9.6 mm, and 10–17 mm, respectively, but the direction of deflection was unpredictable. The needle tip was expected to follow a path that was in the direction of the steering angle (only deflections in positive x-direction), but the actual direction differed in each measurement. This effect is especially present when a large steering angle was applied to the actuated tip. Potentially the force that is required to puncture (parts of) the tissue are too high for the flexible needle to withstand. Increasing the stiffness of the needle and sharpening the tip may resolve this. Twisting of the actuation cables and friction between the cables may also have contributed to the incontrollable steering.

Conclusion

The steerability of a needle with an actuated tip is evaluated. The resulting deflection is related to the steering angle that is applied to the tip, but the direction is still uncontrollable. An improved prototype will be developed with a stiffer shaft and a sharper tip that allows for higher puncture forces. The steering cables will be placed in channels to avoid twisting. Future research will also include the development of an intuitive handle and functionalizing the design for a specific treatment.

Comparison of data acquisition strategies for tomographic reconstruction with an ortho-panoramic system

I. Frosio[1], D. Bianconi[2], N.A. Borghese[1]
[1]University of Milan, Computer Science Dept., Milan, Italy
[2]Cefla SC, Imola (Bo), Italy

Keywords Ortho-panoramic system · Local tomography · Time delay integration · Data acquisition

Purpose

Modern ortho-panoramic systems are sufficiently versatile to allow the acquisition of projection data from different orientations and points of view. Such images can be for local tomographic reconstruction that is suitable to clinical investigation [1]. The most adequate trajectory to acquire such different projection images has been investigated here. In particular two trajectories are examined. In the first, the X-ray tube is maintained still while the sensor rotates around it, achieving in this manner a Cone-Beam (CB) like trajectory. In the second modality, a parallel translation of the sensor and of the tube is used to acquire projections with a Fan-Beam (FB) like geometry. The pros and cons of these two trajectories are analyzed under different points of view. More in detail, for both of them, we have evaluated through simulations the following aspects: quality of the reconstructed volume, acquisition time and dose, feasibility of the trajectory with respect to mechanical constraints of the apparatus.

Methods

To compare the CB/FB-like trajectories, we simulated a set of projections, using the parameters of a commercial ortho-panoramic system (Hyperion by MyRay [2]). 11 projections taken from −20° to +20° were simulated with a source to image distance of 550 mm. We have simulated a Time Delay Integration (TDI) sensor of 1,536 × 64 pixels of size 0.096 mm. At 383 mm from the emitter, the aperture of the useful radiation cone was 40 mm. The reconstructed volume was composed of 50 × 267 × 704 anisotropic voxels of size 1 mm × 0.15 mm × 0.15 mm. Each projection was composed of 1,536 × 598 pixels, at 12 bpp, for both CB ad FB trajectories.

The absorbent objects used in simulations were ellipsoids (whose projection was analytically computed) resembling three teeth inside the jaw. An additional ellipsoid represented the nerve channel. In simulation #1, objects lied completely inside the reconstructed volume, to avoid the introduction of glaring and band artifacts [3]. This allows comparing the quality of the volumes reconstructed with the two acquisition trajectories independently from truncation artifacts. In simulation #2 additional ellipsoids were added to simulate the cranial structure, the condyle and the teeth outside the reconstructed volume. This situation is coherent with the real setup and it adds glaring and band artifacts inside the reconstructed volume.

Volume reconstruction was performed with the Simultaneous Algebraic Reconstruction Technique (SART), stopping it after 5 iterations to avoid noise amplification [4].

To obtain a CB-like geometry, the X-ray source does not move and the linear sensor covers an arch centered in the source. The charges are shifted backwards inside the sensor at a frequency related to the motion speed (Fig. 1). The focus of the projection is in this case stationary, coincident with the emitter-ray tube.

To obtain a FB-like geometry, the X-ray source translates parallel to the sensor on a straight path while the charges inside the sensor shift backwards at frequency related to the motion speed (Fig. 1). The focus of the projection in the horizontal plane is in this case at infinity while in the vertical plane is coincident with the X-ray tube.

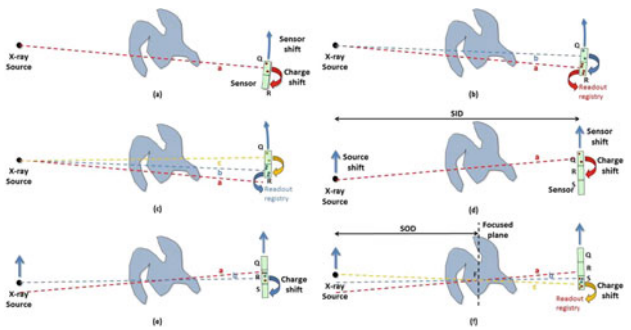

Fig. 1 Panels (**a–c**) and (**d–f**) show respectively the acquisition of a CB and FB like projection

Table 1 Volume quality indexes computed in simulations

Simulation	Volume	Trajectory	MI [bit]	UC	ρ	RMSE [mm^{-1}]
#1	Full	CB	0.2043	0.7655	0.6674	0.0032
#1	Full	FB	0.2047	0.7655	0.6282	0.0032
#2	Full	CB	0.5399	0.4684	0.5346	0.0057
#2	Full	FB	0.5578	0.4811	0.5510	0.0056
#2	Central	CB	0.4987	0.5973	0.5984	0.0072
#2	Central	FB	0.5080	0.6080	0.6004	0.0072

To evaluate the quality of the reconstructed volumes, we employed the Root Mean Squared Error (RMSE), the Mutual Information (MI), the Uncertainty Coefficient (UC) and the Spearman's Correlation Index (ρ) computed between the ground true and the reconstructed volumes. The last three indexes were chosen because, differently from RMSE, they are poorly affected by a bias or a scaling of the estimated absorption coefficients. This is in fact not important considering that the volume slices are generally stretched before they are visualized on a display. Finally, in simulation #2, the indexes were computed both on the entire volumes and only in their central portion where glaring and band artifacts were not present.

Results

Table 1 shows the quality indexes computed in simulations #1 and #2. For Simulation #1, all the quality indices are similar for the two acquisition strategies. ρ is higher for the CB-like trajectory, but, as it is the only index and visual inspection of the reconstructed slices does not reveal any significant difference between the volumes reconstructed from CB-like or FB-like trajectory, the difference cannot be considered meaningful. In simulation #2 all the indices assign a better quality to FB-like trajectory, when the entire volume is considered, but the difference becomes negligible when only the central portion of the volume is considered. The slightly lower quality for CB-like data can be explained by the larger extension of the band/glaring artifacts in CB-like trajectory with respect to FB-like trajectory.

By a theoretical point of view, acquisition time (and consequently the dose) resulted comparable for CB and FB trajectories. However, two different types of motion of the arm supporting the X-ray tube and the sensor are implemented, rotational for CB-like trajectory and translational for FB-like trajectory. As a consequence, the apparatus movement is very different for the two trajectories and the possible collision of the machine with the patient or with external structures may pose different constraints on the two trajectories.

Conclusion

CB-like and FB-like trajectories are comparable in terms of quality of the reconstructed volume. Reconstruction performed with CB-like trajectories achieve a slightly lower quality due to the higher extension of the bands and glaring artifacts associated to limited angle tomography, but these can be corrected as, for instance, in [5]. By a practical point of view, the choice of CB-like or FB-like trajectory has to be performed considering mainly the mechanical constraints of the radiographic apparatus (e.g., maximum linear and angular speed, inertia of the system, maximum positive and negative acceleration).

References

[1] Frosio I, Borghese N (2007) Tomosynthesis through a time delay integration sensor. In: Nuclear Science Symposium Conference Record, 2007. NSS '07. IEEE, vol. 5, pp. 3823–3825
[2] My Ray website, http://www.my-ray.com.
[3] Zhang Y, Chan HP, Sahiner B, Wei J, Ge J, Zhou C, Hadjiiski LM (2009) Artifact reduction methods for truncated projections in iterative breast tomosynthesis reconstruction, J. Comput. Assist. Tomogr., 33(3):426–435.

[4] Kak AC, Slaney M (2001) Principles of Computerized Tomographic Imaging, SIAM.
[5] Frosio I, Borghese NA (Feb. 2013) Local algebraic tomography with artifact correction, submitted to IEEE Trans. Biomed. Imag.

The geometric calibration of an open cone-beam CT system for arbitrary scanning trajectories

F. Stopp[1], A.J. Wieckowski[2], S. Engel[2], F. Fehlhaber[2], M. Käseberg[2], E. Keeve[1,2]
[1]Charité, Universitätsmedizin Berlin, Department of Maxillofacial Surgery and Clinical Navigation, Berlin, Germany
[2]Fraunhofer-Institute for Production Systems and Design Technology IPK, Department of Medical Technology, Berlin, Germany

Keywords Cone-beam CT · Geometric calibration · Scanning trajectory · Acquisition geometry · Volume reconstruction

Purpose

The image quality in cone-beam computed tomography (CT) is directly dependent on the precise knowledge of the projection geometry during image acquisition. Most methods for determination of the geometric parameters (position of the X-ray source focal point and position and orientation of the image plane) are focused on conventional cone-beam CT systems with circular scanning trajectories (e.g., [1]). Because the fixed arrangement of X-ray source to image detector can be disadvantageous in intraoperative use, we develop a first experimental prototype of an open cone-beam CT system for interventional surgery (ORBIT) (Fig. 1a, b). The X-ray source is fixed on a robot-arm and the digital flat-panel detector will be moved by a motorized mechanism directly connected to the patient table. This system concept allows free alignment of X-ray source and detector to the patient and offers new opportunities for non-planar scanning trajectories. Therefore we developed a calibration method to determine the geometric parameters for arbitrary scanning trajectories.

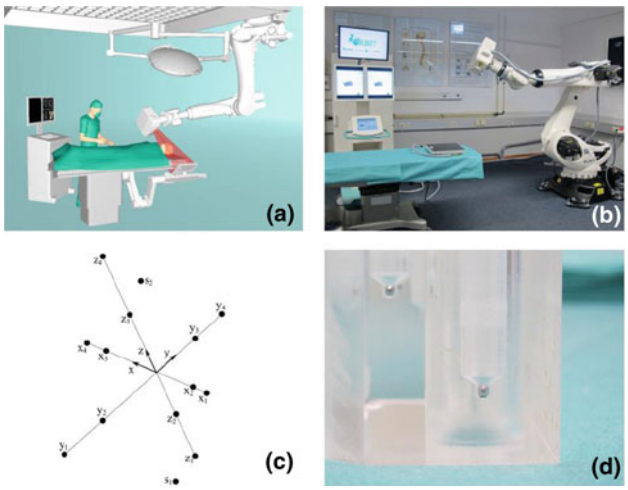

Fig. 1 **a** Open cone-beam CT system ORBIT with an X-ray source fixed on a ceiling mounted robot arm and a robot-guided flat panel detector directly connected with the patient table; **b** Actual prototype of ORBIT using a floor-mounted robot arm (Kuka KR 150 R2700 extra), a pulsed X-ray source (Ziehm Vision R 20 kW) and a currently fixed flat-panel detector (Varian PaxScan 3030+); **c** Model of the 14 steel ball calibration object; **d** Close-up view of the manufactured calibration object

Methods

We enhanced the method proposed in [2] by introducing an asymmetrical marker arrangement and constructed and manufactured a calibration object with 14 steel balls of 3 mm diameter. Four balls lie on each of the three orthogonal axes and two balls on a space diagonal (Fig. 1c, d). Our method incorporates robust marker center detection and geometrical analysis of the projected calibration object independent of occurring overlaps. To obtain and validate the correct marker assignment, we analyze the re-projection errors of a few possible solutions. Afterwards, the resulting marker assignment is used to determine the initial geometric parameter set. By a following non-linear optimization, the resulting geometric parameters are refined to increase the calibration accuracy. Our proposed method can deal with arbitrary directions of projections and there are no restrictions on the used scanning trajectory.

Results

We first simulated a freely defined scanning trajectory (Fig. 2a) by generating artificial projection images of our calibration object with predefined geometric parameters (according to our system set-up characteristics: 298 mm × 298 mm image size with 1,536 × 1,536 pixel and approximately 1,050 mm X-ray source to detector distance). Afterwards we used these artificial projection images to calculate the geometric parameters by means of our calibration method. The differences between the calculated and the predefined real parameters over 100 images are shown in Table 1.

Furthermore we applied our calibration method on the current system prototype set-up. We acquired 360 images of our calibration object by moving the X-ray source circularly above the detector (Fig. 2a). Again, we calculated the geometric parameters of each single image and applied the same scanning trajectory on three vertebral bodies of the lumbar spine. Based on the calculated geometric parameters and the 360 projection images we reconstructed the scanned volume with a simultaneous algebraic reconstruction technique. In Fig. 2b–d the vertebral test bodies and an axial and coronal slice of the reconstructed volume are shown.

Conclusion

The presented errors from the simulation (shown in Table 1) result from the errors in marker center detection of the ball markers in the projection images ($\mu = 0.007$ mm, $\sigma = 0.007$ mm) and the parameter determination with our calibration method. By applying our method on the current system set-up, additional errors influence the resulting calibration accuracy: the repeatability of the X-ray source positioning by the robot-arm and inaccuracies of the manufactured

Table 1 Differences between real and calculated geometric parameters of image center position, image orientation and X-ray source position (N = 100)

	μ	σ	Max
Image center position error [mm]			
x	0.025	0.023	0.138
y	0.029	0.049	0.449
z	0.046	0.058	0.531
Image orientation error (euler angles) [deg]			
α	0.004	0.009	0.089
β	0.003	0.002	0.012
γ	0.002	0.002	0.009
X-ray source position error [mm]			
x	0.209	0.168	0.762
y	0.237	0.349	2.975
z	0.349	0.372	3.132

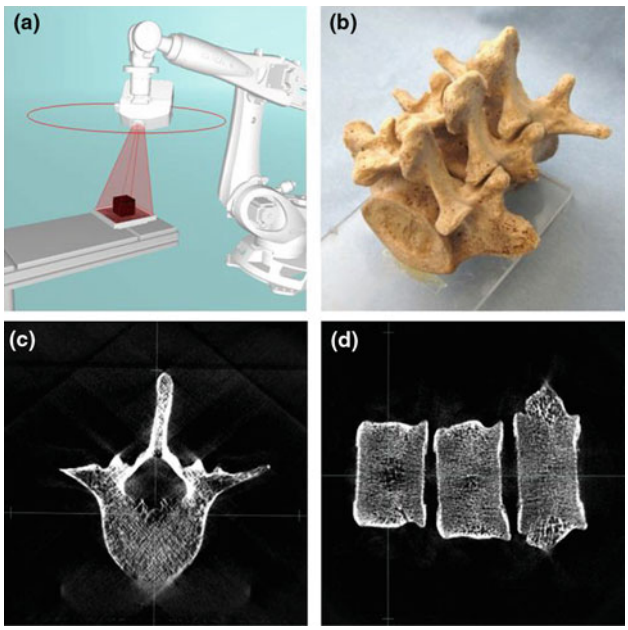

Fig. 2 **a** Executed and calibrated scanning trajectory with a fixed flat-panel detector; **b** Vertebral bodies of the lumbar spine; **c** Axial slice of the reconstructed volume; **d** Coronal slice of the reconstructed volume

calibration object. Errors caused by the movement of the X-ray source during the image acquisition are excluded at the moment, since the image acquisition is currently done in defined fixed positions.

In the first reconstruction result the lower edges of the body and the spinal canal were not reconstructed sufficiently (Fig. 2c). The reason for this is the currently fixed image detector and the limited-angle X-ray source trajectory (Fig. 2a). In further project work we will build up the motorized mechanism to move the flat-panel detector independently to the X-ray source and execute freely definable complete scanning trajectories. To compensate occurring mechanical instabilities, we will perform an additional online calibration method during the image acquisition.

Acknowledgments
This work is funded by the German Federal Ministry of Education and Research (BMBF), research grant 01EZ1115A-C.

References

[1] Cho Y, Moseley DJ, Siewerdsen JH, Jaffray DA, "Accurate technique for complete geometric calibration of cone-beam computed tomography systems," Medical Physics, vol. 32, no. 4, p. 968, 2005.

[2] Mennessier C, Clackdoyle R, Noo F, "Direct determination of geometric alignment parameters for cone-beam scanners.," Physics in medicine and biology, vol. 54, no. 6, pp. 1633–60, Mar. 2009.

Quantitative Assessment of Liver Fat with Dual Energy CT: Comparison with MR Spectroscopy

T. Hyodo[1], M. Kudo[2], P. Lamb[3], P. R.S. Mendonça[4], M. Okada[1], N. Yada[5], O. Maenishi[6], K. Ishii[1], T. Murakami[1]
[1]Kinki University Faculty of Medicine, Dept. of Radiology, Osaka-Sayama, Japan
[2]GE Healthcare Japan, CT research group, Tokyo, Japan
[3]GE Global Research, Biomedical Image Analysis Lab, Niskayuna, NY, USA
[4]GE Global Research, Image Analytics Lab, Niskayuna, NY, USA
[5]Kinki University Faculty of Medicine, Dept. of Gastroenterology and Hepatology, Osaka-Sayama, Japan
[6]Kinki University Faculty of Medicine, Dept. of Pathology, Osaka-Sayama, Japan

Keywords Non-alcoholic steatohepatitis · Dual energy CT · Fat fraction · Fast kV switching

Purpose
There is a clinical need for non-invasive method for hepatic steatosis assessment—e.g., diagnosis of nonalcoholic fatty liver disease (NAFLD) and steatohepatitis; and liver donor selection. The current gold standard technique for evaluation of hepatic fat is MR spectroscopy (MRS) which separate fat and water resonances and subsequently provide an accurate fat fraction measurement [1]. Unenhanced conventional CT provides high performance in qualitative diagnosis of macrovesicular steatosis when concentration of liver fat exceeds 30 %, but it is not so useful clinically [2]. Here we developed an algorithm for fast kVp-switching dual-energy CT (DECT) data to quantify the volume percentage of hepatic fat: Multi-material decomposition (MMD), as developed and implemented in [3], augments the ideal solution assumption with a non-negativity constraint and allows for the discrimination of more than three materials. This makes MMD an ideal technique for working with CT images of the human body. The purpose of this study was to assess the accuracy of the new algorithm with using fast kVp-switching DECT in quantification of hepatic fat deposition in patients with suspected hepatic steatosis, by comparing with MRS.

Methods
This prospective study was approved by an institutional review board. Thirty-six patients with suspected hepatic steatosis (mean body mass index, 25 [range, 19–36]) underwent DECT (140 and 80 kVp) and single-voxel proton MRS within 4 weeks prior to liver biopsy. The histopathological diagnosis was simple fatty change-steatohepatitis, n = 15; non-alcoholic steatohepatitis, n = 15; acute hepatitis, n = 1; chronic hepatitis, n = 4; cirrhosis, n = 1. Fat volume fraction (FVF, %) maps were generated from DECT data, based on the multi-material decomposition method. Hepatic parenchymal FVF was measured by using the average measurement from three regions-of-interest (size, 200 mm^2) corresponding to the planned biopsy site. FVF measurements obtained by DECT and MRS were correlated with histopathologic grade of steatosis by the NAFLD activity score (NAS) [4]: One-way analysis of variance with Tukey multiple comparison test was performed. Spearman's class correlation was used to correlate FVF from each of DECT (averaged over two observers) and MRS with histopathologic steatosis grade. Interobserver agreement was assessed by Bland–Altman analysis and calculation of the intraclass correlation coefficient (ICC).

Results
Histopathologically, NAS steatosis scores were 0 in 7 patients, 1 in 16 patiens, 2 in 10 patients, and 3 in 3 patients. The ICC for interobserver reliability with regard to the FVF measurements on DECT was 0.999 (95 % confidence interval, 0.998 to 0.999). The Bland–Altman plot indicated no bias and the 95 % limits of agreement for interobserver agreement were −0.457 % to 0.438 %. There was good correlation between hepatic FVF of each DECT ($\rho = 0.67$; $p < 0.0001$) and MRS ($\rho = 0.77$; $p < 0.0001$) and histopathologic steatosis score (Fig. 1). Bland–Altman plot of FVFs obtained from DECT and MRS revealed the proportional bias by the significant slope of the line regressing the difference on the average ($r = -0.62$; $p = 5.7 \times 10^{-5}$, Fig. 2a). The relative difference plot revealed a mean percentage difference of −5.80 % with 95 % confidence limits of −13.5 % and 1.87 % (Fig. 2b).

Conclusion
The applicability and reproductivity of MMD from a DECT were good for characterizing hepatic fat content, although slightly less correlation with histological finging was observed than in MRS.

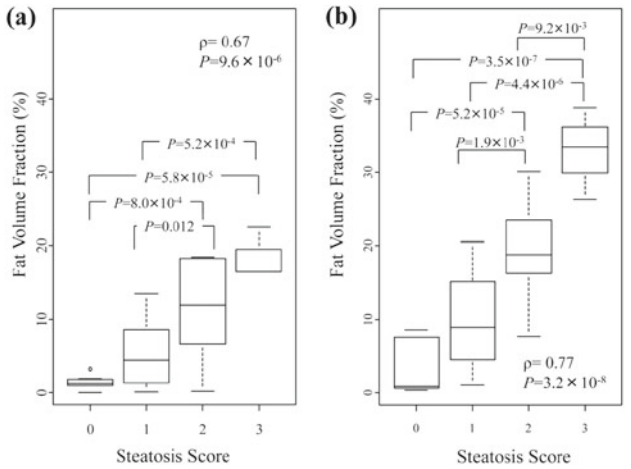

Fig. 1 Box plots comparing hepatic fat volume fraction measured by DECT (**a**) and MRS (**b**) to histopathologic hepatic steatosis score in 36 patients. *Top* and *bottom* of boxes represent 25th–75th percentiles of data values. *Line in box* represents median value. *Circle* indicates outlier

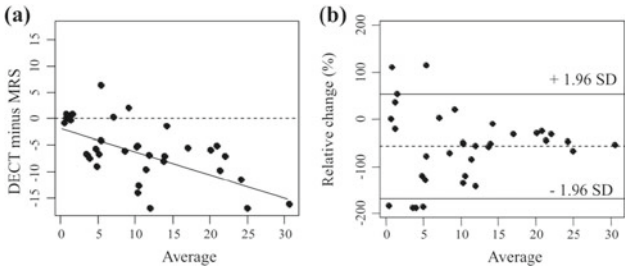

Fig. 2 Bland-Altman plot of FVFs obtained from DECT and MRS. **a** An ideal mean percentage difference of 0 is indicated by a dotted line. The existence of a proportional bias is shown by the significant slope of the line (*solid line*) regressing the difference on the average. **b** The percentage difference plot between FVFs obtained from DECT and MRS as the comparison method on the y-axis. The mean percentage difference is indicated by a *dotted line*. The limits of agreement for the mean percentage difference, as defined by 95 % confidence limits, are indicated by *solid lines*

References

[1] Bernard CP, Liney, GP, Manton, DJ, Turnbull, LW & Langton, CM (2008) Comparison of fat quantification methods: a phantom study at 3.0T. Journal of magnetic resonance imaging : JMRI 27(1):192–7

[2] Park SH, Kim, PN, Kim, KW, Lee, SW, Yoon, SE, Park, SW, Ha, HK, Lee, MG, Hwang, S, Lee, SG, Yu, ES & Cho, EY (2006) Macrovesicular hepatic steatosis in living liver donors: use of CT for quantitative and qualitative assessment. Radiology 239(1):105–12

[3] Mendonça PRS, Bhotika, R, Maddah, M, Thomsen, B, Dutta, S, Licato, PE & Joshi, MC (2010) Multi-material decomposition of spectral CT images.76221W–21W

[4] Brunt EM, Kleiner, DE, Wilson, LA, Belt, P & Neuschwander-Tetri, BA (2011) Nonalcoholic fatty liver disease (NAFLD) activity score and the histopathologic diagnosis in NAFLD: distinct clinicopathologic meanings. Hepatology 53(3):810–20

Comparison of digital tomosynthesis and computed tomography to evaluate prosthesis: a study on the phantom

T. Gomi[1], M. Nakajima[2], T. Umeda[1], T. Takeda[1], A. Okawa[3]
[1]Kitasato University, School of Allied Health Sciences, Sagamihara, Japan
[2]Hosoda Clinic, Radiology, Tokyo, Japan
[3]Nagoya University, Graduate School of Medicine, Nagoya, Japan

Keywords Tomosynthesis · Computed tomography · Prosthesis · Artifact reduction

Purpose

Digital tomosynthesis (DT) is a limited-angle method for image reconstruction. In this technique, a projection dataset of an object acquired at regular intervals during a single-acquisition pass is used to reconstruct planar sections post priori. Tomosynthetic slices exhibit high resolution in planes that are parallel to the detector plane. DT enhances the existing advantages of conventional tomography, including low radiation dose, short examination time, and easy low-cost availability of longitudinal tomographs, which do not include the partial-volume effect.

DT using the filtered-backprojection (FBP) algorithm gives a satisfactory overall performance, but its effectiveness depends considerably on the region of the image. This type of DT gives good results that are independent of the type of metal present in the patient and effectively removes noise artifacts, especially at greater distances from the metal objects. In addition, flexibility in choosing DT imaging parameters on the basis of the desired final images and generation of high-quality images may be beneficial.

Imaging by X-ray computed tomography (CT) has improved over the past three decades and is now a powerful tool in medical diagnostics. It has become an essential, noninvasive imaging technique since the advent of spiral-CT imaging in the 1990 s, which has led to shorter scan times and improved three-dimensional spatial resolution. CT provides a high resolution in the tomographic plane but limited resolution in the axial direction. However, the quality of images generated by a CT scanner can still be reduced by the presence of metal objects in the field of view. The imaging of patients with metal implants, such as marker pins, dental fillings, or hip prostheses, may give rise to artifacts, such as bright and dark streaks, cupping, and capping. This susceptibility to artifacts is mostly due to quantum noise, scattered radiation, and beam hardening. Metal artifacts influence the image quality by reducing the contrast and obscuring details, thus hindering the ability to detect the structures of interest and possibly leading to misdiagnosis. Therefore, photon starvation is probably the most significant cause of metal artifacts.

Methods for reducing metal artifacts aim to improve the quality of affected images. Recently, modified-iterative and wavelet-reconstruction techniques, which are practical approaches, have produced promising results. However, these methods cannot be combined with the fast interpolative techniques available with the robust FBP algorithm, which is the standard reconstruction technique implemented in modern CT scanners.

We evaluated DT and modern CT reconstruction used in metal-artifact reduction. Cases of prosthetic phantoms (titanium) were used to compare DT [conventional FBP, metal-artifact-reduction (MAR) processing, simultaneous-iterative-reconstruction technique (SIRT)], and CT (conventional FBP and adaptive statistical iterative reconstruction).

Methods

The DT system (SonialVision Safire II, Shimadzu Co., Kyoto, Japan) consists of an X-ray tube with a 0.4-mm focal spot and a 362.88 × 362.88-mm digital flat-panel detector composed of amorphous selenium. DT was performed linearly with a total acquisition time of 6.4 s and an acquisition angle of 40°. CT scans were

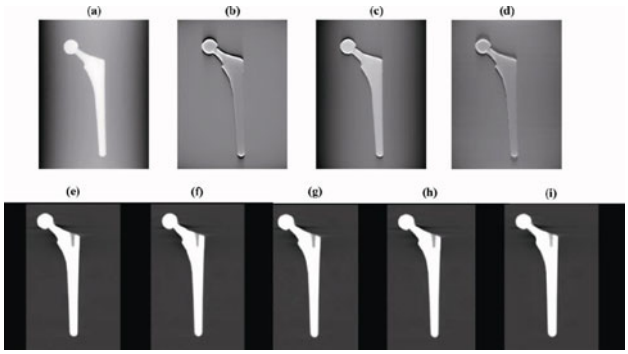

Fig. 1 Comparison between excellent tomosynthesis images and those obtained from the imaging algorithms of MAR processing (W = high), conventional FBP, SIRT (60 iterations) in the in-focus plane, and CT (conventional FBP and iterative reconstruction). MAR processing provides a better visualization of the hip-prosthesis phantom by eliminating, blurring, and reducing the artifacts, above, and the visualized planes, below. **a** projection; **b** tomosynthesis FBP; **c** tomosynthesis MAR high; **d** tomosynthesis SIRT iteration 60; **e** CT FBP; **f** CT iterative 20 %; **g** CT iterative 40 %; **h** CT iterative 60 %; **i** CT iterative 100 %

performed on a multislice CT scanner (64-slice Discovery CT 750HD scanner; GE Healthcare Corp., Milwaukee, WI, USA) with 120 kVp, 150 mA, 0.625 mm × 64 collimation, "STND" reconstruction kernel, and a 1-s gantry-rotation time at a beam pitch of 0.984.

The effectiveness of this method for enhancing the visibility of a prosthetic phantom was quantified in terms of the intensity profile and root-mean-square error (RMSE), and the removal of ghosting artifacts was quantified in terms of the artifact-spread function (ASF). Different reconstruction methods in the in-focus plane (the reference image was a straight projected radiographic image) were used to compare RMSEs. ASF metrics were used to quantify the artifacts observed in planes outside the focal-image plane. These artifacts were generated from real features located in the focal-image plane and, therefore, resembled those features.

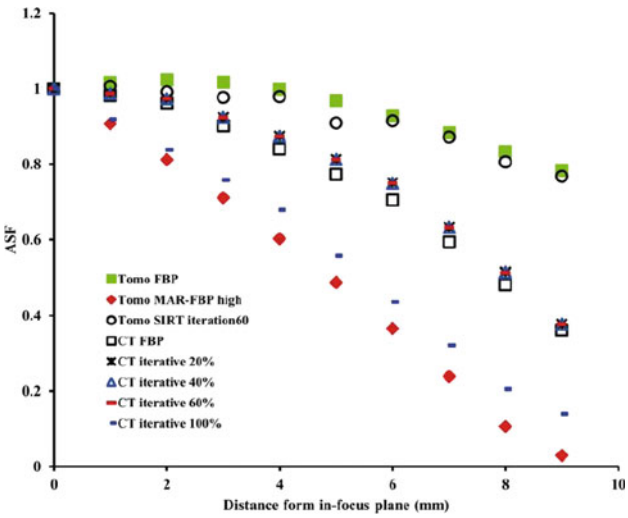

Fig. 2 Comparison between ASF versus distance from the in-focus plane for tomosynthesis and CT. The ASF *chart* shows that tomosynthesis with MAR processing results in the maximum removal of metal artifacts

Results

A comparison of each of the images, intensity profiles, and RMSEs between the DT images (MAR processing and the iterative algorithm) and CT (100 % adaptive statistical iterative reconstruction) images revealed decreased numbers of metal and beam-hardening artifacts in the reconstructed images. Furthermore, the MAR processing technique enabled higher-contrast detectability than that obtained by the existing FBP algorithm (Fig. 1). In the reconstructed images obtained from MAR processing, the quantum-noise structure decreased, and the noise structure was slightly smoother.

The error image was smaller in the MAR DT imageson the near in-focus plane, the intensity profile showed the beam-hardening effect, and streak artifacts were reduced in the SIRT DT and adaptive statistical iterative reconstruction CT images. The ASF performance of the algorithms were ranked in descending order: (1) MAR DT, (2) CT (iterative reconstruction), (3) SIRT DT, and (4) conventional FBP DT (Fig. 2).

Conclusion

The potential usefulness of MAR DT for evaluating a prosthetic phantom was demonstrated. MAR DT could be further evaluated in comparison with CT because of its flexibility and ability to suppress metal artifacts by an appropriate selection of an MAR algorithm. In addition, understanding the potential of MAR DT imaging will improve the diagnostic accuracy in clinical applications.

Measuring pleural fluid volume from CT image

K. Abe[1], H. Takeo[1], Y. Donomae[1], Y. Kuroki[2], Y. Nagai[3]
[1]Kanagawa Institute of Technology, Department of Electrical and Electronic Engineering, Atsugi, Japan
[2]Tochigi Cancer Center, Diagnostic Imaging Division, Utsunomiya, Japan
[3]National Cancer Center, Radiology, Tokyo, Japan

Keywords Pleural fluid · CT image · Regional extraction · Lung

Purpose

Due to recent advances in imaging technology, diagnosis assisted by imaging processing of computed tomography (CT) images is entering the mainstream. CT is therefore likely to be actively applied in medical examinations in the future.

Ordinarily, the pleural cavity contains minute amounts of pleural fluid. Increases in pleural fluid are attributable to conditions such as increased vascular permeability of capillary vessels, increased pressure in capillary vessels, and reduced blood protein level. It is also caused by diseases such as cardiac failure, liver cirrhosis, pneumonia, and cancer.

In this study, we propose a method extracting pleural fluid regions using CT images and measuring flexural fluid volume. In the application of CT imaging to thorax examinations and follow-ups, the proposed method will make possible quantitative determination of the necessity for treatment based on factors such as the presence or absence of pleural fluid amounts, changes to it, and other such factors.

Methods

As shown in Fig. 1, for each CT image slice, the proposed method extracts planarly the pleural fluid region and obtains the region's area. These extracted areas are then added up to calculate volume of pleural fluid.

(1) Determining seed points

A seed point is set as criteria for use in extraction. Labeling processing and target organ determination are performed based on the coordinates and pixel values of this point. The seed point of each slice is the coordinates of the centroid of the geometrical figure obtained from the extracted region of the previous slice.

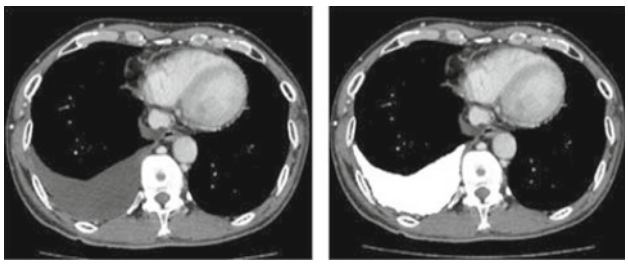

Fig. 1 Extraction of pleural fluid regions

(2) Extracting lung contours
Pre-processing that extracts lung contours using rib data is performed. Lung contour information is then used to extract the lung air space region, pleural fluid region, and heart region. This pre-processing is used for such tasks as removing unwanted parts consequential to the extraction of pleural fluid volume employing CT values and differentiating air regions on images to which CT values cannot be applied.
(3) Extracting lung air space [1, 2]
Labeling is performed first in the proposed method. However, labeling by itself does not provide correct region extraction because of the large number of holes in the image. This is dealt with by applying morphological closing using circular structural elements to fill in the holes. The proposed method excludes large blood vessels such as the pulmonary artery from the region during labeling. However, due to use of closing, the extraction performed includes such structures as fine blood vessels in the lung region.
(4) Extracting the pleural fluid region
After extracting the boundary between heart and pleural fluid regions, either processing (a) or (b) is applied depending on boundary brightness.
(4–1) Boundary is bright
Region extraction based on CT values is executed inside of the lung contour extracted in step (2). The labeling and morphology described in (3) above is used for extraction. Because part of the heart area resembles the CT value, the heart region is extracted during pre-processing and excluded. This enables extraction of just the pleural region.
(4–2) Boundary is not bright
Depending on CT image precision, region extraction from the CT value may not be possible. In such cases, the lung air space region, heart region, and part of the blood vessel region are subtracted from the lung contour interior to obtain just the pleural fluid region.

Results

Using the algorithm described in section 2, processing was used to measure pleural fluid volume in a total of 8 cases, 5 of the CT images of healthy subjects (group A) and 3 with pleural fluid associated with their condition (group B). Table 1 shows the results along with the results of lung air space extraction performed concurrently.

Table 1 Computed cardiothoracic volumetric ratios

No	Lung air space (cm^3)	Pleural fluid region (cm^3)	Pleural fluid ratio (%)
A01	5,039	0	0
A02	5,462	5	0.09
A03	5,873	0	0
A04	5,404	0	0
A05	4,847	0	0
B01	3,779	130	3.33
B02	3,792	540	12.49
B03	2,296	1,147	33.31

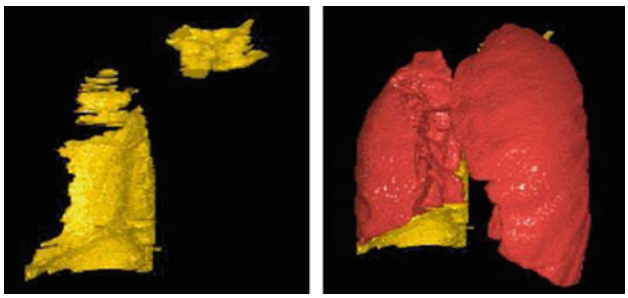

Fig. 2 3D display of results of pleural fluid extraction. (*Left*) Pleural fluid region only (*Right*) Pleural fluid and lung air space (*Red*: lung air space, *Yellow*: pleural fluid region)

Figure 2 shows the extraction images resulting from application of the proposed method.

The proposed method was applied to 8 cases, including the 3 cases of disease with associated pleural fluid. The results demonstrate tentatively the feasibility of pleural fluid region extraction using the proposed method. However, precision of contour extraction of the apical pulmonary region remains an issue for future study.

Conclusion

A method for performing volumetric measurement using CT images was developed as a proposed method for measuring pleural fluid volume. We succeeded in developing an automated method for measuring pleural fluid volume. Evaluation testing on 8 cases of original data demonstrated the potential of the application of the proposed method in the quantitative measurement of pleural fluid.

References

[1] Kass M, Witkin A, Terzopoulos D: Snakes: Active Contour Models. Int J Comput vis 1: 321–331, 1988
[2] Malladi R, Sethian JA, Vemuri BC: Shape Modeling with Front Propagation: A Level Set Approach. IEEE Trans Pattern Anal Mach Intell 17: 158–175, 1995

Cadaveric and in vivo human joint imaging based on differential phase contrast by X-ray Talbot-Lau interferometry

J. Tanaka[1], M. Nagashima[2], K. Kido[3], S. Nagatsuka[3], A. Momose[4]
[1]Saitama Medical University Hospital, Radiology, Iruma-gun, Japan
[2]Saitama Medical University, Dept. of Anatomy, Iruma-gun, Japan
[3]Konica Minolta M&G Inc., Hachioji, Japan
[4]Tohoku University, Multidisciplinary Research for Advanced Materials, Sendai, Japan

Keywords X-ray interferometry · New imaging technology · In vivo imaging · Cadavers and normal volunteers

Purpose

We developed an X-ray phase imaging system based on Talbot-Lau interferometry in which a usual X-ray generator is used, and started to study for clinical application. The purpose of this study was to explore the feasibility of clinical diagnosis of this innovative X-ray grating interferometry system which does not depend on a synchrotron, on imaging of human finger joints in a hospital.

Methods

X-ray Talbot interferometry based on the Talbot effect is a relatively new differential phase-contrast technique, in which the refraction of X-rays is captured through interference and is visualized as distortion of Moiré pattern. The system consists of a conventional X-ray

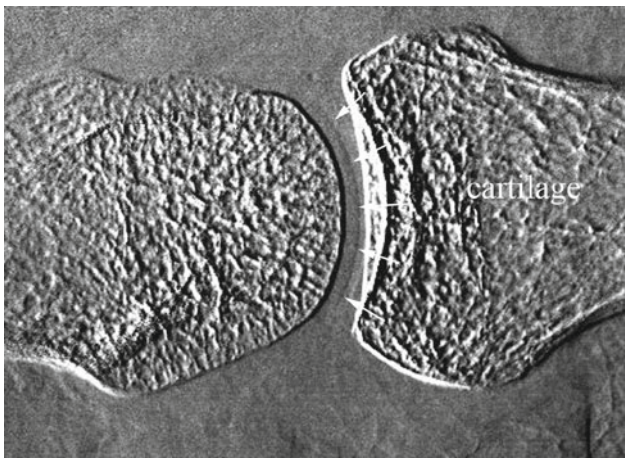

Fig. 1 With the differential phase contrast image, the cartilages were clearly depicted in the metacarpo-phalangeal (MP) joints of the thumb and the third finger

generator, three X-ray gratings arranged in an X-ray beam (therefore it is called as "grating interferometry"), an object holder, an X-ray image sensor, and a computer for image processing. This X-ray imaging system can provide simultaneously three characteristic images which include the absorption contrast, the differential phase contrast, and the visibility contrast images, corresponding to images due to the attenuation by an object, the refraction on the edges between different materials, and the small angle X-ray scattering from microscopic structures, respectively. With the development of highly accurate X-ray gratings with high aspect, this system can be applied to imaging human body. With this system, human cadaveric specimen fixed in formalin were imaged at first, then twenty normal volunteers and sixteen patients suffering from rheumatoid arthritis were examined, at 40 kV with approximately 19 s exposure at 1.4 m distance with a dose of several mGy at the skin. The obtained images of the cadaver were compared with the macroscopic anatomical findings, and the images of the volunteers and the patients were compared with the images of MRI. All of these studies were done with the approval of the university ethics committee. All of the healthy volunteers and the patients provided written informed consent.

Results

Although the absorption contrast images of finger joints were similar to conventional X-ray images, it was not possible to recognize fine details of bone structures with the visibility contrast images. However, with the differential phase contrast image, the cartilages were clearly depicted in the metacarpo-phalangeal (MP) joints of the thumb and the third finger (Fig. 1), which were not observed in the conventional image. The results showed that the fixation in formalin had no bad influence upon the cartilage contrast and sufficient sensitivity can be expected in vivo imaging. In some differential phase contrast images from the patients of rheumatoid arthritis, destruction of joint cartilages were clearly depicted and were confirmed by the comparison with MRI.

Conclusion

New imaging technique based on Talbot-Lau X-ray interferometry can be applied to clinical study for visualization of subtle changes in soft tissues in musculoskeletal examinations. With its high sensitivity in depicting the cartilages in fingers, the X-ray grating interferometry has the potential to detect rheumatoid arthritis at an earlier stage than with conventional method. Phase-shift X-ray imaging may become a considerable option in the medical field and our research should proceed to the next step to confirm its clinical value.

Functional chest radiography with a portable dynamic FPD: Detection of blood flow impairment based on "Circulation map" during cardiac pumping

R. Tanaka[1], S. Sanada[1], M. Oda[2,3], M. Suzuki[2,3], K. Sakuta[4,5], H. Kawashima[4,5], H. Iida[4]
[1]Kanazawa University, Radiological Technology, Kanazawa, Japan
[2]Kanazawa University Hospital, General and Cardiothoracic Surgery, Kanazawa, Japan
[3]Kanazawa University, Thoracic, Cardiovascular and General Surgery, Kanazawa, Japan
[4]Kanazawa University Hospital, Radiology, Kanazawa, Japan
[5]Kanazawa University Graduate School of Medical Science, Health Sciences, Kanazawa, Japan

Keywords Circulation · Pulmonary blood flow · Functional imaging · Flat panel detector (FPD) · Chest radiography

Purpose

Recent advances in X-ray detector and digital image post-processing technology have facilitated the performance of sequential radiography with extremely low doses. Lung and cardiac function can be assessed in a simple, low dose and cost-effective way with dynamic chest radiography based on a flat-panel detector (FPD). Of particular note is blood flow evaluation based on changes in pixel values on dynamic chest radiographs without contrast media. There have been many reports showing the feasibility of pulmonary densitometry [1–3]. Some studies succeeded in blood circulation mapping based on changes in pixel value during cardiac pumping [4, 5]. However, there has been no report demonstrating a normal projection of cardiothoracic blood circulation on dynamic chest radiographs, which is essential as diagnostic criteria for the diagnosis of blood flow disorders with dynamic chest radiography. This study was performed to establish a normal cardiothoracic blood circulation map projected as changes in pixel value on dynamic chest radiographs and to evaluate the diagnostic performance of blood flow disorders based on the newly-developed diagnostic criteria in clinical cases.

Methods

Study population: Dynamic chest radiographs of 10 patients (Abnormal, n = 4; Normal, n = 6) were obtained in this study. The patients had been diagnosed to be normal (51–84 years old; mean, 58 years old; M:F = 2:4) or abnormal (31–73 years old; mean, 69 years old; M:F = 4:0) in terms of pulmonary blood circulation based on findings on CT, lung perfusion scintigraphy, and other clinical findings. Approval for the study was obtained from our institutional review board, and the patients gave their written informed consent to participation in this study.

Image acquisition: Dynamic chest radiographs were obtained using a portable dynamic FPD system (Test Model) (CXDI-50RF; Canon, Japan), which was capable of both radiography and fluoroscopy. Fifty images were obtained in 10 s on exposure conditions as follows: 120 kV, 0.1 mAs/frame, SID 1.5 m, 5.0 frames per second (fps). Imaging was performed during respiration, in the standing position, and posteroanterior (PA) direction. The total exposure dose was almost the same amount of those in conventional chest radiography in two projections (PA + LA).

Image analysis: Fig. 1 shows the overall scheme of our algorithm. The images composing a whole cardiac phase during breath-holding were determined based on the movement of diaphragm and left ventricular wall, and one cardiac cycle was selected for the analysis. For visual evaluation, inter-frame differences were calculated and mapped on the original image as blood circulation vector map. The absolute values were then summed through a single cardiac phase, and the results were visualized in color scale as a blood circulation map.

Statistical analysis: Regions of interest (ROIs) were manually located on the lung and cardiac areas, and the maximum differences in pixel values during a single cardiac phase were measured in each

area. To address the relationship among the hilar and peripheral regions at the hilar level, right and left in symmetrical positions at each lung area, and three lung areas at each lung, we examined the null hypothesis that there were no differences among the measurement results of each area by Wilcoxon test.

Clinical evaluation: To evaluate the diagnostic performance, the resulting images were compared to perfusion scintigrams in patients with pulmonary blood flow impairments.

Results

Normal circulation map: In all normal controls, the pixel values measured in atrium, lung area, and aortic arch increased in the systole phase and decreased in the diastole phase, reflecting changes in normal circulation. Whereas, the pixel values measured in the ventricles changed in reverse, i.e., decreased in the systole phase and increased in the diastole phase. In addition, the resulting blood circulation map showed a left–right symmetric distribution decreasing from the hilar region to the peripheral region of the lung (Fig. 1).

Statistical analysis: There was significant difference between the changes in pixel values measured in the hilar region and those measured in the peripheral region of the lung.

Clinical evaluation: Many abnormal cases showed a nonuniform distribution on the blood circulation map, which were different from the normal pattern. These findings were confirmed on the perfusion scintigrams (Fig. 2).

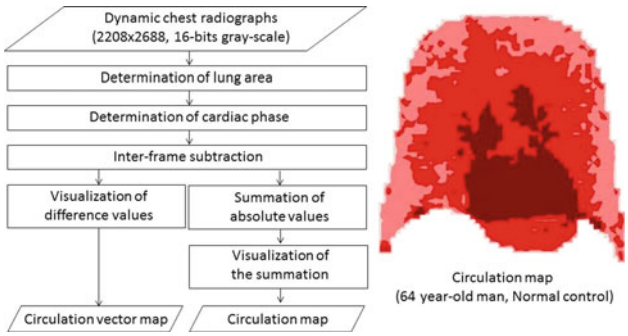

Fig. 1 Overall scheme of our algorithm and the resulting image

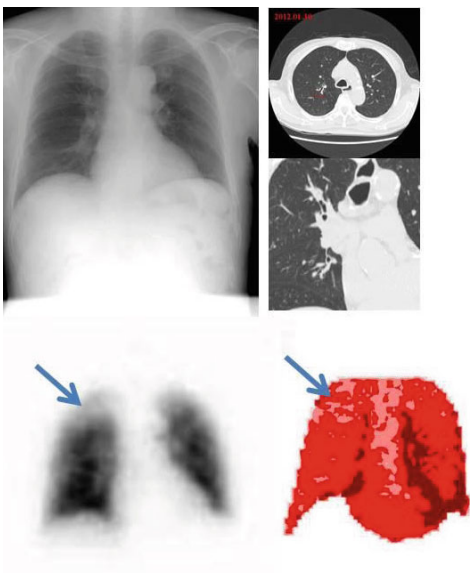

Fig. 2 Blood circulation map (72 year-old man, R-lung cancer)

Conclusion

Cardiothoracic blood circulation was demonstrated as changes in pixel value on dynamic chest radiographs and the normal pattern could be defined as follows; Increase of pixel value in the systole phase and decrease of pixel value in the diastole phase, left–right symmetric distribution of amount of change, decreasing from the hilar region to the peripheral region of the lung. Pulmonary blood flow impairments could be detected as the exception to the normal blood circulation map developed in this study. Further studies are required to establish a concrete normal pattern by increasing the number of normal subjects and to develop a computerized method to detect abnormal areas.

Acknowledgments

This work was supported by A grants-in-aid of The Cardiovascular Research Fund, Tokyo, Japan, Grant-in-aid for Scientific Research (C) of Ministry of Education, Culture, Sports, Science and Technology, JAPAN (Grant number : 24601007), Canon Inc., Tokyo, Japan. Authors are thankful for the technical support of Osamu Tsujii and Takashi Ogura from Canon Inc., Yasushi Kishitani from TOYO corporation, and staffs at Dept. of Radiology, Kanazawa university hospital.

References

[1] Silverman NR, Intaglietta M, Tompkins WR (1973) Pulmonary ventilation and perfusion during graded pulmonary arterial occlusion. J Appl Physiol 34:726–731

[2] Bursch JH (1985) Densitometric studies in digital subtraction angiography: assessment of pulmonary and myocardial perfusion. Herz 10:208–214

[3] Liang J, Jarvi T, Kiuru A et al. (2003) Dynamic chest image analysis: model-based perfusion analysis in dynamic pulmonary imaging. J Appl Signal Process 5:437–448

[4] Tanaka R, Sanada S, Tsujioka K, Matsui T, Takata T, Matsui O (2008) Development of a cardiac evaluation method using a dynamic flat-panel detector (FPD) system: a feasibility study using a cardiac motion phantom. Radiological physics and technology 1:27–32

[5] Tanaka R, Sanada S, Fujimura M, Yasui M, Tsuji S, Hayashi N, Nanbu Y, Matsui O (2009) Pulmonary blood flow evaluation using a dynamic flat-panel detector: Feasibility study with pulmonary diseases. IJCARS, 4:449–454

MR-enhancement imaging of stent-less aortic valve conduit

M. Fatahi[1], E. Immel[1,2], B. Cox[1], R. Boyd[2], A. Melzer[1]
[1]IMSaT, Institute for Medical Science and Technology, Medical Imaging, Dundee, United Kingdom
[2]Vueklar Cardiovascular, Edinburgh, United Kingdom

Keywords MRI imaging · Aortic heart valve · Resonator · Larmor frequency

Purpose

Detailed visualization and localization of cardiovascular implants such as Stent-less aortic heart valve during MR guided procedures has an important role in those procedures. In MR imaging, the only visible structures are those contain water molecules with excitable proton spin, therefore suitable visualization technique has to be applied to cardiovascular implants. In this study MR-Enhancement imaging of stent-less aortic heart valve is achieved through the incorporation of a wireless resonator which is tuned to 63.8 MHz (Proton Larmor frequency at 1.5 T MRI).

Methods

The special design of the stent-less Aortic valve conduit and the skirt feature at the proximal end mimic the natural aortic root geometry. A resonant circuit which is tuned to the Larmor frequency of the MRI system, will enhance the externally applied RF pulses via inductive

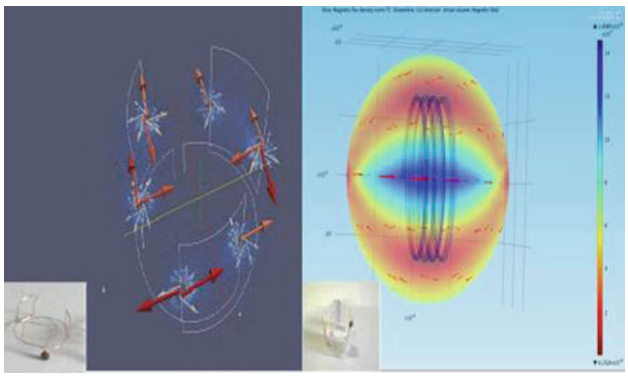

Fig. 1 Electromagnetic simulation of wireless resonators three loop coil (L) and solenoid(R)

coupling, in particular for pulses applied with a small flip angle[1,2,3]. As a result local signal intensity enhancement can be achieved in target area.

The resonant circuit consists of a coil made of insulated copper wire and a non-magnetic Surface Mounted Device capacitor tuned to the Larmor frequency. The resonator is initially tuned in the air, and then adjusted in both water and saline solution (Nacl 0.9 %). Use of these simple materials and components enabled us to quickly and inexpensively assess the functionality of resonator and evaluate the feasibility of the method. This does not reflect the final design of the wireless resonator, which would be constructed using approved, bio and MR-compatible materials. In order to optimize the homogeneity, uniformity and the quality of the design, Electromagnetic simulation has been done using COMSOL 4.3 and MATLAB software for resonators before designing (Fig. 1).

MRI scanning was performed on the GE Signa HDX, 1.5T MR Unit, with a GE 8-channel head coil in two experiments of without and with the flow. The MRI sequences used were taken from the standards for testing of devices for MR- compatibility. The Stent-less valve was mounted inside a plastic cylinder, the ends of which were connected by silicone tubing to a Heart–Lung Machine (Maquet HL-30) to create pulsatile and a constant flow through the valve. The plastic cylinder containing the valve was placed inside a box filled with PAA (Polyacrylic acid). Flow through the valve was set to the following parameters:

Fluid: water, Temperature range: 25–35 °C, Pressure 60–120 mm, 2.96 l/min, Heart rate 64 beats/min, Systole 22 % of the total cycle.

Results

This study demonstrates that high resolution MR images of the stent-less aortic valve replacement system may be feasible when employing MR-Enhancement wireless resonators to locally enhance signal intensity. This initial evaluation has helped to characterize potential configurations of the MR Enhancement resonator, but the final design of the resonator for the valve requires more testing, modeling and simulation to meet all the necessary requirements, including bio-compatibility, MR compatibility.

Signal intensity plot in different location of the coil was approximately symmetric which indicates that resonator can give us a homogenous enhancement. The signal intensity is approximately 3–4 times with MR-Enhancement resonator than without (Fig. 2)

Conclusion

The main advantages of this wireless resonant circuit are being less complicated and more cost-effective. By having high contrast images and better visualization of the heart valve, we may bypass the need for MRI contrast agents. This could be very beneficial in terms of procedural cost, time and complexity.

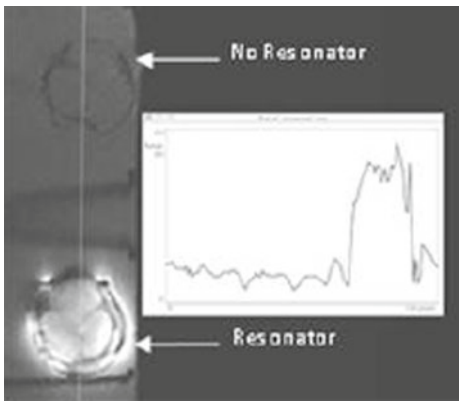

Fig. 2 Signal intensity plot across valve with (*bottom*) and without (*Top*) MR-Enhancement resonator in axial and sagittal view (FGR, TE = 2. 5 ms, TR = 15 ms, Slice Thickness = 3 mm)

Acknowledgments

This work is supported by Integrating Interventional Imaging Operation System (IIIOS) project which has received funding from EU FP7 under grant agreement no 238802.Vascutek Ltd. Inchinnan, has provided the Stentless aortic heart valve conduit replacement system in this work.

References

[1] Quick HH, 2007, Interventional MR: Devices, Applications, Electromagnetic safety concern, 18th Int. Zurich Symposium on EMC, Munich 2007

[2] Burl M, Coutts G, Young IR. Tuned fiducial markers to identify body locations with minimal perturbation of tissue magnetization. *Magn Reson MED*. 1996;36(3):491–3.

[3] Immel E, Melzer A, MRI guided delivery and retrieval of a resonant vena cava filter in a porcine animal model, American Journal of Cardiology, Vol. 104, No. 6, Supplement, 2009, p. 196D–196D.

Automated detection of vertebral osteophytosis on [18F]-NaF PET/CT

R. Summers[1], H. Munoz[1], J. Yao[1], J. Burns[2], P. Choyke[3], K. Kurdziel[3]

[1]National Institutes of Health, Radiology & Imaging Sciences, Bethesda, MD, USA

[2]University of California, Irvine School of Medicine, Department of Radiological Sciences, Irvine, USA

[3]National Cancer Institute, NIH, Molecular Imaging Program, Bethesda, MD, USA

Keywords Osteophyte · Computer aided detection · Degenerative disc disease · Pet

Purpose

[18F]-NaF PET acts as a marker of regional osteoblastic activity in bone, and has proven useful in the detection of osteoblastic neoplastic processes. However, other synchronous or metachronous benign osteoblastic processes can occur, obscuring diagnosis of neoplastic lesions. Degenerative change of the spine, which includes degenerative disc disease (DDD), is multifactorial in etiology and increases in frequency with age. Osteophytes at the vertebral apophyses develop as part of this degenerative process. These osteophytes can demonstrate increased radionuclide uptake on [18F]-NaF PET through associated focal increases in osteoblastic activity, and can impede the recognition of spinal vertebral metastatic lesions. Osteophytes are

osseous excrescences, often with associated focal cortical thickening and sclerosis. We thus present a fully-automated method to detect degenerative osteophytes on [18F]-NaF PET/CT by segmenting, detaching, and topologically deforming (or "unwrapping") the cortical shell of the vertebral body on CT images, and by measuring co-registered PET/CT features.

Methods

The method exploits the fact that degenerative osteophytes of the spine are typically hyperdense, continuous or piecewise continuous with the cortical shell of the parent vertebrae, and occur in characteristic vertebral body locations. The method has four distinct steps. First, segmentation of the spine is performed on a CT scan by thresholding and morphological operations to locate and partition individual vertebrae. A cylindrical dual-surface model is localized at each vertebral body, and is driven to segment the cortical shell from the underlying medulla by internal forces, image potential forces, and logical constraints between the interior and exterior surfaces. Second, the cortical shell is vertically transected posteriorly and unwrapped along the cylindrical coordinate system of the surfaces. The mean intensity between the two surfaces is projected onto a 2D homeomorphic map, with a horizontal axis based on the angle from the vertebral center with respect to the pedicles and a vertical axis based on the height of the vertebral body. The method currently focuses on the vertebral body, and we exclude the pedicles, spinal canal and processes from further processing. Third, osteophyte candidates are extracted from the individual 2D maps by thresholding and applying a gradient map. The hyperdense regions of DDD have higher Hounsfield units than the surrounding cortical shell. These initial 2D detections are mapped back into 3D space with a one-to-one correspondence to generate additional 3D features. The individual 2D maps are linked to maps of the neighboring vertebrae to generate features. These features are based on the fact that DDD forms due to biomechanical stress and associated osteophytosis often occurs in an oblique longitudinal pattern across multiple vertebrae. Third, the original 2D detections are used as seed points in a level-set operation. This segments DDD foci that were affected by poor segmentation by the dual surfaces with more accuracy and generates additional 3D features. Lastly, the 3D segmentations on the CT scan are mapped to a registered [18F]-NaF PET scan (Fig. 1). There is high uptake of [18F]-NaF in areas of high metabolic activity in the bones. The PET scan is used to generate additional features based on the Standardized Uptake Value (SUV) of the candidate and the surrounding region.

This system was evaluated using ten whole-body [18F]-NaF PET/CT scans (9 males, 1 female, age range 49–85, mean age: 65) that have DDD, and might also have sclerotic metastases in the spine. The CT scans have a slice thickness of 5 mm, while the PET scans have a slice thickness of 4 mm. All sclerotic metastases and DDD were manually labeled by a radiologist forming a reference standard. There are in total 229 DDD findings. A committee of support vector machines (SVM) was used for classification. Leave-one-out cross-validation was performed. The ROCKIT toolkit was used for FROC analysis.

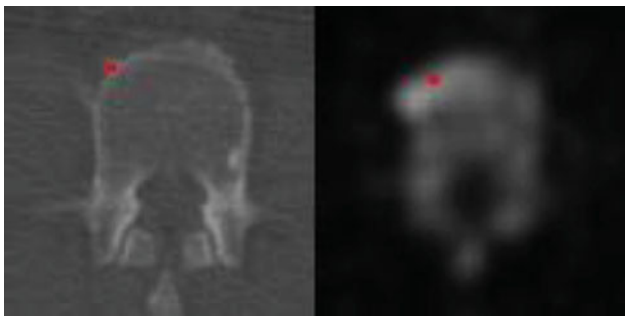

Fig. 1 Example of vertebral degenerative disease on CT and [18F]-NaF PET

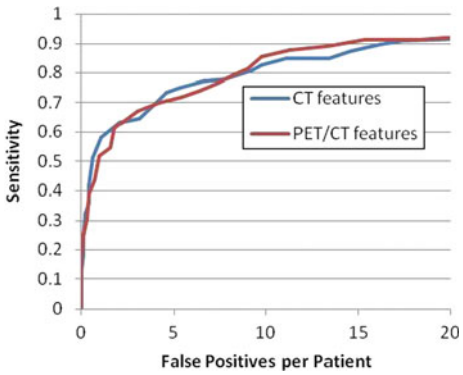

Fig. 2 FROC analysis

Results

The sensitivity of this method is 85 % at 9.8 false positives per case, with 75 % of lesions detected before the classifier. The sensitivity was 82 % at 9.8 false positives per case without usage of PET features (Fig. 2).

Conclusion

We proposed a novel method to detect degenerative osteophytosis of the spine utilizing PET/CT scans. This can be employed when automatically detecting sclerotic metastases, which may generate DDD false positives.

Virtual scintigraphy: a computerized method to assist the interpretation of thyroid scintigrams

B. Thiering[1,2], J. Nagarajah[2], H.-G. Lipinski[1]
[1]Biomedical Imaging Group, University of Applied Sciences and Arts Dortmund, Germany
[2]Department of Nuclear Medicine, University Hospital Essen, Germany

Keywords Thyroid · Scintigram · 3D-reconstruction · Virtual scintigraphy

Purpose

Conventional scintigraphy as a standard device for thyroid imaging merely represents a two-dimensional projection of the distribution of the radionuclide activity in the thyroid tissue. A direct comparison of a 2D scintigram with the spatial structure of the thyroid and thereby possibly existing nodules therefore is only possible to a limited extent. Since modern imaging methods (CT, MRT) provide three-dimensional image data of the thyroid, a virtual scenario of a diseased thyroid based on a spatial reconstruction of the organ can be developed. Thus, a three-dimensional reconstruction of the thyroid is required within subsequently various heterogeneities of thyroid tissue can be modeled which represent different storage behavior of thyroid tissue in comparison with nodules.

Ideally, "normal" tissue is provided with a defined storage capacity whereby thyroid-voxels can be labeled by a fixed gray-scale value. Pathological tissue, however, is able to store radionuclides either in an increased ("hot nodules") or a reduced ("cold nodules") amount, which can be encoded by higher or lower gray-scale value. Intensity, number, location and shape of the nodules can be modified within certain limits, so that even complex pathological situations can be created within the 3D-thyroid-scene. Finally, a virtual scintigram can be derived from the projection of the defined 3D-scene of one of a diseased modeled thyroid on a virtual scanning plane. In doing so, the differently created scenarios can be stored in a database as 3D-models as well as virtual scintigrams. The latter can be compared with real scintigrams and the related 3D-models can be assigned to the virtual scintigram which possibly makes the interpretation of the real scintigram easier.

Methods

In order to create a virtual (reference-)scene of the thyroid, axial CT-images of the thyroid area of five patients have been generated (52 scans each, 512 × 512 image resolution, 4.5 mm slice thickness, 0.6 mm pixel spacing; Siemens Somatom Sensation 16 device). Within the scope of an image pre-processing the CT-image data restricted to the thyroid area have been undergone a data smoothing (median and Gaussian filter respectively). By visual control it has empirically been proven that a Curvature Flow Image Filter achieved the best results. In order to maximize the resolution of the z-axis, the number of image layers has been extended from an original number of 52 layers to 208 layers by means of the VTK-class vtkImageResample. The layers have been interpolated axis-relatedly. A „nearest-neighbour"-interpolation has been selected as interpolation method. With the help of a global gray-scale value threshold the thyroid tissue area has been binarized and subsequently segmented using Region Growing method. Finally, on the basis of the five separately calculated thyroid models an average thyroid model has been generated.

Via manually determined seed points, cold and hot nodules have been inserted in the homogenous, segmented image layers of the thyroid tissue in order to simulate a heterogeneous tissue. All thyroid voxels that characterize the pathological tissue have been declared with different intensities (gray-scale values). Via vertical search beams along the z-axis, the simulated, thyroid-volume has been projected onto a planar scintigraphy plane. After the procedure the voxel gray-scales values have been summed up by means of the integral method and have subsequently been scaled. The results of this raycast integration have been projected onto a virtual, scintigram plane as 2D-pixels (so called virtual scintigram). Finally, the simulated scintigram has been smoothed by a Gaussian filter. Simultaneously, real thyroid scintigrams of patients with suspected thyroid tumors have been made by a dedicated thyroid camera (Intermedical, MiniCam, 128 × 128 image resolution, 1,1 mm pixel spacing) after injecting ca. 60 MBq 99 m-Tc i.v. ca. 20 min p.i.

Results

By means of the mentioned modeling techniques various pathological 3D-scenes of the thyroid could be created. Figure 1a shows the spatial reconstruction of the reference thyroid which was derived from five different CT-image data sequences of "normal" thyroids. Within this reconstructed virtual organ, heterogeneous distributed radionuclide absorption capacities could be simulated in a way they are typically expected for benign or malignant diseases of the thyroid tissue. Figure 1b shows the position of each of a hot and a cold nodule of which the positions within the tissue were stereoscopically monitored. Figure 1c shows this monitoring process that was performed by means of a PLANAR^{TM}-monitor. After the activation of the tissue a scintigram can be simulated. Figure 1d shows an example for such a "raw" virtual scintigram, which could be "transformed" into a more realistic form by adding noise (cf. Fig. 1e).

The inhomogeneity of the virtual thyroid tissue was systematically varied. The generated virtual scintigrams were then stored into an image database. Reflecting realistic pathological situations we identified 186 different cases of virtual scintigrams containing either cold or hot (mono- or bilateral oriented) nodules. The number of created nodules run from 1 up to 8 for each thyroid hemisphere having different intensities, positions and sizes. Totally, we stored 744 virtual scintigrams and corresponding 3D-scenes in a data base saved as reference scintigrams. A real scintigram was compared to the reference images by means of cross-correlation (cc-) techniques. If the calculated (normed) cc-coefficient reached values > 0.8 both virtual scintigram and the corresponding 3D-scene were retrieved from image data base and screened on a monitor.

As an example, Fig. 2a shows a real scintigram containing multiple hot nodules which is compared to a virtual scintigram (Fig. 2b) retrieved from the data base by means of best cross correlation fit

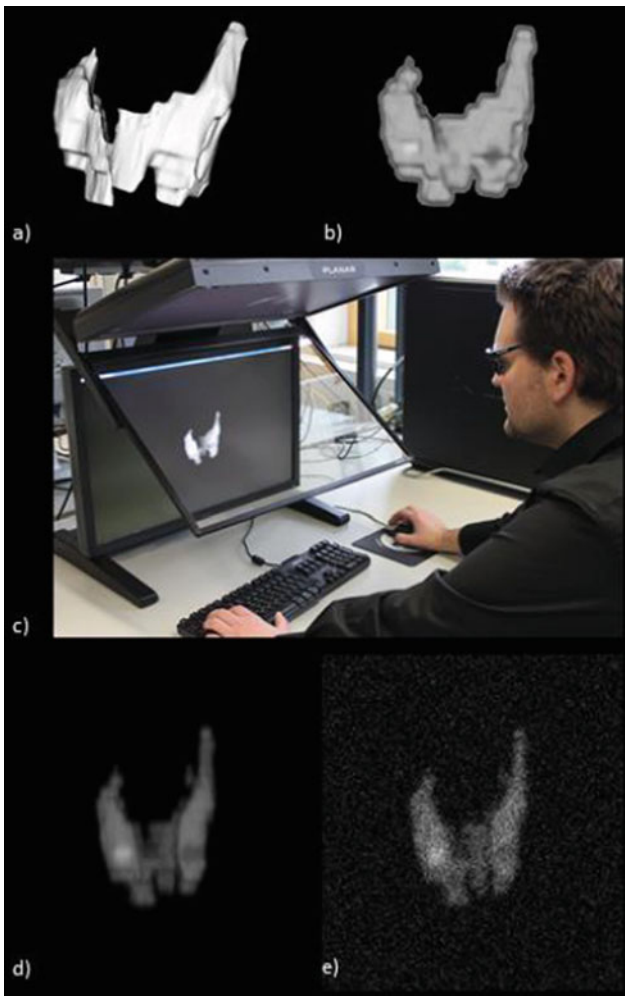

Fig. 1 **a** Spatial reconstruction of the reference thyroid, **b** thyroid with hot and cold nodule, **c** stereoscopic monitoring process, **d** raw virtual scintigram, **e** virtual scintigram by adding noise

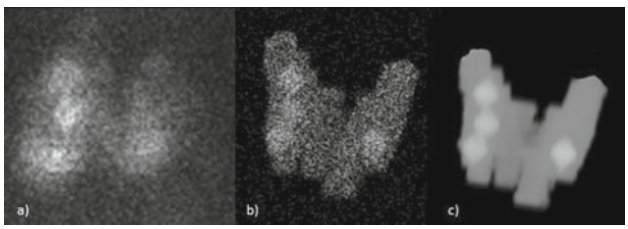

Fig. 2 **a** Real scintigram, **b** virtual scintigram from database, **c** corresponding spatial virtual scene

(cc-coefficient 0.91). The corresponding spatial virtual scene is presented in Fig. 2c.

Conclusion

We introduced a 3D-based virtual scintigraphic method to assist the interpretation of 2D-scintigrams. After creating a virtual reference thyroid diverse scenes of pathologic nodules were performed and transformed into realistic scintigram images. The variation of nodules (size, position, radionuclide intensity) done under stereoscopic visual control showed that a basis of less than 1,000 virtual scintigrams reflects most of the pathological situations observed in real

scintigrams. Cross correlation techniques between virtual and real scintigram image data allowed for a retrieval of virtual scintigrams similar to the real scintigram and, finally, the corresponding 3D-Scenes. Thus, virtual scintigraphy may be a helpful additional method to assist the clinical interpretation of planar scintigrams.

Computer-assisted system for diagnosing degenerative dementia using cerebral blood flow SPECT and 3D-SSP: a Multicenter Study

K. Ishii[1], K. Ito[2], A. Nakanishi[3], S. Kitamura[4], H. Kageyama[5], A. Terashima[6]
[1]Kinki University Faculty of Medicine, Department of Radiology, Osaka sayama, Japan
[2]National Center for Geriatrics and Gerontology, Department of Clinical and Experimental Neuroimaging, Obu, Japan
[3]Juntendo University School of Medicine, Dept. of Radiology, Tokyo, Japan
[4]Nippon Medical School, Kawasaki, Japan
[5]Hakodate-Shintoshi Hospital, Hakodate, Japan
[6]Hyogo Brain and Heart Center, Institute for Aging Brain and Cognitive Disorders, Himeji, Japan

Keywords Dementia · Alzheimer · SPECT · 3D-SSP

Purpose

Due to increasing numbers of patients with dementia, more physicians who do not specialize in brain nuclear medicine are being asked to interpret single photon emission computed tomography (SPECT) images of cerebral blood flow. We conducted a multicenter review to determine whether a computer-assisted diagnostic system (Z-score summation analysis method: ZSAM) using N-isopropyl-p-[^{123}I] iodoamphetamine (IMP) brain perfusion SPECT and three-dimensional stereotactic surface projections (3D-SSP) can differentiate Alzheimer's disease (AD)/dementia with Lewy bodies (DLB) and non-AD/DLB in institutions using various types of gamma cameras.

Methods

We determined the normal thresholds of Z-sum (summed Z-score) within a template region of interest (ROI) for each SPECT device and then compared them with the Z-sums of patients and calculated the accuracy of the differential diagnosis by ZSAM. We compared the diagnostic accuracy between ZSAM and visual assessment by four radiographic interpreters (three experienced nuclear medicine physicians and one neurologist). For visual assessment, diagnoses of AD/DLB versus non-AD/DLB based on the conventional IMP-SPECT and 3D-SSP Z-score images were classified as follows: definite non-AD/DLB, probable non-AD/DLB, indeterminate, probable AD/DLB and definite AD/DLB. We enrolled 202 patients with AD (mean age, 76.8 years), 40 with DLB (mean age 76.3 years) and 36 with non-AD/DLB (progressive supranuclear palsy [PSP], n = 10; frontotemporal dementia [FTD], n = 20; slowly progressive aphasia, n = 2 and one each with idiopathic normal pressure hydrocephalus [iNPH], corticobasal degeneration [CBD], multiple system atrophy [MSA] and Parkinson's disease [PD]) who underwent IMP cerebral blood flow SPECT imaging at each participating institution.

Results

The ZSAM sensitivity to differentiate between AD/DLB and non-AD/DLB in all patients, as well as those with mini-mental state examination (MMSE) scores of ≥24 and 20–23 points were 88.0, 78.0 and 88.4 %, respectively, with specificity of 50.0, 44.4 and 60.0 %, respectively. The diagnostic accuracy rates were 83.1, 72.9 and 84.2 %, respectively. The areas under (AUC) receiver operating characteristics (ROC) curves for visual inspection by four expert radiographic interpreters were 0.74–0.84, 0.66–0.85 and 0.81–0.93, respectively, in the same patient groups. The diagnostic accuracy rates were 70.9–89.2 %, 50.9–84.8 % and 76.2–93.1 %, respectively, Fig. 1.

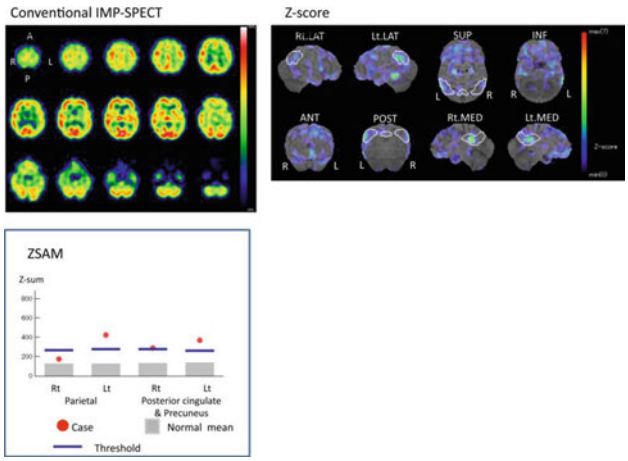

Fig. 1 Four radiographic interpreters and the Z-score summation analysis method (ZSAM) evaluations assigned a 73-year-old woman with AD and MMSE of 28 points to the AD/DLB group. Conventional SPECT and Z-score images indicated a blood flow reduction in the parietal temporal lobe, and she was assigned to the AD/DLB group when both the normal thresholds of 1.64 and 1.96 SD of determination criteria were applied in ZSAM

Conclusion

The diagnostic accuracy of ZSAM to differentiate AD/DLB from other types of dementia or degenerative diseases regardless of severity was equal to that of visual assessment by expert interpreters even across several institutions. These findings suggested that ZSAM could serve as a supplementary tool to help expert evaluators who differentially diagnose dementia from SPECT images by visual assessment.

Dynamic acquisition SPECT/CT for quantitative evaluation of time activity curves in head and neck cancer lymphoscintigraphy: Potential benefits for intraoperative sentinel lymph node resection

N. Hall[1], E. Byrum[1], J. Zhang[1], A. Agrawal[2], S. Povoski[3], M. Knopp[1]
[1]The Ohio State University, Radiology, Columbus, USA
[2]The Ohio State University, Otolaryngology, Columbus, USA
[3]The Ohio State University, Surgical Oncology, Columbus, USA

Keywords Dynamic SPECT/CT · Lymphoscintigraphy · Phantom · 3D region of interest (ROI)

Purpose

Single photon emission computed tomography/computed tomography (SPECT/CT) data sets inherently provide the opportunity for quantification by way of attenuation correction similar to that of positron emission tomography/computed tomography (PET/CT). Dynamic dataset acquisition with SPECT/CT is more challenging than dynamic acquisition using PET/CT with the currently available technology due to the restriction of not obtaining data from all angles simultaneously. This limitation can be partially overcome by acquiring multiple (6) rapid sequential SPECT scans during the same timeframe as a standard SPECT/CT scan (~20 min) and generating a time activity curve. The purpose of this work was to demonstrate that dynamically acquired SPECT/CT data collected on patients undergoing lymphoscintigraphy for head and neck cancer can accurately identify, localize and produce quantitatively accurate time activity curves for sentinel lymph nodes (SLN) when correlated with nodal activity from in vivo and ex vivo gamma probe counts.

Methods

Proof of concept was accomplished via phantom data acquired dynamically with a 16 slice SPECT/CT scanner in continuous mode for 6 cycles at 200 s/cycle. Each dual head spin (6 total) was segmented into 32 (5.625°) angles and counts from both heads (total and geometric mean) were calculated and summed for the specified region of interest (ROI) (saline bag) to obtain a total activity for each of the 6 spins. This was done while 200 uCi Tc-99 m pertechnetate in 10 ml saline was infused at a constant rate into a 50 cc saline bag containing 40 cc saline (agitated with O_2) suspended in a Jaszczak phantom filled with water during the dynamic scan acquisition. Attenuation corrected SPECT/CT data sets were then reconstructed and quantified.

Using the same acquisition technique, dynamic SPECT/CT data was acquired immediately (9 patients) post-injection of the novel, non-particulate, soluble ($\leq$ 7 nm), receptor-targeted (CD206) molecular agent ^{99m}Tc-tilmanocept (TcTP; Navidea Biopharmaceuticals, Dublin, OH) for head and neck cancer lymphoscintigraphy. Head and neck cancer patients undergoing SLN biopsy were injected (intradermal) with 18.5 MBq of either TcTP (0.1 cc) (n = 7) or TcSC (0.5 cc) (n = 9). Dynamic SPECT/CT (limited CT exposure) imaging occurred immediately for 18–21 min ($\sim$3 min/rotation).

Associated activities (counts) were measured using a 3D ROI tool with an isocontour setting (50 %) and decay corrected to time of injection. The regions of activity included the injection site as well as any areas of activity which were associated with lymph nodes. For the 50 % isocontour setting, total activity per unit volume was plotted with respect to each spin. Time-activity curves for each lymph node and injection site were calculated and slopes of the uptake curves were calculated.

Results

For the phantom study, the total counts and geometric mean of counts for both camera heads, were summed for all 32 angles and were plotted for 6 consecutive and sequential spins over 20 min. This generated an R^2 value of 0.9999 and 0.9997, respectively. Within the 32 angles of each rotation, there was variability in counts likely related in part to varying distance of the camera heads from the phantom and attenuation from the table.

For the 9 head and neck cancer patients undergoing SLN resection, the dynamic SPECT/CT lymphoscintigraphy images that were acquired immediately post-injection demonstrated peak uptake in the SLNs within the first 10–12 min following intraoral injection. Where appropriate, the plots were fitted to a curve. According to these observations, a simultaneous injection and scan start time yields a time activity relationship with respect to SNL radiotracer uptake that is similar to that seen in the phantom.

Conclusion

Dynamic SPECT/CT data acquisition is capable of generating quantitatively accurate data sets that represent changes in activity in both phantom lesions and clinical lymphscintigraphy studies binned in 3 min intervals or less. Resultant data can be reconstructed into diagnostic quality SPECT/CT images and quantified using ROI techniques. This methodology may have already proven clinically useful for accurately identifying the exact location of sentinel nodes and shows promise for predicting quantitatively the activity relationships in resected lymph nodes. This computer assisted technique could also be useful in assessing new radiopharmaceuticals as well as in adding dynamic and quantitative capabilities to standard nuclear medicine procedures.

Multi-modality computer assisted quantification of radiopharmaceutical distribution and prediction of response to therapy in ^{90}Y microsphere radioembolization

M. Robertson[1], N. Hall[1], J. Zhang[1], C. Wright[1], H. Khabiri[1], M. Knopp[1]
[1]The Ohio State University, Radiology, Columbus, United States

Keywords SPECT/CT · Deformable co-registration · Gradient based segmentation · Radioembolization

Purpose

Treatment planning for selective radioembolization (RE) therapy of liver metastases includes angiographic evaluation in combination with ^{99m}Tc macroaggregated albumin (MAA) hepatic artery perfusion scintigraphy (HAP). This is typically performed after diagnostic contrast enhanced computed tomography (CT) of the liver. Regions of interest (ROI) are drawn around liver tumors and normal liver in order to determine the dose of ^{90}Y labeled microspheres to administer. The MAA scan quantifies and provides a visual assessment of the degree of radiopharmaceutical shunting to the lungs and/or gastrointestinal tract in order to ensure that ^{90}Y RE therapy is safe in each individual patient. The assumption that is made when performing this technique is that the MAA distributes in the same pattern, to the same organs and in the same proportions as ^{90}Y microspheres when administered selectively into the hepatic artery. The purpose of this study is to compare manual and computer assisted techniques for quantitative determination of the distribution of pre-therapy MAA and the ^{90}Y microsphere therapy administrations with respect to the diagnostic contrast enhanced CT scan.

Methods

Patients scheduled for ^{90}Y microsphere RE who underwent diagnostic contrast enhanced CT for tumor volume calculation and MAA HAP single photon emission computed tomography/computed tomography (SPECT/CT) for detection of extra hepatic shunting prior to therapy between November 2010 and August 2012 were evaluated. ROIs were drawn on the MAA HAP and ^{90}Y microsphere SPECT/CT scans to match tumor volumes identified and drawn on contrast enhanced diagnostic CT. Maximum counts per pixel for both MAA HAP and ^{90}Y microsphere scans within the tumor volume ROI identified on contrast enhanced CT. In addition, normal mean background counts per pixel were measured and used to calculate tumor to background ratios (T:B).

As an adjunctive comparison, a novel deformable registration method designed to improve alignment of images with the same intensity or significantly different intensities, such as contrast: noncontrast and noncontrast:noncontrast, respectively, were used for improved co registration comparisons of SPECT activity (^{99m} Tc and ^{90}Y) and the corresponding tumor regions on the diagnostic CT. A gradient-based image segmentation technique, PET Edge, which has been shown to have improved accuracy compared to intensity threshold methods for tumor segmentation was used to automatically contour areas of increased radiotracer accumulation on the SPECT images. Radiopharmaceutical distribution and tumor to background ratios were correlated with tumor type, progression, stability or response, and degree of contrast enhancement using both the manual and computer assisted techniques.

Results

Twenty-two patients with complete data sets were evaluated. 9/13 patients had higher T:B ratios with HAP MAA compared to ^{90}Y microspheres in the group that responded to therapy or had stable disease compared to 5/9 having higher ratios in the progression group. Patients that had MAA T:B ratios greater than 1.5 were more likely to have response to therapy or stable disease. 10/13 patients in the responder/stable group had T:B ratios greater than 1.5 while only 3/9 patients in the progression category met these criteria.

The HAP MAA T:B ratios were higher than ^{90}Y in most cases and the higher HAP MAA T:B ratios correlated with better tumor response HAP MAA distribution and could be used to predict response to therapy prior to ^{90}Y microsphere administrate. There was a correlation between degree of contrast enhancement and degree of difference between HAP MAA and ^{90}Y T:B ratios. Results for the manual and computer assisted methods of quantification were similar while the computer assisted method was significantly more efficient, requiring only a fraction of the time to process each set of imaging data.

Conclusion

The computer assisted techniques present herein could potentially be used to predict response to ^{90}Y RE therapy. This computer assisted multi-modal approach for image quantification and comparison of radiopharmaceutical distributions may prove useful not only in predicting response to therapy but also in quantifying specific tumor/liver dosimetry. The added benefit of significantly improved efficiency with the semi-automated deformable registration and gradient-based image segmentation techniques for defining areas of increased radioactivity may allow for the integration of these techniques into clinical practice.

Ultrasonographic differentiation of small angiomyolipoma from renal cell carcinoma by measurement of relative echogenecity on PACS

J.Y. Cho[1], M.S. Lee[1], S.H. Kim[1]
[1]Seoul National University Hospital, Radiology, Seoul, South Korea

Keywords Kidney · Angiomyolipoma · Renal cell carcinoma · PACS · Sonography

Purpose

Most angiomyolipoms (AMLs) are hyperechoic relative to the renal parenchyma, whereas most renal cell carcinomas (RCCs) are hypoechoic. However, RCCs and AMLs are indistinguishable in terms of tumor echogenicity because of the wide spectra of echogenicity of both tumors. Small RCCs (<3 cm) are predominantly hyperechoic and easily confused with AMLs [1, 2]. With CT, AMLs can be diagnosed with high accuracy by detecting the intratumoral fat component, and differentiation is seldom problematic in daily practice. However, 4.5–14 % of AMLs have no gross fat on CT, and are referred to as AMLs with minimal fat or non-fatty AMLs. Many non-fatty AMLs are not distinguishable from other hyperechoic tumors, such as RCCs, and usually diagnosed after surgery [3, 4]. Although ultrasonographic findings of non-fatty AMLs may be homogeneous, isoechoic, well-defined lesions [5], no studies have distinguished non-fatty AMLs from RCCs.

The aim of this study was to retrospectively evaluate the diagnostic value of measuring the RE of the mass to the renal sinus and cortex in differentiating small RCCs from AMLs with or without visible fat on ultrasonography by measuring ROIs in PACS (Fig. 1).

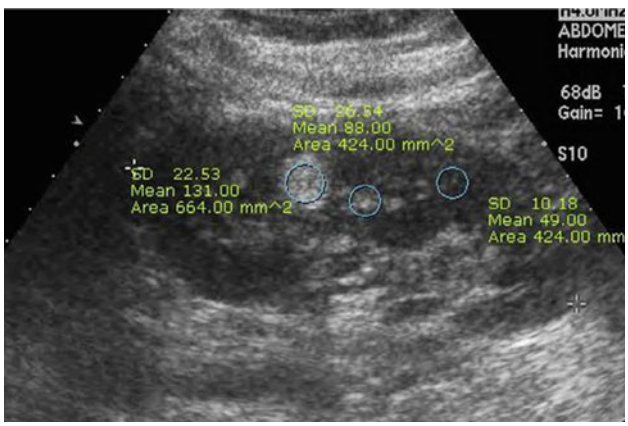

Fig. 1 Measurement of relative echogenicity of a small renal mass on PACS

Materials and Methods

Thirty-six cases of <3 cm, pathologically-proven RCCs and 42 cases of size-matched AMLs were enrolled. We measured the grayscale representing echogenicity of the mass, the renal cortex, and the sinus fat on PACS using a ROI cursor. The RE of the tumor was calculated by setting the grayscale of the renal cortex and sinus fat as 0 and 100 %, respectively. We compared REs of AMLs and RCCs, including subgroups of each tumor. ROC analyses between RCCs and AMLs or non-fatty AMLs were performed for obtaining diagnostic performance (Az value) of RE measurement and for extracting sensitivities of RE with fixed specificities of 90 and 95 %.

Results

The average patient age was similar between the RCC (52.4 years) and AML groups (55.1 years; $p = .364$). The female-to-male ratio was greater in the AML group (27:15) than the RCC group (14:22; $p < .01$). The mean diameter of RCCs was 2.2 cm (range, 0.7–3.0 cm). The mean diameter of the clear cell and non-clear cell types was 2.2 cm (SD, 0.68 cm) and 2.1 cm (SD, 0.59 cm), respectively ($p = 0.960$). The mean diameter of AMLs was 1.5 cm (range, 0.6–2.7 cm). The mean diameter of fatty AMLs and non-fatty AMLs was 1.6 cm (SD, 0.65 cm) and 1.4 cm (SD, 0.59 cm), respectively ($p = 0.836$).

The average RE of the AML and RCC groups were 99.0 % (SD, 26.8 %) and 44.1 % (SD, 36.5 %), respectively ($p < .001$). The REs of clear and non-clear cell RCCs were 39.2 % (SD, 41.8 %) and 51.0 % (SD, 27.4 %), respectively ($p = 0.124$). The REs of fatty and non-fatty AMLs were 106.3 % (SD, 25.6 %) and 86.0 % (SD, 24.4 %), respectively ($p = 0.027$). RE differences were also significant between the non-fatty AMLs and clear cell RCCs ($p < .05$) and the non-fatty AMLs and non-clear cell RCCs ($p < .05$).

The ROC curve analysis for differentiating RCCs from AMLs showed that RE has good diagnostic power (Az = 0.895 with 95 % CI, 0.820–0.970; $p < .01$). The optimal cutoff value of the RE was 68.5 %, with 91 % sensitivity and 81 % specificity. The cut-off RE values to differentiate AMLs from RCCs at set specificities of 90 and 95 % were 85.1 and 96.7 %, with sensitivities of 69 and 55 %, respectively. The ROC curve analysis for differentiating RCCs from non-fatty AMLs also showed that RE has good diagnostic power (Az = 0.840 with 95 % CI, 0.731–0.949; $p < .01$). The optimal cutoff value of RE was 56.8 %, with 80 % sensitivity and 64 % specificity. The cut-off RE values to differentiate non-fatty AMLs from RCCs at set specificities of 90 and 95 % were 85.5 and 96.7 %, with sensitivities of 53 and 40 %, respectively.

Conclusion

The measurement of RE on PACS shows that small AMLs, including non-fatty AMLs, have a significantly higher RE than small RCCs, regardless of the histologic type of RCC. With simplicity, convenience, and easy applicability of sonography, measurement of RE on PACS may be helpful in the differential diagnosis of small AMLs and RCCs.

References

[1] Yamashita Y, Ueno S, Makita O, et al. Hyperechoic renal tumors: anechoic rim and intratumoral cysts in US differentiation of renal cell carcinoma from angiomyolipoma. (1993) Radiology 188:179–182

[2] Zebedin D, Kammerhuber F, Uggowitzer MM, Szolar DH. Criteria for ultrasound differentiation of small angiomyolipomas (<or = 3 cm) and renal cell carcinomas. (1998) Rofo 169:627–632

[3] Kim JK, Kim SH, Jang YJ, et al. Renal angiomyolipoma with minimal fat: differentiation from other neoplasms at double-echo chemical shift FLASH MR Imaging. (2006) Radiology 239:174–180

[4] Milner J, McNeil B, Alioto J, et al. Fat poor renal angiomyolipoma: patient, computerized tomography and histological findings. (2006) J Urol 176:905–909
[5] Hosokawa Y, Kinouchi T, Sawai Y, et al. Renal angiomyolipoma with minimal fat. (2002) Int J Clin Oncol 7:120–123

Real-time reconstruction and visualization of navigated 3D ultrasound images

M. Kastrop[1], C. Winne[1], E. Keeve[1,2]
[1]Fraunhofer Institute for Production Systems and Design Technology IPK, Medical Technology, Berlin, Germany
[2]Charité, Universitätsmedizin Berlin, Maxillofacial Surgery and Clinical Navigation, Berlin, Germany

Keywords 3D ultrasound · Real-time reconstruction · GPGPU · Freehand acquisition

Purpose

The identification and assessment of tissues based on 2D ultrasound (US) images is demanding. It requires experience to recognize its shape and size. The physician is faced with the mentally challenging task of combining the 2D image data with the probe movement to derive a three-dimensional shape. Here 3D ultrasound enables an enhanced visualization of soft tissues that makes this effort obsolete. We realize 3D ultrasound by reconstructing and visualizing a 3D volume based on navigated 2D US images. This supports the physician by displaying the 3D US data in arbitrary slice or 3D views.

For an easy intraoperative use an immediate feedback of the reconstruction results is crucial. Therefore, the reconstruction and visualization must be performed in parallel to enable real-time update of the displayed reconstructed 3D data. To meet these requirements, we decided to realize the reconstruction algorithms and visualization methods on a graphics processing unit (GPU) which enables massive parallelism of calculations with a large number of processing units.

Methods

State-of-the-art technology offers application programming interfaces for massive parallel programming on GPUs. Our system uses CUDA for the voxel-based reconstruction algorithm [1] and OpenGL and GLSL for the visualization with a ray-caster. This combination benefits from the OpenGL interoperability interface of CUDA: it enables concurrent access to the same memory on the GPU by the reconstruction and visualization methods. This obviates the need for extra copy operations between GPU and main memory of the central processing unit (CPU) and is crucial for the real-time execution.

The single steps of our reconstruction algorithm are listed below. It updates the volume within the region that lies in between the last two 2D US images.

1. Upload the image data of two consecutive images into the GPU memory.
2. Determine voxels in the region of interest (ROI) between the two images: therefore, we cast rays through the columns of the volume that are oriented towards the same direction as the normal of the first image plane (see Fig. 1a). This will result in two intersection points per column that will both lead to concrete voxel positions again. All voxels of the related column that lie in between these two voxels are added to the ROI.
3. Compute interpolated gray values for all ROI voxels using a distance-weighted measure based on the gray values of the nearest pixels in the two images (see Fig. 1b).

An additional problem occurs when the probe is excessively moved and the current image position is located outside the initial 3D volume. To be still able to charge such kind of image data into the volume, we have introduced a shift operation that moves the volume according to the probe movement and shifts backwards the previously reconstructed 3D image data.

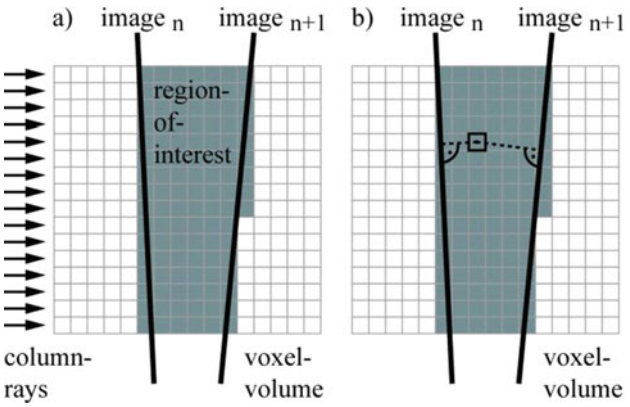

Fig. 1 **a** Determining voxels in ROI by casting rays through the volume; **b** Computing the voxel intensity by a distance-weighted sum of the nearest two pixels

In order to visualize the reconstruction result a ray-caster will frequently render the volume into an application window. Thereby the size of the window will take proportional effect on the duration of the rendering process, since the ray-caster operates on each pixel of the image plane.

Results

We evaluated our reconstruction using an upper mid-range graphics card and measured the duration of a single reconstruction update of the US volume, the number of processed voxels during reconstruction and the time to render the volume texture.

As input we have a PAL video stream of 2D US images with 25 fps and an image size of 720 × 576 pixels. The output is written to a 400 × 400 × 400 volume texture with a voxel size of 0.3 mm. The volume texture stores two 8-bit values per voxel, one for luminance and one for masking information.

Figure 2 shows the benchmark results—measured with an NVIDIA GeForce 580 GTX. The upper plot shows the reconstruction duration contrasting the number of updated voxels in the ROI. The mean reconstruction duration was determined with 7.1 ms (blue line) and the minimal and mean number of voxels in the region of interest per step (red line) amounted to 160,000 and 277,520, respectively. As can be seen from that plot the duration of reconstruction correlates well with the number of updated voxels in the ROI which increases

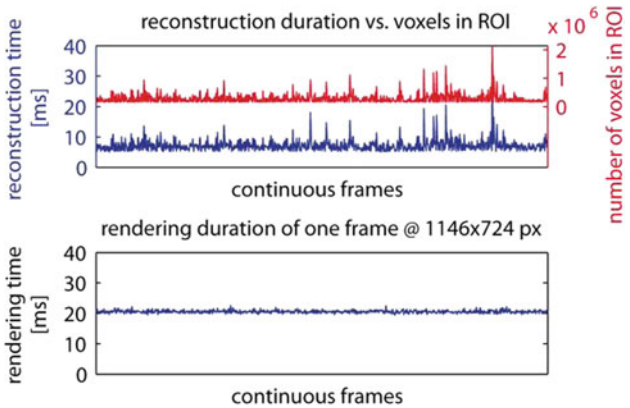

Fig. 2 Reconstruction duration versus voxels in ROI and rendering duration—measured with an NVIDIA GeForce 580 GTX

with larger probe velocity. Compared to [2] we achieve about the same speed but with a higher resolution in image and volume size.

The lower plot shows the rendering time of the volume within a window with a size of 1,146 × 724 pixels. The average of the measured values is 20.05 ms. Shift operations caused by the probe motion occur on average every 23 images in our test case and need about 160 ms on average.

The duration of the reconstruction and the maximum intensity projection (MIP) rendering in a sum is about 27.15 ms which is less than the 40 ms time-slot per image of the 25 frames-per-second video stream. Consequently our implementation delivers a real-time performance. Rarely occurring volume shifts that exceed the limit of 40 ms can be compensated quickly since there is still a gap of about 12 ms where the graphics card is not used by our implementation.

Conclusion

We present a new method for 3D reconstruction of 2D ultrasound images which uses graphics hardware to reconstruct and concurrently visualizes the resulting ultrasound volume data in real-time. The proposed reconstruction method updates the resulting ultrasound volume continuously, as new ultrasound images are present. This enables ultrasound 3D image data generation with immediate visual feedback for the physician. Measurements with current graphics hardware verify the real-time capability. Speed improvements of future graphics cards will be used to increase the size of the resulting volume as well as the reconstruction quality.

References

[1] Solberg OV, Lindseth F, Torp H, Blake RE, Nagelhus Hernes TA (2007) Freehand 3D ultrasound reconstruction algorithms—a review. Ultrasound in Medicine & Biology 33(7):991–1009

[2] Dai Y, Tian J, Dong D, Yan G, Zheng H (2010) Real-time visualized freehand 3D ultrasound reconstruction based on GPU. IEEE Transactions on Information Technology in Biomedicine 14(6):1338–1345

An improved method for hepato-renal ratio assessment in the diagnosis of hepatosteatosis: a feasibility study

A. Sboarina[1], S. Perandini[2], A. Fenzi[1]
[1]Department of Surgery Section of Medical Physics, University of Verona, Italy
[2]Department of Radiology, AOUI Verona, Italy

Keywords Hepatic-renal ratio · Steatosis · Ultrasound

Purpose

The hepato-renal ratio (HRR) is a non-invasive method for liver steatosis quantification based on ultrasound image analysis. Its effectiveness has been validated in literature by means of liver biopsy [1] and ^{1}H magnetic resonance spectroscopy [2].

In this paper we propose a new and improved method for ROI selection and HRR assessment, designed to minimize both inter-observer and inter-scan variability.

Materials and methods

The dataset comprises 98 images of 32 patients. For 23 patients, more than one scan was performed.

For every scan two regions of interest (ROIs) of the liver parenchyma and the renal cortex were selected. The ROIs had to be as homogeneous as possible and positioned as near as possible to the center of the image. ROI selection was performed by two operators (operator 1 and operator 2).

For the selection of ROIs three methods (implemented in MeVisLab) were used as follows:

1. Square: two square ROIs of about 1 cm^2 for the hepatic parenchyma, and 0.25 cm^2 for the renal cortex were selected. The centers of the ROIs were positioned at the same y-coordinate.

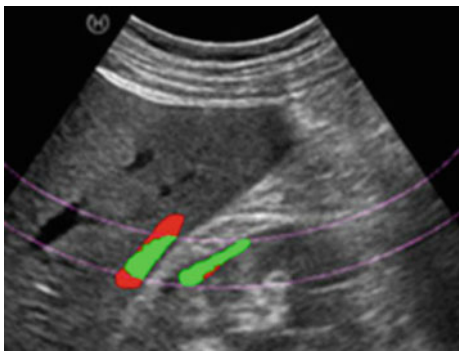

Fig. 1 ROI normalization: the ROIs segmented by the irregular method are shown in *red*. The normalized ROIs are overlaid in *green*. The fuchsia lines correspond to the outermost clusters which are common to the two ROIs

2. Ellipse: two ellipsoidal or circular ROIs were selected as large as possible and positioned approximately at the same depth. The selection was made by operator 1. Six months later, this operator repeated the selection, using the square method.
3. Irregular: two ROIs with free shape were selected as large as possible and positioned approximately at the same depth. The selection was made by operator 2.

The ROIs segmented by the ellipse and irregular method were post-processed. Post-processing consists of ROIs normalization and of smoothing out the related normalized histograms (implemented in Matlab). ROI normalization (Fig. 1) is obtained from carrying out two tasks: first the distance of every image pixel from the probe was calculated by the Euclidean distance transform. Secondly for every cluster (set of image pixels which have the same distance from the probe) two groups of pixels were selected belonging respectively to the liver ROI and to the kidney ROI; the largest group was reduced to the size of the smallest eliminating its outermost pixels. The first task was implemented in MeVisLab and the second task was achieved using an automatic procedure implemented in Matlab

In our study only the scans with normalized ROI above 211 pixels were considered. HRR is defined as the ratio of the gray scale mean value of the pixels within two given ROIs of the liver and kidney.For the square ROIs the HRR was calculated by the related normalized histograms. For the ellipse and Irregular ROIs the HRR was evaluated on the basis of the related smoothed histograms resulting from post-processing. The square method is analogous to the one presented in [2] and was therefore used as a reference for HRR evaluation. The Ellipse method is a specific application of the irregular method and was used to verify the reproducibility of the new techniques introduced in this study. In order to evaluate inter-scan variability (variability of HRR for different US scans in the same patient) the results obtained from the two scans of the same patient with maximum absolute difference of the HRR were compared. The analysis was carried out by studying: the mean difference (MD) the lower limit of agreement (LL) and upper limit of agreement (UL) according to the definitions of Bland and Altman and the "Wilcoxon rank sum test for equal medians". A p value <0.05 was considered to indicate statistical significance.

Results

In the experiment we encountered numerous difficulties using the square and the ellipse methods, often obliging operators to repeat the selection. Using the free boundary selection method (Irregular) facilitated the selection of the ROIs, enabling larger areas to be analyzed. In particular the mean numbers of pixels of the square ROIs were: 718 for the liver and 177 for the kidney; the mean number of pixels of the normalized ROIs were: 643 for the ROIs selected by the

Table 1 Results of the HRR comparisons

	LL	UL	MD	*p* Value
Irregular^{PP} versus square	−0.54	0.53	−0.001	0.52
Ellipse^{PP} versus square	−0.54	0.48	−0.03	0.14
Ellipse^{PP} versus irregular^{pp}	−0.52	0.46	−0.03	0.46

Ellipse method and 1,324 for the ROIs selected by the irregular method.

The main results of the HRR comparisons obtained by different methods are summarized in Table 1. For the sake of brevity we give the HRR calculation based on the post-processing of the ROIs with apex PP.

In the assessment of HRR inter-scan variability the LL UL MD and *p* Values were respectively: −0.76, 0.95, 0.10 and 0.25 for the Square method; −0.73,0.89, 0.08 and 0.25 for the Ellipse^{PP} method; −0.45, 0.49, 0.02 and 0.39 for the Irregular^{PP} method.

Conclusions

The differences between the HRRs obtained by the Ellipse^{PP} and Irregular^{PP} methods and those obtained with the Square method are not statistically significant. The respective ranges of agreement and the modulus of the mean differences (for both comparisons: Irregular ^{PP} vs Square and Ellipse^{PP} vsSquare) are lower than those resulting from the inter-scan analysis of the reference method (Square method) demonstrating comparable clinical efficacy.

The differences between the HRRs obtained by the Ellipse^{PP} and Irregular^{PP} methods are not statistically significant demonstrating the reproducibility of the new technique.

In the inter-scan analysis the Irregular^{PP} method gave a smaller mean difference and range of agreement than Square one. This is probably due to the large ROIs provided by the Irregular method. It is reasonable to assume that the larger the ROI sizes, the better the representation of the pathology. Furthermore this technique leaves the operator free to focus only on the representativeness and homogeneity of the ROIs without worrying about their accurate positioning in the image, their shape and/or maximum dimension, making the procedure fast and user friendly.

References

[1] de Almeida E, Borges VF, Diniz AL, Cotrim HP, et al.(2013) Sonographic Hepatorenal Ratio: A Noninvasive Method to Diagnose Nonalcoholic Steatosis. J Clin Ultrasound 41(1):18–25

[2] Mancini M, Prinster A, Annuzzi G, et al. (2009) Sonographic hepatic-renal ratio as indicator of hepatic steatosis: comparison with ^{1}H magnetic resonance spectroscopy. Metabolism 58(12): 1724–30

Catheterization for balloon-occluded retrograde transvenous obliteration guided by fly-through module of New Virtual Endoscopic System

M. Tomikawa[1], T. Akahoshi[2], M. Oda[3], R. Kumashiro[1], M. Uemura[4], S. Ieiri[1], K. Mori[5], M. Hashizume[1,2,4]

[1]Kyushu University Hospital, Department of Advanced Medicine and Innovative Technology, Fukuoka, Japan

[2]Faculty of Medical Sciences, Kyushu University, Department of Advanced Medical Initiatives, Fukuoka, Japan

[3]Graduate School of Information Science, Nagoya University, Department of Media Science, Nagoya, Japan

[4]Center for Advanced Medical Innovation, Kyushu University, Fukuoka, Japan

[5]Nagoya University, Information and Communications Headquarters, Nagoya, Japan

Keywords Catheterization · B-RTO · Virtual endoscopy · Navigation

Purpose

Balloon-occluded retrograde transvenous obliteration (BRTO) is an endovascular technique that was refined in Japan as one of the effective therapeutic options in the management of bleeding gastric varix in portal hypertensive patients. BRTO is also an effective therapy for sclerosis of de novo portosystemic shunts complicated by hepatic encephalopathy. A BRTO procedure involves occlusion of outflow veins of the de novo portosystemic shunts, such as gastrorenal and splenorenal shunt, using an occlusion balloon followed by the injection of sclerosing agent directly into the outflow veins endovascularly. While de novo vasculatures in portal hypertensive patients are often highly complex with their forms and numerous branches, advancing a balloon-catheter as deep as possible into the outflow veins is crucial but often found out to be a technically tough procedure. Although the ordinary preoperative images can be utilized as a simulation for the procedure, manipulation of the catheter is often difficult and BRTO sometimes ends up unsuccessful. New Virtual Endoscopic System (NewVES) is a computer-generated simulation of endoscopic images derived from multidetector-row computed tomography (MDCT) data sets. This technique allows exploration of the inner surfaces of the vasculatures; this information can be helpful during the catheterization for BRTO. However, no application with virtual endoscopic images to the BRTO procedures has been reported. We herein describe the preliminary report of adapting NewVES, especially its fly-through vision and automatic fly-through path track retrieval to performing BRTO.

Methods

Patients and data acquisition: We studied 5 consecutive portal hypertensive patients with either gastric varix or hepatic encephalopathy undergoing BRTO. All patients had previously undergone MDCT to acquire the data sets for NewVES to generate virtual endoscopy. To acquire contrast-enhanced MDCT images, nonionic contrast agent was infused rapidly at a rate of 40 mg I/kg for 25 s using an automated injector. Early venous phase scanning with the slice thickness of 1 mm were started 30 s after early arterial phase scanning. *Generation of virtual endoscopy:* The vessel wall is well defined with NewVES, as it has a significantly lower density than that of the contrast-enhanced lumen. The intensity threshold is set at the largest value that gives a reasonable result. The automatic fly-through path track retrieval that was superimposed on a volume-rendered 3D reconstruction with the simultaneous display of multiplanar reformation and endoscopic fly-through view enabled an accurate simulation of the catheterization procedures. *BRTO procedures:* After access of the right femoral vein using standard angiographic technique and placement of a 6–12 French sheath, BRTO was performed with a balloon catheter introduced through the sheath under biplane anteroposterior and lateral X-ray fluoroscopy. The catheter was advanced through left renal vein to a complicatedly developed abnormal vein to be occluded. After confirming the satisfactory selective position of the tip-mounted balloon of the catheter, the sclerosing agent was injected endovascularly. *Data analyses:* We have compared the complexity of major portosystemic shunt (single or multiple), the successful rate and the procedural duration of BRTO of these 5 patients, with those factors of 11 patients who had undergone BRTO without the NewVES simulation.

Results

We performed BRTO with the simulation monitor put aside the fluoroscopic operative table. During the procedures on the patients, the monitor clearly showed the direction that the catheter should be advanced to with the automatic fly-through path track retrieval that was superimposed on a volume-rendered 3D reconstruction, and the NewVES simulation was found to be sufficient to accurately advance the catheter (Fig. 1). We were able to observe the inner space, fly through the complex outflow vein, and continue navigating deeply into the shunt or varix. In the four successful cases, manipulation of the catheter was performed without any difficulty under the guidance

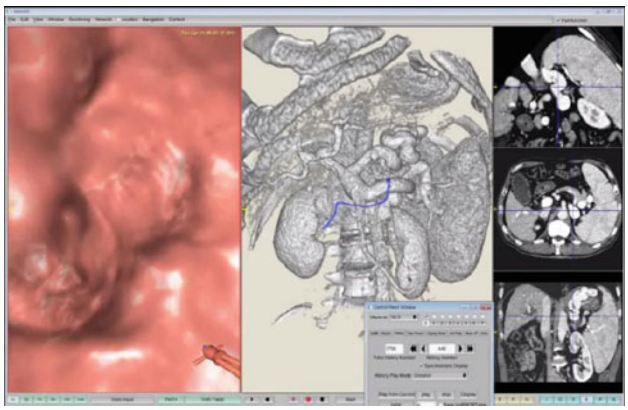

Fig. 1 A monitor shows a fly-through view moving ahead (*left*), and the automatic fly-through path track retrieval superimposed on a volume-rendered 3D reconstruction is indicated in the middle picture

Table 1 Factors on BRTO between the procedures without fly-through view simulation and those with simulation

Factor	Without simulation (n=11)	With simulation (n=5)	P value
Complexity of major portosystemic shunt (single / multiple)	3 / 8	2 / 3	ns
Successful / unsuccessful	8 / 3	4 / 1	ns
Procedural duration (minute)	191	143	0.23

of the simulation monitor. There were no differences between the patients with the simulation and the patients without simulation in the complexity of major portosystemic shunt, the successful rate and the procedural duration of BRTO (Table 1). Postoperative outcomes for the patients were excellent and they were discharged from our hospital approximately 7 days after BRTO.

Conclusion

Virtual endoscopy by NewVES provides unique information regarding the ductal lumen and the direction of catheterization that is of use for the shunt occlusion. This study has however several limitations. Because of small sample size, there were no significant differences in any factors. It might be expected that the duration would be shorter and the successful rate would increase while the complexity of the de novo portosystemic shunt remains unchanged. Furthermore, NewVES can be expected to predict the success of BRTO procedure. Although the result was preliminary, the fly-through module of NewVES was feasible and possibly useful. In future studies with adequate numbers of patients, elaborated method for accurate simulation of the catheterization of BRTO would be developed.

Development of an assisted diagnostic system for retinopathy that applies temporal subtraction to funduscopy images

Y. Ban[1], K. Abe[1], Y. Donomae[1], H. Takeo[1], Y. Takahashi[2], Y. Nagai[3]
[1]Kanagawa Institute of Technology, Electrical and Electronic Engineering, Atsugi, Japan
[2]Takahashi Eye Clinic, Isehara, Japan
[3]National Cancer Center, Radiology, Tokyo, Japan

Keywords Funduscopy image · Applies time lapse subtraction · Diabetic retinopathy · Affine transformation

Purpose

Recently, funduscopic image examinations using a fundus camera have become a widely performed part of medical checkups. The number of people having such examinations for early detection of diabetic retinopathy, a cause of blindness, is also rising. Diabetic retinopathy is one of the three major diabetic complications, which have a high probability of occurring within ten years of start of the disease.

This study proposes a method that utilizes continuous funduscopic images of a patient to indicate quantitatively the relation between the patient's condition and the differential value between two images. Quantitatively indicating the continuous changes in the patient's funduscopy images serves the purpose of assisting physicians in diagnosing diabetic retinopathy.

Methods

Blood vessel intersections are extracted from multiple continuous funduscopy images taken for a single person. After performing alignment using the affine transformation, the differential value between the first examination image, Fig. 1a, and a time lapse image, Fig. 1b is obtained and the results evaluated.

(1) Pre-processing of target image

Images used are 256 level RGB color images, each with a resolution of 1,604 × 1,214 pixels.

Next, color funduscopy images are converted into gray-scale images comprising only the Green component [1]. This is done because the contrast between blood vessel regions and other regions is increased on gray-scale images generated from the Green component. These images are then used for the following processing.

(2) Extracting blood vessels and characteristic points

To extract blood vessels, binarization is performed using the pixel value for blood vessels as the threshold value. To eliminate noise during this process, opening is executed using 8-line structuring elements extending from the origin. Next, 8-connected thinning is performed. Any pixel of an image subjected to thinning that has at least 3 pixels around it is either a branch point or an intersection point. Such points are regarded as characteristic points.

(3) Image alignment using the affine transformation (linear transformation)

To positionally align the original image f(xi,yi) with the continuous change image g(xi,yi), image g'(xi,yi), which was subjected to affine transformation (linear transformation), is obtained. The formula is as follows:

$$X_i = m * x_i * \cos - m * y_i * \sin + A$$
$$Y_i = m * x_i * \sin + m * y_i * \cos + B$$

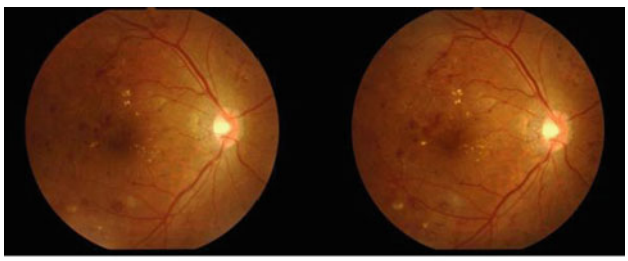

(a)The first examination image (b)A time lapse image

Fig. 1 Funduscopy image

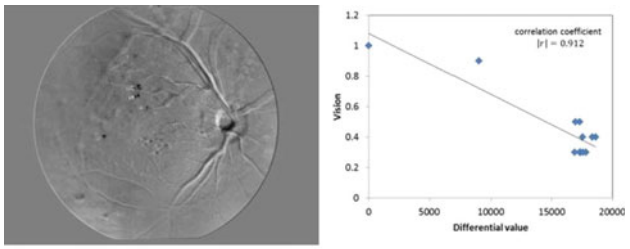

Fig. 2 Differential image and differential value versus vision

$$\begin{pmatrix} X_i \\ Y_i \end{pmatrix} = m \begin{pmatrix} \cos\theta & -\sin\theta \\ \sin\theta & \cos\theta \end{pmatrix} \begin{pmatrix} x_i \\ y_i \end{pmatrix} + \begin{pmatrix} A \\ B \end{pmatrix}$$

where scaling coefficient m is set to 1.

In the taking of a funduscopy photograph for fundus examination, the forehead and chin are held in place by the funduscopy stand. As long as the same stand is used, any positional shift is mostly limited to eye movement. The above formula was therefore defined because it can be assumed that positioning will comprise only simple rotation or parallel shift involving no scaling.

(4) Generating the differential image

The differential image is generated from the images aligned in (3), g' and f.

(5) Calculation of the differential value

The mean sum of squares of the pixel value of the differential image is calculated as the differential value.

Results

The proposed method was tested by applying it to 12 funduscopy images comprising 1 first examination image and 11 time lapse change images. In this study, only images for the right eye were used. Figure 2a shows an image obtained by the proposed method.

Figure 2b shows the relationship between differential value for each time lapse change image-first examination image alignment and vision at each time.

A correlation coefficient absolute value of 0.912 for differential value and vision was obtained, suggesting a high correlation.

Conclusion

We succeeded in developing a method for obtaining the differential value of a first examination image and continuous change funduscopic image that we propose for an assisted diagnostic system for diabetic retinopathy. Using this method, a high correlation was found between the continuous change of retinopathy and vision.

Reference

[1] J.J. Staal, M.D. Abramoff, M. Niemejier, M.A. Viergever, B. van Ginneken, "Ridge-based vessel segmentation in color images of the retina," IEEE Trans. On Med Imaging, vol.23, no.4, pp.501–509, 2004

Detection of retina NFL and RPE layers in OCT images

W. Wieclawek[1], M. Rudzki[1]
[1]Silesian University of Technology, Department of Informatics and Medical Equipment, Gliwice, Poland

Keywords Optical coherence tomography · Retina · Segmentation · Edge detection · Layers segmentation

Purpose

One of important steps during analysis of Optical Coherence Tomography (OCT) scans from ophthalmology examination is detection of retina layers. The anatomy of retina consists of 12 layers oriented almost parallel to each other. However, only 8 of them are important during medical diagnosis of pathologies, from which worth mentioning are: full-thickness macular hole, central serous chorioretinopathy, macular edema, epiretinal membrane, vitreomacular traction and retinitis pigmentosa and chloroquine retinopathy [1]. Most important layers are visible and marked in Fig. 1.

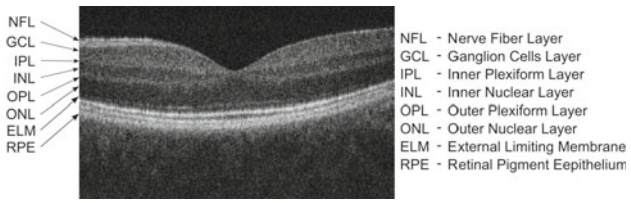

Fig. 1 The retina layers for typical OCT scan

The difficulty during OCT image analysis is localization of the layers and measurement of distances between them. Additionally, high resolution of OCT scans causes considerable local noise. In this study the algorithm to fully automatic segmentation of three basic layers is proposed.

Methods

The algorithm performs layers detection in two stages: 1. preprocessing, 2. detection of layers boundaries, 3. correction of detected boundaries if sections are discontinuous.

The first step of proposed algorithm is image quality improvement because high resolution of scans causes undesirable granularity. Typical methods like spatial averaging or median filtering are insufficient, because localization of edges becomes changed. Only anisotropic diffusion seems practical. Anisotropic diffusion not only reduces local noise, but also ensures invariance of edges location [2]. In the presented method a modified anisotropic diffusion where horizontal direction of smoothing is preferred is used.

Layers localization is then performed by analysis of image profiles taken column-wise from image obtained after preprocessing (Fig. 2a). Starting from upper image border the first large-scale gradient maximum represents NFL and first large-scale local maximum represents RPE layer (Fig. 2b). The filtered image is also subject to Fuzzy c-Means clustering (FCM) into 3 classes (low, medium and high intensity regions). In FCM for defuzzification the operator maximum is used. For initial placement of the layers boundaries results from profile analysis are used. Inter-class boundaries found after

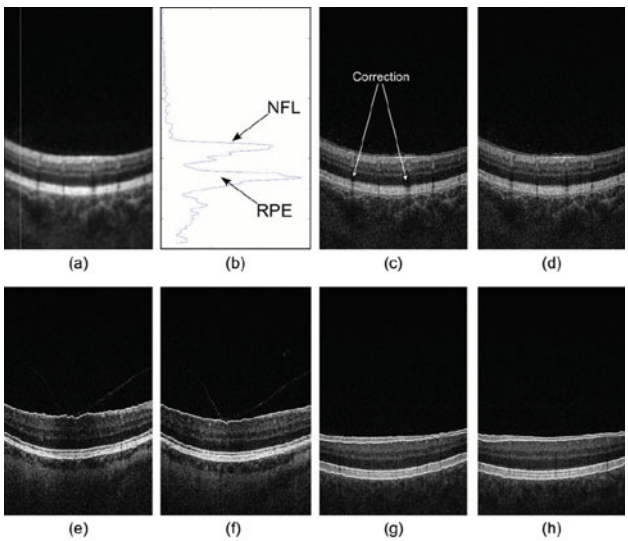

Fig. 2 Segmentation of retina layers in OCT images

defuzzification are utilized to obtain final localizations of layers RPE and NFL borders.

The last stage of the method is a correction procedure of layers segments found in the second stage. This step is required in image regions containing considerable shadows caused by blood vessels (Fig. 2c).Correction step uses local differences between coordinates of pixels detected as boundaries. If there is large difference between segments this indicates the segment has to be corrected. After region of interest selection around discontinuous segment its coordinates are recalculated using the diffused image and dominant direction of the layer (Fig. 2d).

Results

Proposed algorithm was evaluated using OCT images without pathologies as well as containing minor ones that do not cause large discontinuities in layers. Exemplary results are presented in Fig. 2d–h. It can be seen that NFL and RPE layers are correctly segmented. Used correction stage ensures that proper results are also obtained in case when layers are discontinuous due to considerable shadows from vasculature (Fig. 2c, d). The correction stage ensures proper delineation of layers.The developed method is still in premature stage for full quantitative analysis.

Initial studies were conducted on GCL layer detection and decomposition of RPE layer into sub-layers (Fig. 2e–h). Outcomes seem promising and further research is being conducted in this matter.

Conclusion

Decomposition of retina into its anatomical layers is medically important and frequently encountered in literature problem which is still not solved. The method for automatic detection of two basic layers presented in this paper follows this trend. Performance of the algorithm seems to be effective for OCT image series without considerable pathologies. The method is a starting point for further research aimed at not only detection but also measurement of their thickness.

Acknowledgement

Authors would like to thank OPTOPOL Technology S.A. Zawiercie, Poland, for valuable cooperation and providing the images.

References

[1] Ko TH, Fujimoto JG, Schuman JS, Paunescu LA, Kowalevicz AM, Hartl I, Drexler W, Wollstein G, Ishikawa H, Duker JS (2005) Comparison of Ultrahigh- and Standard- Resolution Optical Coherence Tomography for Imaging Macular Patholog. Ophthalmology 112(11):1922.e1–1922.e15.

[2] Więcławek W (2010) Quality Improvement of the OCT Images. In Computer Assisted Radiology and Surgery, 23rd International Congress and Exhibition, Int J CARS 5 (Suppl 1):S418–419.

Anatomical Dependence of Stress–Strain States in the Human Stomach

A. Yasser[1], R. Miftahof[1]

[1]Arabian Gulf University, Physiology, Manama, Bahrain

Keywords Computer-aided detection · Mallory-weiss syndrome · Human stomach · Mathematical model

Purpose

High endurance and enormous functionality of abdominal viscera depend on the biomechanical properties of their tissues and specific arrangements of their internal components. The distinctive anatomical appearance of organs is strongly influenced by the force systems to which they are subjected and correlates with their structural advantages. Anatomically, the human stomach possesses three distinct shapes: the "bull-horn", the "fish hook" and the "intermediate". Physiological responses of the stomach to internal and external mechanical stimuli (pressure) depend entirely on the inherent activity of histomorphological elements and their topographical organization within gastric tissue.

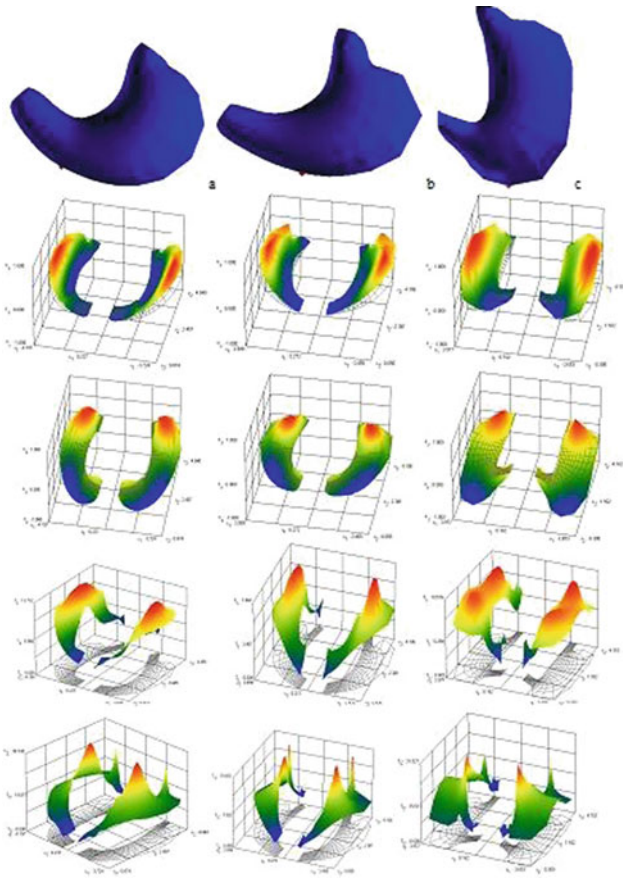

Fig. 1 The axial deformation and circumferential force distribution in the "bull-horn" (*1*), "fish-hook" (*2*), intermediate (*3*) shapes of the stomach at $t = 1.6$ s of the dynamic process of loading

Mallory-Weiss syndrome—a pathological condition—is characterized by tears of the mucosal and submucosal layers of the stomach and is associated with lifethreatening gastrointestinal bleeding. It affects predominantly males, (M:F = 1.5:1) and accounts for approximately 5 % of all upper gastrointestinal bleedings [1, 2]. An increase in intraabdominal pressure, along with the intraluminal pressure of the stomach, changes in mechanical tensile properties of the wallper se [3] are thought to contribute to the development of these tears. However, the exact mechanism of these tears remains unknown.

The aim of this study is to study the dynamics of stress–strain distribution in the human stomach of different anatomical shapes and evaluate their role in the development of mucosal and submucosal tears observed in Mallory-Weiss syndrome.

Methods

A biomechanical model of the stomach that incorporated the detailed anatomical, physiological and mechanical properties of the tissue and organ's function was constructed. The dynamics of stress–strain distribution in the human stomach of the three different anatomical configurations subjected to intraluminal pressure changes was analyzed using ABS Technologies® computational platform.

Results

Results of numerical simulations revealed differences in the dynamics of stress–strain distribution in the stomach among the various anatomical shapes.Wrinkling and the formation of creases were observed

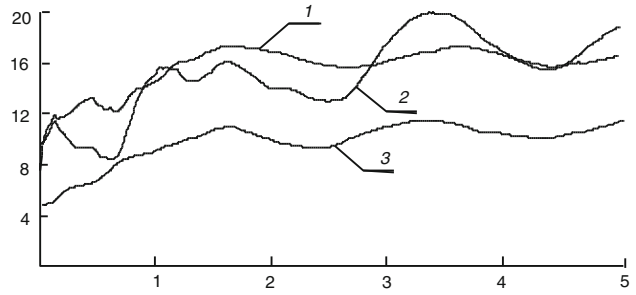

Fig. 2 Dynamics of total force changes in the lesser curvature of the stomach under intraluminal pressure loading. Here: *1*—"bull horn", *2*—"fish hook", *3*—intermediate shape

in the cardiac region of the stomach in all three shapes to varying degrees. Zero strain values were recorded in these regions. Uniaxial deformations in the "bull horn" stomach were seen along the lesser curvature and the antrum-pyloric region. In the "fish hook" and intermediate shape areas of uniaxial deformation extended beyond the lesser curvature to include most of the greater and a small part in the fundus (Fig. 1). The high level of stress was recorded along the cadiac notch in both the "hook-shaped" and the "bull-horn" stomach and along the lesser curvature in the intermediate-shape organ (Fig. 2).

Conclusion

The pattern of stress–strain distribution in the stomach provides valuable quantitative, along with qualitative, information about the pathogenesis of blunt abdominal trauma with rupture of the stomach wall, e.g., Mallory-Weiss Syndrome and separation of the stomach from the esophagus. Knowledge of the dynamics of stress–strain development in different shaped stomachs helps improve diagnosis of trauma of the stomach and also assists in establishing effective, rational, preventive measures.

Acknowledgments

This work was in part supported by a donation from Al Baraka Banking Group B.S.C., Manama, Bahrain. We also thank AGU for supporting our research endeavor.

References

[1] John DJB, Masterton JP (1974) The Mallory-Weiss syndrome. Br Med J 1:140–143.

[2] Akhtar AJ, Padda MS (2011) Natural history of Mallory-Weiss tears in African American and Hispanic patients. J Natl Med Assosc 5:103

[3] Egorov VI et al. (2002) Mechanical properties of the human gastrointestinal tract. J Biomech 35:1417–1425

Browse the Human in 3D view on tablets—Web-based software tool AnatomyMap serves educational purposes particular in pre-clinical teaching environment

R. Unterhinninghofen[1], R. Talanow[2], F. Rengier[3], S. Doll[4], F. Giesel[2]
[1]Kalruher Institute of Technology (KIT), Institut für Anthropomatik, Karlsruhe, Germany
[2]University Hospital Heidelberg, Nuclear Medicine, Heidelberg, Germany
[3]University Hospital Heidelberg, Diagnostic and Interventional Radiology, Heidelberg, Germany
[4]University of Heidelberg, Anatomy, Germany, Germany

Keywords Medical education · Anatomy · 3D volume rendering · CT data

Purpose

High-quality volume rendering of CT data produces appealing views of the human body. While commercial workstations are designed to support diagnostics or therapy planning, our in-house developed web-based software tool AnatomyMap serves educational purposes.

Methods

Data is displayed in 2D and 3D views together with labels of anatomical structures. The user can scroll, rotate, zoom, pan, trim, or change window/level. For each structure an appropriate view is predefined that can be reached in an animated flight. In exercise mode the user assigns names to empty labels using drag'n drop. The server is based on our framework MEDIFRAME supporting interactive server-side rendering and streaming over the web. The client is a Microsoft Silverlight application.

Results

Until now, 30 CT datasets of different body parts, including head, neck, thorax, abdomen, and extremities were manually labeled with (normal) anatomical structures. Additionally, 12 CT datasets were labeled with specific pathological structures.

Conclusion

In anatomy classes AnatomyMap proved to be an excellent and motivating extension to the anatomical atlas. In its web-based version it may serve as ubiquitous learning tool for students or continuing education